

1 A search for sparticles in zero lepton final states

2 Russell W. Smith

3 Submitted in partial fulfillment of the

4 requirements for the degree of

5 Doctor of Philosophy

6 in the Graduate School of Arts and Sciences

7 COLUMBIA UNIVERSITY

8 2016

9

© 2016

10

Russell W. Smith

11

All rights reserved

12

## ABSTRACT

13

A search for sparticles in zero lepton final states

14

Russell W. Smith

15 TODO : Here's where your abstract will eventually go. The above text is all in the  
16 center, but the abstract itself should be written as a regular paragraph on the page,  
17 and it should not have indentation. Just replace this text.



---

*Contents*

19	<b>Contents</b>	i
20	<b>1 Introduction</b>	1
21	<b>2 The Standard Model</b>	5
22	2.1 Overview	5
23	2.2 Field Content	5
24	2.3 Deficiencies of the Standard Model	15
25	<b>3 Supersymmetry</b>	21
26	3.1 Supersymmetric theories : from space to superspace	21
27	3.2 Minimally Supersymmetric Standard Model	24
28	3.3 Phenomenology	30
29	3.4 How SUSY solves the problems with the SM	32
30	3.5 Conclusions	34
31	<b>4 The Large Hadron Collider</b>	37
32	4.1 Basics of Accelerator Physics	37
33	4.2 Accelerator Complex	40
34	4.3 Large Hadron Collider	41
35	4.4 Dataset Delivered by the LHC	43
36	<b>5 The ATLAS detector</b>	49

37	5.1	Magnets	50
38	5.2	Inner Detector	52
39	5.3	Calorimetry	56
40	5.4	Muon Spectrometer	60
41	5.5	Trigger System	65
42	<b>6</b>	<b>Object Reconstruction</b>	<b>71</b>
43	6.1	Primitive Object Reconstruction	71
44	6.2	Physics Object Reconstruction and Quality Identification	77
45	<b>7</b>	<b>Recursive Jigsaw Reconstruction</b>	<b>103</b>
46	7.1	Razor variables	103
47	7.2	Recursive Jigsaw Reconstruction	108
48	7.3	Variables used in the search for zero lepton SUSY	114
49	<b>8</b>	<b>A search for supersymmetric particles in zero lepton final states with the Recursive Jigsaw Technique</b>	<b>121</b>
50	8.1	Simulation samples	121
51	8.2	Event selection	123
52	8.3	Background estimation	130
54	<b>9</b>	<b>Results</b>	<b>157</b>
55	9.1	Signal region distributions	157
56	9.2	Systematic Uncertainties	160
57	9.3	Limits and Model-dependent Exclusions	162
58	<b>Conclusion</b>		<b>169</b>
59	9.4	New Section	169
60	<b>Bibliography</b>		<b>171</b>

61	<b>Additional N-1 plots</b>	<b>185</b>
62	Compressed region N-1 plots	185



---

*Acknowledgements*



---

*Dedication*



*Introduction*

67 Particle physics is a remarkably successful field of scientific inquiry. The ability to  
 68 precisely predict the properties of a exceedingly wide range of physical phenomena,  
 69 such as the description of the cosmic microwave background [1, 2], the understanding  
 70 of the anomalous magnetic dipole moment of the electron [3, 4], and the measurement  
 71 of the number of weakly-interacting neutrino flavors [5] is truly amazing.

72 The theory that has allowed this range of predictions is the *Standard Model*  
 73 of particle physics (SM). The Standard Model combines the electroweak theory of  
 74 Glashow, Weinberg, and Salam [6–8] with the theory of the strong interactions, as  
 75 first envisioned by Gell-Mann and Zweig [9, 10]. This quantum field theory (QFT)  
 76 contains a number of particles, whose interactions describe phenomena up to the TeV  
 77 scale. These particles are manifestations of the fields of the Standard Model, after  
 78 application of the Higgs Mechanism. The particle content of the SM consists only of  
 79 six quarks, six leptons, four gauge bosons, and a scalar Higgs boson.

80 The Standard Model has some theoretical and experimental deficiencies. The SM  
 81 contains 26 free parameters<sup>1</sup>. We would like to understand these free parameters  
 82 in terms of a more fundamental theory.

83 The major theoretical concern of the Standard Model, as it pertains to this thesis,  
 84 is the *hierarchy problem* [11–15]. The light mass of the Higgs boson (125 GeV) should  
 85 be quadratically dependent on the scale of UV physics, due to the quantum corrections

---

<sup>1</sup>This is the Standard Model corrected to include neutrino masses. These parameters are the fermion masses (6 leptons, 6 quarks), CKM and PMNS mixing angles (8 angles, 2 CP-violating phases), W/Z/Higgs masses (3), the Higgs field expectation value, and the couplings of the strong, weak, and electromagnetic forces (3  $\alpha_{force}$  ).

86 from high-energy physics processes. The most perplexing experimental issue is the  
87 existence of *dark matter*, as demonstrated by galactic rotation curves [16–22]. This  
88 data has shown that there exists additional matter which has not yet been seen  
89 interacting with the particles of the Standard Model. There is no particle in the SM  
90 which can act as a candidate for dark matter.

91 Both of these major issues, as well as numerous others, can be solved by the  
92 introduction of *supersymmetry* (SUSY) [15, 23–35]. In supersymmetric theories, each  
93 SM particles has a so-called *superpartner*, or sparticle partner, differing from given SM  
94 particle by 1/2 in spin. These theories solve the hierarchy problem, since the quantum  
95 corrections induced from the superpartners exactly cancel those induced by the SM  
96 particles. In addition, these theories are usually constructed assuming *R*–parity,  
97 which can be thought of as the “charge” of supersymmetry, with SM particles having  
98  $R = 1$  and sparticles having  $R = -1$ . In collider experiments, since the incoming  
99 SM particles have total  $R = 1$ , the resulting sparticles are produced in pairs. This  
100 produces a rich phenomenology, which is characterized by significant hadronic activity  
101 and large missing transverse energy ( $E_T^{\text{miss}}$ ), which provide significant discrimination  
102 against SM backgrounds [36].

103 Despite the power of searches for supersymmetry where  $E_T^{\text{miss}}$  is a primary  
104 discriminating variable, there has been significant interest in the use of other variables  
105 to discriminate against SM backgrounds. These include searches employing variables  
106 such as  $\alpha_T$ ,  $M_{T,2}$ , and the razor variables ( $M_R, R^2$ ) [37–47]. In this thesis, we  
107 will present the first search for supersymmetry using the novel Recursive Jigsaw  
108 Reconstruction (RJR) technique. RJR can be considered the conceptual successor  
109 of the razor variables. We impose a particular final state “decay tree” on an events,  
110 which roughly corresponds to a simplified Feynmann diagram in decays containing  
111 weakly-interacting particles. We account for the missing degrees of freedom associated  
112 with weakly-interacting particles by a series of simplifying assumptions, which allow

113 us to calculate our variables of interest at each step in the decay tree. This allows  
114 an unprecedented understanding of the internal structure of the decay and additional  
115 variables to reject Standard Model backgrounds.

116 This thesis describes a search for the superpartners of the gluon and quarks, the  
117 gluino and squarks, in final states with zero leptons, with  $13.3 \text{ fb}^{-1}$  of data using  
118 the ATLAS detector. We organize the thesis as follows. The theoretical foundations  
119 of the Standard Model and supersymmetry are described in Chapters 2 and 3. The  
120 Large Hadron Collider and the ATLAS detector are presented in Chapters 4 and 5.  
121 The reconstruction of physics objects is presented in Chapter 6. Chapter 7 provides  
122 a detailed description of Recursive Jigsaw Reconstruction and a description of the  
123 variables used for the particular search presented in this thesis. Chapter 8 presents  
124 the details of the analysis, including details of the dataset, object reconstruction,  
125 and selections used. In Chapter 9, the final results are presented; since there is no  
126 evidence for a supersymmetric signal in the analysis, we present the final exclusion  
127 curves in simplified supersymmetric models.



*The Standard Model*130 **2.1 Overview**

131 The Standard Model (SM) is another name for a theory of the internal symmetry  
 132 group  $SU(3)_C \otimes SU(2)_L \otimes U(1)_Y$  and its associated set of parameters. The SM is the  
 133 culmination of years of work in both theoretical and experimental particle physics. In  
 134 this thesis, we take the view that theorists construct a model with the field content and  
 135 symmetries as inputs, and write down the most general Lagrangian consistent with  
 136 those symmetries. Assuming this model is compatible with nature (in particular, the  
 137 predictions of the model are consistent with previous experiments), experimentalists  
 138 are responsible for testing the parameters by measurements.

139 Additional theoretical background is in ?? . The philosophy and notations are  
 140 inspired by [48, 49].

141 **2.2 Field Content**

The Standard Model field content is

$$\begin{aligned} \text{Fermions} &: Q_L(3, 2)_{+1/3}, U_R(3, 1)_{+4/3}, D_R(3, 1)_{-2/3}, L_L(1, 2)_{-1}, E_R(1, 1)_{-2} \\ \text{Scalar (Higgs)} &: \phi(1, 2)_{+1} \\ \text{Vector Fields} &: G^\mu(8, 1)_0, W^\mu(1, 3)_0, B^\mu(1, 1)_0 \end{aligned} \tag{2.1}$$

142 where the  $(A, B)_Y$  notation represents the irreducible representation under  $SU(3)$   
 143 and  $SU(2)$ , with  $Y$  being the electroweak hypercharge. Each of these fermion fields

144 has an additional index, representing the three generation of fermions.

145 We observed that  $Q_L, U_R$ , and  $D_R$  are triplets under  $SU(3)_C$ ; these are the *quark*  
146 fields. The *color* group,  $SU(3)_C$  is mediated by the *gluon* field  $G^\mu(8, 1)_0$ , which has  
147 8 degrees of freedom. The fermion fields  $L_L(1, 2)_{-1}$  and  $E_R(1, 1)_{-2}$  are singlets under  
148  $SU(3)_C$ ; we call them the *lepton* fields.

149 Next, we note the “left-handed” (“right-handed”) fermion fields, denoted by  $L(R)$   
150 subscript, The left-handed fields form doublets under  $SU(2)_L$ . These are mediated  
151 by the three degrees of freedom of the “W” fields  $W^\mu(1, 3)_0$ . These fields only act  
152 on the left-handed particles of the Standard Model. This is the reflection of the  
153 “chirality” of the Standard Model The left-handed and right-handed particles are  
154 treated differently by the electroweak forces. The right-handed fields,  $U_R, D_R$ , and  
155  $E_R$ , are singlets under  $SU(2)_L$ .

156 The  $U(1)_Y$  symmetry is associated to the  $B^\mu(1, 1)_0$  boson with one degree of  
157 freedom. The charge  $Y$  is known as the electroweak hypercharge.

158 To better understand the phenomenology of the Standard Model, let us investigate  
159 each of the *sectors* of the Standard Model separately.

## 160 Electroweak sector

The electroweak sector refers to the  $SU(2)_L \otimes U(1)_Y$  portion of the Standard Model gauge group. Following our philosophy of writing all gauge-invariant and renormalizable terms, the electroweak Lagrangian can be written as

$$\mathcal{L} = W_a^{\mu\nu} W_{\mu\nu}^a + B^{\mu\nu} B_{\mu\nu} + (D^\mu \phi)^\dagger D_\mu \phi - \mu^2 \phi^\dagger \phi - \lambda (\phi^\dagger \phi)^2. \quad (2.2)$$

where  $W_a^{\mu\nu}$  are the three ( $a = 1, 2, 3$ ) gauge bosons associated to the  $SU(2)_L$  gauge group,  $B^{\mu\nu}$  is the one gauge boson of the  $U(1)_Y$  gauge group, and  $\phi$  is the complex Higgs multiplet. The covariant derivative  $D^\mu$  is given by

$$D^\mu = \partial^\mu + \frac{ig}{2} W_a^\mu \sigma_a + \frac{ig'}{2} B^\mu \quad (2.3)$$

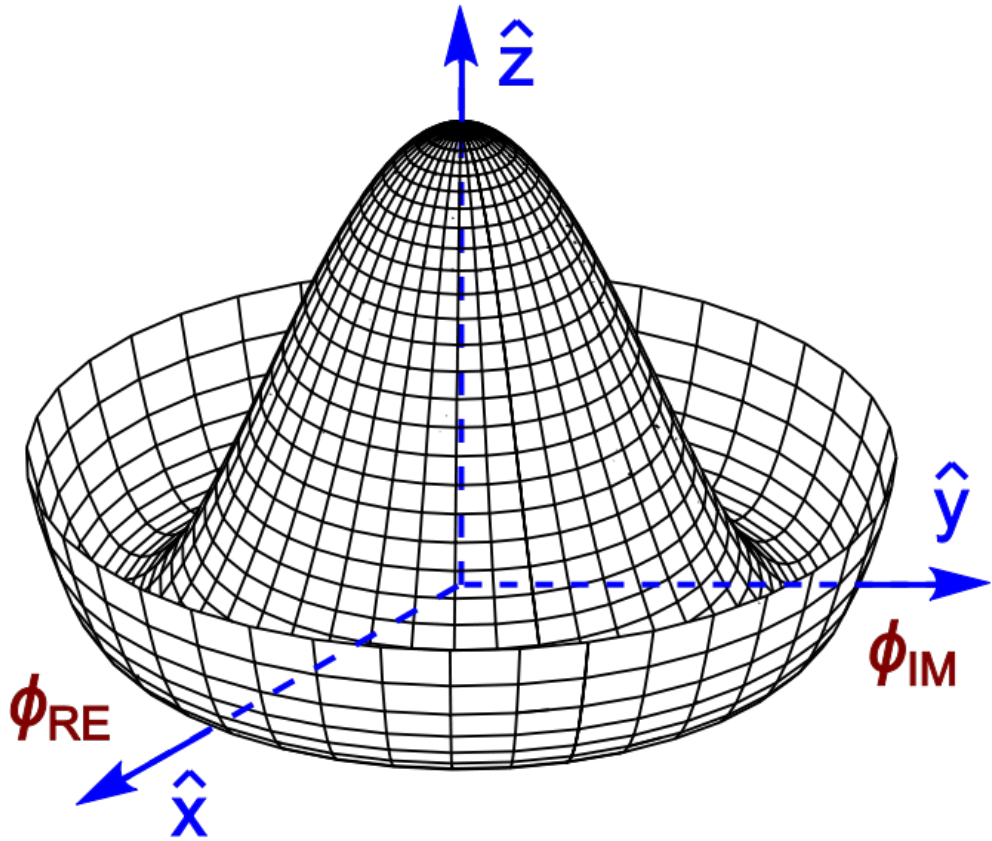


Figure 2.1: Sombrero potential

where  $i\sigma_a$  are the Pauli matrices times the imaginary constant, which are the generators for  $SU(2)_L$ , and  $g$  and  $g'$  are the  $SU(2)_L$  and  $U(1)_Y$  coupling constants, respectively. The field strength tensors  $W_a^{\mu\nu}$  and  $B^{\mu\nu}$  are given by the commutator of the covariant derivative associated to each field

$$B^{\mu\nu} = \partial^\mu B^\nu - \partial^\nu B^\mu \quad (2.4)$$

$$W_a^{\mu\nu} = \partial^\mu W_a^\nu - \partial^\nu W_a^\mu - g\epsilon_{abc}W_a^\mu W_b^\nu, \quad i = 1, 2, 3$$

161

162     The terms in the Lagrangian Eq. (2.2) proportional to  $\mu^2$  and  $\lambda$  make up the  
 163     “Higgs potential” [50]. As normal (see Appendix ??), we restrict  $\lambda > 0$  to guarantee  
 164     our potential is bounded from below, and we also require  $\mu^2 < 0$ , which gives us the  
 165     standard “sombrero” potential shown in Fig. 2.1.

This potential has infinitely many minima at  $\langle \phi \rangle = \sqrt{2m/\lambda}$ . The ground state is *spontaneously* broken by the choice of ground state, which induces a vacuum expectation value (VEV). Without loss of generality, we can choose the Higgs field  $\phi$  to point in the real direction, and write the Higgs field  $\phi$  in the following form :

$$\phi = \frac{1}{\sqrt{2}} \exp\left(\frac{i}{v} \sigma_a \theta_a\right) \begin{pmatrix} 0 \\ v + h(x) \end{pmatrix}. \quad (2.5)$$

We choose a gauge to rotate away the dependence on  $\theta_a$ , such that we can write simply

$$\phi = \frac{1}{\sqrt{2}} \begin{pmatrix} 0 \\ v + h(x) \end{pmatrix}. \quad (2.6)$$

Now, we can see how the masses of the vector bosons are generated from the application of the Higgs mechanism. We plug Eq. Eq. (2.6) back into the electroweak Lagrangian, and only showing the relevant mass terms in the vacuum state where  $h(x) = 0$  see that (dropping the Lorentz indices) :

$$\begin{aligned} \mathcal{L}_M &= \frac{1}{8} \left| \begin{pmatrix} gW_3 + g'B & g(W_1 - iW_2) \\ g(W_1 + iW_2) & -gW_3 + g'B \end{pmatrix} \begin{pmatrix} 0 \\ v \end{pmatrix} \right|^2 \\ &= \frac{g^2 v^2}{8} \left[ W_1^2 + W_2^2 + \left( \frac{g'}{g} B - W_3 \right)^2 \right] \end{aligned} \quad (2.7)$$

Defining the *Weinberg* angle  $\tan(\theta_W) = g'/g$  and the following *physical* fields :

$$W^\pm = \frac{1}{\sqrt{2}} (W_1 \mp iW_2) \quad (2.8)$$

$$Z^0 = \cos \theta_W W_3 - \sin \theta_W B$$

$$A^0 = \sin \theta_W W_3 + \cos \theta_W B$$

we can write the piece of the Lagrangian associated to the vector boson masses as

$$\mathcal{L}_{MV} = \frac{1}{4} g^2 v^2 W^+ W^- + \frac{1}{8} (g^2 + g'^2) v^2 Z^0 Z^0. \quad (2.9)$$

and we have the following values of the masses for the vector bosons :

$$\begin{aligned} m_W^2 &= \frac{1}{4}v^2g^2 \\ m_Z^2 &= \frac{1}{4}v^2(g^2 + g'^2) \\ m_A^2 &= 0 \end{aligned} \tag{2.10}$$

We thus see how the Higgs mechanism gives rise to the masses of the  $W^\pm$  and  $Z$  boson in the Standard Model. As expected, the mass of the photon is zero. The  $SU(2)_L \otimes U(1)_Y$  symmetry of the initially massless  $W_{1,2,3}$  and  $B$  fields is broken to the  $U(1)_{EM}$ . Of the four degrees of freedom in the complex Higgs doublet, three are “eaten” when we give mass to the  $W^\pm$  and  $Z_0$ , while the other degree of freedom is the Higgs particle, as discovered in 2012 by the ATLAS and CMS collaborations [51, 52].

### 173 Quantum Chromodynamics

Quantum chromodynamics (or the theory of the *strong* force) characterizes the behavior of *colored* particles, collectively known as *partons*. The partons of the Standard Model are the (fermionic) quarks, and the (bosonic) gluons. The strong force is governed by  $SU(3)_C$ , an unbroken symmetry in the Standard Model, which implies the gluon remains massless. Defining the covariant derivative for QCD as

$$D^\mu = \partial^\mu + ig_s G_a^\mu L_a, a = 1, \dots, 8 \tag{2.11}$$

where  $L_a$  are the generators of  $SU(3)_C$ , and  $g_s$  is the coupling constant of the strong force. The QCD Lagrangian then is given by

$$\mathcal{L}_{\text{QCD}} = i\bar{\psi}_f D_\mu \gamma^\mu \psi_f - \frac{1}{4} G_{a,\mu\nu} G_a^{\mu\nu} \tag{2.12}$$

where the summation over  $f$  is for quarks *families*, and  $G_a^{\mu\nu}$  is the gluon field strength tensor, given by

$$G_a^{\mu\nu} = \partial^\mu G_a^\nu - \partial^\nu G_a^\mu - g_s f^{abc} G_b^\mu G_c^\nu, a, b, c = 1, \dots, 8 \tag{2.13}$$

174 where  $f^{abc}$  are the structure constants of  $SU(3)_C$ , which are analogous to  $\epsilon_{abc}$  for  
175  $SU(2)_L$ . The kinetic term for the quarks is contained in the standard  $\partial_\mu$  term, while  
176 the field strength term contains the interactions between the quarks and gluons, as  
177 well as the gluon self-interactions.

178 Written down in this simple form, the QCD Lagrangian does not seem much  
179 different from the QED Lagrangian, with the proper adjustments for the different  
180 group structures. The gluon is massless, like the photon, so one could naïvely expect  
181 an infinite range force, and it pays to understand why this is not the case. The  
182 reason for this fundamental difference is the gluon self-interactions arising in the  
183 field strength tensor term of the Lagrangian. This leads to the phenomena of *color*  
184 *confinement*, which describes how one only observes color-neutral particles alone in  
185 nature. In contrast to the electromagnetic force, particles which interact via the  
186 strong force experience a *greater* force as the distance between the particles increases.  
187 At long distances, the potential is given by  $V(r) = -kr$ . At some point, it is more  
188 energetically favorable to create additional partons out of the vacuum than continue  
189 pulling apart the existing partons, and the colored particles undergo *fragmentation*.  
190 This leads to *hadronization*. Bare quarks and gluons are actually observed as sprays  
191 of hadrons (primarily kaons and pions). These sprays are known as *jets*, which are  
192 what are observed by experiments.

193 It is important to recognize the importance of understanding these QCD inter-  
194 actions in high-energy hadron colliders such as the LHC. Since protons are hadrons,  
195 proton-proton collisions such as those produced by the LHC are primarily governed  
196 by the processes of QCD. In particular, by far the most frequent process observed in  
197 LHC experiments is dijet production from gluon-gluon interactions, as can be seen  
198 (Fig. 2.2). These gluons that interact are part of the *sea* particles inside the proton; the  
199 simple  $p = uud$  model does not apply. The main *valence*  $uud$  quarks are constantly  
200 interacting via gluons, which can themselves radiate gluons or split into quarks, and

## Standard Model Production Cross Section Measurements

Status: August 2016

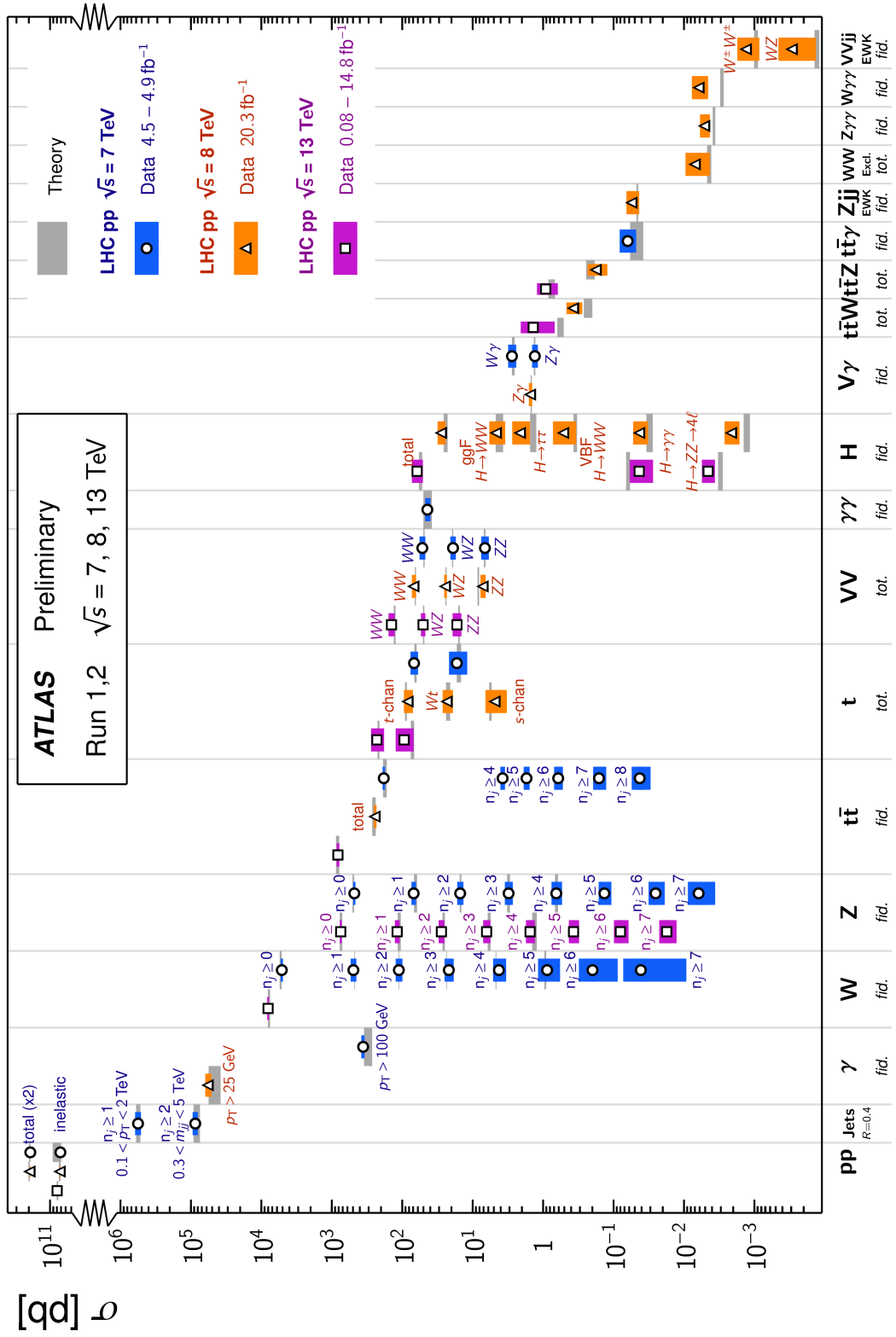


Figure 2.2: Cross-sections of various Standard Model processes

so on. A more useful understanding is given by the colloquially-known *bag* model [53, 54], where the proton is seen as a “bag” of (in principle) infinitely many partons, each with energy  $E < \sqrt{s} = 6.5$  TeV. One then collides this (proton) bag with another, and views the products of this very complicated collision, where calculations include many loops in nonperturbative QCD calculations.

Fortunately, we are generally saved by the QCD factorization theorems [55]. This allows one to understand the hard (i.e. short distance or high energy)  $2 \rightarrow 2$  parton process using the tools of perturbative QCD, while making series of approximations known as a *parton shower* model to understand the additional corrections from nonperturbative QCD. We will discuss the reconstruction of jets by experiments in Ch. 6.

## Fermions

We will now look more closely at the fermions in the Standard Model [56].

As noted earlier in Sec. 2.2, the fermions of the Standard Model can be first distinguished between those that interact via the strong force (quarks) and those which do not (leptons).

There are six leptons in the Standard Model, which can be placed into three *generations*.

$$\begin{pmatrix} e \\ \nu_e \end{pmatrix}, \begin{pmatrix} \mu \\ \nu_\mu \end{pmatrix}, \begin{pmatrix} \tau \\ \nu_\tau \end{pmatrix} \quad (2.14)$$

There is the electron ( $e$ ), muon ( $\mu$ ), and tau ( $\tau$ ), each of which has an associated neutrino ( $\nu_e, \nu_\mu, \nu_\tau$ ). Each of the so-called charged (“electron-like”) leptons has electromagnetic charge  $-1$ , while the neutrinos all have  $q_{EM} = 0$ .

Often in an experimental context, lepton is used to denote the stable electron and metastable muon, due to their striking experimental signatures. Taus are often treated separately, due to their much shorter lifetime of  $\tau_\tau \sim 10^{-13}s$ . These decay

223 through hadrons or the other leptons, so often physics analyses at the LHC treat  
224 them as jets or leptons, as will be done in this thesis.

225 As the neutrinos are electrically neutral, nearly massless, and only interact via the  
226 weak force, it is quite difficult to observe them directly. Since LHC experiments rely  
227 overwhelmingly on electromagnetic interactions to observe particles, the presence of  
228 neutrinos is not observed directly. Neutrinos are instead observed by the conservation  
229 of four-momentum in the plane transverse to the proton-proton collisions, known as  
230 *missing transverse energy*.

There are six quarks in the Standard Model : up, down, charm, strange, top, and bottom. Quarks are similar organized into three generations :

$$\begin{pmatrix} u \\ d \end{pmatrix}, \begin{pmatrix} c \\ s \end{pmatrix}, \begin{pmatrix} t \\ b \end{pmatrix} \quad (2.15)$$

231 where we speak of “up-like” quarks and “down-like” quarks.

232 Each up-like quark has charge  $q_{up} = 2/3$ , while the down-like quarks have  $q_{down} =$   
233  $-1/3$ . At the high energies of the LHC, one often makes the distinction between  
234 the light quarks ( $u, d, c, s$ ), the bottom quark, and top quark. In general, due to  
235 the hadronization process described above, the light quarks, with masses  $m_q < \sim$   
236 1.5 GeV are indistinguishable by LHC experiments. Their hadronic decay products  
237 generally have long lifetimes and they are reconstructed as jets.<sup>1</sup>. The bottom quark  
238 hadronizes primarily through the  $B$ -mesons, which generally travels a short distance  
239 before decaying to other hadrons. This allows one to distinguish decays via  $b$ -quarks  
240 from other jets. This procedure is known as *b-tagging* and will be discussed more in  
241 Ch.Ch. 5.

242 Due to its large mass, the top quark decays before it can hadronize. There are  
243 no bound states associated to the top quark. The top is of particular interest at

---

<sup>1</sup>In some contexts, charm quarks are also treated as a separate category, although it is quite difficult to distinguish charm quarks from the other light quarks at high energy colliders.

## Standard Model Interactions (Forces Mediated by Gauge Bosons)



Figure 2.3: The interactions of the Standard Model

- 244 the LHC; it has a striking signature through its most common decay mode  $t \rightarrow Wb$ .  
 245 Decays via tops, especially  $t\bar{t}$  are frequently an important signal decay mode, or an  
 246 important background process.

### 247 **Interactions in the Standard Model**

- 248 We briefly overview the entirety of the fundamental interactions of the Standard  
 249 Model. These can also be found in Fig. 2.3.

250 The electromagnetic force, mediated by the photon, interacts with via a three-

251 point coupling all charged particles in the Standard Model. The photon thus interacts  
252 with all the quarks, the charged leptons, and the charged  $W^\pm$  bosons.

253 The weak force is mediated by three particles : the  $W^\pm$  and the  $Z^0$ . The  $Z^0$  can  
254 interacts with all fermions via a three-point coupling. A real  $Z_0$  can thus decay to  
255 a fermion-antifermion pair of all SM fermions except the top quark, due to its large  
256 mass. The  $W^\pm$  has two important three-point interactions with fermions. First, the  
257  $W^\pm$  can interact with an up-like quark and a down-like quark; an important example  
258 in LHC experiments is  $t \rightarrow Wb$  The coupling constants for these interactions are  
259 encoded in the unitary matrix known as the Cabibbo–Kobayashi–Maskawa (CKM)  
260 matrix [57, 58], and are generally known as flavor-changing interactions. Secondly,  
261 the  $W^\pm$  interacts with a charged lepton and its corresponding neutrino. In this case,  
262 the unitary matrix that corresponds to CKM matrix for quarks is the identity matrix,  
263 which forbids (fundamental) vertices such as  $\mu \rightarrow We$ . For leptons, instead this is  
264 a two-step process :  $\mu \rightarrow \nu_m u W \rightarrow \nu_m u \bar{\nu}_e e$ . Finally, there are the self-interactions  
265 of the weak gauge bosons. There is a three-point and four-point interaction. All  
266 combinations are allowed which conserve electric charge.

267 The strong force is mediated by the gluon, which as discussed above also carries  
268 the strong color charge. There is the fundamental three-point interaction, where a  
269 quark radiates a gluon. Additionally, there are the three-point and four-point gluon-  
270 only interactions.

## 271 2.3 Deficiencies of the Standard Model

272 The Standard Model has been enormously successful. This relatively simple theory is  
273 capable of explaining a very wide range of phenomenom, which ultimately break down  
274 to combinations of nine diagrams shown in Fig. 2.3 at tree level. Unfortunately, there  
275 are some unexplained problems with the Standard Model. We cannot go through all

$m_e$	Electron mass	511 keV
$m_\mu$	Muon mass	105.7 MeV
$m_\tau$	Tau mass	1.78 GeV
$m_u$	Up quark mass	1.9 MeV ( $m_{\bar{MS}} = 2\text{GeV}$ )
$m_d$	Down quark mass	4.4 MeV ( $m_{\bar{MS}} = 2\text{GeV}$ )
$m_s$	Strange quark mass	87 MeV ( $m_{\bar{MS}} = 2\text{GeV}$ )
$m_c$	Charm quark mass	1.32 GeV ( $m_{\bar{MS}} = m_c$ )
$m_b$	Bottom quark mass	4.24 GeV ( $m_{\bar{MS}} = m_b$ )
$m_t$	Top quark mass	172.7 GeV (on-shell renormalization)
$\theta_{12}$ CKM	12-mixing angle	13.1°
$\theta_{23}$ CKM	23-mixing angle	2.4°
$\theta_{13}$ CKM	13-mixing angle	0.2°
$\delta$ CKM	CP-violating Phase	0.995
$g'$	U(1) gauge coupling	0.357 ( $m_{\bar{MS}} = m_Z$ )
$g$	SU(2) gauge coupling	0.652 ( $m_{\bar{MS}} = m_Z$ )
$g_s$	SU(3) gauge coupling	1.221 ( $m_{\bar{MS}} = m_Z$ )
$\theta_{QCD}$	QCD vacuum angle	~0
VEV	Higgs vacuum expectation value	246 GeV
$m_H$	Higgs mass	125 GeV

Table 2.1: Parameters of the Standard Model. For values dependent on the renormalization scheme, we use a combination of the on-shell normalization scheme [59–62] and modified minimal subtraction scheme with  $m_{\bar{MS}}$  as indicated in the table [63]

276 of the potential issues in this thesis, but we will motivate the primary issues which  
 277 naturally lead one to *supersymmetry*, as we will see in Ch. 3.

The Standard Model has many free parameters, shown in Tab. 2.1. In general, we prefer models with less free parameters. A great example of this fact, and the primary experimental evidence for EWSB, is the relationship between the couplings of the weak force and the masses of the gauge bosons of the weak force :

$$\rho \equiv \frac{m_W^2}{m_Z^2 \cos^2 \theta_W} \stackrel{?}{=} 1 \quad (2.16)$$

278 where ? indicates that this is a testable prediction of the Standard Model (in  
 279 particular, that the gauge bosons gain mass through EWSB). This relationship has  
 280 been measured within experimental and theoretical predictions. We would like to  
 281 produce additional such relationships, which would exist if the Standard Model is a

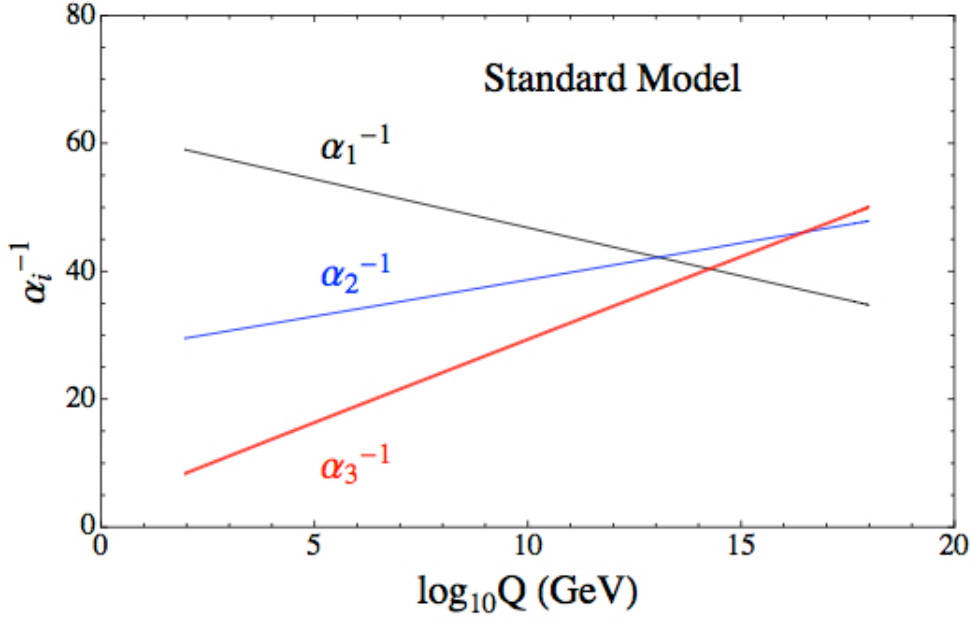


Figure 2.4: The running of Standard Model gauge couplings. The Standard Model couplings do not unify at high energies, which indicates it cannot completely describe nature through the Planck scale.

282 low-energy approximation of some other theory.

283 An additional issue is the lack of *gauge coupling unification*. The couplings of  
 284 any quantum field theory “run” as a function of the distance scales (or inversely,  
 285 energy scales) of the theory. The idea is closely related to the unification of the  
 286 electromagnetic and weak forces at the so-called *electroweak scale* of  $O(100 \text{ GeV})$ .  
 287 One would hope this behavior was repeated between the electroweak forces and the  
 288 strong force at some suitable energy scale. The Standard Model does not exhibit this  
 289 behavior, as we can see in Fig. 2.4.

But, the most significant problem with the Standard Model is the *hierarchy problem*. In its most straightforward incarnation, the Higgs scalar field is subject to quantum corrections through loop diagrams, as shown in Fig. 2.5. For demonstration, we use the contributions from the top quark, since the top quark has the largest Higgs Yukawa coupling due to its large mass. In general, we should expect these corrections to quadratically depend on the scale of the ultraviolet physics,  $\Lambda$ . Briefly assume

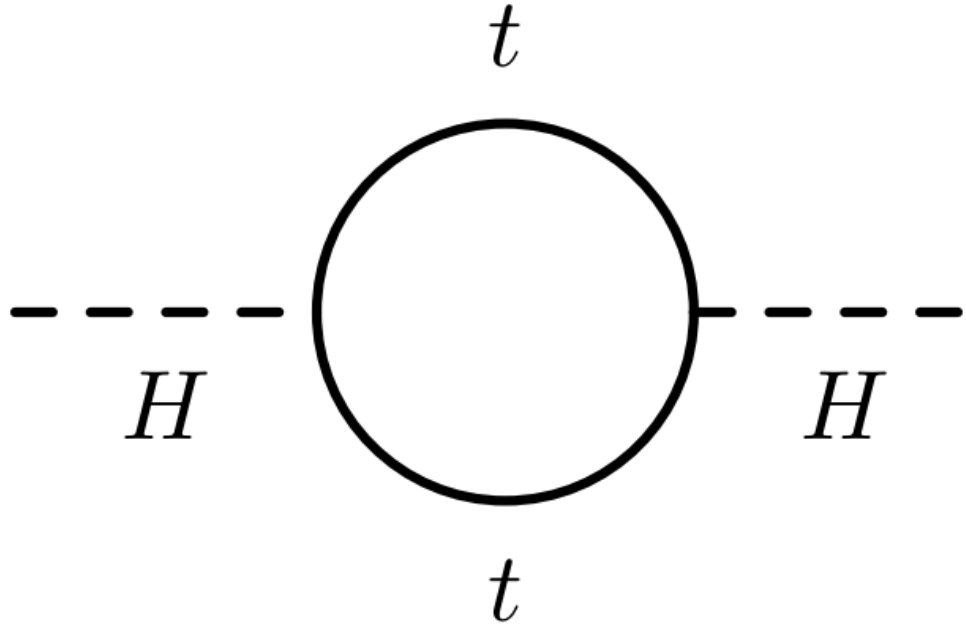


Figure 2.5: The dominant quantum loop correction to the Higgs mass in the Standard Model.

there is no new physics before the Planck scale of gravity,  $\Lambda_{\text{Planck}} = 10^{19}$  GeV. In this case, we expect the corrections to the Higgs mass to be

$$\delta m_H^2 \approx \left( \frac{m_t}{8\pi^2 \langle \phi \rangle_{VEV}} \right)^2 \Lambda_{\text{Planck}}^2. \quad (2.17)$$

290 To achieve the miraculous cancellation required to get the observed Higgs mass of  
 291 125 GeV, one needs to then set the bare Higgs mass  $m_0$ , our input to the Standard  
 292 Model Lagrangian, itself to a *precise* value  $\sim 10^{19}$  GeV. This extraordinary level of  
 293 parameter finetuning is quite undesirable, and within the framework of the Standard  
 294 Model alone, there is little that can be done to alleviate this issue.

295 An additional concern, of a different nature, is the lack of a *dark matter* candidate  
 296 in the Standard Model. Dark matter was discovered by observing galactic rotation  
 297 curves, which showed that much of the matter that interacts gravitationally is invisible  
 298 to our (electromagnetic) telescopes [16–22]. The postulation of the existence of dark  
 299 matter, which interacts at least through gravity, allows one to understand these galactic

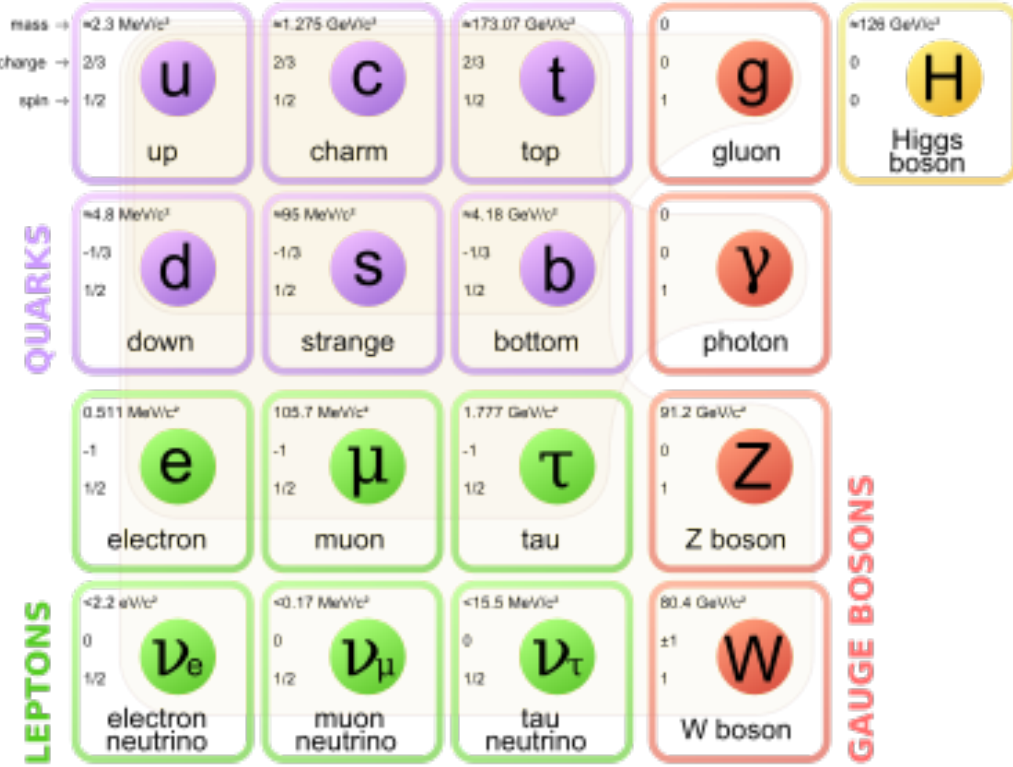


Figure 2.6: Particles of the Standard Model

300 rotation curves. Unfortunately, no particle in the Standard Model could possibly be  
 301 the dark matter particle. The only candidate truly worth another look is the neutrino,  
 302 but it has been shown that the neutrino content of the universe is simply too small  
 303 to explain the galactic rotation curves [22, 64]. The experimental evidence from  
 304 the galactic rotations curves thus show there *must* be additional physics beyond the  
 305 Standard Model, which is yet to be understood.

306 In the next chapter, we will see how these problems can be alleviated by the theory  
 307 of supersymmetry.



*Supersymmetry*

310 This chapter will introduce supersymmetry (SUSY) [15, 23–35]. We will begin  
 311 by introducing the concept of a *superspace*, and discuss some general ingredients of  
 312 supersymmetric theories. This will include a discussion of how the problems with the  
 313 Standard Model described in Ch. 2 are naturally fixed by these theories.

314 The next step is to discuss the particle content of the *Minimally Supersymmetric*  
 315 *Standard Model* (MSSM). As its name implies, this theory contains the minimal  
 316 additional particle content to make Standard Model supersymmetric. We then discuss  
 317 the important phenomenological consequences of this theory, especially as it would  
 318 be observed in experiments at the LHC.

319 **3.1 Supersymmetric theories : from space to  
 320 superspace**

321 **Coleman-Mandula “no-go” theorem**

322 We begin the theoretical motivation for supersymmetry by citing the “no-go” theorem  
 323 of Coleman and Mandula [65]. This theorem forbids *spin-charge unification*. It  
 324 states that all quantum field theories which contain nontrivial interactions must be  
 325 a direct product of the Poincaré group of Lorentz symmetries, the internal product  
 326 of gauge symmetries, and the discrete symmetries of parity, charge conjugation,  
 327 and time reversal. The assumptions which go into building the Coleman-Mandula

theorem are quite restrictive, but there is solution, which has become known as *supersymmetry* [26, 66]. In particular, we must introduce a *spinorial* group generator  $Q$ . Alternatively, and equivalently, this can be viewed as the addition of anti-commuting coordinates. Space plus these new anti-commuting coordinates is then called *superspace* [67]. We will not investigate this view in detail, but it is also a quite intuitive and beautiful way to construct supersymmetry [15].

### 334 Supersymmetry transformations

A *supersymmetric* transformation  $Q$  transforms a bosonic state into a fermionic state, and vice versa :

$$Q |\text{Fermion}\rangle = |\text{Boson}\rangle \quad (3.1)$$

$$Q |\text{Boson}\rangle = |\text{Fermion}\rangle \quad (3.2)$$

To ensure this relation holds,  $Q$  must be an anticommuting spinor. Additionally, since spinors are inherently complex,  $Q^\dagger$  must also be a generator of the supersymmetry transformation. Since  $Q$  and  $Q^\dagger$  are spinor objects (with  $s = 1/2$ ), we can see that supersymmetry must be a spacetime symmetry. The Haag-Lopuszanski-Sohnius extension [66] of the Coleman-Mandula theorem [65] is quite restrictive about the forms of such a symmetry. Here, we simply write the (anti-) commutation relations [15] :

$$Q_\alpha, Q_{\dot{\alpha}}^\dagger = -2\sigma_{\alpha\dot{\alpha}\mu} P_\mu \quad (3.3)$$

$$Q_\alpha, Q_{\dot{\beta}} = Q_{\dot{\alpha}}^\dagger, Q_{\dot{\beta}}^\dagger = 0 \quad (3.4)$$

$$[P^\mu, Q_\alpha] = [P^\mu, Q_{\dot{\alpha}}^\dagger] = 0 \quad (3.5)$$

### 335 Supermultiplets

In a supersymmetric theory, we organize single-particle states into irreducible representations of the supersymmetric algebra which are known as *supermultiplets*.

338 Each supermultiplet contains a fermion state  $|F\rangle$  and a boson state  $|B\rangle$ . These two  
339 states are known as *superpartners*. These are related by some combination of  
340  $Q$  and  $Q^\dagger$ , up to a spacetime transformation.  $Q$  and  $Q^\dagger$  commute with the mass-  
341 squared operator  $-P^2$  and the operators corresponding to the gauge transformations  
342 [15]: in particular, the gauge interactions of the Standard Model. In an unbroken  
343 supersymmetric theory, this means the states  $|F\rangle$  and  $|B\rangle$  have exactly the same mass,  
344 electromagnetic charge, electroweak isospin, and color charges. One can also prove  
345 [15] that each supermultiplet contains the exact same number of bosonic ( $n_B$ ) and  
346 fermion ( $n_F$ ) degrees of freedom. We now explore the possible types of supermultiples  
347 one can find in a renormalizable supersymmetric theory.

348 Since each supermultiplet must contain a fermion state, the simplest type of  
349 supermultiplet contains a single Weyl fermion state ( $n_F = 2$ ) which is paired with  
350  $n_B = 2$  scalar bosonic degrees of freedom. This is most conveniently constructed  
351 as single complex scalar field. We call this construction a *scalar supermultiplet* or  
352 *chiral supermultiplet*. The second name is indicative, as only chiral supermultiplets  
353 can contain fermions whose right-handed and left-handed components transform  
354 differently under the gauge interactions (as of course happens in the Standard Model).

355 The second type of supermultiplet we construct is known as a *gauge supermul-*  
356 *tiplet*. We take a spin-1 gauge boson (which must be massless due to the gauge  
357 symmetry, so  $n_B = 2$ ) and pair this with a single massless Weyl spinor<sup>1</sup>. The gauge  
358 bosons transform as the adjoint representation of their respective gauge groups  
359 Their fermionic partners, which are known as gauginos, must also. In particular,  
360 the left-handed and right-handed components of the gaugino fermions have the same  
361 gauge transformation properties.

362 Excluding gravity, this is the entire list of supermultiplets which can participate  
363 in renormalizable interactions in what is known as  $N = 1$  supersymmetry. This

---

<sup>1</sup>Choosing an  $s = 3/2$  massless fermion leads to nonrenormalizable interactions.

means there is only one copy of the supersymmetry generators  $Q$  and  $Q^\dagger$ . This is essentially the only “easy” phenomenological choice, since it is the only option in four dimensions which allows for the chiral fermions and parity violations to be built into the Standard Model. We will not look further into  $N > 1$  supersymmetry in this thesis.

The primary goal, after understanding the possible structures of the multiplets above, is to fit the Standard Model particles into a multiplet, and therefore make predictions about their supersymmetric partners. We explore this in the next section.

## 3.2 Minimally Supersymmetric Standard Model

To construct what is known as the MSSM [15, 68–71], we need a few ingredients and assumptions. First, we match the Standard Model particles with their corresponding superpartners of the MSSM. We will also introduce the naming of the superpartners (also known as *sparticles*). We discuss a very common additional restraint imposed on the MSSM, known as  $R$ –parity. We also discuss the concept of soft supersymmetry breaking and how it manifests itself in the MSSM.

### Chiral supermultiplets

The first thing we deduce is directly from Sec. 3.1. The bosonic superpartners associated to the quarks and leptons *must* be spin 0, since the quarks and leptons must be arranged in a chiral supermultiplet. This is essential, since the chiral supermultiplet is the only one which can distinguish between the left-handed and right-handed components of the Standard Model particles. The superpartners of the quarks and leptons are known as *squarks* and *sleptons*, or *sfermions* in aggregate. (for “scalar quarks”, “scalar leptons”, and “scalar fermion”). The “s-” prefix can also be added to the individual quarks i.e. *selectron*, *sneutrino*, and *stop*. The notation

388 is to add a  $\sim$  over the corresponding Standard Model particle i.e.  $\tilde{e}$ , the selectron is  
 389 the superpartner of the electron. The two-component Weyl spinors of the Standard  
 390 Model must each have their own (complex scalar) partner i.e.  $e_L, e_R$  have two distinct  
 391 partners :  $\tilde{e}_L, \tilde{e}_R$ . As noted above, the gauge interactions of any of the sfermions are  
 392 identical to those of their Standard Model partners.

Due to the scalar nature of the Higgs, it must obviously lie in a chiral supermultiplet. To avoid gauge anomalies and ensure the correct Yukawa couplings to the quarks and leptons [15], we must add additional Higgs bosons to any supersymmetric theory. In the MSSM, we have two chiral supermultiplets. The SM (SUSY) parts of the multiplets are denoted  $H_u(\tilde{H}_u)$  and  $H_d(\tilde{H}_d)$ . Writing out  $H_u$  and  $H_d$  explicitly:

$$H_u = \begin{pmatrix} H_u^+ \\ H_u^0 \end{pmatrix} \quad (3.6)$$

$$H_d = \begin{pmatrix} H_d^0 \\ H_d^- \end{pmatrix} \quad (3.7)$$

393 we see that  $H_u$  looks very similar to the SM Higgs with  $Y = 1$ , and  $H_d$  is symmetric  
 394 with  $+ \rightarrow -$  and  $Y = -1$ . The SM Higgs boson,  $h_0$ , is a linear superposition of the  
 395 neutral components of these two doublets. The SUSY parts of the Higgs multiplets,  
 396  $\tilde{H}_u$  and  $\tilde{H}_d$ , are each left-handed Weyl spinors. For generic spin-1/2 sparticles, we  
 397 add the “-ino” suffix. We then call the partners of the two Higgs collectively the  
 398 *Higgsinos*.

### 399 Gauge supermultiplets

400 The superpartners of the gauge bosons must all be in gauge supermultiplets since  
 401 they contain a spin-1 particle. Collectively, we refer to the superpartners of the  
 402 gauge bosons as the gauginos.

403 The first gauge supermultiplet contains the gluon, and its superpartner, which is  
 404 known as the *gluino*, denoted  $\tilde{g}$ . The gluon is of course the SM mediator of  $SU(3)_C$

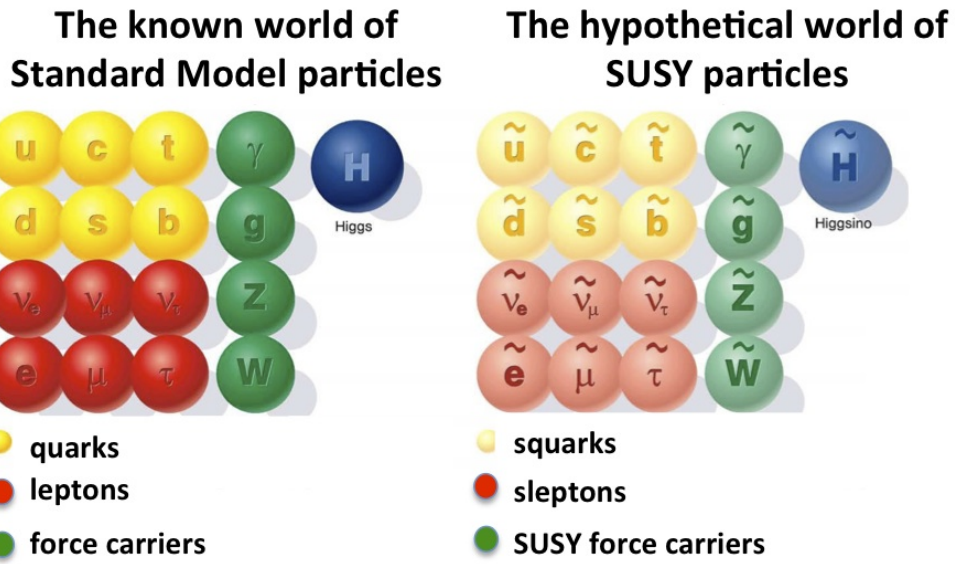


Figure 3.1: Particles of the MSSM

405 The gluino is also a colored particle, subject to  $SU(3)_C$ . From the SM before EWSB,  
 406 we have the four gauge bosons of the electroweak symmetry group  $SU(2)_L \otimes U(1)_Y$  :  
 407  $W^{1,2,3}$  and  $B^0$ . The superpartners of these particles are thus the *winos*  $\tilde{W}^{1,2,3}$  and  
 408 *bino*  $\tilde{B}^0$ , where each is placed in another gauge supermultiplet with its corresponding  
 409 SM particle. After EWSB, without breaking supersymmetry, we would also have the  
 410 zino  $\tilde{Z}^0$  and photino  $\tilde{\gamma}$ .

411 The entire particle content of the MSSM can be seen in Fig. 3.1.

412 At this point, it's important to take a step back. Where are these particles?  
 413 As stated above, supersymmetric theories require that the masses and all quantum  
 414 numbers of the SM particle and its corresponding sparticle are the same. Of course,  
 415 we have not observed a selectron, squark, or wino. The answer, as it often is, is that  
 416 supersymmetry is *broken* by the vacuum state of nature [15].



Figure 3.2: This Feynmann diagram shows how proton decay is induced in the MSSM, if one does not impose  $R$ -parity.

### 417 **$R$ -parity**

This section is a quick aside to the general story.  $R$  – parity refers to an additional discrete symmetry which is often imposed on supersymmetric models. For a given particle state, we define

$$418 \quad R = (-1)^{3(B-L)+2s} \quad (3.8)$$

418 where  $B, L$  is the baryon (lepton) number and  $s$  is the spin. The imposition of  
 419 this symmetry forbids certain terms from the MSSM Lagrangian that would violate  
 420 baryon and/or lepton number. This is required in order to prevent proton decay, as  
 421 shown in Fig. 3.2<sup>2</sup>. .

422 In supersymmetric models, this is a  $\mathbb{Z}_2$  symmetry, where SM particles have  $R = 1$   
 423 and sparticles have  $R = -1$ . We will take  $R$  – parity as part of the definition of  
 424 the MSSM. We will discuss later the *drastic* consequences of this symmetry on SUSY  
 425 phenomenology

### 426 **Soft supersymmetry breaking**

The fundamental idea of *soft* supersymmetry breaking [15, 34, 35, 72, 73] is that we would like to break supersymmetry without reintroducing the quadratic divergences

---

<sup>2</sup>Proton decay can actually be prevented by allowing only one of the four potential R-parity violating terms to survive.

we discussed at the end of Chapter Ch. 2. We write the Lagrangian in a form :

$$\mathcal{L}_{\text{MSSM}} = \mathcal{L}_{\text{SUSY}} + \mathcal{L}_{\text{soft}} \quad (3.9)$$

427 In this sense, the symmetry breaking is “soft”, since we have separated out the  
 428 completely symmetric terms from those soft terms which will not allow the quadratic  
 429 divergences to the Higgs mass.

430 The explicitly allowed terms in the soft-breaking Lagrangian are [35]:

431 • Mass terms for the scalar components of the chiral supermultipletss

432 • Mass terms for the Weyl spinor components of the gauge supermultipletss

433 • Trilinear couplings of scalar components of chiral supermultiplets

In particular, using the field content described above for the MSSM, the softly-broken portion of the MSSM Lagrangian can be written

$$\mathcal{L}_{\text{soft}} = -\frac{1}{2} \left( M_3 \tilde{g} \tilde{g} + M_2 \tilde{W} \tilde{W} + M_1 \tilde{B} \tilde{B} + c.c. \right) \quad (3.10)$$

$$- \left( \tilde{u} a_u \tilde{Q} H_u - \tilde{d} a_d \tilde{Q} H_d - \tilde{e} a_e \tilde{L} H_d + c.c. \right) \quad (3.11)$$

$$- \tilde{Q}^\dagger m_Q^2 \tilde{Q} - \tilde{L}^\dagger m_L^2 \tilde{L} - \tilde{u} m_u^2 \tilde{u}^\dagger - \tilde{d} m_d^2 \tilde{d}^\dagger - \tilde{e} m_e^2 \tilde{e}^\dagger \quad (3.12)$$

$$- m_{H_u}^2 H_u^* H_u - m_{H_d}^2 H_d^* H_d - (b H_u H_d + cc). \quad (3.13)$$

434 where we have introduced the following notations :

435 1.  $M_3, M_2, M_1$  are the gluino, wino, and bino masses.

436 2.  $a_u, a_d, a_e$  are complex  $3 \times 3$  matrices in family space.

437 3.  $m_Q^2, m_u^2, m_d^2, m_L^2, m_e^2$  are hermitian  $3 \times 3$  matrices in family space.

438 4.  $m_{H_u}^2, m_{H_d}^2, b$  are the SUSY-breaking contributions to the Higgs potential.

439 We have written matrix terms without any sort of additional notational decoration  
 440 to indicate their matrix nature, and we now show why. The first term Item 1 is the  
 441 set of mass terms for the gluino, wino, and bino. The second term Item 2, containing  
 442  $a_u, a_d, a_e$ , has strong constraints from experiments [74, 75]. We will assume that  
 443 each  $a_i, i = u, d, e$  is proportional to the Yukawa coupling matrix :  $a_i = A_{i0}y_i$ . The  
 444 third term Item 3 can be similarly constrained by experiments [68, 75–82]. We will  
 445 assume the elements of the fourth term Item 4 contributing to the Higgs potential as  
 446 well as all of the Item 1 terms must be real, which limits the possible CP-violating  
 447 interactions to those of the Standard Model. We thus only consider flavor-blind,  
 448 CP-conserving interactions within the MSSM.

The important mixing for mass and gauge interaction eigenstates in the MSSM occurs within electroweak sector, in a process akin to EWSB in the Standard Model. The neutral portions of the Higgsinos doublets and the neutral gauginos ( $\tilde{H}_u^0, \tilde{H}_d^0, \tilde{B}^0, \tilde{W}^0$ ) of the gauge interaction basis mix to form what are known as the *neutralinos* of mass basis :

$$M_{\tilde{\chi}} = \begin{pmatrix} M_1 & 0 & -c_\beta s_W m_Z & s_\beta s_W m_Z \\ 0 & M_2 & c_\beta c_W m_Z & -s_\beta c_W m_Z \\ -c_\beta s_W m_Z & c_\beta c_W m_Z & 0 & -\mu \\ s_\beta s_W m_Z & -s_\beta c_W m_Z & -\mu & 0 \end{pmatrix} \quad (3.14)$$

449 where  $s(c)$  are the sine and cosine of angles related to EWSB, which introduced  
 450 masses to the gauginos and higgsinos. Diagonalization of this matrix gives the four  
 451 neutralino mass states, listed without loss of generality in order of increasing mass :  
 452  $\tilde{\chi}_{1,2,3,4}^0$ .

453 The neutralinos, especially the lightest neutralino  $\tilde{\chi}_1^0$ , are important ingredients  
 454 in SUSY phenomenology.

455 The same process can be done for the electrically charged gauginos with  
 456 the charged portions of the Higgsino doublets along with the charged winos

457  $(\tilde{H}_u^+, \tilde{H}_d^+, \tilde{W}^+, \tilde{W}^-)$ . This leads to the *charginos*, again in order of increasing mass :  
458  $\tilde{\chi}_{1,2}^\pm$ .

459 

### 3.3 Phenomenology

460 We are finally at the point where we can discuss the phenomenology of the MSSM,  
461 in particular as it manifests itself at the energy scales of the LHC.

462 As noted above in Sec. 3.2, the assumption of *R*–parity has important conse-  
463 quences for MSSM phenomenology. The SM particles have  $R = 1$ , while the sparticles  
464 all have  $R = -1$ . Simply, this is the “charge” of supersymmetry. Since the particles  
465 of LHC collisions ( $pp$ ) have total incoming  $R = 1$ , we must expect that all sparticles  
466 will be produced in *pairs*. An additional consequence of this symmetry is the fact  
467 that the lightest supersymmetric particle (LSP) is *stable*. Off each branch of the  
468 Feynmann diagram shown in Fig. 3.3, we have  $R = -1$ , and this can only decay to  
469 another sparticle and a SM particle. Once we reach the lightest sparticle in the decay,  
470 it is absolutely stable. This leads to the common signature  $E_T^{\text{miss}}$  for a generic SUSY  
471 signal.

472 For this thesis, we will be presenting an inclusive search for squarks and gluinos  
473 with zero leptons in the final state. This is a very interesting decay channel, due to  
474 the high cross-sections of  $\tilde{g}\tilde{g}$  and  $\tilde{q}\tilde{q}$  decays, as can be seen in Sec. 3.3 [83].

475 This is a direct consequence of the fact that these are the colored particles of the  
476 MSSM. Since the sparticles interact with the gauge groups of the SM in the same way  
477 as their SM partners, the colored sparticles, the squarks and gluinos, are produced  
478 and decay as governed by the color group  $SU(3)_C$  with the strong coupling  $g_S$ . The  
479 digluino production is particularly copious, due to color factor corresponding to the  
480 color octet of  $SU(3)_C$ .

481 In the case of disquark production, the most common decay mode of the squark in

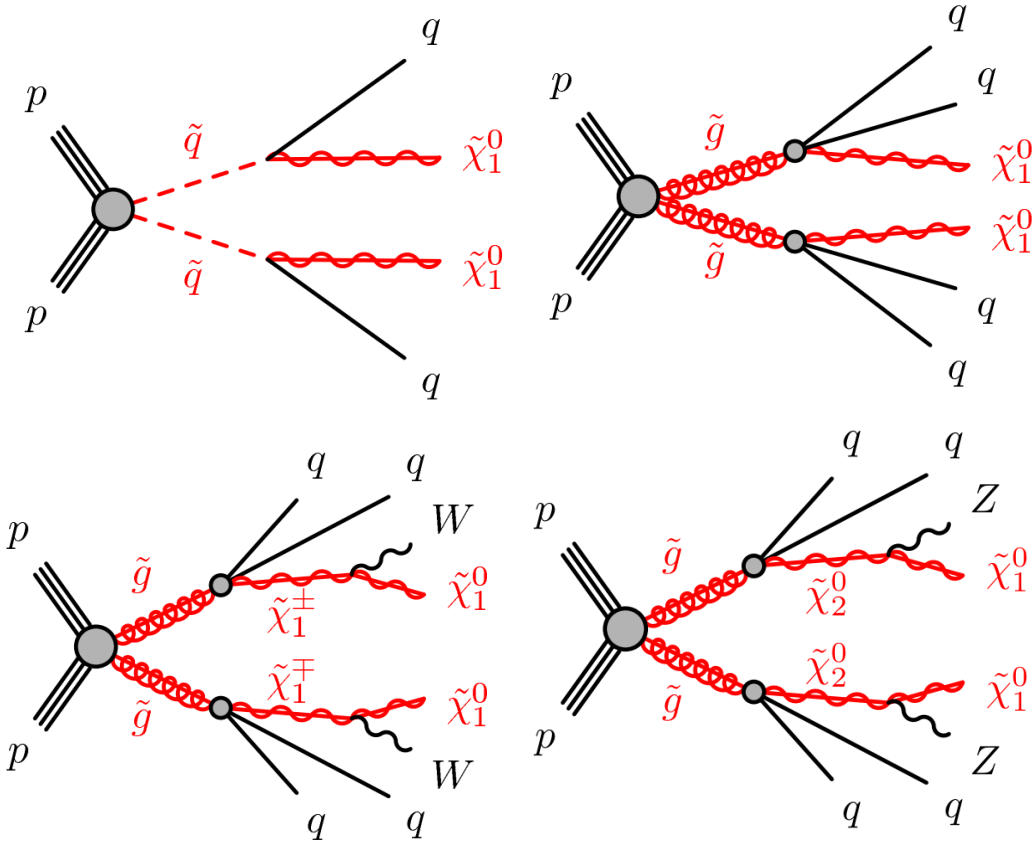


Figure 3.3: SUSY signals considered in this thesis

the MSSM is a decay directly to the LSP plus a single SM quark [15]. This means the basic search strategy of disquark production is two jets from the final state quarks, plus missing transverse energy for the LSPs. There are also cascade decays, the most common of which, and the only one considered in this thesis, is  $\tilde{q} \rightarrow q\chi_1^\pm \rightarrow qW^\pm\chi_1^0$ .

For digluino production, the most common decay is  $\tilde{g} \rightarrow g\tilde{q}$ , due to the large  $g_S$  coupling. The squark then decays as listed above. In this case, we generically search for four jets and missing transverse energy from the LSPs.

In the context of experimental searches for SUSY, we often consider *simplified models*. These models make certain assumptions which allow easy comparisons of results by theorists and experimentalists. In the context of this thesis, the simplified models will make assumptions about the branching ratios described in the preceding paragraphs. In particular, we will often choose a model where the decay of interest

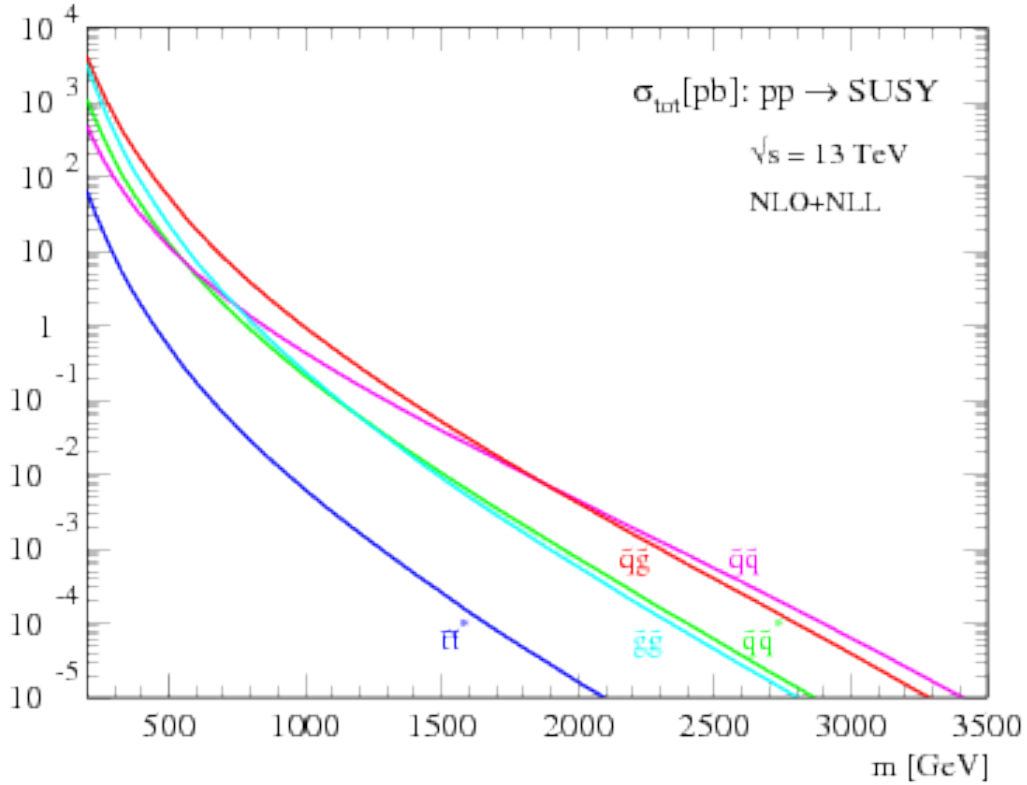


Figure 3.4: SUSY production cross-sections as a function of sparticle mass at  $\sqrt{s} = 13 \text{ TeV}$ .

494 occurs with 100% branching ratio. This is entirely for ease of interpretation, but it is  
495 important to recognize that these are more a useful comparison tool, especially with  
496 for setting limits, than a strict statement about the potential masses of sought-after  
497 beyond the Standard Model particle.

## 498 3.4 How SUSY solves the problems with the SM

499 We now return to the issues with the Standard Model as described in Ch. 2 to see  
500 how these issues are solved by supersymmetry.

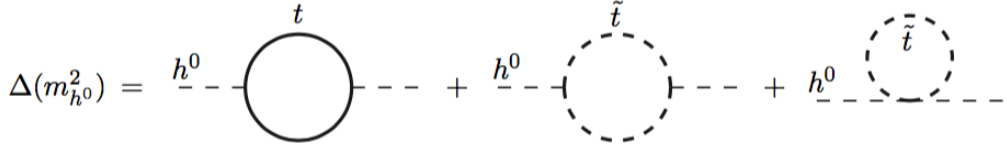


Figure 3.5: Loop diagrams correct the Higgs mass in the MSSM

### 501 Quadratic divergences to the Higgs mass

The quadratic divergences induced by the loop corrections to the Higgs mass, for example from the top Yukawa coupling, goes as

$$\delta m_H^2 \approx \left( \frac{m_t}{8\pi^2 \langle \phi \rangle_{VEV}} \right)^2 \Lambda_{Planck}^2. \quad (3.15)$$

502 The miraculous thing about SUSY is each of these terms *automatically* comes with  
 503 a term which exactly cancels this contribution [15]. The fermions and bosons  
 504 have opposite signs in this loop diagram to all orders in perturbation theory, which  
 505 completely solves the hierarchy problem. This is the strongest motived reason for  
 506 supersymmetry.

### 507 Gauge coupling unification

508 An additional motivation for supersymmetry is seen by the gauge coupling unification  
 509 high scales. In the Standard Model, as we saw the gauge couplings fail to unify at  
 510 high energies. In the MSSM and many other forms of supersymmetry, the gauge  
 511 couplings unify at high energy, as can be seen in Fig. 3.6. This provides additional  
 512 aesthetic motivation for supersymmetric theories.

### 513 Dark matter

514 As we discussed previously, the lack of any dark matter candidate in the Standard  
 515 Model naturally leads to beyond the Standard Model theories. In the Standard Model,  
 516 there is a natural dark matter candidate in the lightest supersymmetric particle [15]



Figure 3.6: The running of Standard Model gauge couplings: compare to Fig. 2.4. The MSSM gauge couplings nearly intersect at high energies.

517 The LSP would in dark matter experiments be called a *weakly-interacting massive*  
 518 *particle* (WIMP), which is a type of cold dark matter [22, 84]. These WIMPs would  
 519 only interact through the weak force and gravity, which is exactly as a model like  
 520 the MSSM predicts for the neutralino. In Fig. 3.7, we can see the current WIMP  
 521 exclusions for a given mass. The range of allowed masses which have not been  
 522 excluded for LSPs and WIMPs have significant overlap. This provides additional  
 523 motivation outside of the context of theoretical details.

### 524 3.5 Conclusions

525 Supersymmetry is the most well-motivated theory for physics beyond the Standard  
 526 Model. It provides a solution to the hierarchy problem, leads to gauge coupling  
 527 unification, and provides a dark matter candidate consistent with galactic rotation  
 528 curves. As noted in this chapter, due to the LSPs in the final state, most SUSY



Figure 3.7: WIMP exclusions from direct dark matter detection experiments.

529 searches require a significant amount of missing transverse energy in combination  
 530 with jets of high transverse momentum. However, there is some opportunity to do  
 531 better than this, especially in final states where one has two weakly-interacting LSPs  
 532 on opposite sides of some potentially complicated decay tree. We will see how this is  
 533 done in Ch. 7.



*The Large Hadron Collider*

536 The Large Hadron Collider (LHC) produces high-energy protons which collide at the  
 537 center of multiple large experiments at CERN on the outskirts of Geneva, Switzerland  
 538 [85]. The LHC produces the highest energy collisions in the world, with a design  
 539 center-of-mass energy of  $\sqrt{s} = 14$  TeV, which allows the experiments to investigate  
 540 physics at higher energies than previous colliders. This chapter will summarize the  
 541 basics of accelerator physics, especially with regards to discovering physics beyond  
 542 the Standard Model. We will describe the CERN accelerator complex and the LHC.

543 **4.1 Basics of Accelerator Physics**

544 This section follows closely the presentation of [86].

Simple particle accelerators simply rely on the acceleration of charged particles in a static electric field. Given a field of strength  $E$ , charge  $q$ , and mass  $m$ , this is simply

$$a = \frac{qE}{m}. \quad (4.1)$$

545 For a given particle with a given mass and charge, this is limited by the static electric  
 546 field which can be produced, which in turn is limited by electrical breakdown at high  
 547 voltages.

548 There are two complementary solutions to this issue. First, we use the *radio*  
 549 *frequency acceleration* technique. We call the devices used for this *RF cavities*. The  
 550 cavities produce a time-varied electric field, which oscillate such that the charged

551 particles passing through it are accelerated towards the design energy of the RF  
 552 cavity. This oscillation forces the particles into *bunches*, since particles which are  
 553 slightly off the central energy induced by the RF cavity are accelerated towards the  
 554 design energy.

Second, one bends the particles in a magnetic field, which allows them to pass through the same RF cavity over and over. This second process is often limited by *synchrotron radiation*, which describes the radiation produced when a charged particle is accelerated. The power radiated is

$$P \sim \frac{1}{r^2} \left( E/m \right)^4 \quad (4.2)$$

555 where  $r$  is the radius of curvature and  $E, m$  is the energy (mass) of the charged  
 556 particle. Given an energy which can be produced by a given set of RF cavities (which  
 557 is *not* limited by the mass of the particle), one then has two options to increase the  
 558 actual collision energy : increase the radius of curvature or use a heavier particle.  
 559 Practically speaking, the easiest options for particles in a collider are protons and  
 560 electrons, since they are copiously produced in nature and do not decay<sup>1</sup>. Given the  
 561 dependence on mass, we can see why protons are used to reach the highest energies.  
 562 The tradeoff for this is that protons are not point particles, and we thus we don't  
 563 know the exact incoming four-vectors of the protons. This is a reflection of the “bag  
 564 model” discussed in Ch. 2, where each proton is actually a bag of incoming quarks  
 565 and gluons, which individually contribute to the total proton energy.

The particle *beam* refers to the bunches combined. An important property of a beam of a particular energy  $E$ , moving in uniform magnetic field  $B$ , containing particles of momentum  $p$  is the *beam rigidity* :

$$R \equiv rB = p/c. \quad (4.3)$$

---

<sup>1</sup>Muon colliders are a potential future option at high energies, since the relativistic  $\gamma$  factor gives them a relatively long lifetime in the lab frame.

566 The linear relation between  $r$  and  $p$ , or alternatively  $B$  and  $p$  have important  
 567 consequences for LHC physics. For hadron colliders, this is the limiting factor on  
 568 going to higher energy scales; one needs a proportionally larger magnetic field to  
 569 keep the beam accelerating in a circle.

570 Besides the rigidity of the beam, the most important quantities to characterize  
 571 a beam are known as the (normalized) *emittance*  $\epsilon_N$  and the *betatron function*  $\beta$ .  
 572 These quantities determine the transverse size  $\sigma$  of a relativistic beam  $v \leq c$  beam :  
 573  $\sigma^2 = \beta^* \epsilon_N / \gamma_{\text{rel}}$ , where  $\beta^*$  is the value of the betatron function at the collision point  
 574 and  $\gamma_{\text{rel}}$  is the Lorentz factor.

These quantities determine the *instantaneous luminosity*  $L$  of a collider, which combined with the cross-section  $\sigma$  of a particular physics process, give the rate of the physics process :

$$R = L\sigma. \quad (4.4)$$

The instantaneous luminosity  $L$  is given by :

$$L = \frac{f_{\text{rev}} N_b^2 F}{4\pi\sigma^2} = \frac{f_{\text{rev}} n N_b^2 \gamma_{\text{rel}} F}{4\pi\beta^* \epsilon_N}. \quad (4.5)$$

575 Here we have introduced the frequency of revolutions  $f_{\text{rev}}$ , the number of bunches  $n$ ,  
 576 the number of protons per bunch  $N_b^2$ , and a geometric factor  $F$  related to the crossing  
 577 angle of the beams.

The *integrated luminosity*  $\int L dt$  gives the total number of a particular physics process  $P$ , with cross-section  $\sigma_P$ .

$$N_P = \sigma_P \int L dt. \quad (4.6)$$

578 Due to this simple relation, one can also quantify the “amount of data delivered” by  
 579 a collider simply by  $\int L dt$ .



Figure 4.1: The CERN accelerator complex. Copyright CERN.

## 4.2 Accelerator Complex

The Large Hadron Collider is the last accelerator in a chain of accelerators which together form the CERN accelerator complex, shown in Fig. 4.1. The protons begin their journey to annihilation in a hydrogen source, where they are subsequently ionized. The first acceleration occurs in the Linac 2, a linear accelerator composed of RF cavities. The protons leave the Linac 2 at an energy of 50 MeV and enter the Proton Synchrotron Booster (PSB). The PSB contains four superimposed rings, which accelerate the protons to 1.4 GeV. The protons are then injected into the Proton Synchrotron (PS). This synchrotron increases the energy up to 25 GeV. After leaving the PS, the protons enter the Super Proton Synchrotron (SPS). This is the last step before entering the LHC ring, and the protons are accelerated to 450 GeV. From the SPS, the protons are injected into the beam pipes of the LHC. The process

592 to fill the LHC rings with proton bunches from start to finish typically takes about  
593 four minutes.

594 **4.3 Large Hadron Collider**

The Large Hadron Collider is the final step in the CERN accelerator complex, and produces the collisions analyzed in this thesis. From the point of view of experimentalists on the general-purpose ATLAS and CMS experiments, the main goal of the LHC is to deliver collisions at the highest possible energy, with the highest possible instantaneous luminosity. The LHC was installed in the existing 27 km tunnel used by the Large Electron Positron (LEP) collider [87]. This allowed the existing accelerator complex at CERN, described in the previous section, to be used as the injection system to prepare the protons up to 450 GeV. Many aspects of the LHC design were decided by this very constraint, and specified the options allowed to increase the energy or luminosity. In particular, the radius of the tunnel was already specified. From Eq.Eq. (4.3), this implies the momentum (or energy) of the beam is entirely determined by the magnetic field. Given the 27 km circumference of the LEP tunnel, one can calculate the required magnetic field to reach the 7 TeV per proton design energy of the LHC :

$$r = C/2\pi = 4.3 \text{ km} \quad (4.7)$$

$$\rightarrow B = \frac{p}{rc} = 5 \text{ T} \quad (4.8)$$

595 In fact, the LHC consists of eight 528 m straight portions consisting of RF cavities,  
596 used to accelerate the particles, and 8 circular portions which bend the protons  
597 around the LHC ring. These circular portions actually have a slightly smaller radius  
598 of curvature  $r = 2804$  m, and require  $B = 8.33$  T. To produce this large field,  
599 superconducting magnets are used.

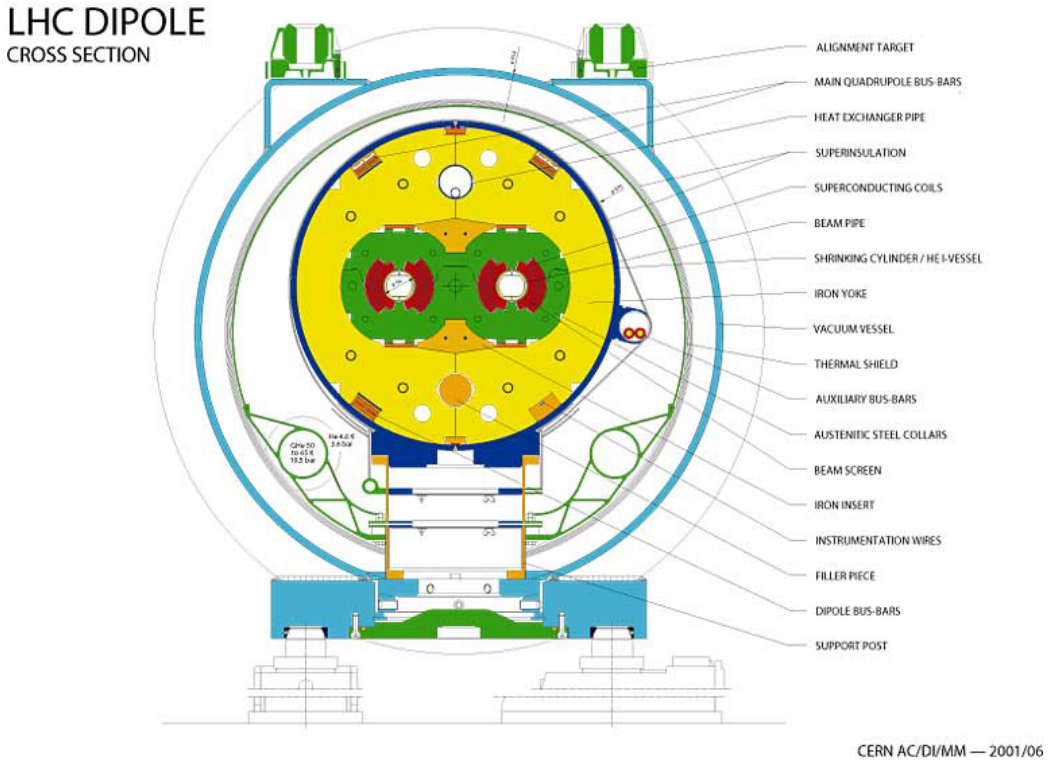


Figure 4.2: Schematic of an LHC dipole magnet. Copyright CERN.

## 600 Magnets

601 There are many magnets used by the LHC machine, but the most important are  
 602 the 1232 dipole magnets. A schematic is shown in Fig. Fig. 4.2 and a photograph is  
 603 present in Fig. 4.3.

604 The magnets are made of Niobium and Titanium. The maximum field strength is  
 605 10 T when cooled to 1.9 Kelvin. The magnets are cooled by superfluid helium, which  
 606 is supplied by a large cryogenic system. Due to heating between the eight helium  
 607 refrigerators and the beampipe, the helium is cooled in the refrigerators to 1.8 K.

608 A failure in the cooling system can cause what is known as a *quench*. If the  
 609 temperature goes above the critical superconducting temperature, the metal loses its  
 610 superconducting properties, which leads to a large resistance in the metal. This leads  
 611 to rapid temperature increases, and can cause extensive damages if not controlled.

612 The dipole magnets are 16.5 meters long with a diameter of 0.57 meters. There

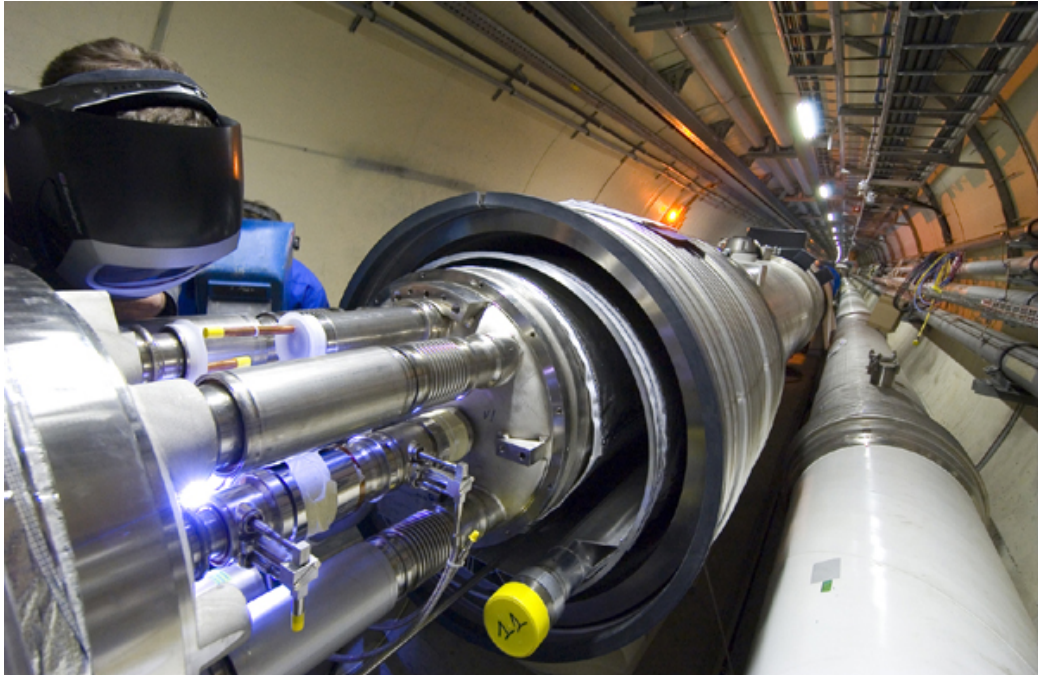


Figure 4.3: Photograph of a technician connecting an LHC dipole magnet. Copyright CERN.

613 are two individual beam pipes inside each magnet, which allows the dipoles to house  
614 the beams travelling in both directions around the LHC ring. They curve slightly,  
615 at an angle of 5.1 mrad, which carefully matches the curvature of the ring. The  
616 beampipes inside of the magnets are held in high vacuum to avoid stray interactions  
617 with the beam.

## 618 **4.4 Dataset Delivered by the LHC**

619 In this thesis, we analyze the data delivered by the LHC to ATLAS in the 2015 and  
620 2016 datasets. The beam parameters relevant to this dataset are available in Tab. 4.1.  
621

622 The peak instantaneous luminosity delivered in 2015 (2016) was  $L =$   
623  $5.2(11) \text{ cm}^{-2}\text{s}^{-1} \times 10^{33}$ . One can note that the instantaneous luminosity delivered in  
624 the 2016 dataset exceeds the design luminosity of the LHC. The total integrated

Parameter	Injection	Extraction
Energy (GeV)	450	7000
Rigidity (T-m)	3.8	23353
Bunch spacing (ns)	25	25
Design Luminosity ( $\text{cm}^{-2}\text{s}^{-1} \times 10^3$ )	-	1.0
Bunches per proton beam	2808	2808
Protons per bunch	1.15 e11	1.15 e11
Beam lifetime (hr)	-	10
Normalized Emittance $\epsilon_N$ (mm $\mu\text{rad}$ )	3.3	3.75
Betatron function at collision point $\beta^*$ (cm)	-	55

Table 4.1: Beam parameters of the Large Hadron Collider.

625 luminosity delivered was  $13.3 \text{ fb}^{-1}$ . In Fig. 4.4, we display the integrated luminosity  
 626 per day for 2015 and 2016.

## 627 Pileup

628 *Pileup* is the term for the additional proton-proton interactions which occur during  
 629 each bunch crossing of the LHC. At the beginning of the LHC physics program, there  
 630 had not been a collider which averaged more than a single interaction per bunch  
 631 crossing. In the LHC, each bunch crossing (or *event*) generally contains multiple  
 632 proton-proton interactions. An simulated event with many *vertices* can be seen in  
 633 Fig. 4.5. The so-called *primary vertex* (or *hard scatter vertex*) refers to the vertex  
 634 which has the highest  $\Sigma p_T^2$  The summation occurs over the *tracks* in the detector,  
 635 which we will describe later [ATL-INDET-PUB-2009-001]. We then distinguish  
 636 between *in-time* pileup and *out-of-time* pileup. In-time pileup refers to the additional  
 637 proton-proton interactions which occur in the event. Out-of-time pileup refers to  
 638 effects related to proton-proton interactions previous bunch crossings.

639 We quantify in-time pileup by the number of “primary”<sup>2</sup> vertices in a particular  
 640 event. To quantify the out-of-time pileup, we use the average number of interactions

---

<sup>2</sup>The primary vertex is as defined above, but we unfortunately use the same name here.

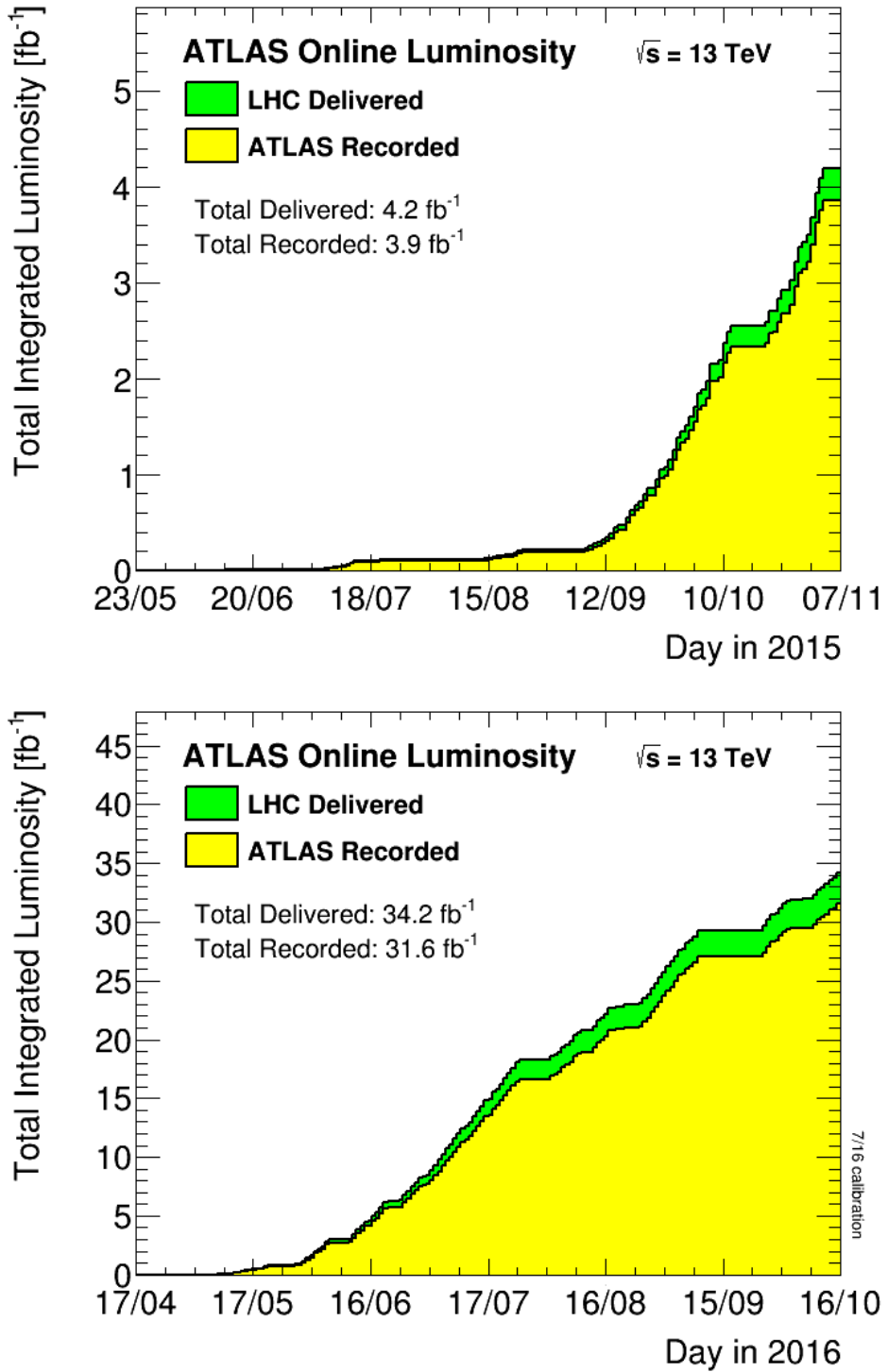


Figure 4.4: Integrated Luminosity delivered by the LHC and collected by ATLAS in the 2015 and 2016 datasets.

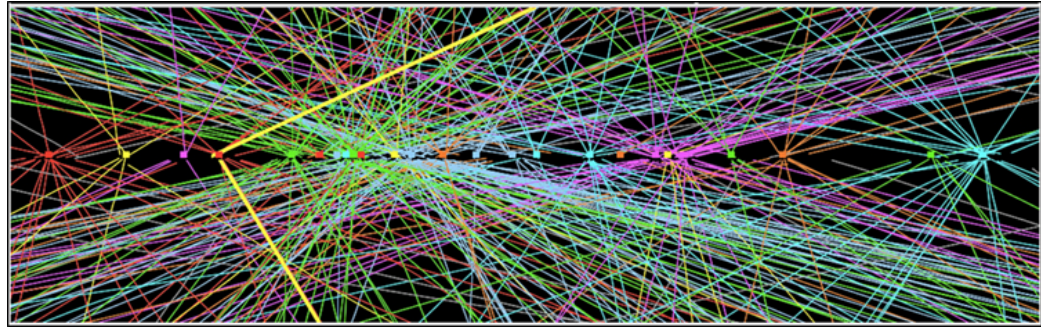


Figure 4.5: Simulated event with many pileup vertices.

641 per bunch crossing  $\langle \mu \rangle$ . In Fig. 4.6, we show the distribution of  $\mu$  for the dataset  
642 used in this thesis.



Figure 4.6: Mean number of interactions per bunch crossing in the 2015 and 2016 datasets.



*The ATLAS detector*

645 The dataset analyzed in this thesis was taken by the ATLAS detector [88], which  
 646 is located at the “Point 1” cavern of the LHC, just across the street from the main  
 647 CERN campus. The much-maligned acronym stands for *A Toroidal LHC ApparatuS*.  
 648 ATLAS is a massive cylindrical detector, with a radius of 12.5 m and a length of  
 649 44 m, with nearly hermitic coverage around the collision point. Each of the many  
 650 subdetectors plays a role in measuring the energy, momentum, and type of the particles  
 651 produced in collisions delivered by the LHC. These subdetectors are immersed in  
 652 a hybrid solenoid-toroid magnet system which allows for precise measurements of  
 653 particle momenta. The central solenoid magnet contains a magnetic field of 2 T. A  
 654 schematic of the detector is shown in Fig. 5.1.

655 The *inner detector* (ID) lies closest to the collision point, and contains three  
 656 separate subdetectors. It provides pseudorapidity<sup>1</sup> coverage of  $|\eta| < 2.5$  for charged  
 657 particles. The tracks reconstructed from the inner detector hits are used to  
 658 reconstruct the primary vertices and to determine the momemta of charged particles.  
 659 The ATLAS *calorimeter* consists of two subdetectors, known as the *electromagnetic*  
 660 and *hadronic* calorimeters. These detectors stop particles and measure their energy

---

<sup>1</sup>ATLAS uses a right-handed Cartesian coordinate system. The origin is defined by the nominal beam interaction point. The positive- $z$  direction is defined by the incoming beam travelling counterclockwise around the LHC. The positive- $x$  direction points towards the center of the LHC ring from the origin, and the positive- $y$  direction points upwards towards the sky. For particles of transverse (in the  $x - y$  plane) momentum  $p_T = \sqrt{p_x^2 + p_y^2}$  and energy  $E$ , it is generally most convenient fully describe this particle’s kinematics as measured by the detector in the  $(p_T, \phi, \eta, E)$  basis. The angle  $\phi = \arctan(p_y/p_x)$  is the standard azimuthal angle, and  $\eta = \ln \tan(\theta/2)$  is known as the pseudorapidity, and defined based on the standard polar angle  $\theta = \arccos(p_z/p_T)$ . For locations of detector elements, both  $(r, \phi, \eta)$  and  $(z, \phi, \eta)$  can be useful.



Figure 5.1: The ATLAS detector. Copyright CERN.

661 deposition. The calorimeters provide coverage out to pseudorapidity of  $|\eta| < 4.9$ . The  
 662 muon spectrometer is aptly named, as it measures muons, which are the only particles  
 663 which generally reach the outer portions of the detector. In this region, we have the  
 664 large tracking systems of the muon spectrometer, which provide precise measurements  
 665 of muon momenta. The muon spectrometer has pseudorapidity coverage of  $|\eta| < 2.7$ .

## 666 5.1 Magnets

667 ATLAS contains multiple magnetic systems. Primarily, we are concerned with the  
 668 solenoid, used by the inner detector, and the toroids located outside of the ATLAS  
 669 calorimeter. A schematic is shown in Fig. 5.2. These magnetic fields are used to bend  
 670 charged particles, which subsequently allows one to measure their momentum.

671 The ATLAS central solenoid is a 2.3 m diameter, 5.3 m long solenoid at the center  
 672 of the ATLAS detector. It produces a uniform magnetic field of 2 T. An important  
 673 design constraint for the central solenoid was the decision to place it in between

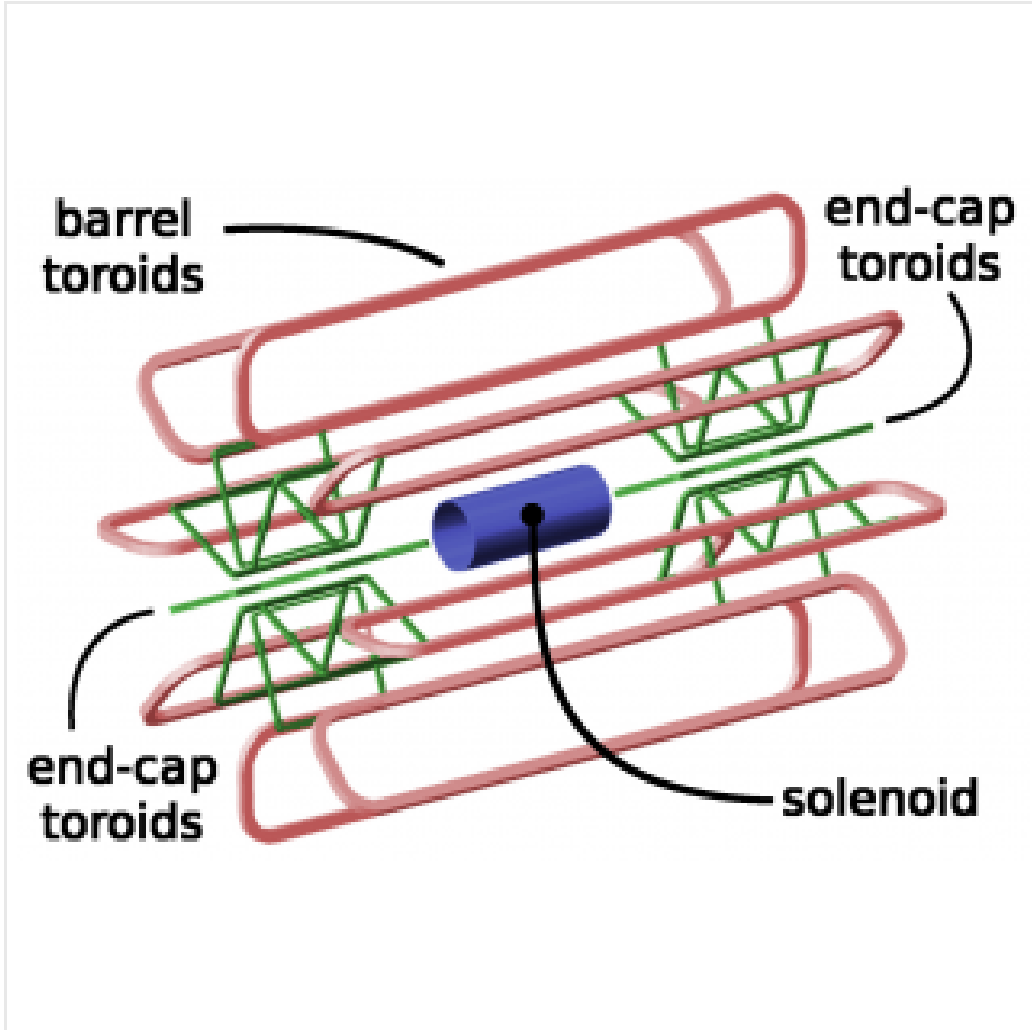


Figure 5.2: The ATLAS magnet system. Copyright CERN.

674 the inner detector and the calorimeters. To avoid excessive energy deposition which  
675 could affect calorimeter measurements, the central solenoid must be as transparent  
676 as possible<sup>2</sup>.

677 The toroid system consists of eight air-core superconducting barrel loops, which  
678 give ATLAS its distinctive shape. There are also two endcap air-core magnets. These  
679 produce a magnetic field in a region of approximately 26 m in length and 10 m of  
680 radius. The magnetic field in this region is non-uniform.

---

<sup>2</sup>This is also one of the biggest functional differences between ATLAS and CMS In CMS, the solenoid is outside of the calorimeters.



Figure 5.3: The ATLAS inner detector. Copyright CERN.

## 681 5.2 Inner Detector

682 The ATLAS inner detector consists of three separate tracking detectors, which are  
 683 known as, in order of increasing distance from the interaction point, the Pixel  
 684 Detector, Semiconductor Tracker (SCT), and the Transition Radiation Tracker  
 685 (TRT). When charged particles pass through these tracking layers, they produce  
 686 *hits*, which using the known 2 T magnetic field, allows the reconstruction of *tracks*.  
 687 Tracks are used as inputs for reconstruction of many higher-level physics objects,  
 688 such as electrons, muons, photons, and  $E_T^{\text{miss}}$ . Accurate track reconstruction is thus  
 689 crucial for precise measurements of charged particles.

## 690 Pixel Detector

691 The ATLAS pixel detector consists four layers of silicon “pixels” [89]. This refers  
 692 to the segmentation of the active medium into pixels, which provide precise 3D hit  
 693 locations. The layers are known as the “Insertable” B-Layer (IBL), the B-Layer (or

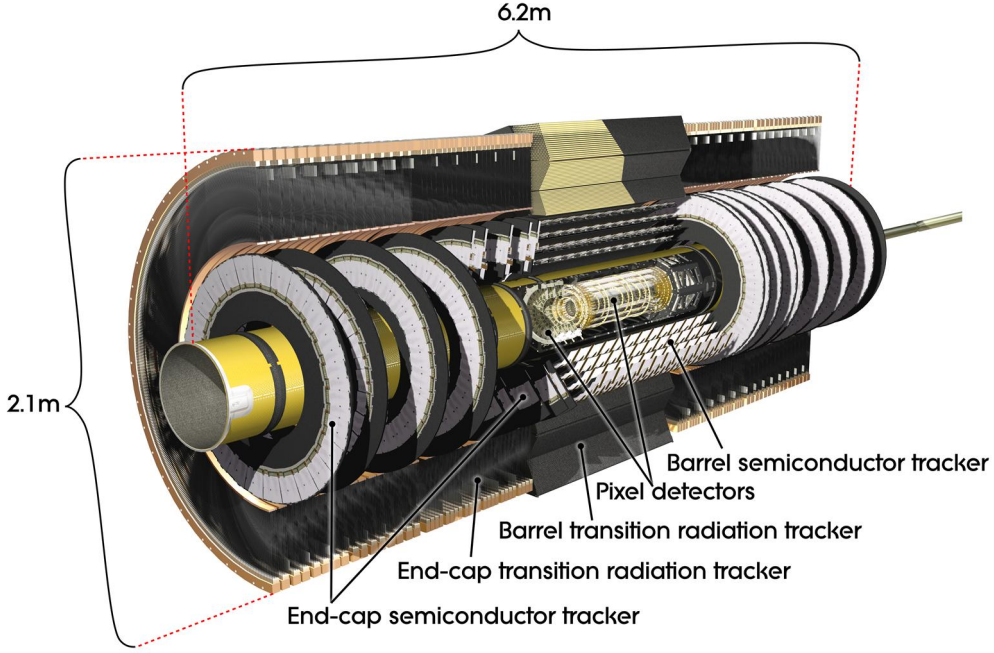


Figure 5.4: The ATLAS pixel detector. Copyright CERN.

694 Layer-0), Layer-1, and Layer-2, in order of increasing distance from the interaction  
 695 point. These layers are close to the interaction point, and therefore experience  
 696 significant radiation exposure.

697 Layer-1, Layer-2, and Layer-3 were installed with the initial construction of  
 698 ATLAS. They contain front-end integrated electronics (FEI3s) bump-bonded to 1744  
 699 silicon modules. Each module is  $250 \mu\text{m}$  in thickness and contains 47232 pixels.  
 700 These pixels have planar sizes of  $50 \times 400 \mu\text{m}^2$  or  $50 \times 600 \mu\text{m}^2$ , to provide highly  
 701 accurate location information. The FEI3s are mounted on long rectangular structures  
 702 known as staves, which encircle the beam pipe. A small tilt to each stave allows full  
 703 coverage in  $\phi$ . These layers are at radii of 50.5 mm, 88.5 mm, and 122.5 mm from  
 704 the interaction point.

705 The IBL was added to ATLAS after Run1 in 2012 at a radius of 33 mm from the  
 706 interaction point [90]. The IBL was required to preserve the integrity of the pixel  
 707 detector as radiation damage leads to inoperative pixels in the other layers. The IBL

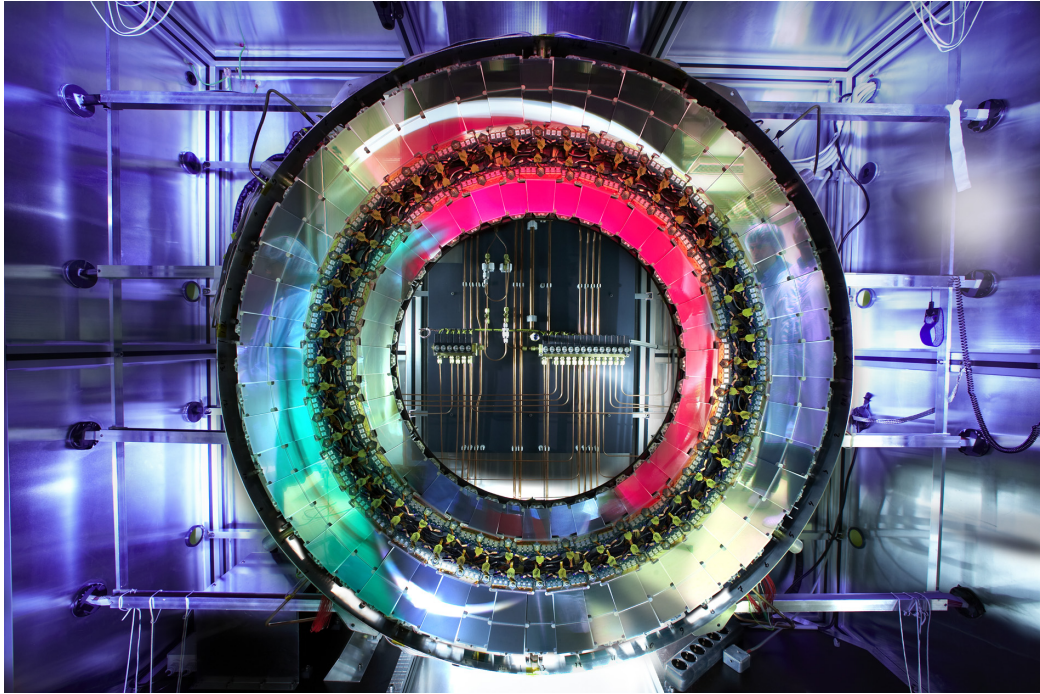


Figure 5.5: A ring of the Semiconductor Tracker. Copyright CERN.

708 consists of 448 FEI4 chips, arranged onto 14 staves. Each FEI4 has 26880 pixels, of  
709 planar size  $50 \times 250 \mu\text{m}$ . This smaller granularity was required due to the smaller  
710 distance to the interaction point.

711 In total, a charged particle passing through the inner detector would expect to  
712 leave four hits in the pixel detector.

### 713 Semiconductor Tracker

714 The SCT is a silicon strip detector directly beyond Layer-2 of the pixel detector [91].  
715 The dual-sensors of the SCT contain  $2 \times 768$  individual strips. Each strip has area  
716  $6.4 \text{ cm}^2$ . The SCT dual-sensor is double-layered, at a relative angle of 40 mrad.  
717 Together, these layers provide the necessary 3D information for track reconstruction.  
718 There are four of these double-layers, at radii of 284 mm, 355 mm, 427 mm, and 498  
719 mm. These double-layers provide hits comparable to those of the pixel detector. The  
720 SCT provides an four additional hits to reconstruct tracks for each charged particle.

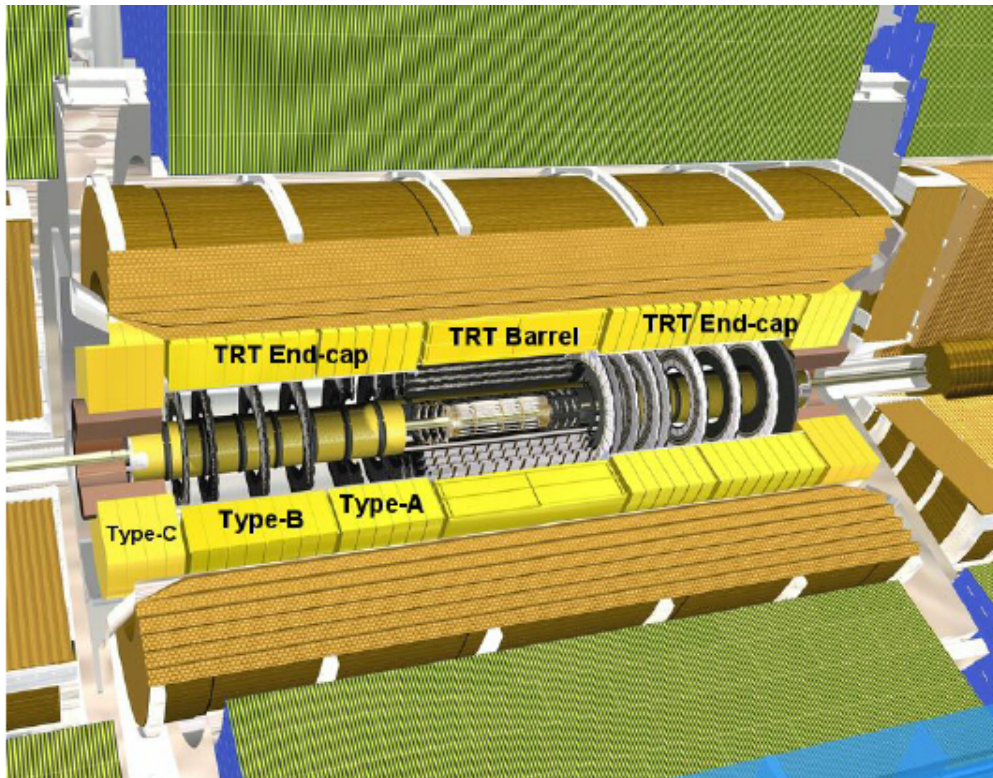


Figure 5.6: A schematic of the Transition Radiation Tracker. Copyright CERN.

## 721    Transition Radiation Tracker

722    The Transition Radiation Tracker is the next detector radially outward from the SCT.  
723    It contains straw drift tubes. Each tube contains a tungsten gold-plated wire of  $32 \mu\text{m}$   
724    diameter held under high voltage (-1530 V) with the edge of the Kapton-aluminum  
725    tube. They are filled with a gas mixture of primarily xenon that is ionized when  
726    a charged particle passes through the tube. The ions are collected by the “drift”  
727    due to the voltage inside the tubes, which is read out by the electronics. Due to  
728    the dielectric difference between the gas and tubes, transition radiation is induced.  
729    This is important for distinguishing electrons from their predominant background of  
730    minimum ionizing particles. Generally, electrons have a much larger Lorentz factor  
731    than minimum ionizing particles, which leads to additional transition radiation. This  
732    is used to discriminate electrons from background in electron reconstruction.

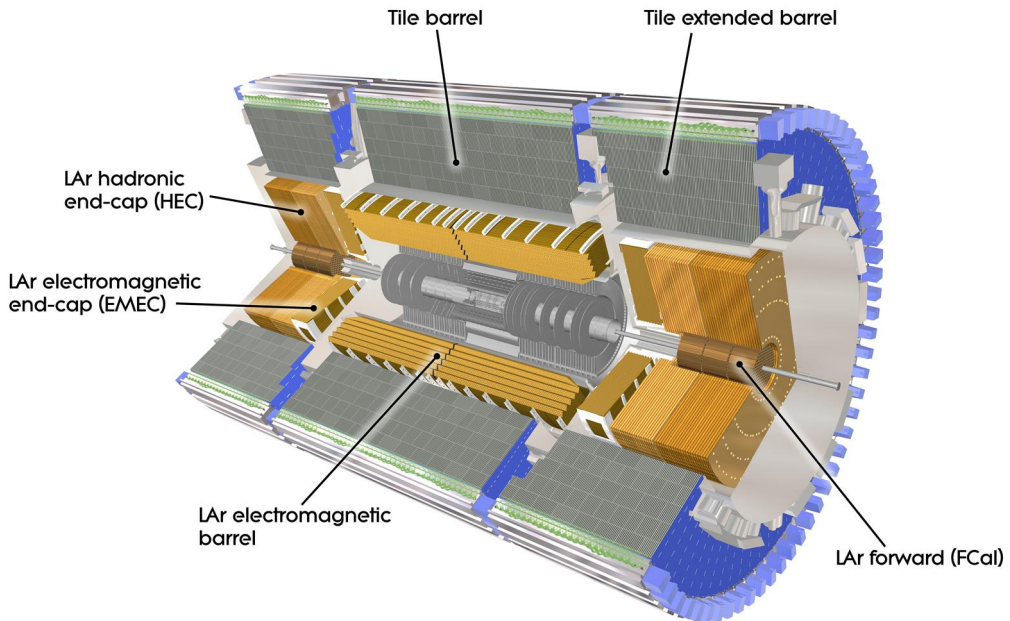


Figure 5.7: The ATLAS calorimeter. Copyright CERN.

### <sup>733</sup> 5.3 Calorimetry

<sup>734</sup> The calorimetry of the ATLAS detector also includes multiple subdetectors which  
<sup>735</sup> allow precise measurements of the electrons, photons, and hadrons produced in  
<sup>736</sup> collisions delivered by the LHC. Calorimeters work by stopping particles in their  
<sup>737</sup> material and measuring the energy deposition. This energy is deposited as a  
<sup>738</sup> cascade of particles induce from interactions with the detector material known as  
<sup>739</sup> *showers*. ATLAS uses *sampling* calorimeters, alternating a dense absorbing material  
<sup>740</sup> to induce showers with an active layer to measure energy depositions by the induced  
<sup>741</sup> showers. Since some energy is deposited into the absorption layers as well, the energy  
<sup>742</sup> depositions must be properly calibrated for the detector.

<sup>743</sup> Electromagnetic objects (electrons and photons) and hadrons have different  
<sup>744</sup> interaction properties. We use different types of calorimeters to accurately measure  
<sup>745</sup> these classes of objects, which we call *electromagnetic* and *hadronic* calorimeters.  
<sup>746</sup> ATLAS contains multiple separate calorimeters : the liquid argon (LAr) electro-

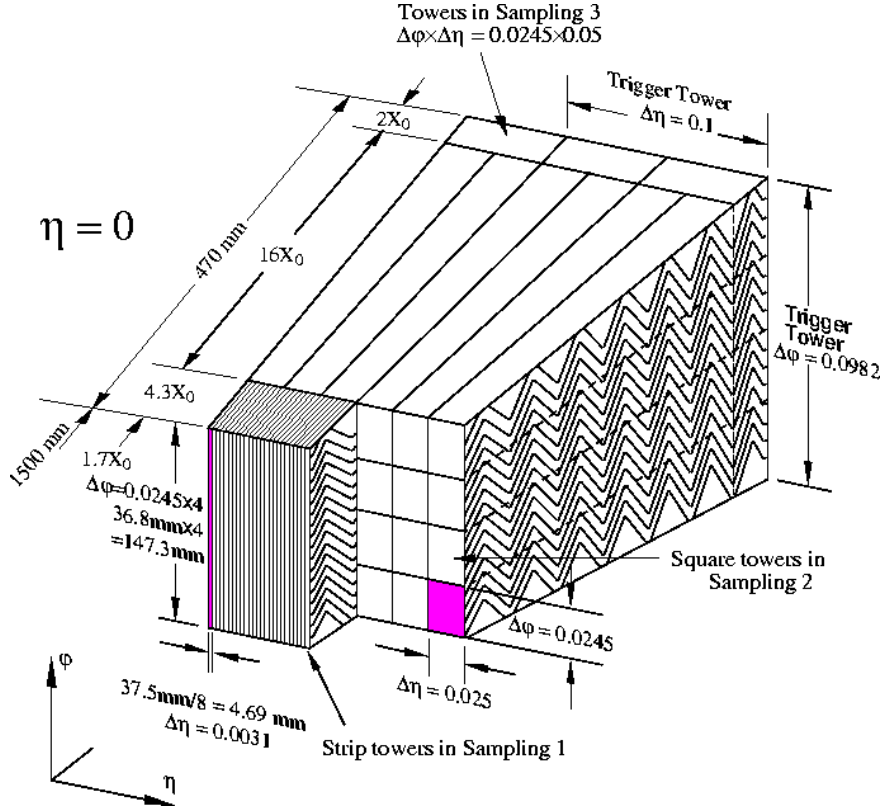


Figure 5.8: A schematic of a subsection of the barrel LAr electromagnetic calorimeter.  
Copyright CERN.

747 magnetic barrel calorimeter, the Tile barrel hadronic calorimeter, the LAr endcap  
 748 electromagnetic calorimeter, the LAr endcap hadronic calorimeter, and the LAr  
 749 Forward Calorimeter (FCal). Combined, these provide full coverage in  $\phi$  up to  
 750  $|\eta| < 4.9$ . They are shown in Fig. 5.7.

## 751 Electromagnetic Calorimeters

752 The electromagnetic calorimeters of the ATLAS detector consist of the barrel and  
 753 endcap LAr calorimeters. These are arranged into an “accordion” shape, shown  
 754 in Fig. 5.8, which allows full coverage in  $\phi$  and significant coverage in  $\eta$  while  
 755 still allowing support structures for detector operation. The accordion is made of  
 756 layers with liquid argon (active detection material) and lead (absorber) to induce  
 757 electromagnetic showers. The LAr EM calorimeters are each more than 20 radiation

758 lengths deep, which provides the high stopping power necessary to properly measure  
759 the electromagnetic showers.

760 The barrel component of the LAr EM calorimeter extends from the center of the  
761 detector out to  $|\eta| < 1.475$ . The calorimeter has a presampler, which measures the  
762 energy of any EM shower induced before the calorimeter. This has segmentation of  
763  $\Delta\eta = 0.025, \Delta\phi = .01$ . There are three “standard” layers in the barrel, which have  
764 decreasing segmentation into calorimeter *cells* as one travels radially outward from  
765 the interaction point. The first layer has segmentation of  $\Delta\eta = 0.003, \Delta\phi = .1,$   
766 and is quite thin with a depth of 4 radiation lengths. It provides precise  $\eta$  and  
767  $\phi$  measurements for incoming EM objects. The second layer is the deepest at 16  
768 radiation lengths, with a segmentation of  $\Delta\eta = 0.025, \Delta\phi = 0.025$ . It is primarily  
769 responsible for stopping the incoming EM particles, which dictates its large relative  
770 thickness, and measures most of the energy of the incoming particles. The third layer  
771 is only 2 radiation lengths deep, with a rough segmentation of  $\Delta\eta = 0.05, \Delta\phi = .025$ .  
772 The deposition in this layer is primarily used to distinguish hadrons interacting  
773 electromagnetically and entering the hadronic calorimeter from the strictly EM  
774 objects which are stopped in the second layer.

775 The barrel EM calorimeter has a similar overall structure, but extends from  $1.4 <$   
776  $|\eta| < 3.2$ . The  $\eta$  segmentation is smaller in the endcap than the barrel, while the  
777  $\phi$  segmentation is the same. In total, the EM calorimeters contain about 190000  
778 individual calorimeter cells.

## 779 Hadronic Calorimeters

780 The hadronic calorimetry of ATLAS sits directly outside the EM calorimetry. It  
781 contains three subdetectors : the barrel Tile calorimeter, the endcap LAr calorimeter,  
782 and the Forward LAr Calorimeter. Similar to the EM calorimeters, these are  
783 sampling calorimeters that alternate steel (dense material) with an active layer

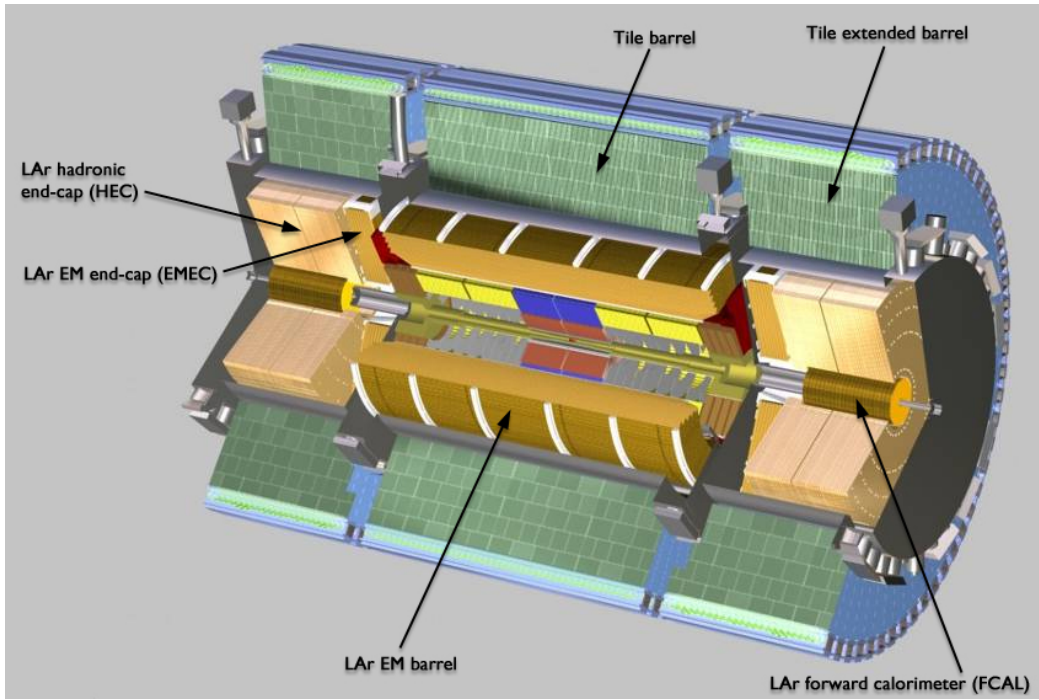


Figure 5.9: A schematic of Tile hadronic calorimeter. Copyright CERN.

784 (plastic scintillator).

785 The barrel Tile calorimeter extends out to  $|\eta| < 1.7$ . It has three layers, which  
 786 combined give about 10 interaction lengths to provide excellent stopping power for  
 787 hadrons. This is critical to avoid excess *punchthrough* to the muon spectrometer  
 788 beyond the hadronic calorimeters. The first layer has a depth of 1.5 interaction  
 789 lengths. The second layer is again the thickest at a depth of 4.1 interaction lengths.  
 790 Most of the energy of incoming particles is deposited in the second layer. Both  
 791 the first and second layer have segmentation of  $\Delta\eta = 0.1, \Delta\phi = 0.1$ . Generally,  
 792 one does not need as fine granularity in the hadronic calorimeter, since the energy  
 793 depositions in the hadronic calorimeters will be summed into the composite objects as  
 794 jets. The third layer has a thickness of 1.8 interaction lengths, with a segmentation of  
 795  $\Delta\eta = 0.2, \Delta\phi = 0.1$ . The use of multiple layers gives information about the induced  
 796 hadronic shower as it propagates through the detector material.

797 The endcap LAr hadronic calorimeter is a sampling calorimeter which covers the

798 region  $1.5 < |\eta| < 3.2$ . Liquid argon is the active material and it uses a copper  
799 absorber. Unlike the other sampling calorimeters in ATLAS, it does not use the  
800 accordion shape. Instead, it is a flat detector perpendicular to the interaction point.  
801 The segmentation varies with  $\eta$ , ranging from cells of size  $\Delta\eta = 0.1, \Delta\phi = 0.1$  in the  
802 center region to  $\Delta\eta = 0.2, \Delta\phi = 0.2$  in the forward region.

803 The forward LAr calorimeter is the last subdetector of the ATLAS calorimetry.  
804 Of those subdetectors which are used for standard reconstruction techniques, the  
805 FCal sits at the most extreme values of  $3.1 < |\eta| < 4.9$ . The FCal itself is made of  
806 three subdetectors: the electromagnetic FCal1 and hadronic FCal2 and FCal3. The  
807 absorber in FCal1 is copper, with a liquid argon active medium. FCal2 and FCal3  
808 also use a liquid argon active medium, with a tungsten absorber.

## 809 5.4 Muon Spectrometer

810 The muon spectrometer sits outside the hadronic calorimetry, with pseudorapidity  
811 coverage out to  $|\eta| < 2.7$ . The MS is a huge detector, with some detector elements  
812 existing as far as 11 m in radius from the interaction point. This system is used  
813 almost exclusively to measure the momenta of muons. These systems provide a  
814 rough measurement, which is used in triggering (described in Sec. 5.5), and a precise  
815 measurement to be used in offline event reconstruction. The MS produces tracks in a  
816 similar way to the ID. The hits in each subdetector are recorded and then tracks are  
817 produced from these hits. Muon spectrometer tracks are largely independent of the  
818 ID tracks due to the independent solenoidal and toroidal magnet systems used in the  
819 ID and MS respectively. The MS consists of four separate subdetectors: the barrel  
820 region is covered by the Resistive Plate Chambers (RPCs) and Monitored Drift Tubes  
821 (MDTs) while the endcaps are covered by MDTs, Thin Gap Chambers (TGCs), and  
822 Cathode Strip Chambers (CSCs).

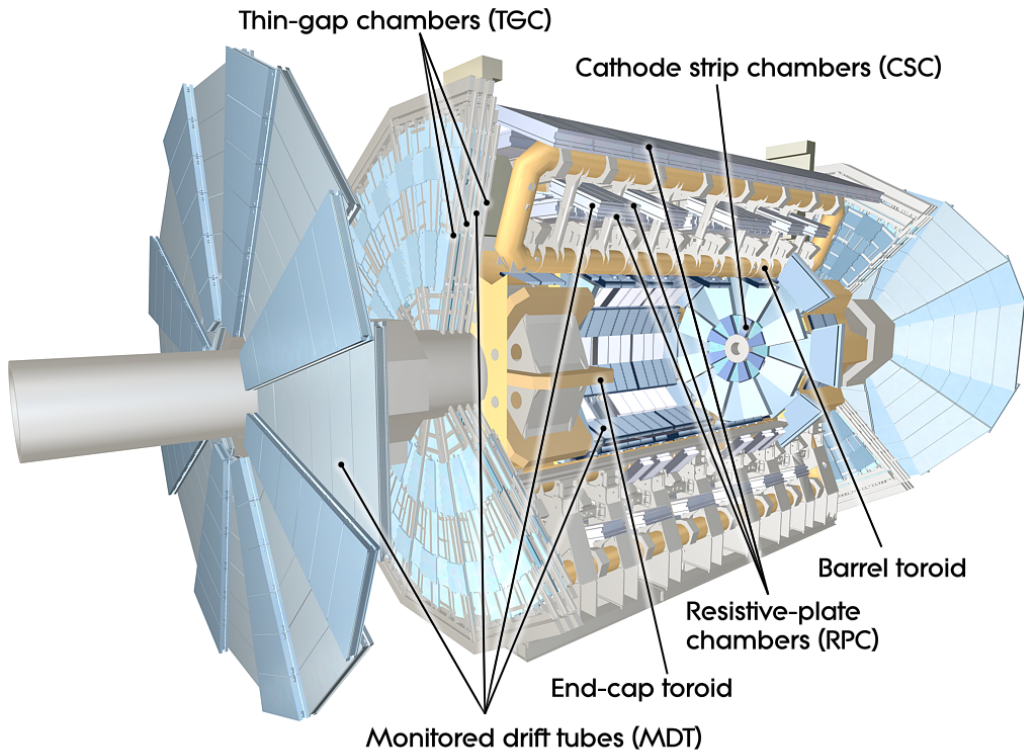


Figure 5.10: The ATLAS muon spectrometer. Copyright CERN.

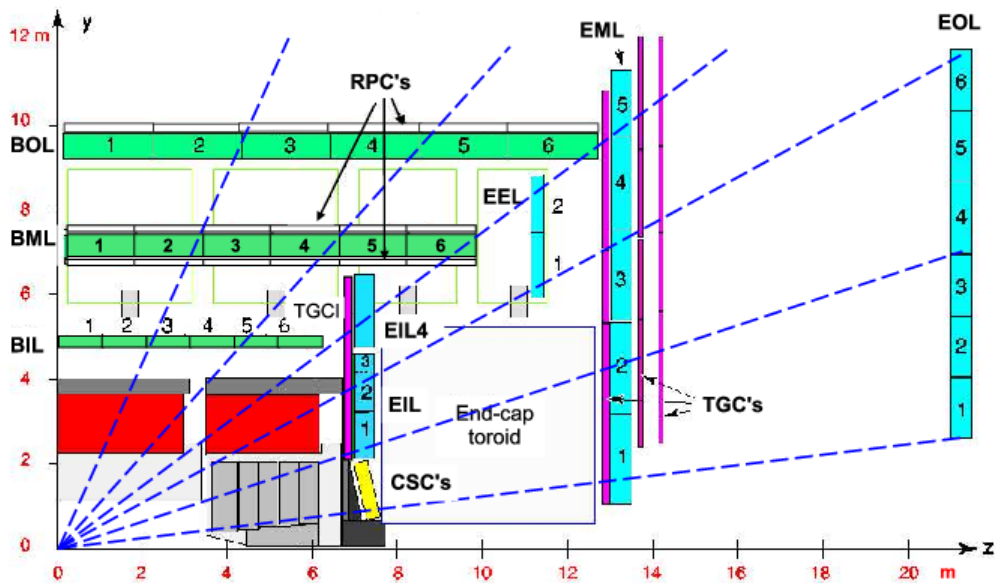


Figure 5.11: A schematic in  $z/\eta$  showing the location of the subdetectors of the muon spectrometer. Copyright CERN.

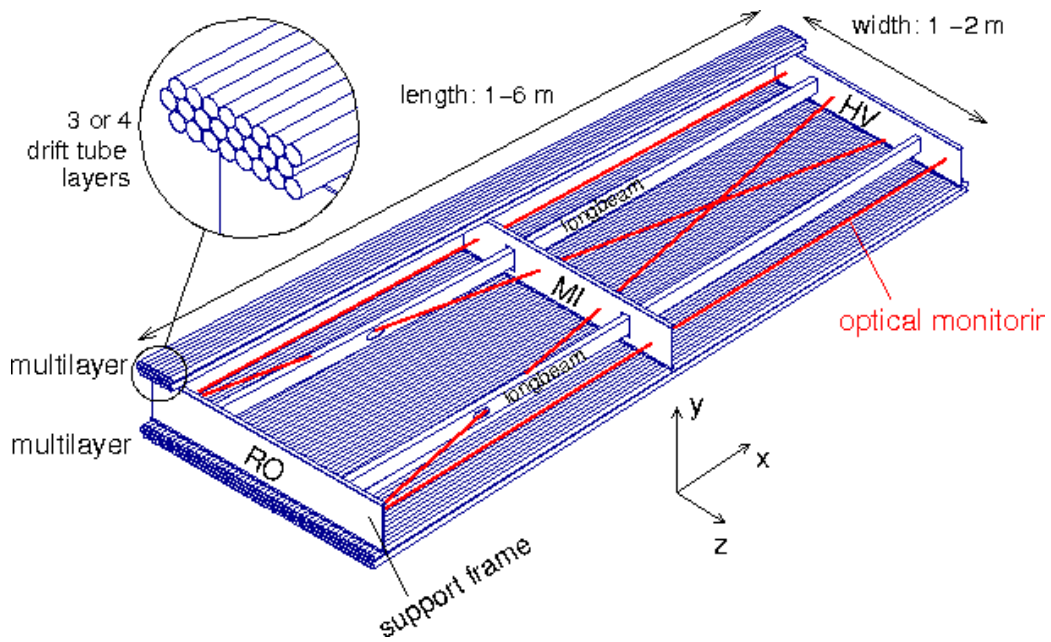


Figure 5.12: Schematic of a Muon Drift Tube chamber. Copyright CERN.

### 823 Monitored Drift Tubes

824 The MDT system is the largest individual subdetector of the MS. MDTs provide  
825 precision measurements of muon momenta as well as fast measurements used for  
826 triggering. There are 1088 MDT chambers providing coverage out to pseudorapidity

827  $|\eta| < 2.7$ . Each consists of an aluminum tube containing an argon-CO<sub>2</sub> gas mixture.  
828 In the center of each tube there 50  $\mu\text{m}$  diameter tungsten-rhenium wire at a voltage of  
829 3080 V. A muon entering the tube will induce ionization in the gas, which will “drift”  
830 towards the wire due to the voltage. One measures this ionization as a current in the  
831 wire. The current comes with a time measurement related to how long it takes the  
832 ionization to drift to the wire.

833 These tubes are layered in a pattern shown in Fig. 5.12. Combining the  
834 measurements from the tubes in each layer gives good position resolution. The  
835 system consists of three subsystems of these layers, at 5 m, 7 m, and 9 m from the  
836 interaction point. The innermost layer is directly outside the hadronic calorimeter.  
837 The combination of these three measurements gives precise momenta measurements  
838 for muons.

## 839 Resistive Plate Chambers

840 The RPC system is alternated with the MDT system in the barrel. The first two layers  
841 of RPC detectors surround the second MDT layer while the third is outside the final  
842 MDT layer. The RPC system covers pseudorapidity  $|\eta| < 1.05$ . Each RPC consists  
843 of two parallel plates at a distance of 2 mm surrounding a C<sub>2</sub>H<sub>2</sub>F<sub>4</sub> mixture. The  
844 electric field between these plates is 4.9k kV/mm. Just as in the MDTs, an incoming  
845 muon ionizes the gas, and the deposited ionization is collected by the detector (in this  
846 case on the plates). It is quite fast, but with a relatively poor spatial resolution of  
847 1 cm. Still, it can provide reasonable  $\phi$  resolution due to its large distance from the  
848 interaction point. This is most useful in triggering, where the timing requirements  
849 are quite severe. The RPCs also complement the MDTs by providing a measurement  
850 of the non-bending coordinate.



Figure 5.13: Photo of the installation of Cathode Strip Chambers and Monitored Drift Tubes. Copyright CERN.

## 851    Cathode Strip Chambers

852    The CSCs are used in place of MDTs in the first layer of the endcaps. This region,  
 853    at  $2.0 < |\eta| < 2.7$ , has higher particle multiplicity at close distance to the interaction  
 854    point from low-energy photons and neutrons. The MDTs are not equip to deal with  
 855    the high particle rate in this region, so the CSCs were designed to deal with this  
 856    deficiency.

857    Each CSC consists multiwire proportional chambers, oriented radially outward  
 858    from the interaction point. These chambers overlap partially in  $\phi$ . The wires contain  
 859    a gas mixture of argon and  $\text{CO}_2$ , which is ionized when muons enter. The detectors  
 860    operate with a voltage of 1900 V, with much lower drift times than the MDTs. They  
 861    provide less hits than MDTs, but their lower drift times lower uptime and reduce the  
 862    amount of detector overload.

863    The CSCs are arranged into four planes on the wheels of the muon spectrometer,  
 864    as seen in Fig. Fig. 5.13. There are 32 CSCs in total, with 16 on each side of the  
 865    detector in  $\eta$ .

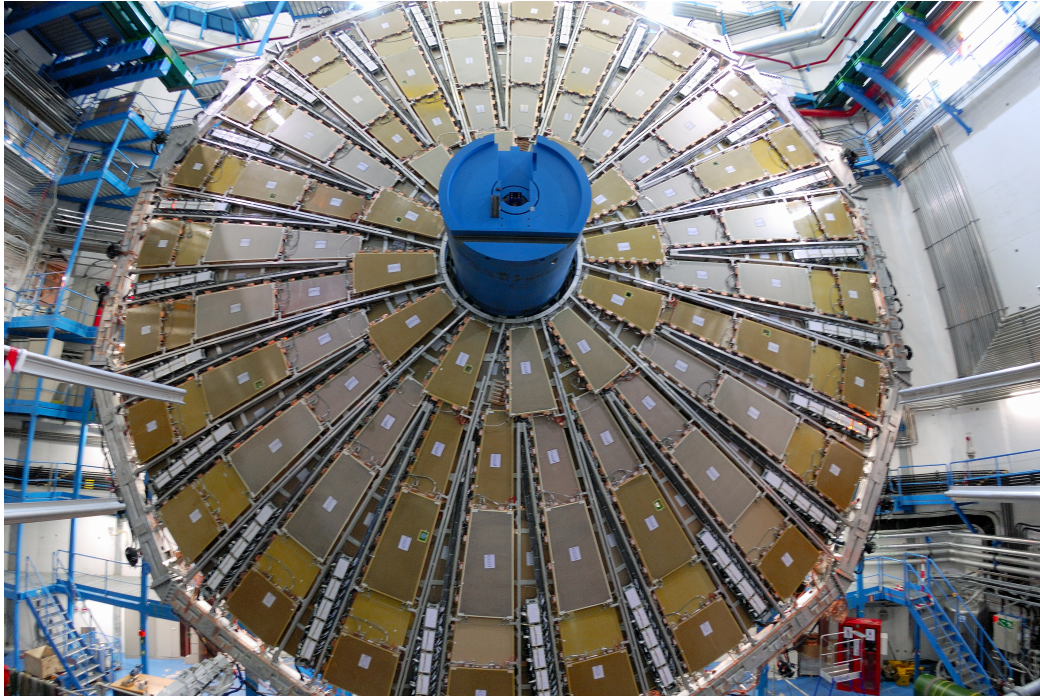


Figure 5.14: Photo of a muon Big Wheel, consisting of Thin Gap Chambers.  
Copyright CERN.

## 866 **Thin Gap Chambers**

867 The TGCs serve the purpose of the RPCs in the endcap at pseudorapidity of  $1.05 <$   
868  $|\eta| < 2.4$ , by providing fast measurements used for triggering. They are multiwire  
869 proportional chambers similar to the CSCs. The fast readouts necessary for triggering  
870 are provided by a high electric field and a small wire-to-wire distance of 1.8 mm.  
871 These detectors provide both  $\eta$  and  $\phi$  information, allowing the trigger to use as  
872 much information as possible when selecting events.

## 873 **5.5 Trigger System**

874 The data rate delivered by the LHC is staggering [92]. In the 2016 dataset, the  
875 collision rate was 40 MHz, meaning a *bunch spacing* of 25 ns. In each of the event,  
876 there are many proton-proton collisions. Most of the collisions are uninteresting,  
877 such as elastic scattering of protons, or even inelastic scattering leading to low-energy

878 dijet events. These low-energy events have have been studied in detail in previous  
879 experiments.

880 Even if one is genuinely interested in these events, it's *impossible* to save all of  
881 the information available in each event. If all events were written "to tape" (as the  
882 jargon goes), ATLAS would store terabytes of data per second. We are limited to only  
883 about 1000 Hz readout by computing processing time and storage space. We thus  
884 implement a *trigger* which provides fast inspection of events to drastically reduce  
885 the data rate from the 40 MHz provided by the LHC to the 1000 Hz we can write to  
886 tape for further analysis.

887 The ATLAS trigger system consists of a two-level trigger, known as the Level-  
888 1 trigger (L1 trigger) and the High-Level Trigger (HLT)<sup>3</sup>. Trigger selections are  
889 organized into *trigger chains*, where events passing a particular L1 trigger are passed  
890 to a corresponding HLT trigger. For example, one would require a particular high- $p_T$   
891 muon at L1, with additional quality requirements at HLT. One can also use HLT  
892 triggers as prerequisites for each other, as is done in some triggers requiring both jets  
893 and  $E_T^{\text{miss}}$ .

## 894 **Level-1 Trigger**

895 The L1 trigger is hardware-based, and provides the very fast rejection needed to  
896 quickly select events of interest. The L1 trigger uses only what is known as *prompt*  
897 data to quickly identify interesting events. Only the calorimeters and the triggering  
898 detectors (RPCs and TGCs) of the MS are fast enough to be considered at L1,  
899 since the tracking reconstruction algorithms used by the ID and the more precise  
900 MS detectors are very slow. This allows quick identification of events with the

---

<sup>3</sup>In Run1, ATLAS ran with a three-level trigger system. The L1 was essentially as today. The HLT consisted of two separate systems known as the L2 trigger and the Event Filter (EF). This was changed to the simpler system used today during the shutdown between Run1 and Run2.

901 most interesting physical objects: large missing transverse momentum and high- $p_T$   
902 electrons, muons, and jets.

903 L1 trigger processing is done locally. This means that events are selected without  
904 considering the entire available event. Energy deposits over some threshold are  
905 reconstructed as *regions of interest* (RoIs). These RoIs are then compared using  
906 pattern recognition hardware to “expected” patterns for the given RoIs. Events with  
907 RoIs matching these expected patterns are then handed to the HLT through the  
908 Central Trigger Processor. This step lowers the data rate down to about 75 kHz.

909 **High-Level Trigger**

910 After passing the L1 trigger, events are passed to the HLT, which takes the incoming  
911 data rate from  $\sim$ 75 kHz down to the  $\sim$ 1 kHz that can be written to tape. The HLT  
912 performs much like a simplified offline reconstruction, using many common quality  
913 and analysis cuts to eliminate uninteresting events. This is done by using computing  
914 farms located close to the detector, which process events in parallel. Individually,  
915 each event which enters the computing farms takes about 4 seconds to reconstruct.  
916 However, some events take significantly longer to reconstruct, which necessitates  
917 careful monitoring of the HLT to ensure smooth operation.

918 HLT triggers are targeted to a particular physics process, such as a  $E_T^{\text{miss}}$  trigger,  
919 single muon trigger, or multijet trigger. The collection of all triggers is known as  
920 the trigger *menu*. Since many low-energy particles are produced in collisions, it is  
921 necessary to set a *trigger threshold* on the object of interest. Due to the changing  
922 luminosity conditions of the LHC, these thresholds change constantly. The most  
923 common strategy is to increase the trigger thresholds with increasing instantaneous  
924 luminosity. This allows an approximately constant number of events to be written  
925 for further analysis. Triggers which have rates higher than those designated by the  
926 menu are *prescaled*. A prescaled trigger only records every  $n$ th event which passes

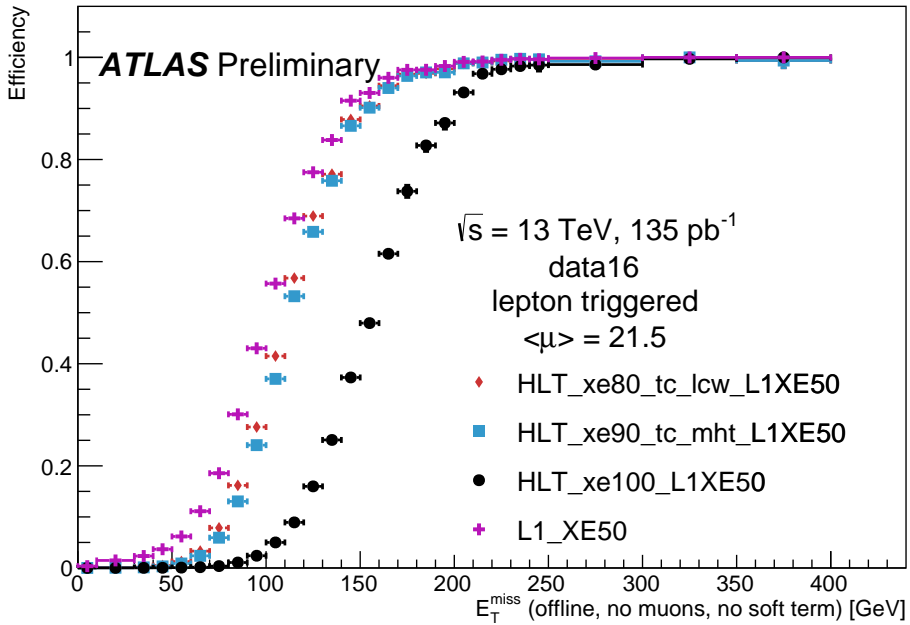


Figure 5.15: Turn-on curves for the  $E_T^{\text{miss}}$  triggers used in this thesis.

the trigger requirements, where  $n$  is the prescale value. Inne wishes to investigate all data events passing some set of analysis cuts, so often one uses the “lowest threshold unprescaled trigger”. *Turn-on curves* allow one to select the needed offline analysis cut to ensure the trigger is fully efficient. An example turn-on curve for the  $E_T^{\text{miss}}$  triggers used in the signal region of this analysis is shown in Fig. 5.15.

The full set of the lowest threshold unprescaled triggers considered here can be found in Tab. 5.1. These are the lowest unprescaled triggers associated to the SUSY signal models and Standard Model backgrounds considered in this thesis. More information can be found in [92].

Physics Object	Trigger	$p_T$ Threshold (GeV)	Level-1 Seed	Requirements	Rate (Hz)
<b>2015 Data</b>					
$E_T^{\text{miss}}$	HLT_xe70	70	L1_XE50	-	60
Muon	HLT_mu24_loose	24	L1_MU15	isolated, loose	130
Muon	HLT_mu50	50	L1_MU15	-	30
Electron	HLT_e24_lhmedium_iloose	24	L1_EM20VH	medium OR isolated, loose	140
Electron	HLT_e60_lhmedium	60	L1_EM20VH	medium	10
Electron	HLT_e120_lhloose	120	L1_EM20VH	loose	<10
Photon	HLT_g120_loose	120	L1_EM20VH	loose	20
<b>2016 Data</b>					
$E_T^{\text{miss}}$	HLT_xe100_mht_L1XE50	100	L1_XE50	-	180
Muon	HLT_mu24_ivarmedium	24	L1_MU20	medium	120
Muon	HLT_mu50	50	L1_MU20	-	40
Electron	HLT_e24_lhtight_nod0	24	L1_EM22VHI	tight with no $d_0$ OR loose	110
Electron	HLT_e60_lhmedium_nod0	60	L1_EM22VHI	medium with no $d_0$	10
Electron	HLT_e140_lhloose_nod0	140	L1_EM22VHI	loose with no $d_0$	<10
Photon	HLT_g140_loose	140	L1_EM22VHI	loose	20

Table 5.1: High-Level Triggers used in this thesis. Descriptions of loose, medium, tight, and isolated can be found in [92]. The  $d_0$  cut refers to a quality cut on the vertex position, which was removed from many triggers in 2016 to increase sensitivity to displaced vertex signals. For most triggers, the increased thresholds in 2016 compared to 2016 were designed to keep the rate approximately equal.



## *Object Reconstruction*

938 This chapter describes the reconstruction algorithms used within ATLAS. We will  
939 make the distinction between the “primitive” objects which are reconstructed from  
940 the detector signals from the “composite” physics objects we use in measurements  
941 and searches for new physics.

### 942 **6.1 Primitive Object Reconstruction**

943 The primitive objects reconstructed by ATLAS are *tracks* and (calorimeter) *clusters*.  
944 These are reconstructed directly from tracking hits and calorimeter energy deposits  
945 into cells. Tracks can be further divided into inner detector and muon spectrom-  
946 eter tracks. Calorimeter clusters can be divided into sliding-window clusters and  
947 topological clusters (topoclusters).

#### 948 **Inner Detector Tracks**

949 Inner detector tracks are reconstructed from hits in the inner detector [93, 94] These  
950 hits indicate that a charged particle has passed through the detector material. Due  
951 to the 2 T solenoid in the inner detector, the hits associated with any individual  
952 particle will be curved. The amount of curvature determines the momentum of the  
953 particle. In any given event, there are upwards of  $10^4$  hits, making it impossible to do  
954 any sort of combinatorics to reconstruct tracks. There are two algorithms used by  
955 ATLAS track reconstruction, known as *inside-out* and *outside-in*.

956       ATLAS first employs the inside-out algorithm. One assumes the track begins  
957 at the interaction point. Moving out from the interaction point, one creates track  
958 seeds. Track seeds are proto-tracks constructed from three hits. These hits can be  
959 distributed as three pixel hits, two pixel hits and one SCT hit, or three SCT hits.  
960 One extrapolates the track and uses a combinatorial Kalman filter [93], which adds  
961 the rest of the pixel and SCT hits to the seeds. This is done seed by seed, so it  
962 avoids the combinatorial complexity involved with checking all hits with all seeds.  
963 At this point, the algorithm applies an additional filter to avoid ambiguities from  
964 nearby tracks. The TRT hits are added to the seeds using the same method. After  
965 this procedure, all hits are associated to a track.

966       The next step is to determine the correct kinematics of the track. This is  
967 done by applying a fitting algorithm which outputs the best-fit track parameters  
968 by minimizing the track distance from hits, weighted by each hit's resolution. These  
969 parameters are  $(d_0, z_0, \eta, \phi, q/p)$  where  $d_0$  ( $z_0$ ) is the transverse (longitudinal) impact  
970 parameter and  $q/p$  is the charge over the track momenta. This set of parameters  
971 uniquely defines the measurement of the trajectory of the charged particle associated  
972 to the track. An illustration of a track with these parameters is shown in Fig. 6.1.

973       The other track reconstruction algorithm is the outside-in algorithm. As the  
974 name implies, we start from the outside of the inner detector, in the TRT, and  
975 extend the tracks in toward the interaction point. One begins by seeding from  
976 TRT hits, and extending the track back towards the center of the detector. The  
977 same fitting procedure is used as in the inside-out algorithm to find the optimal  
978 track parameters. This algorithm is particularly important for finding tracks which  
979 originate from interactions with the detector material, especially the SCT. For tracks  
980 from primary vertices, this often finds the same tracks as the inside-out algorithm,  
981 providing an important check on the consistency of the tracking procedure.

982       In the high luminosity environment of the LHC, even the tracks reconstructed

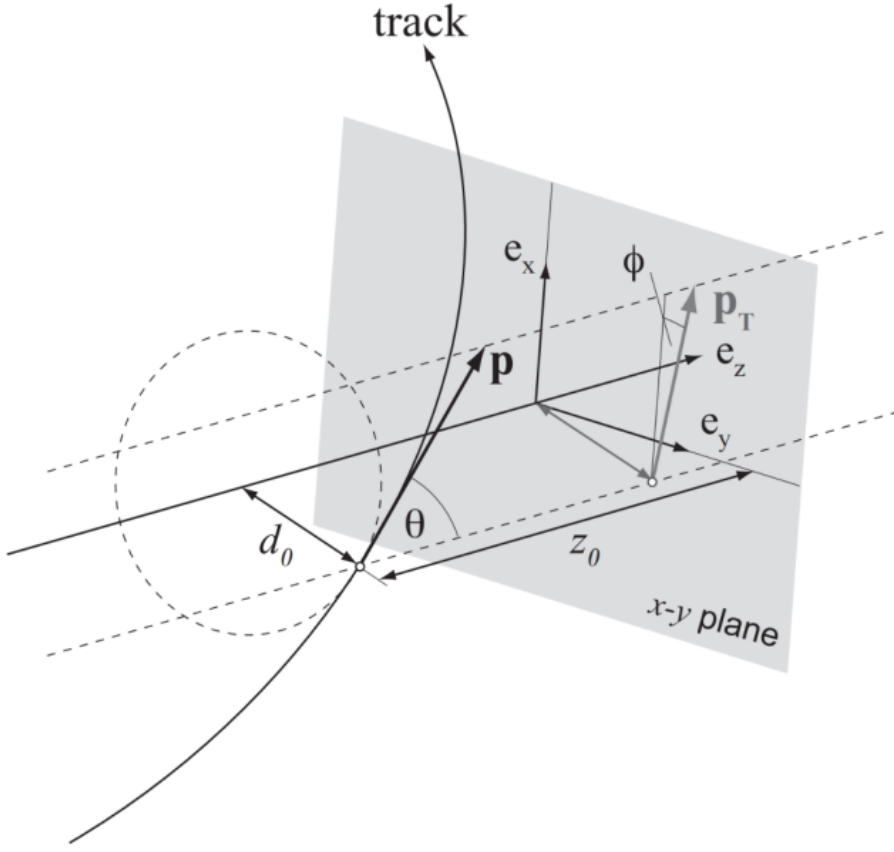
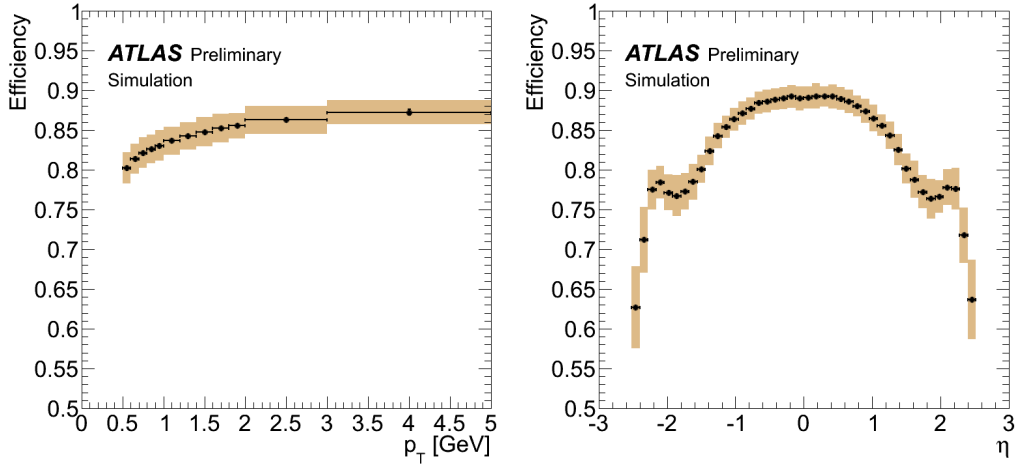


Figure 6.1: The parameters associated to a track.

from precision detectors such as those of ATLAS inner detector can sometimes lead to fake tracks from simple combinatoric chance. Several quality checks are imposed after track fitting which reduce this background. Seven silicon (pixel + SCT) hits are required for all tracks. No more than two *holes* are allowed in the pixel detector. Holes are expected measurements from the track that are missing in the pixel detector. Finally, tracks with poor fit quality, as measured by  $\chi^2/ndf$ , are also rejected. Due to the high quality of the silicon measurements in the pixel detector and SCT, these requirements give good track reconstruction efficiency, as seen in Fig. 6.2 for simulated events [95].



(a) Track reconstruction as a function of  $p_T$ . (b) Track reconstruction as a function of  $\eta$ .

Figure 6.2: Track reconstruction efficiency as a function of track  $p_T$  and  $\eta$ . The efficiency is defined as the number of reconstructed tracks divided by the number of generate charged particles.

## 992 Sliding-window clusters

993 The sliding-window algorithm is a way to combine calorimeter cells into composite  
 994 objects (clusters) to be used as inputs for other algorithms [96]. Sliding-window  
 995 clusters are the primary inputs to electron and photon reconstruction, as described  
 996 below. The electromagnetic calorimeter has high granularity, with a cell size of  
 997  $(\eta, \phi) = (.025, .025)$  in the coarsest second layer throughout most of the calorimeter.  
 998 The “window” consists of 3 by 5 cells in the  $(\eta, \phi)$  space. All layers are added on  
 999 this same 2D space. One translates this window over the space and seeds a cluster  
 1000 whenever the energy sum of the cells is maximized. If the seed energy is greater  
 1001 than 2.5 GeV, this seed is called a sliding-window cluster. This choice was motivated  
 1002 to optimize the reconstruction efficiency of proto-electrons and proto-photons while  
 1003 rejecting fakes from electronic noise and additional particles from pileup vertices.

1004 **Topological clusters**

1005 Topoclusters are the output of the algorithm used within ATLAS to combine  
1006 hadronic and electromagnetic calorimeter cells in a way which extracts signal from  
1007 a background of significant electronic noise [97]. They are the primary input to the  
1008 algorithms which reconstruct jets.

1009 Topological clusters are reconstructed from calorimeter cells in the following way.  
1010 First, one maps all cells onto a single  $\eta - \phi$  plane so one can speak of *neighboring*  
1011 cells. Two cells are considered neighboring if they are in the same layer and directly  
1012 adjacent, or if they are in adjacent layers and overlap in  $\eta - \phi$  space. The *significance*  
1013  $\xi_{\text{cell}}$  of a cell during a given event is

$$\xi_{\text{cell}} = \frac{E_{\text{cell}}}{\sigma_{\text{noise},\text{cell}}} \quad (6.1)$$

1014 where  $\sigma_{\text{noise},\text{cell}}$  is measured for each cell in ATLAS and  $E_{\text{cell}}$  measures the current  
1015 energy level of the cell. One thinks of this as the measurement of the energy *over*  
1016 *threshold* for the cell.

1017 Topocluster *seeds* are defined as calorimeter cells which have a significance  $\xi_{\text{cell}} >$   
1018 4. These are the inputs to the algorithm. One iteratively tests all cells adjacent  
1019 to these seeds for  $\xi_{\text{cell}} > 2$ . Each cells passing this selection is then added to the  
1020 topocluster, and the procedure is repeated. When the algorithm reaches the point  
1021 where there are no additional adjacent cells with  $\xi_{\text{cell}} > 2$ , every positive-energy cell  
1022 adjacent to the current proto-cluster is added. The collection of summed cells is a  
1023 topocluster. An example of this procedure for a simulation dijet event is shown in  
1024 Fig. 6.3.

1025 There are two calibrations used for clusters [98]. These are known as the  
1026 electromagnetic (EM) scale [99] and the local cluster weighting (LCW) scale [97].  
1027 The EM scale is the energy read directly out of the calorimeters as described. This  
1028 scale is appropriate for electromagnetic processes. The LCW scale applies additional

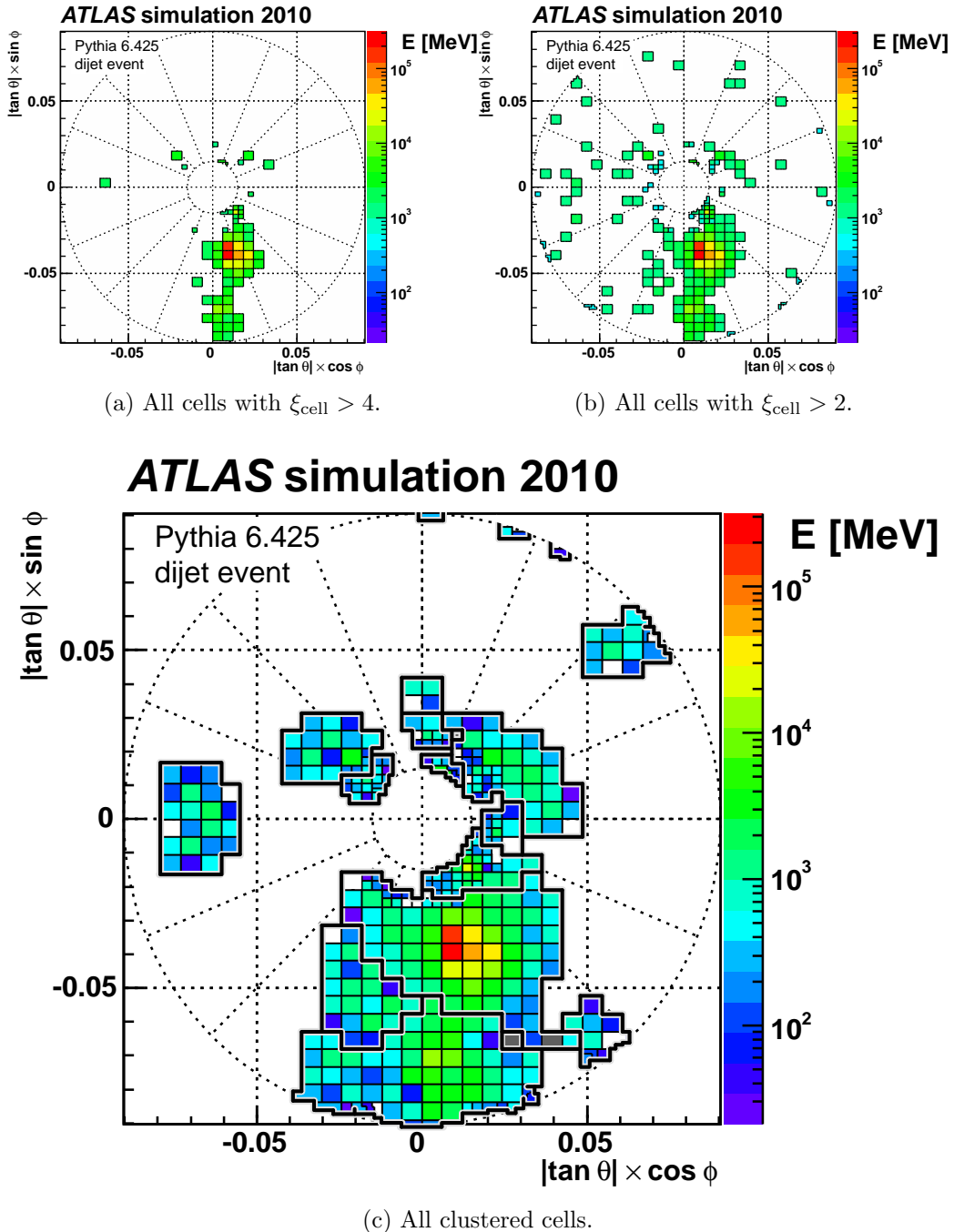


Figure 6.3: Example of topoclustering on a simulated dijet event.

1029 scaling to the clusters based on the shower development. The cluster energy can be  
1030 corrected for calorimeter noncompensation and the differences in the hadronic and  
1031 electromagnetic calorimeters' responses. This scale provides additional corrections  
1032 that improve the accuracy of hadronic energy measurements. This thesis only uses  
1033 the EM scale corrections. LCW scaling requires additional measurements that only  
1034 became available with additional data. Due to the jet calibration procedure that  
1035 we will describe below, it is also a relatively complicated procedure to rederive the  
1036 “correct” jet energy.

## 1037 Muon Spectrometer Tracks

1038 Muon spectrometer tracks are fit using the same algorithms as the ID tracks, but  
1039 different subdetectors. The tracks are seeded by hits in the MDTs or CSCs. After  
1040 seeding in the MDTs and CSCs, the hits from all subsystems are refit as the final  
1041 MS track. These tracks are used as inputs to the muon reconstruction, as we will see  
1042 below.

## 1043 6.2 Physics Object Reconstruction and Quality

### 1044 Identification

1045 There are essentially six objects used in ATLAS searches for new physics: electrons,  
1046 photons, muons,  $\tau$ -jets, jets, and  $E_T^{\text{miss}}$ . The reconstruction of these objects is  
1047 described here. In this thesis,  $\tau$  lepton jets are not treated differently from other  
1048 hadronic jets, and we will not consider their reconstruction algorithms. A very  
1049 convenient summary plot is shown in Fig. 6.4.

1050 One often wishes to understand “how certain” we are that a particular object  
1051 is truly the underlying physics object. In ATLAS, we often generically consider, in

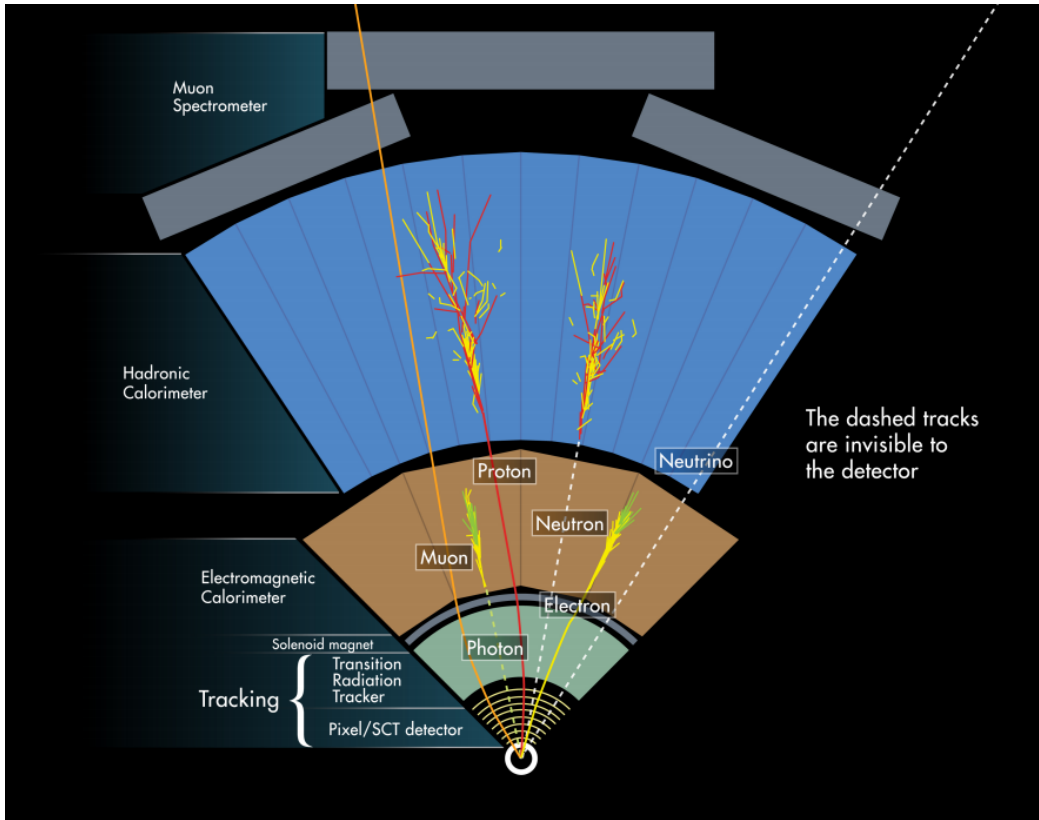


Figure 6.4: The interactions of particles with the ATLAS detector. Solid lines indicate the particle is interacting with the detector, while dashed lines are shown where the particle does not interact.

1052 order, *very loose*, *loose*, *medium*, and *tight* objects<sup>1</sup>. These are ordered in terms of  
 1053 decreasing object efficiency, or equivalently, decreasing numbers of fake objects. We  
 1054 will also describe briefly the classification of objects into these categories.

1055 In this thesis, since we present a search for new physics in a zero lepton final state,  
 1056 we will provide additional details about jet and  $E_T^{\text{miss}}$  reconstruction.

---

<sup>1</sup> These are not all used for all objects, but it's conceptually useful to think of these different categories.

## 1057 Electrons and Photons

### 1058 Reconstruction

1059 The reconstruction of electrons and photons (often for brevity called “electromagnetic  
1060 objects”) is very similar [96, 100, 101]. This is because the reconstruction begins  
1061 with the energy deposit in the calorimeter in the form of an electromagnetic shower.  
1062 For any incoming  $e/\gamma$ , many more electrons and photons are produced in the shower.  
1063 The measurement in the calorimeter is similar for these two objects.

1064 One begins the reconstruction of electromagnetic objects from the sliding-window  
1065 clusters reconstructed from the EM calorimeter. These  $E > 2.5$  GeV clusters the  
1066 the primary seed for electrons and photons. One then looks for all ID tracks within  
1067  $\Delta R < 0.3$ , where  $\Delta R = \sqrt{\Delta\eta^2 + \Delta\phi^2}$ . We “match” the track and cluster if they are  
1068 within  $\Delta\phi < 0.2$  in the direction of track curvature, or  $\Delta\phi < 0.05$  in the direction  
1069 opposite the track curvature. Those track-cluster seeds with tracks pointing to the  
1070 primary vertex are reconstructed as electrons.

1071 For photons, we have two options to consider, known as *converted* and *unconverted*  
1072 photons. Due to the high energy of the LHC collisions, typical photons have energy  
1073  $>\sim 1$  GeV. At this scale, photons interact almost exclusively via pair-production  
1074 in the presence of the detector material, as shown in Fig. 6.5 [56]. If the track-  
1075 cluster seed has a track which does not point at the primary vertex, we reconstruct  
1076 this object as a converted photon. This happens since the photon travels a distance  
1077 before decay into two electrons, and see the tracks coming from this secondary vertex.  
1078 Those clusters which do not have any associated tracks are then reconstruced as an  
1079 unconverted photon.

1080 The final step in electromagnetic object reconstruction is the final energy value.  
1081 This process is different between electrons and photons due to their differing  
1082 signatures in the EM calorimeter. In the barrel, electrons energies are assigned as

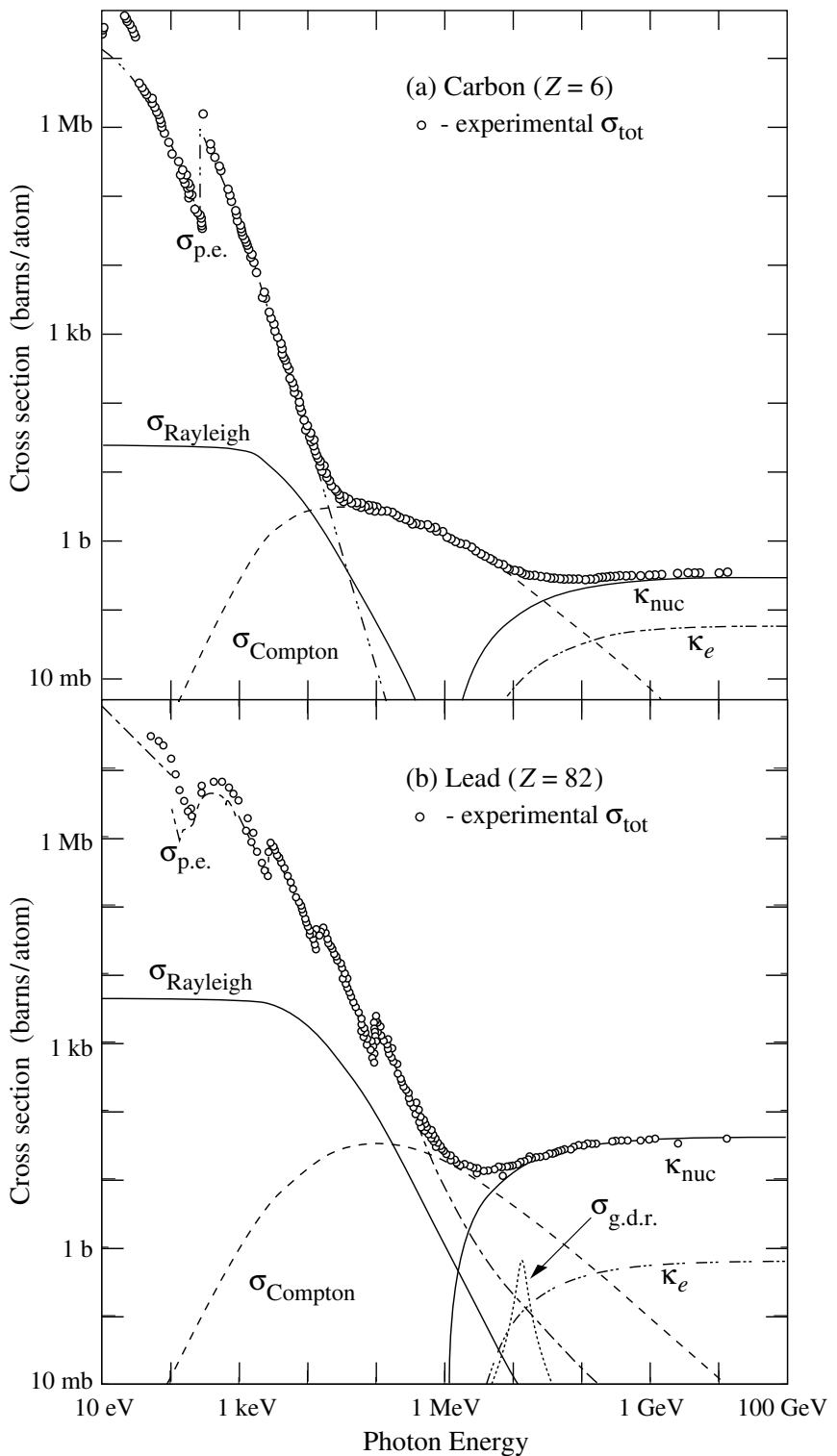


Figure 6.5: Photon total cross sections as a function of energy in carbon and lead, showing the contributions of different processes [56].

1083 the sum of the 3 clusters in  $\eta$  and 7 clusters in  $\phi$  to account for the electron curving  
1084 in the  $\phi$  direction. Barrel photons are assigned the energy sum of (3, 5) clusters in  
1085  $(\eta, \phi)$  space. In the endcap, the effect of the magnetic field on the electrons is smaller,  
1086 and there is a coarser granularity. Both objects sum the (5, 5) clusters for their final  
1087 energy value.

## 1088 Quality Identification

1089 Electrons have a number of important backgrounds which can give fakes. Fake  
1090 electrons come primarily from secondary vertices in hadron decays or misidentified  
1091 hadronic jets. To reduce these backgrounds, quality requirements are imposed on  
1092 electron candidates. Loose electrons have requirements imposed on the shower  
1093 shapes in the electromagnetic calorimeter and on the quality of the associated ID  
1094 track. There is also a requirement that there is a small energy deposition in the  
1095 hadronic calorimeter behind the electron, to avoid jets being misidentified as electrons  
1096 (low hadronic leakage). Medium and tight electrons have increasingly stronger  
1097 requirements on these variables, and additional requirements on the isolation (as  
1098 measured by  $\Delta R$ ) and matching of the ID track momentum and the calorimeter  
1099 energy deposit.

1100 Photons are relatively straightforward to measure, since there are few background  
1101 processes [102]. The primary is pion decays to two photons, which can cause a jet  
1102 to be misidentified as photon. Loose photons have requirements on the shower shape  
1103 and hadronic leakage. Tight photons have tighter shower shape cuts, especially on  
1104 the high granularity first layer of the EM calorimeter. The efficiency for unconverted  
1105 tight photons as a function of  $p_T$  is shown in

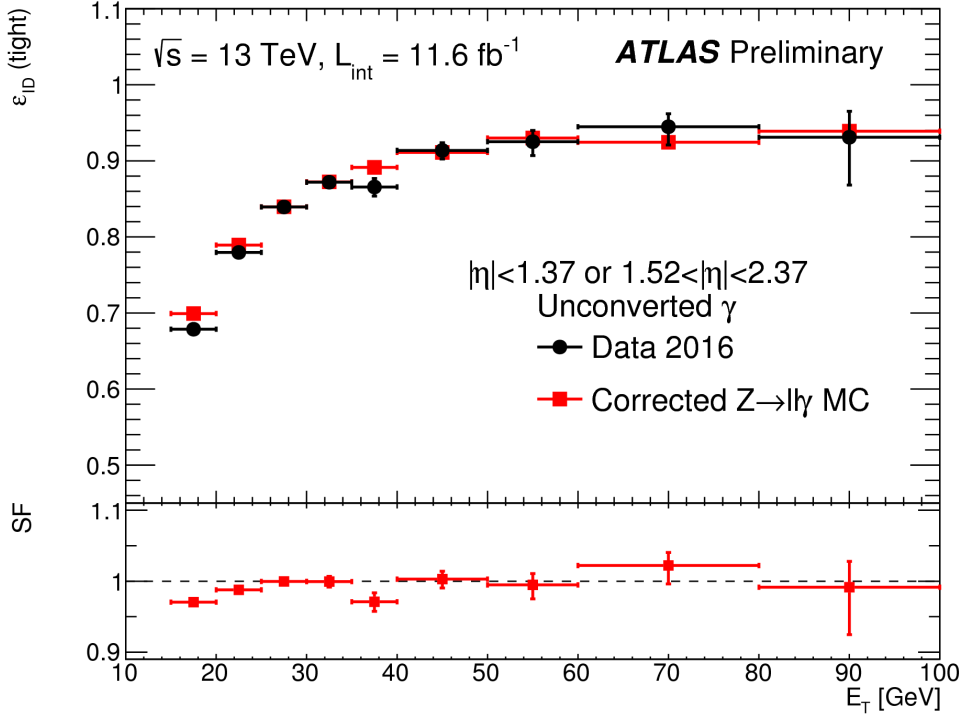


Figure 6.6: Unconverted photon efficiency as measured in [102].

## 1106 Muons

### 1107 Reconstruction

1108 Muons are reconstructed using measurements from all levels of the ATLAS detec-  
 1109 tor [103]. They leave a ID track, a small, characteristic deposition in the EM calorime-  
 1110 ter, and then a track in the muon spectrometer. The primary reconstruction technique  
 1111 produces a so-called *combined* muon. “Combined” means using a combination of the  
 1112 ID and MS tracks to produce the final reconstructed muon kinematics. This is done  
 1113 by refitting the hits associated to both tracks, and using this refit track for the muon  
 1114 kinematics.

### 1115 Quality Identification

Several additional criteria are used to assure muon measurements are free of significant background contributions, especially from pion and kaon decays to muons.

Muons produced via these decay processes are often characterized by a “kink”. Candidate muons with a poor fit quality, characterized by  $\chi^2/\text{n.d.f.}$ , are thus rejected. Additionally, the absolute difference in momentum measurements between the ID and MS provide another handle, since the other decay products from hadron decays carry away some amount of the initial hadron momentum. This is measured by

$$\rho' = \frac{|p_T^{\text{ID}} - p_T^{\text{MS}}|}{p_T^{\text{Combined}}}. \quad (6.2)$$

Additionally, there is a requirement on the  $q/p$  significance, defined as

$$S_{q/p} = \frac{|(q/p)^{\text{ID}} - (q/p)^{\text{MS}}|}{\sqrt{\sigma_{\text{ID}}^2 + \sigma_{\text{MS}}^2}}. \quad (6.3)$$

1116 The  $\sigma_{\text{ID,MS}}$  in the denominator of Eq. Eq. (6.3) are the uncertainties on the corre-  
 1117 sponding quantity from the numerator. Finally, cuts are placed on the number of  
 1118 hits in the various detector elements.

1119 Subsequently tighter cuts on these variables allow one to define the different muon  
 1120 identification criteria. Loose muons have the highest reconstruction efficiency, but  
 1121 the highest number of fake muons, since there are no requirements on the number  
 1122 of subdetector hits and the loosest requirements on the suite of quality variables.  
 1123 Medium muons consist of Loose muons with tighter cuts on the quality variables.  
 1124 They also require more than three MDT hits in at least two MDT layers. These are  
 1125 the default used by ATLAS analyses. Tight muons have stronger cuts than those of  
 1126 the medium selection, and reducing the reconstruction efficiency. The reconstruction  
 1127 efficiency as a function of  $p_T$  can be seen for Medium muons in Fig. 6.7.

## 1128 Jets

1129 Jets are composite objects corresponding to many physical particles [56, 104, 105]  
 1130 This is a striking difference from the earlier particles. Fortunately, we normally (and  
 1131 in this thesis) only need information about the original particle produced in the

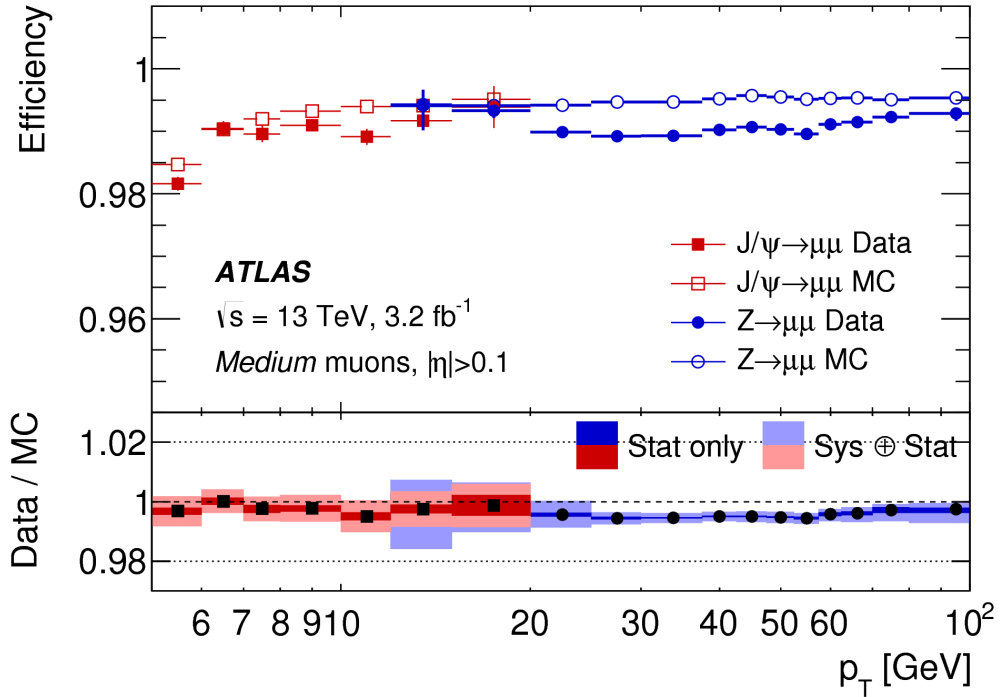


Figure 6.7: Medium muon efficiency as measured in [103].

primary collision. In the SM, this corresponds to quarks and gluons. Due to the hadronization process, free quarks and gluons spontaneously hadronize and produce a hadronic shower, which we call a jet. These showers can be measured by the EM and hadronic calorimeters, and the charged portions can be measured in the ID. The first step is to combine these measurements into a composite object representing the underlying physical parton. This is done via jet algorithms.

## Jet Algorithms

It might seem straightforward to combine the underlying physical particles into a jet. There are three important characteristics required for any jet reconstruction algorithm to be used by ATLAS.

- Collinear safety - if any particle with four-vector  $p$  is replaced by two particles of  $p_1, p_2$  with  $p = p_1 + p_2$ , the subsequent jet should not change

1144 • Radiative (infrared) safety - if any particle with four-vector  $p$  radiates a particle  
1145 of energy  $\alpha \rightarrow 0$ , the subsequent jet should not change

1146 • Fast - the jet algorithm should be “fast enough” to be useable by ATLAS  
1147 computing resources

1148 The first two requirements can be seen in terms of requirements on soft gluon emission.

1149 Since partons emit arbitrarily soft gluons freely, one should expect the algorithms

1150 to not be affected by this emission. The final requirement is of course a practical

1151 limitation.

The algorithms in use by ATLAS (and CMS) which satisfies these requirements are collectively known as the  $k_T$  algorithms [106–108]. These algorithms iteratively combine the “closest” objects, defined using the following distance measures :

$$d_{ij} = \min(k_{T,i}^{2p}, k_{T,j}^{2p}) \frac{\Delta_{ij}^2}{R^2} \quad (6.4)$$
$$d_{iB} = k_{Ti}^{2p}$$

1152 In Eq.Eq. (6.4),  $k_{T,i}$  is the transverse momentum of  $i$ -th jet *constituent* and  $\Delta_{ij}$  is  
1153 the angular distance  $\Delta R$  between the constituents. Both  $R$  and  $p$  are adjustable  
1154 parameters:  $R$  is known as the (jet) *cone size* and  $p$  regulates the power of the energy  
1155 versus the geometrical scales. The algorithm sequence, for a given set of objects  $i$   
1156 with four-vector  $k$  :

1157 1. Find the minimum distance in the set of all  $d_{ij}$  and  $d_{iB}$ .

1158 2. If the distance is one of the  $d_{ij}$ , combine the input pair of object  $i, j$  and return  
1159 to (1). If the distance is one of the  $d_{iB}$ , remove the object from the list, call it  
1160 a jet, and return to (1).

1161 This process ends when all objects  $i$  have been added to a jet.

1162 Any choice of  $(p, R)$  has requirements of collinear and radiative safety. In essence,  
1163 the choice is then to optimize based on speed and the potential for new physics

1164 discoveries. In ATLAS, we make the choice of  $p = -1$  which is also known as the  
1165 *anti- $k_T$*  algorithm. The choice of  $R = 0.4$  is used for the distance parameter of the  
1166 jets.

1167 The primary “nice” quality of this algorithm can be seen with the following  
1168 example. Consider three inputs to an anti- $k_T$  algorithm, all with  $\eta = 0$  :

1169 • Object 1 :  $(p_T, \phi) = (30 \text{ GeV}, 0)$

1170 • Object 2 :  $(p_T, \phi) = (20 \text{ GeV}, -0.2)$

1171 • Object 3 :  $(p_T, \phi) = (10 \text{ GeV}, 0.2)$

1172 • Object 4 :  $(p_T, \phi) = (1 \text{ GeV}, 0.5)$

1173 In the case shown, it seems natural to first combine the “bigger” objects 1 and 2.  
1174 These then pick up the extra small object 3, and object 4 is not included in the jet.  
1175 This is what is done by the anti- $k_T$  algorithm. The (normal)  $k_T$  algorithm with  $p = 1$   
1176 instead combines the smallest objects, 3 and 4, first. Object 1 and 2 combine to form  
1177 their own jet, instead of these jets picking up object 3. This behavior is not ideal due  
1178 to effects from pileup, as we will see in the next section.

## 1179 Jet Reconstruction

1180 In ATLAS, jets are reconstructed using multiple different objects as inputs, including  
1181 tracks, “truth” objects, calorimeter clusters, and *particle flow objects* (PFOs).  
1182 For physics analyses, ATLAS primarily uses jets reconstructed from calorimeter  
1183 clusters, but we will describe the others here, as they are often used for systematic  
1184 uncertainties.

1185 Calorimeter jets are reconstructed using topoclusters with the anti- $k_T$  algorithm  
1186 with  $R = 0.4$ . The jet reconstruction algorithm is run on the collection of all  
1187 topoclusters reconstructed as in Sec. 6.1. Both EM and LCW scale clusters are

1188 used in the ATLAS reconstruction software and produce two sets of jets for analysis.  
1189 As stated above, this thesis presents an analysis using jets reconstructed using EM  
1190 scale clusters, which we refer to as *EM jets*.

1191 Tracks can be used as inputs to jet reconstruction algorithms. Jets reconstructed  
1192 from tracks are known as *track jets*. Since the ID tracks do not measure neutral  
1193 objects, these jets underestimate the true jet energy. However, these are still useful  
1194 for checks and derivations of systematic uncertainties.

1195 *Truth* jets are reconstructed from *truth* particles. In this case, truth is jargon  
1196 for simulation. In simulation, the actual simulated particles are available and used  
1197 as inputs to the jet reconstruction algorithms. Similarly to track jets, these are not  
1198 useful in and of themselves, but are used in conjunction with studies of reconstructed  
1199 jets.

1200 The last object used as inputs to jet reconstruction algorithms are *particle flow*  
1201 *objects* (PFOs). These are used extensively as the primary input to jet particle  
1202 reconstruction algorithms by the CMS collaboration [109]. Particle flow objects are  
1203 reconstructed by associating tracks and clusters through a combination of angular  
1204 distance measures and detector response measurements to create a composite object  
1205 which contains information from both the ID and the calorimeters. For calorimeter  
1206 clusters which do not have any associated ID track, the cluster is simply the PFO.  
1207 The natural association between tracks and clusters provides easy pileup subtraction  
1208 since tracks are easily associated to the primary vertex. As pileup has increased, the  
1209 utility of using PFOs as inputs to jet reconstruction has increased as well.

## 1210 **Jet Calibration**

1211 Jets as described in the last section are still *uncalibrated*. Even correcting the cluster  
1212 energies using the LCW does not fully correct the jet energy, due to particles losing  
1213 energy in the calorimeters. This is corrected using the *jet energy scale* (JES). The

1214 JES is a series of calibrations which on average restore the correct truth jet energy  
1215 for a given reconstructed jet. The steps to derive the JES are described in Fig. 6.8  
1216 and described here.

1217 The first step is the origin correction. This adjusts the jet to point at the  
1218 primary vertex. Next, is the jet-area based pileup correction. This step subtracts  
1219 the “average” pileup as measured by the energy density  $\rho$  outside of the jets and  
1220 assumes this is a good approximation for the pileup inside the jet. One removes  
1221 energy  $\Delta E = \rho \times A_{\text{jet}}$  in this step. The residual pileup correction applies a final offset  
1222 correction by parametrizing the change in jet energy as a function of the number of  
1223 primary vertices  $N_{\text{PV}}$  and the average number of interactions  $\mu$ . More details can be  
1224 found in [105].

1225 The next step is the most important single correction, known as the AbsoluteE-  
1226 taJES. Due to the use of noncompensation and sampling calorimeters in ATLAS,  
1227 the measured energy of a jet is a fraction of the true energy of the outgoing parton.  
1228 Additionally, due to the use of different technologies and calorimeters throughout the  
1229 detector, there are directional biases induced by these effects. The correction bins a  
1230 multiplicative factor in  $p_{\text{T}}$  and  $\eta$  which scales the reconstructed jets to corresponding  
1231 truth jet  $p_{\text{T}}$ . This step does not entirely correct the jets, since it is entirely a  
1232 simulation-based approach.

1233 The final steps are known as the global sequential calibration (GSC) and the  
1234 residual in-situ calibration. The GSC uses information about the jet showering shape  
1235 to apply additional corrections based on the expected shape of gluon or quark jets.  
1236 The final step is the residual in-situ calibration, which is only applied to data. This  
1237 step uses well-measured objects recoiling off a jet to provide a final correction to the  
1238 jets in data. In the low  $p_{\text{T}}$  region ( $20 \text{ GeV} \lesssim p_{T,\text{jet}} \lesssim 200 \text{ GeV}$ ),  $Z \rightarrow ll$  events are  
1239 used as a reference object. In the  $p_{\text{T}}$  region ( $100 \text{ GeV} \lesssim p_{T,\text{jet}} \lesssim 600 \text{ GeV}$ ), the reference  
1240 object is a photon, while in the high  $p_{\text{T}}$  region ( $p_{T,\text{jet}} \gtrsim 200 \text{ GeV}$ ), the high  $p_{\text{T}}$  jet is

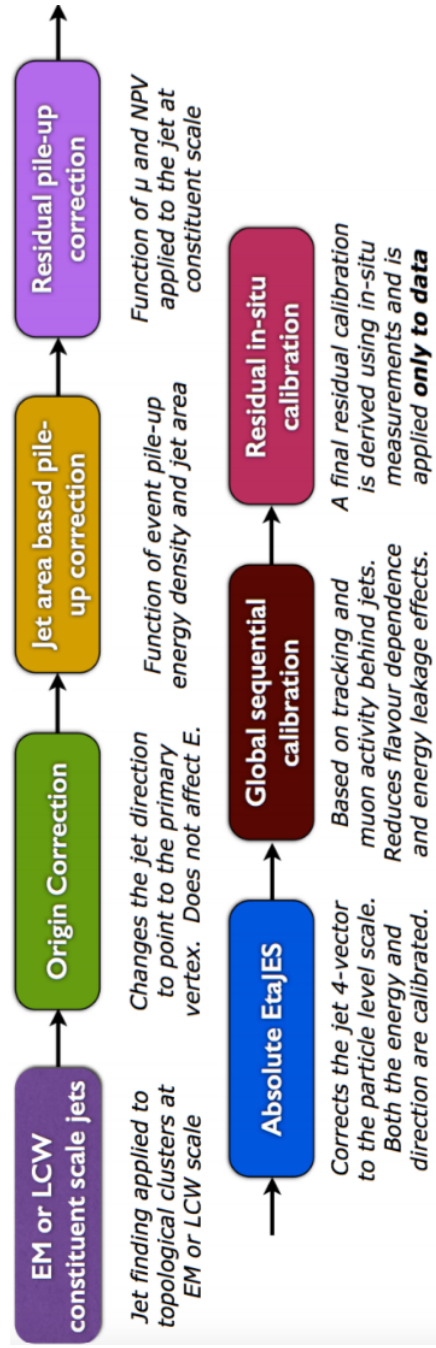


Figure 6.8: The steps used by ATLAS to calibrate jets

1241 compared to multiple smaller  $p_T$  jets. The reference object is the group of multijets.  
 1242 After the application of the residual in-situ calibration, the data and MC scales are  
 1243 identical up to corresponding uncertainties. The combined JES uncertainty as a  
 1244 function of  $p_T$  is shown in Fig. 6.9.

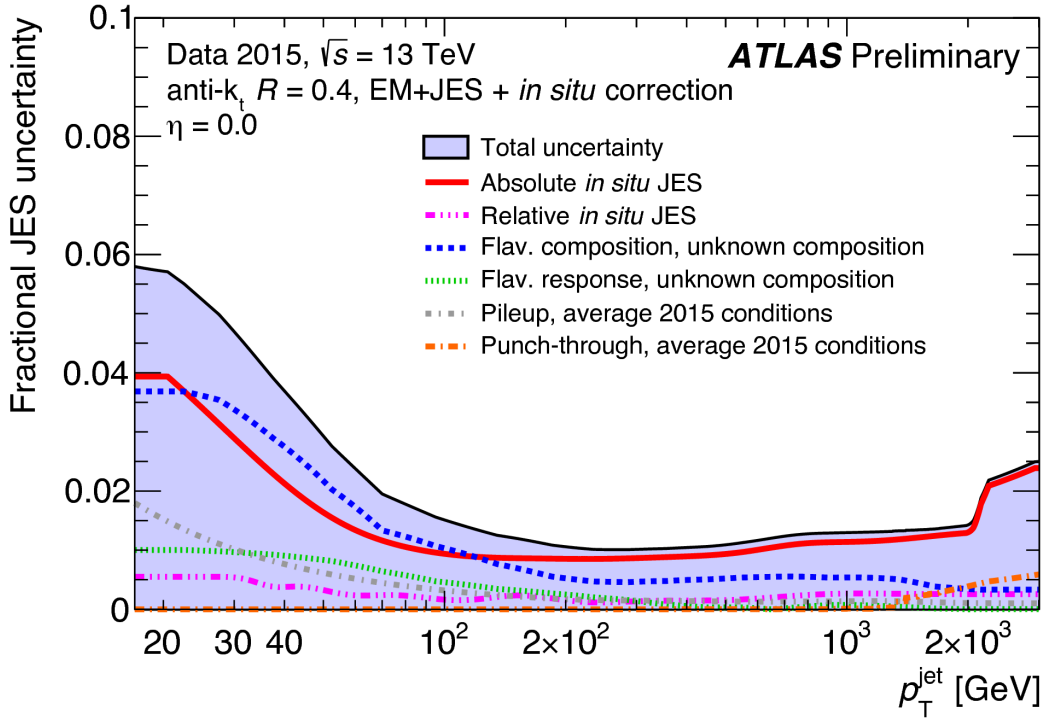


Figure 6.9: Combined jet energy scale uncertainty as a function of  $p_T$  at  $\eta = 0$ .

## 1245 Jet Vertex Tagger

1246 The *jet vertex tagger* (JVT) technique is used to separate pileup jets from those  
 1247 associated to the hard primary vertex [110]. The technique for doing so first involves  
 1248 *ghost association* [111]. Ghost association runs the anti- $k_T$  jet clustering algorithm  
 1249 on a combined collection of the topoclusters and tracks. The tracks *only* momenta  
 1250 are set to zero<sup>2</sup>, with only the directional information included. As discussed above,  
 1251 the anti- $k_T$  algorithm is “big to small”; tracks are associated to the “biggest” jet  
 1252 near them in  $(\eta, \phi)$ . This method uniquely associates each track to a jet, without  
 1253 changing the final jet kinematics.

1254 The JVT technique uses a combination of track variables to determine the  
 1255 likelihood that the jet originated at the primary vertex. For jets which have associated  
 1256 tracks from ghost association, this value ranges from 0 (likely pileup jet) to 1 (likely

---

<sup>2</sup>Not exactly zero, since zero momentum tracks wouldn’t have a well-defined  $(\eta, \phi)$  coordinate, but set to a value obeying  $p_{T,track} << 400$  MeV =  $p_{track,min}$ . This is the minimum momentum for a track to reach the ATLAS inner detector.

1257 hard scatter jet). Jets without associated tracks are assigned  $\text{JVT} = -.1$ . The  
1258 working point of  $\text{JVT} > .59$  is used for jets in this thesis.

## 1259 **B-jets**

1260 Jets originating from bottom quarks (b-jets) can be *tagged* by the ATLAS detec-  
1261 tor [112, 113]. B-hadrons, which have a comparatively long lifetime compared  
1262 to hadrons consisting of lighter quarks, can travel a macroscopic distance inside  
1263 the ATLAS detector. The high-precision tracking detectors identify the secondary  
1264 vertices from these decays and the jet matched to that vertex is called a *b-jet*. The  
1265 MV2c10 algorithm [112, 113], based on boosted decision trees, identifies these jets  
1266 using a combination of variables sensitive to the difference between light-quark and  
1267 b-quark jets. The efficiency of this tagger is 77%, with a rejection factor of 134 for  
1268 light-quarks and 6 for charm jets.

## 1269 **Missing Transverse Momentum**

1270 Missing transverse momentum  $E_{\text{T}}^{\text{miss}}$  [114] is a key observable in searches for new  
1271 physics, especially in SUSY searches [115, 116]. However,  $E_{\text{T}}^{\text{miss}}$  is not a uniquely  
1272 defined object when considered from the detector perspective (as compared to the  
1273 Feynammn diagram), and it is useful to understand the choices that affect the  
1274 performance of this observable in searches for new physics.

### 1275 **$E_{\text{T}}^{\text{miss}}$ Definitions**

*Hard* objects refers to all physical objects as defined in the previous sections. The  
 $E_{\text{T}}^{\text{miss}}$  reconstruction procedure uses these hard objects and the *soft term* to provide  
a value and direction of the missing transverse momentum. The  $E_{x(y)}^{\text{miss}}$  components

are calculated as:

$$E_{x(y)}^{\text{miss}} = E_{x(y)}^{\text{miss, } e} + E_{x(y)}^{\text{miss, } \gamma} + E_{x(y)}^{\text{miss, jets}} + E_{x(y)}^{\text{miss, } \mu} + E_{x(y)}^{\text{miss, soft}}, \quad (6.5)$$

1276 where each value  $E_{x(y)}^{\text{miss, } i}$  is the negative vectorial sum of the calibrated objects defined  
1277 in the previous sections.

1278 For purposes of  $E_T^{\text{miss}}$  reconstruction, we must assign an *overlap removal* ordering.  
1279 This is to avoid double counting of the underlying primitive objects (clusters and  
1280 tracks) which are inputs to the reconstruction of the physics objects. We resolve this  
1281 in the following order : electrons, photons , jets and muons. This is motivated by the  
1282 performance of the reconstruction of these objects in the calorimeters.

1283 The soft term  $E_{x(y)}^{\text{miss, soft}}$  contains all of the primitive objects which are not  
1284 associated to any of the reconstructed physics objects. we need to choose which  
1285 primitive object to use. The primary choices which have been used within ATLAS  
1286 are the *calorimeter-based soft term* (CST) and the *track-based soft term* (TST) [114].  
1287 Based on the soft term choice, we then call  $E_T^{\text{miss}}$  built with a CST (TST) soft term  
1288 simply CST (TST)  $E_T^{\text{miss}}$ . An additional option, which will be important as pileup  
1289 continues to increase, is particle flow  $E_T^{\text{miss}}$  (PFlow  $E_T^{\text{miss}}$ ).

1290 The CST  $E_T^{\text{miss}}$  was used for much of the early ATLAS data-taking. CST  $E_T^{\text{miss}}$   
1291 is built from the calibrated hard objects, combined with the calorimeter clusters  
1292 which are *not* assigned to any of those hard objects. In the absence of pileup, it  
1293 provides the best answer for the “true”  $E_T^{\text{miss}}$  in a given event, due to the impressive  
1294 hermiticity of the calorimeters. Unfortunately, the calorimeters do not know from  
1295 where their energy deposition came, and thus CST is susceptible to drastically reduced  
1296 performance with increasing pileup.

1297 TST  $E_T^{\text{miss}}$  is the standard for ATLAS searches as currently performed by ATLAS.  
1298 TST  $E_T^{\text{miss}}$  is reconstructed using the calibrated hard objects and a soft term from  
1299 the tracks which are not assigned to any of those hard objects. In particular, due  
1300 to the track-vertex association efficiency, one chooses tracks which only come from

1301 the primary vertex. This reduces the pileup contributions to the  $E_T^{\text{miss}}$  measurement.  
1302 However, since the ID tracking system is unable to detect neutral objects, the TST  
1303  $E_T^{\text{miss}}$  is “wrong”. In most searches for new physics, the soft  $E_T^{\text{miss}}$  is generally a small  
1304 fraction of the total  $E_T^{\text{miss}}$ , and thus this bias is not particularly hurtful.

1305 PFlow  $E_T^{\text{miss}}$  uses the PFOs described above to build the  $E_T^{\text{miss}}$ . The PFOs which  
1306 are assigned to hard objects are calibrated, and the PFOs which are not assigned  
1307 to any hard object are added to the soft term. In this context, it is convenient to  
1308 distinguish between “charged” and “neutral” PFOs. Charged PFOs can be seen as  
1309 a topocluster which has an associated track, while neutral PFOs do not. A charged  
1310 PFO is essentially a topocluster which is matched with the primary vertex. The  
1311 neutral PFOs have the same status as the original topoclusters. Thus a “full” PFlow  
1312  $E_T^{\text{miss}}$  should have performance somewhere between TST  $E_T^{\text{miss}}$  and CST  $E_T^{\text{miss}}$ <sup>3</sup>. A  
1313 *charged* PFlow  $E_T^{\text{miss}}$  should be the same as TST.

1314 **Measuring  $E_T^{\text{miss}}$  Performance : event selection**

1315 The question is now straightforward: how do we compare these different algorithms?  
1316 We compare these algorithms in  $Z \rightarrow \ell\ell + \text{jets}$  and  $W \rightarrow \ell\nu + \text{jets}$  events. Due to  
1317 the presence of leptons, these events are well-measured “standard candles”. Here  
1318 we present the results in early 2015 data with  $Z \rightarrow \mu\mu$  and  $W \rightarrow e\nu$  events, as  
1319 shown in [117, 118]. This result was important to assure the integrity of the  $E_T^{\text{miss}}$   
1320 measurements at the higher energy and pileup environment of Run-2.

1321 The  $Z \rightarrow \ell\ell$  selection is used to measure the intrinsic  $E_T^{\text{miss}}$  resolution of the  
1322 detector. Neutrinos only occur in these events from heavy-flavor decays inside of jets,  
1323 and thus  $Z \rightarrow \ell\ell$  events have very low  $E_T^{\text{miss}}$ . This provides an ideal event topology  
1324 to understand the modelling of  $E_T^{\text{miss}}$  mismeasurement. Candidate  $Z \rightarrow \mu\mu$  events  
1325 are first required to pass a muon or electron trigger, as described in Tab. 5.1. Offline,

---

<sup>3</sup>Naively, due to approximate isospin symmetry, about 2/3 of the hadrons will be charged and 1/3 will be neutral.

1326 the selection of  $Z \rightarrow \mu\mu$  events requires exactly two medium muons. The muons are  
 1327 required to have opposite charge and  $p_T > 25$  GeV, and mass of the dimuon system  
 1328 is required to be consistent with the  $Z$  mass  $|m_l - m_Z| < 25$  GeV.

$W \rightarrow \ell\nu$  events are an important topology to evaluate the  $E_T^{\text{miss}}$  modelling in events with real  $E_T^{\text{miss}}$ . This  $E_T^{\text{miss}}$  is from the neutrino, which is not detected. The  $E_T^{\text{miss}}$  in these events has a characteristic distribution with a peak at  $\frac{1}{2}m_W$ . The selection of  $W \rightarrow e\nu$  events begins with the selection of exactly one electron of medium quality. A selection on TST  $E_T^{\text{miss}} > 25$  GeV drastically reduces the background from multijet events where the jet fakes an electron. The transverse mass is used to select the  $W \rightarrow e\nu$  events :

$$m_T = \sqrt{2p_T^\ell E_T^{\text{miss}}(1 - \cos \Delta\phi)}, \quad (6.6)$$

1329 where  $\Delta\phi$  is the difference in the  $\phi$  between the  $E_T^{\text{miss}}$  and the electron.  $m_T$  is required  
 1330 to be greater than 50 GeV.

1331 There are two main ingredients to investigate : the  $E_T^{\text{miss}}$  resolution and the  $E_T^{\text{miss}}$   
 1332 scale.

### 1333 Measuring $E_T^{\text{miss}}$ Performance in early 2015 data : metrics

1334 To compare these algorithms we use the  $E_T^{\text{miss}}$  resolution,  $E_T^{\text{miss}}$  scale, and linearity.  
 1335 Representative distributions of TST  $E_x^{\text{miss}}$ ,  $E_y^{\text{miss}}$ , and  $E_T^{\text{miss}}$  from early 2015 datataking are shown in Fig. 6.10.

The  $E_T^{\text{miss}}$  resolution is an important variable due to the fact that the bulk of the distributions associated to  $E_{x(y)}^{\text{miss}}$  are Gaussian distributed [Aad2012]. However, to properly measure the tails of this distribution, especially when considering non-calorimeter based soft terms, it is important to use the root-mean square as the proper measure of the resolution. This is strictly larger than resolution as measured using a fit to a Gaussian, due to the long tails from i.e. track mismeasurements. The resolution is measured with respect to two separate variables :  $\sum E_T$  and  $N_{\text{PV}}$ .  $\sum E_T$

is an important measure of the “total event activity”. It is defined as

$$\sum E_T = \sum p_T^e + \sum p_T^\gamma + \sum p_T^\tau + \sum p_T^{\text{jets}} + \sum p_T^\mu + \sum p_T^{\text{soft}}. \quad (6.7)$$

1337 The measurement as a function of  $N_{\text{PV}}$  is useful to understand the degradation of  
 1338  $E_T^{\text{miss}}$  performance with increasing pileup. Fig. 6.11 shows the TST  $E_T^{\text{miss}}$  resolution  
 1339 in the early 2015 data compared with simulation. The degradation of the TST  $E_T^{\text{miss}}$   
 1340 performance is shown as a function of pileup  $N_{\text{PV}}$  and total event activity  $\sum E_T$ . We  
 1341 see that the degradation is significant as a function of these variables, but simulation  
 1342 describes the data well.

Another important performance metric is the  $E_T^{\text{miss}}$  scale. This indicates how well we measure the magnitude of the  $E_T^{\text{miss}}$ , as CST  $E_T^{\text{miss}}$  contains additional particles from pileup, while soft neutral particles<sup>4</sup> are ignored by TST  $E_T^{\text{miss}}$ . To determine this in data, we again use  $Z \rightarrow \mu\mu$  events, where the  $Z \rightarrow \mu\mu$  system is treated as a well-measured reference object. The component of  $E_T^{\text{miss}}$  which is in the same direction as the reconstructed  $Z \rightarrow \mu\mu$  system is sensitive to potential biases in the detector response. The unit vector  $\mathbf{A}_Z$  of the  $Z$  system is defined as

$$\mathbf{A}_Z = \frac{\vec{p}_T^{\ell^+} + \vec{p}_T^{\ell^-}}{|\vec{p}_T^{\ell^+} + \vec{p}_T^{\ell^-}|}, \quad (6.8)$$

1343 where  $\vec{p}_T^{\ell^+}$  and  $\vec{p}_T^{\ell^-}$  are the transverse momenta of the leptons from the  $Z$  boson  
 1344 decay. The relevant scale metric is the mean value of the  $\vec{E}_T^{\text{miss}}$  projected onto  $\mathbf{A}_Z$  :  
 1345  $\langle \vec{E}_T^{\text{miss}} \cdot \mathbf{A}_Z \rangle$ . In Fig. 6.12, the scale is shown for the early 2015 dataset. The negative  
 1346 bias, which is maximized at about 5 GeV, is a reflection of two separate effects. The  
 1347 soft neutral particles are missed by the tracking system, and thus ignored in TST  
 1348  $E_T^{\text{miss}}$ . Missed particles due to the limited ID acceptance can also affect the scale.

For events with real  $E_T^{\text{miss}}$ , one can also look at the *linearity* in simulation. This

---

<sup>4</sup>“Soft” here means those particles which are not hard enough to be reconstructed as their own particle, using the reconstruction algorithms above.

is defined as

$$\text{linearity} = \langle \frac{E_T^{\text{miss}} - E_T^{\text{miss,Truth}}}{E_T^{\text{miss,Truth}}} \rangle. \quad (6.9)$$

1349  $E_T^{\text{miss,Truth}}$  refers to “truth” particles as defined before, or the magnitude of the vector  
1350 sum of all noninteracting particles. The linearity is expected to be zero if the  $E_T^{\text{miss}}$   
1351 is reconstructed at the correct scale.

## 1352 Particle Flow Performance

1353 As described above, the resolution, scale, and linearity are metrics to understand the  
1354 performance of the different  $E_T^{\text{miss}}$  algorithms. In this section, we present comparisons  
1355 of the different algorithms, including particle flow, in simulation and using a data  
1356 sample from 2015 of  $80 \text{ pb}^{-1}$ . In these plots, “MET\_PFlow-TST” refers to charged  
1357 PFlow  $E_T^{\text{miss}}$ , while the other algorithms are as described above.

1358 Figs. 6.14 and 6.15 show the resolution and scale in simulated  $Z \rightarrow \mu\mu$  events.  
1359 The resolution curves follow the expected behavior discussed before. Due to the high  
1360 pileup in 2015 run conditions, the CST  $E_T^{\text{miss}}$  resolution is poor, and further degrades  
1361 with increasing pileup and event activity. The “regular” PFlow  $E_T^{\text{miss}}$  shows reduces  
1362 pileup and event activity dependence as compared to the CST. PFlow  $E_T^{\text{miss}}$  can be  
1363 seen as a hybrid of TST  $E_T^{\text{miss}}$  and CST  $E_T^{\text{miss}}$ . The charged PFOs ( $\sim 2/3$ ) are pileup  
1364 suppressed, while the neutral PFOs (or topoclusters) are not. Both charged PFlow  
1365 and TST  $E_T^{\text{miss}}$  show only a small residual dependence on  $N_{\text{PV}}$  and  $\sum E_T$ , since they  
1366 have fully pileup suppressed inputs through track associations.

1367 The scale plots are shown for  $Z+\text{jets}$  events and  $Z$  events with no jets. For the  
1368 nonsuppressed CST, the scale continues to worsen with increasing  $p_T^Z$ . The standard  
1369 PFlow algorithm performs the second worst in the region of high  $p_T^Z$ , but is the best at  
1370 low  $p_T^Z$ . We note the improved scale of the charged PFlow  $E_T^{\text{miss}}$  compared to the TST  
1371  $E_T^{\text{miss}}$ . Considering the resolution is essentially identical, the PFlow algorithm is better  
1372 picking up the contributions from additional neutral particles. In events with no jets,

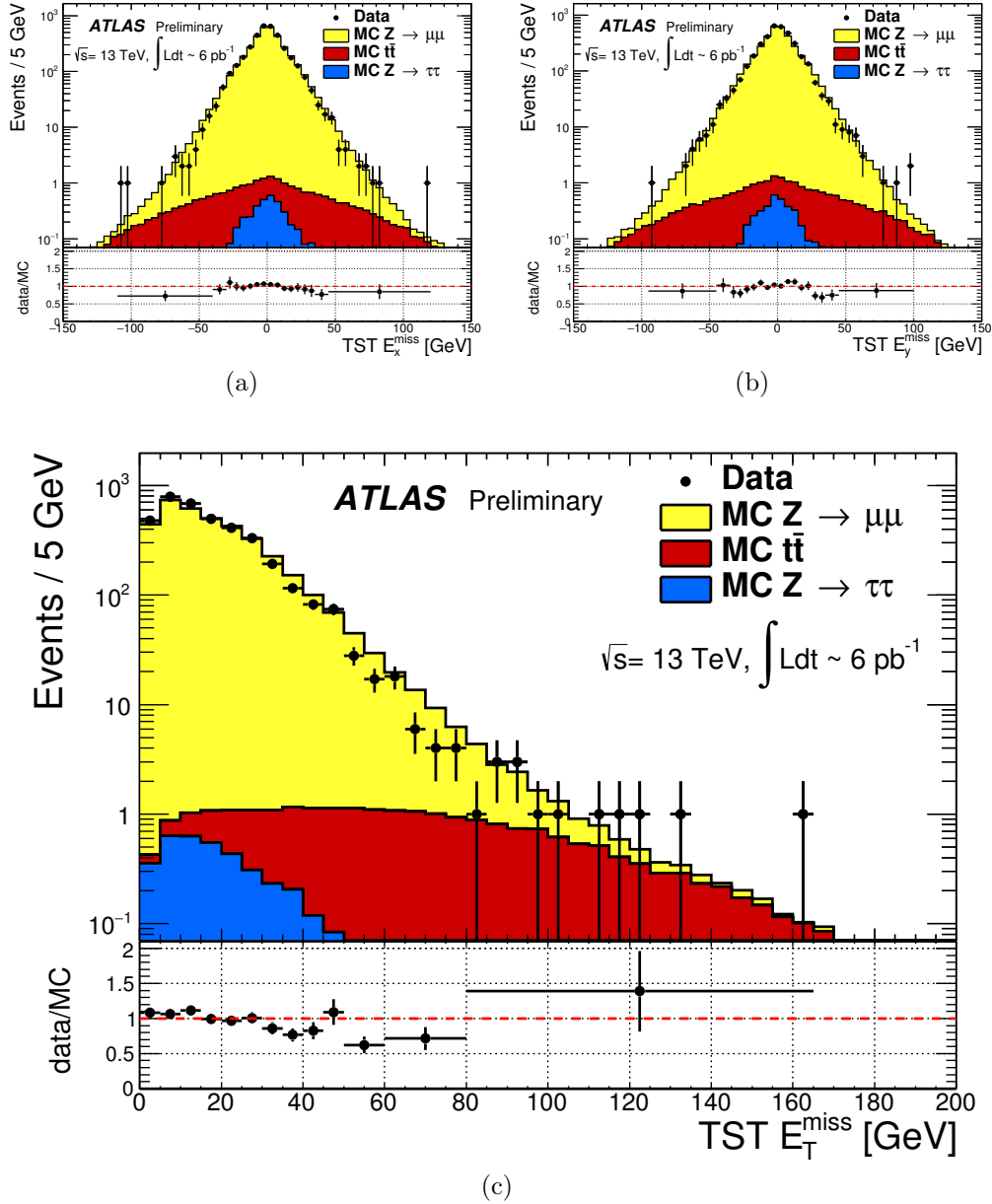


Figure 6.10: TST  $E_x^{\text{miss}}$ ,  $E_y^{\text{miss}}$ , and  $E_T^{\text{miss}}$  distributions of early  $\sqrt{s} = 13$  TeV data compared with simulation after the  $Z \rightarrow \mu\mu$  selection. The data sample consists of  $6 \text{ pb}^{-1}$ .

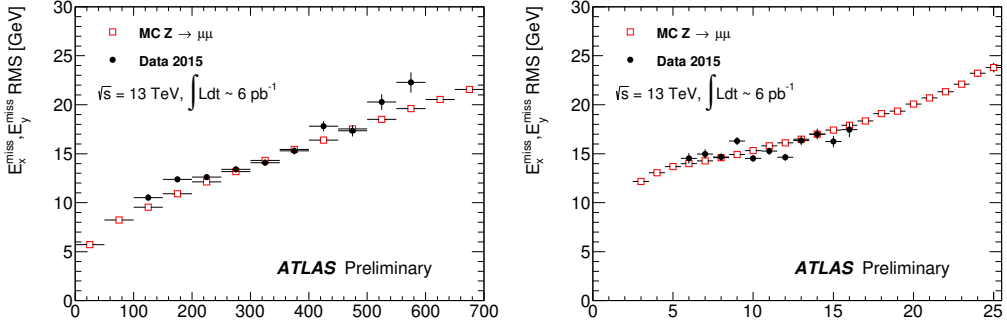


Figure 6.11: Resolution of TST  $E_T^{\text{miss}}$  of early  $\sqrt{s} = 13$  TeV data compared with simulation after the  $Z \rightarrow \mu\mu$  selection. The data sample consists of  $6 \text{ pb}^{-1}$ .

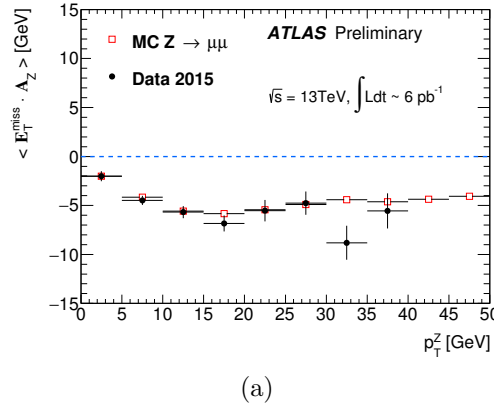


Figure 6.12: Scale of TST  $E_T^{\text{miss}}$  of early  $\sqrt{s} = 13$  TeV data compared with simulation after the  $Z \rightarrow \mu\mu$  selection. The data sample consists of  $6 \text{ pb}^{-1}$ .

1373 the soft term is essentially the only indication of the  $E_T^{\text{miss}}$  mismeasurement, since  
 1374 the muons will be well-measured. In this case, the pileup effects cancel, on average,  
 1375 due to the  $U(1)_\phi$  symmetry of the ATLAS detector, and CST performs rather well  
 1376 compared to the more complicated track-based algorithms. The full PFlow algorithm  
 1377 performs best, since it provides a small amount of pileup suppression on the neutral  
 1378 components from CST.

1379 The resolution and linearity are shown in simulated  $W \rightarrow e\nu$  events in Fig. 6.13.  
 1380 The resolution in  $W \rightarrow e\nu$  events shows a similar qualitative behavior to  $Z \rightarrow$   
 1381  $\mu\mu$  events. The CST  $E_T^{\text{miss}}$  has the worst performance, with charged PFlow  $E_T^{\text{miss}}$

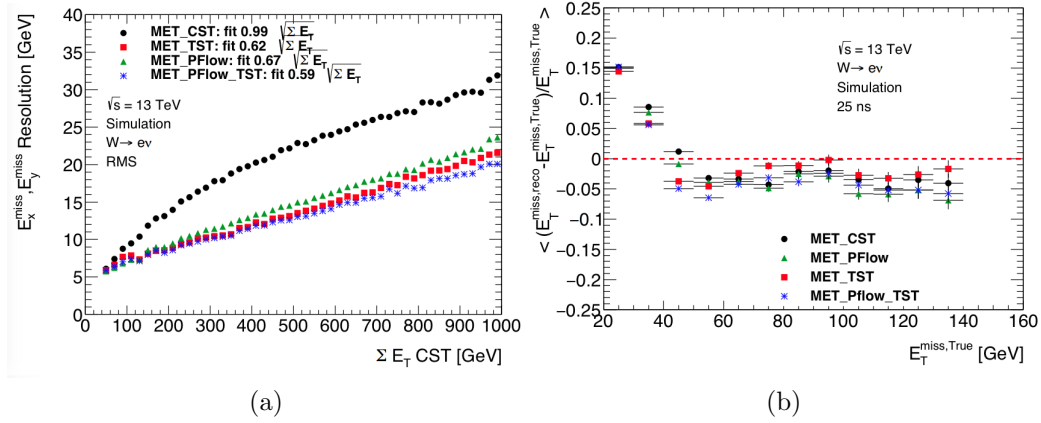


Figure 6.13: Comparison of  $E_{\text{T}}^{\text{miss}}$  resolution and linearity using different  $E_{\text{T}}^{\text{miss}}$  algorithms with simulated  $W \rightarrow e\nu$  events.

1382 performing best. The surprise here is the scale associated to TST  $E_{\text{T}}^{\text{miss}}$  has the  
 1383 strongest performance throughout the space parameterized by  $E_{\text{T}}^{\text{miss},\text{Truth}}$ , except for  
 1384 one bin at  $40 \text{ GeV} < E_{\text{T}}^{\text{miss},\text{Truth}} < 50 \text{ GeV}$ . The scale in these events is best measured  
 1385 using a track-based soft term.

1386 The resolution also investigated in real data passing the  $Z \rightarrow \mu\mu$  selection  
 1387 described above. A comparison of the  $E_{\text{T}}^{\text{miss}}$  between real data and simulation for  
 1388 each algorithm is presented in Fig. 6.16. The resolution as a function of  $\sum E_{\text{T}}$  and  
 1389  $N_{\text{PV}}$  is shown in Fig. 6.17 for this dataset. Overall, the real dataset shows the  
 1390 same general features as the simulation dataset in terms of algorithm performance.  
 1391 However, the performance of all algorithms seems to be significantly worse in data.  
 1392 This is likely due to simplifications made in the simulation: soft interactions which  
 1393 are not simulated have a significant effect on an event level variable such as the  $E_{\text{T}}^{\text{miss}}$   
 1394 resolution.

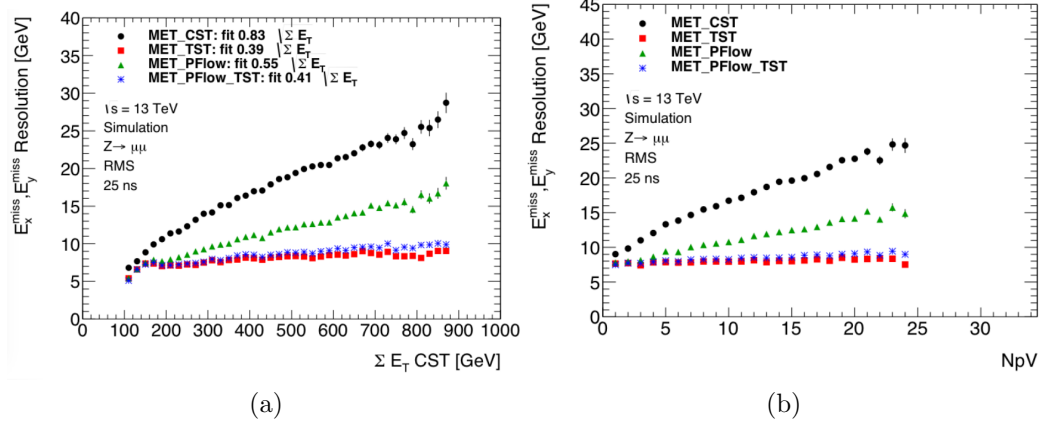


Figure 6.14: Comparison of  $E_T^{\text{miss}}$  resolution using different  $E_T^{\text{miss}}$  algorithms with simulated  $Z \rightarrow \mu\mu$  events.

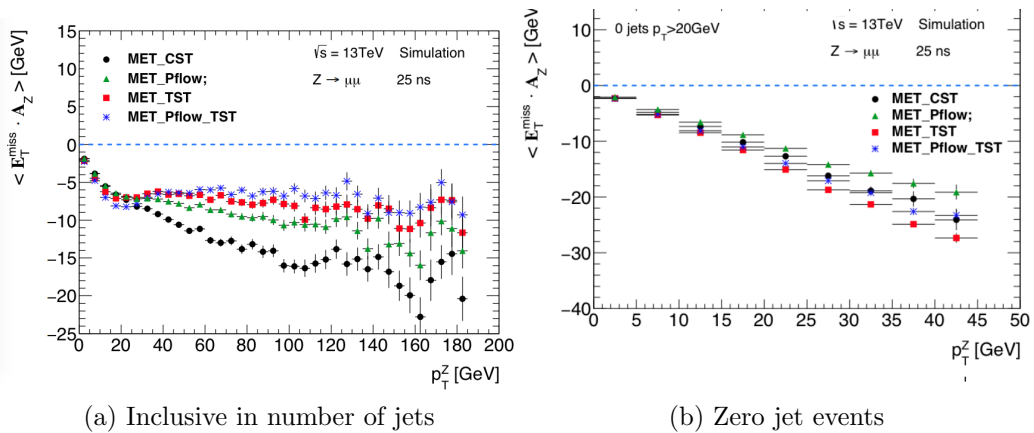


Figure 6.15: Comparison of  $E_T^{\text{miss}}$  scale using different  $E_T^{\text{miss}}$  algorithms with simulated  $Z \rightarrow \mu\mu$  events.

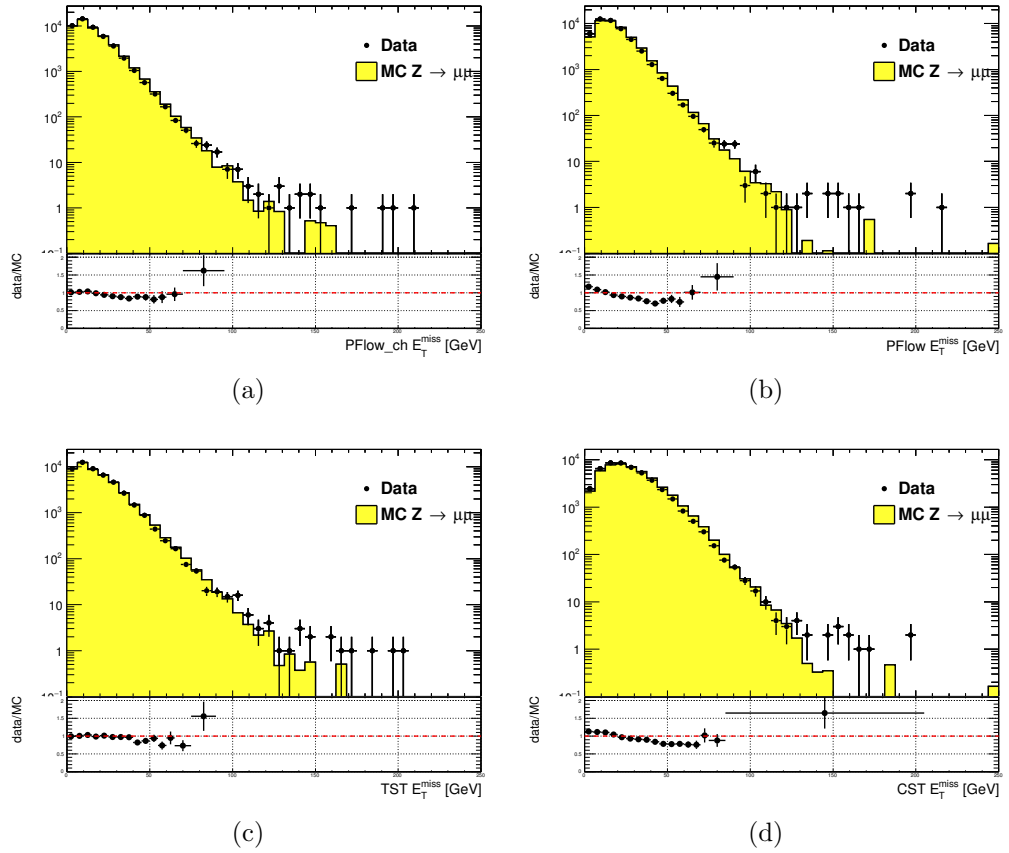


Figure 6.16: Comparison of  $E_T^{\text{miss}}$  distributions using different  $E_T^{\text{miss}}$  algorithms with a data sample of  $80 \text{ pb}^{-1}$  after the  $Z \rightarrow \mu\mu$  selection

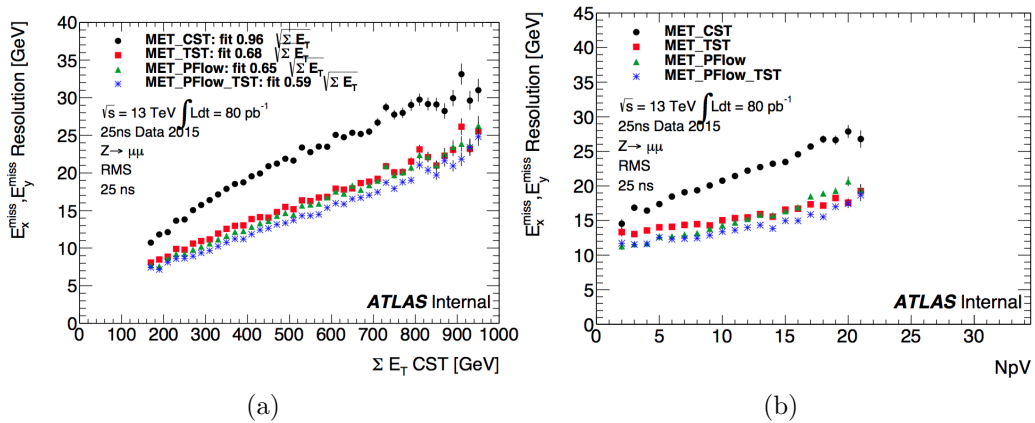


Figure 6.17: Comparison of  $E_T^{\text{miss}}$  resolution using different  $E_T^{\text{miss}}$  algorithms with a data sample of  $80 \text{ pb}^{-1}$  after the  $Z \rightarrow \mu\mu$  selection



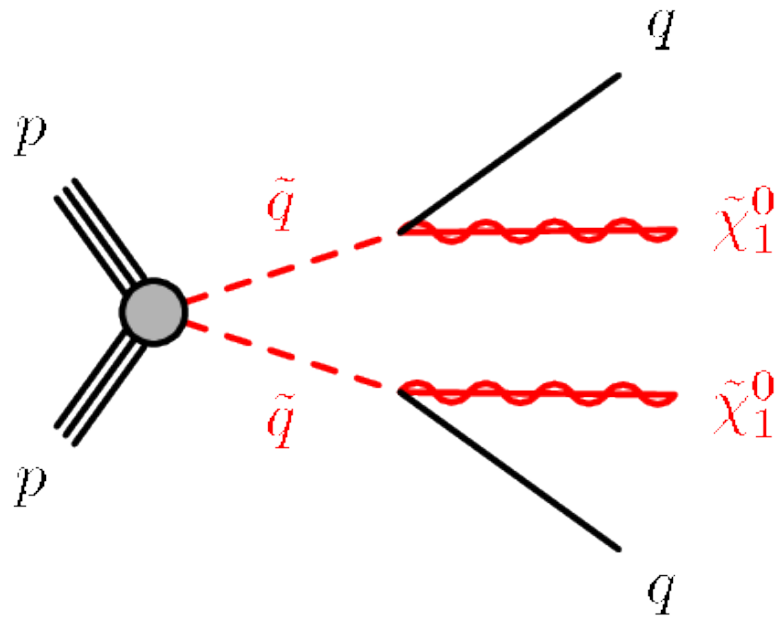
*Recursive Jigsaw Reconstruction*

1397 *Recursive Jigsaw Reconstruction* (RJR) [119, 120] is a novel algorithm used for  
 1398 the analysis presented in this thesis. RJR is the conceptual successor to the razor  
 1399 technique [121, 122], which has been used successfully in many new physics searches  
 1400 [37, 38, 40, 41, 47, 123]. In this chapter, we will first present the razor technique,  
 1401 and describe the razor variables. We will then present the RJR algorithm. After the  
 1402 description of the algorithm, we will describe the precise RJR variables used by this  
 1403 thesis and attempt to provide some physical intuition of what they describe.

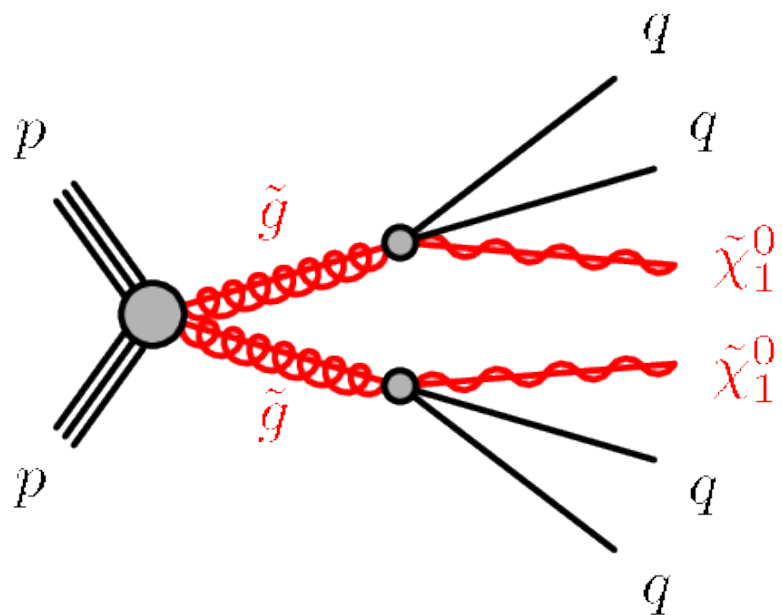
1404 **7.1 Razor variables**1405 **Motivation**

1406 In this thesis, we consider SUSY models where gluinos and squarks are pair-produced.  
 1407 Pair-production is a consequence of the  $R$ -parity imposed in many SUSY models.  
 1408  $R$ -parity violation is highly constrained by limits on proton decay [15], and is often  
 1409 assumed in SUSY model building. The Feynman diagrams considered are shown in  
 1410 Fig. 7.1.

1411 As discussed previously, the consequences of this  $\mathbb{Z}_2$  symmetry are drastic. To un-  
 1412 derstand the utility of the razor variables, the stability of the lightest supersymmetric  
 1413 particle is very important. In many SUSY models, including the ones considered in  
 1414 this thesis, this is the lightest neutralino  $\tilde{\chi}_1^0$ . This means that on either side of a  
 1415 SUSY decay process, where we begin with disparticle production, we have a final



(a) Disquark production



(b) Digluino production

Figure 7.1: Feynman diagrams for the SUSY signals considered in this thesis

1416 state particle which is not detected. Generically, this leads to  $E_T^{\text{miss}}$ . Selections based  
1417 on  $E_T^{\text{miss}}$  are very good at reducing dominant backgrounds, for example from QCD  
1418 backgrounds.

1419 However, there are limitations to searches based on  $E_T^{\text{miss}}$ . Due to jet mismeasurements,  
1420 instrumental failures, finite detector acceptance, nongaussian tails in the  
1421 detector response, and production of neutrinos inside of jets, there are many sources of  
1422 “fake”  $E_T^{\text{miss}}$  which does not correspond to a Standard Model neutrino or new physics  
1423 object such as an LSP. An additional limitation is the complete lack of longitudinal  
1424 information. As events from i.e. QCD backgrounds tend to have higher boosts along  
1425 the  $z$ -direction, this is ignoring an important handle in searches for new physics.  
1426 Finally,  $E_T^{\text{miss}}$  is only one object, which is a measurement for *two* separate LSPs. If one  
1427 could factorize this information somehow, this would provide additional information  
1428 to potentially discriminate against backgrounds. The *razor variables* ( $M_{\Delta}^R, R^2$ ) are  
1429 more robust than standard variables against these effects [121, 122].

## 1430 Derivation of the razor variables

1431 To derive the razor variables ( $M_{\Delta}^R, R^2$ ), we start with a generic situation of the pair  
1432 production of heavy sparticles with mass  $m_{\text{Heavy}}$ .<sup>1</sup> Each sparticle decays to a number  
1433 of observable objects (in this thesis, jets), and an unobservable  $\tilde{\chi}_1^0$  of mass  $m_{\tilde{\chi}_1^0}$ . We  
1434 will combine all of the jets into a *megajet*; this process will be described below. We  
1435 begin by analyzing the decay in the “rough-approximation”, or in modern parlance,  
1436 *razor frame* ( $R$ -frame). This is the frame where each sparticle is at rest. The complete  
1437 set of frames considered in the case of the razor variables is shown in Fig. 7.2.

In the  $R$ -frame, the decay is straightforward to analyze. By construction, there  
are in fact two  $R$ -frame s, and they have identical kinematics. Each megajet has

---

<sup>1</sup>The razor variables have undergone confusing notational changes over the years. We will be self-consistent, but the notation used here may be different from references.

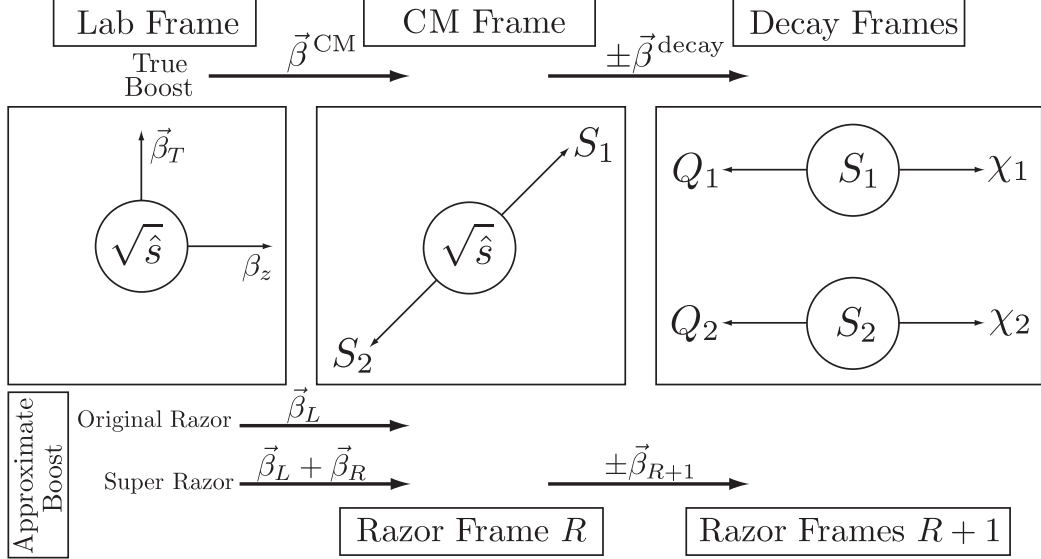


Figure 7.2: Frames considered when applying the razor technique, from [122].

energy  $E_1^R, E_2^R$  in the frame of its parent sparticle, and we define a characteristic mass  $M_R$ :

$$E_1^R = E_2^R = \frac{m_{\text{Heavy}}^2 - m_{\tilde{\chi}_1^0}^2}{2m_{\text{Heavy}}} \quad (7.1)$$

$$M_R = 2 \times E_1^R = 2 \times E_2^R = \frac{m_{\text{Heavy}}^2 - m_{\tilde{\chi}_1^0}^2}{m_{\text{Heavy}}} \quad (7.2)$$

1438 For cases where  $m_{\text{Heavy}} \gg m_{\tilde{\chi}_1^0}$ ,  $M_R$  is an estimator of  $m_{\text{Heavy}}$ . This scenario happens  
 1439 in the SM, such as in  $t\bar{t}$  and  $WW$  events, where the  $\tilde{\chi}_1^0$  is instead a neutrino.

1440 The question now is how to use this simple derivation in the lab frame, where we  
 1441 actually have measurements. There are two related issues: how to combine the jets  
 1442 into the megajets, and how to “transform” (or *boost*) to the  $R$ -frame.

To construct the megajets, the procedure is the following. For a given set of jets  $j_i, i = 0, \dots, n_{\text{jet}}$ , we construct *all* combinations of their four-momenta such that there is at least one jet inside each megajet. Among this set of possible megajets  $\{J_{1,2}\}$ , we make the following unique choice for the megajets. We minimize the following quantity:

$$m_{J_1}^2 + m_{J_2}^2. \quad (7.3)$$

1443 In modern parlance, this is known as a *jigsaw*. It is important to note, this is a  
 1444 *choice*. It may have nice physical qualities or satisfy some convenient intuition about  
 1445 the events, but as we will see later, other choices are possible.

We now describe how we translate our megajet kinematics, measured in the lab frame, to the  $R$ -frame. This is a two-step procedure. We perform two *boosts*: a longitudinal boost  $\beta_L$  and a transverse boost  $\beta_T$ . Schematically,

$$J_1^R \xrightarrow{\beta_T} J_1^{CM} \xrightarrow{\beta_L} J_1^{\text{lab}} \quad (7.4)$$

$$J_2^R \xrightarrow{-\beta_T} J_2^{CM} \xrightarrow{\beta_L} J_2^{\text{lab}} \quad (7.5)$$

$$(7.6)$$

1446 The  $J_{1,2}^{\text{lab}}$  correspond directly to those in the megajet construction. We drop the  
 1447 “lab” designation for the rest of the discussion. The question is how to compute the  
 1448 magnitudes of these boosts, given the missing degrees of freedom.

For the transverse boost  $\beta_T$ , recall the two megajets have equal energies in their  $R$ -frame by construction. This constraint can be reexpressed as a constraint on the magnitude of this boost, in terms of the boost velocity  $\beta_L$  (and Lorentz factor  $\gamma_L$ ):

$$\beta_T = \frac{\gamma_L(E_1 - E_2) - \gamma_L\beta_L(p_{1,z} - p_{2,z})}{\hat{\beta}_T \cdot (\vec{p}_{1,T} + \vec{p}_{2,T})} \quad (7.7)$$

where we have denoted the lab frame four-vectors as  $p_i = (E_i, \vec{p}_{i,T}, p_z)$ . We now make the *choice* for the direction of the transverse boost  $\hat{\beta}_T$ :

$$\hat{\beta}_T = \frac{\vec{p}_{1,T} + \vec{p}_{2,T}}{|\vec{p}_{1,T} + \vec{p}_{2,T}|}. \quad (7.8)$$

1449 This choice forces the denominator of Eq. (7.7) to unity, and corresponds to aligning  
 1450 the transverse boost direction with the sum of the two megajets transverse directions.

For the longitudinal boost, we choose  $\vec{\beta}_L$  along the  $z$ -direction, with magnitude:

$$\beta_L = \frac{p_{1,z} + p_{2,z}}{E_1 + E_2}. \quad (7.9)$$

1451 Viewed in terms of the original parton-parton interactions, this is the choice which  
 1452 “on average” gives  $p_{z,\text{CM}} = 0$ , as we would expect. This well-motivated choice due to  
 1453 the total  $z$  symmetry.

We now have well-motivated guesses for both boosts, which allow us write our original characteristic mass  $M_R$  in terms of the lab frame variables, by application of these two Lorentz boosts to the energies of Eq. (7.1):

$$M_R^2 \xrightarrow{\beta_T} M_{R,\text{CM}}^2 \xrightarrow{\beta_L} M_{R,\text{lab}}^2 = (E_1 + E_2)^2 - (p_{1,z} + p_{2,z})^2. \quad (7.10)$$

Finally, we define an additional mass variable, which include the missing transverse energy  $E_T^{\text{miss}}$ . Importantly, note that we did not use the  $E_T^{\text{miss}}$  in the definition of  $M_R$ , which depends only on the energies of the megajets. Backgrounds with no invisible particles (such as multijet events) must have  $J_1$  and  $J_2$  back to back. Thus, we define the transverse mass:

$$(M_R^T)^2 = \frac{1}{2} \left[ E_T^{\text{miss}}(p_{1,T} + p_{2,T}) - \vec{E}_T^{\text{miss}} \cdot (\vec{p}_{1,T} + \vec{p}_{2,T}) \right]. \quad (7.11)$$

Generally, we have  $M_R^T < M_R$ , so we define a dimensionless ratio (“the razor”):

$$R^2 = \left( \frac{M_R^T}{M_R} \right)^2. \quad (7.12)$$

1454 For signal events, we expect  $R$  to peak around  $R \sim 1/4$ , while backgrounds without  
 1455 real  $E_T^{\text{miss}}$  are expected to have  $R \sim 0$ .

## 1456 7.2 Recursive Jigsaw Reconstruction

1457 Recursive Jigsaw Reconstruction is an algorithm allowing the imposition of a decay  
 1458 tree interpretation on an particular event [119, 120]. The idea is to construct the  
 1459 underlying kinematic variables (the masses and decay angles) on an event-by-event  
 1460 level. This is done “recursively” through a decay tree which corresponds (sometimes  
 1461 approximately) to the Feynmann diagram for the signal process of interest. After

1462 each step of the recursive procedure, the objects are “placed” into one bucket (or  
1463 branch) of the decay tree, and the process is repeated on each frame we have imposed.  
1464 The imposition of these decay trees is done by *jigsaw* rule: a procedure to resolve  
1465 combinatoric or kinematic ambiguities while traversing the decay tree. This procedure  
1466 is performed by the `RestFrames` software packages [124]

1467 In events where all objects are fully reconstructed, this is straightforward, and  
1468 of course has been used for many years in particle physics experiments. Events  
1469 which contain  $E_T^{\text{miss}}$  are more difficult, due to the loss of information: the potential  
1470 for multiple mismeasured or simply unmeasureable objects, such as neutrinos or the  
1471 LSP in SUSY searches. There can also be combinatoric ambiguities in deciding how  
1472 to group objects of the same type; specifically here, we will be concerned with the  
1473 jigsaw rule to associate jets to a particular branch of a decay tree. The jigsaw rules  
1474 we impose will remove these ambiguities. First, we will describe the decay trees used  
1475 in this thesis, and then describe the jigsaw rules we will use. Finally, we will describe  
1476 the variables used in the all-hadronic SUSY search presented in this thesis.

## 1477 Decay Trees

1478 The decay trees imposed in this thesis are shown in Fig. 7.3. Leaving temporarily the  
1479 question of “how” we apply the jigsaw rules, let us compare these trees to the signal  
1480 processes of interest. In particular, we want to compare the Feynman diagrams of  
1481 Fig. 7.1 with the decay trees of Fig. 7.3. The decay tree in ?? corresponds exactly to  
1482 that expected from disquark production, and matches very closely with the principles  
1483 of the razor approach. We first apply a jigsaw rule, indicated by a line, to the  
1484 kinematics of the objects in the *lab* frame. This outputs the kinematics of our event  
1485 in the *parent-parent (PP)* frame, or in the razor terminology, the CM frame. That is,  
1486 the kinematics of this frame are an estimator for the kinematics in the center of mass  
1487 frame of the disquark system. We apply another jigsaw, which splits the objects in the

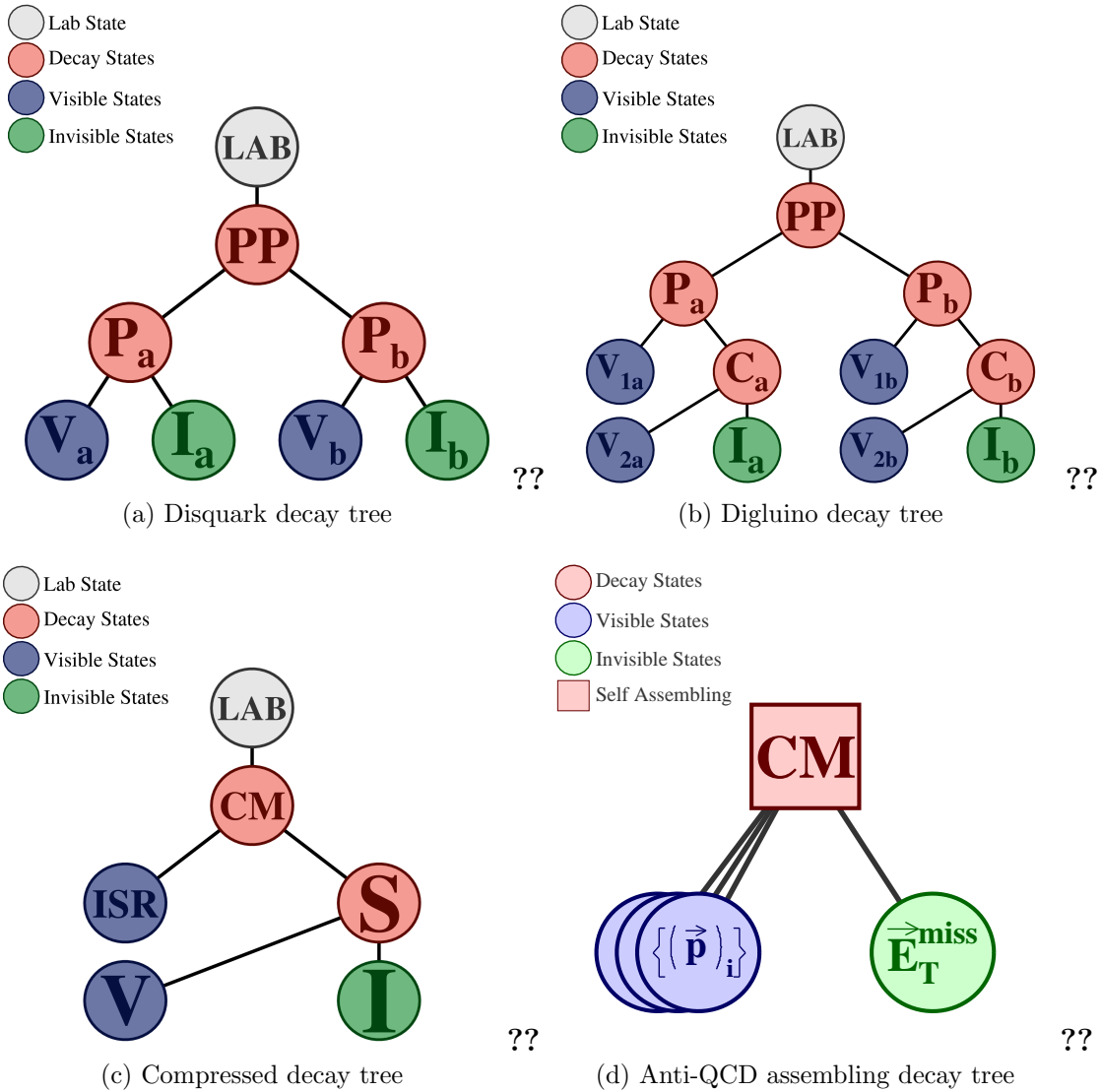


Figure 7.3: RJR decay trees imposed in this thesis

1488  $PP$  frame into two new frames, known as the  $P_a$  and  $P_b$  systems. These are equivalent  
 1489 to the razor frames of the razor technique, and represent proxy frames where each  
 1490 squark is at rest. In  $P_a(P_b)$ , the decay is symmetric between the visible  $V_a(V_b)$  objects  
 1491 and the invisible system  $I_a(I_b)$ . To generate the estimator of the kinematics of the  
 1492  $V_a$ ,  $V_b$ ,  $I_a$ , and  $I_b$  systems in the  $P_a$  and  $P_b$  systems, we apply another jigsaw rule to  
 1493 split the total  $E_T^{\text{miss}}$  between  $P_a$  and  $P_b$ , which allows calculations of these kinematics  
 1494 in these frames. For the case of disquark production, this is the expected decay tree,

1495 and we stop the recursive calculation at that level.

1496 In the case of digluino production, we expect two additional jets, and we can  
1497 perform an additional boost in each of  $P_a$  and  $P_b$ , to what we call the  $C_a$  and  $C_b$  frames.  
1498 The decay tree is shown in ???. In this case we apply a jigsaw at the level of  $P_a(P_b)$   
1499 which separates a single visible object  $V_{1a}$  ( $V_{2a}$ ) from the child frame  $C_a(C_b)$ . This  
1500 child frame represents the hypothesized squark after the decay  $\tilde{g} \rightarrow g\tilde{q}$ , which then  
1501 decays as in the squark case. This gives additional information which will be exploited  
1502 for the gluino specific search regions.

The third decay tree used in this thesis is the *compressed* decay tree. Compressed refers to signal models which have a small splitting between the mass of the proposed sparticle and the  $\tilde{\chi}_1^0$ . In this case, the sparticle decay products (i.e. the jets and  $E_T^{\text{miss}}$ ) do not generally have large scale [119]. Instead, the strategy is generally to look for a large-scale initial state radiation (ISR) jet which is recoiling off the disparticle system. In the case where the LSPs receive no momentum from the sparticle decays, the following approximation holds:

$$E_T^{\text{miss}} \sim -p_T^{\text{ISR}} \times \frac{m_{\tilde{\chi}_1^0}}{m_{\text{sparticle}}} \quad (7.13)$$

1503 where  $p_T^{\text{ISR}}$  is the transverse momentum associated to the entire ISR system.

1504 RJR offers a natural and straightforward way to exploit this feature in events  
1505 containing ISR. One imposes the simple decay tree in ?? with associated jigsaw rules.  
1506 With suitable jigsaw rules, this decay tree “picks out” the large  $p_T$  ISR jet, recoiling  
1507 off the  $E_T^{\text{miss}}$  and additional radiation from the sparticle decays. This provides a  
1508 convenient set of variables to understand compressed scenarios.

1509 There is one other decay tree, shown in ???. This is special, as it is only used for  
1510 the purpose of QCD rejection, and does not directly map to a sparticle decay chain.  
1511 Due to the large production cross-sections of QCD events, even very rare large jet  
1512 mismeasurements can lead to significant  $E_T^{\text{miss}}$  which can enter the signal region. To  
1513 reduce these backgrounds, one usually rejects events which contain jets which are

1514 “too close” by some distance metric to the  $E_T^{\text{miss}}$  in the event. Generally, in the past,  
1515 the distance metric has been defined as simply the angular distance  $\Delta R$ .

1516 The *self-assembling tree* can be seen as defining a distance metric which depends  
1517 on the magnitudes of the  $E_T^{\text{miss}}$  and jets rather than simply their distance in angular  
1518 space. Depending on the exact kinematics, the one or two closest jets are found, and  
1519 label the  $E_T^{\text{miss}}$  *siblings*.

1520 In this section, we have seen how one imposes particular decay trees on an event  
1521 to produce a basis of kinematic variables in the approximated frames relevant to  
1522 the hypothesized sparticle decay chain. This explains why we call this procedure  
1523 “recursive”: we can continue the procedure through as many steps of a decay tree as  
1524 we want, and each application of a jigsaw rule is dependent on the variables produced  
1525 in the last step. The question, of course, is *what are these jigsaw rules?*.

## 1526 Jigsaw Rules

1527 Jigsaw rules are the fundamental step that allow the recursive definitions of the  
1528 variables of interest. We want rules which allow us to fully define kinematic variables  
1529 at each step in a decay tree. The only possible solution to fully define the event  
1530 kinematics in terms of the frames of the hypothesized decays is the imposition of  
1531 external constraints to eliminate additional degrees of freedom. In principle, these  
1532 need not have any particular physical motivation. Instead, the jigsaw rules are a  
1533 way to resolve the mathematical ambiguities to fully reconstruct the full decay chain  
1534 kinematics. However, most practical jigsaw rules also have some reasonable physical  
1535 motivation, which we will also elucidate.

1536 In the original razor point of view, some jigsaw rules can be seen as the definitions  
1537 of the boosts which relate the different frames of interest, while other rules allow one  
1538 to combine multiple objects and place them into a particular hemisphere (previously  
1539 megajet). These are the two forms of jigsaw rules: combinatoric and kinematic. As

1540 we have stressed before, the jigsaw rules are a *choice*; as long as a particular jigsaw  
1541 rule allows the definition of variables at each step in a decay tree, it is “as valid” as  
1542 any other rule.

Practically speaking, in this thesis we use only a small subset of possible jigsaw rules. The combinatoric jigsaw rule we use has already been introduced as megajet construction above. The minimization of

$$m_{J_1}^2 + m_{J_2}^2. \quad (7.14)$$

1543 is a jigsaw rule to deal with the combinatoric ambiguity implicit in which jets go in  
1544 which hemisphere. This is the jigsaw rule used in the decay trees when going from  
1545 one frame to two frames such as  $PP \rightarrow P_a, P_b$ .

1546 We will use three other jigsaw rules, which are both kinematic jigsaw rules. One  
1547 has already been used in the razor technique. The minimization of  $\beta_L$  will be used  
1548 as the jigsaw rule in the first step of each decay tree: the lab frame to the  $PP/\text{CM}$   
1549 frame. This is in effect the imposition of longitudinal boost invariance, as we expect  
1550 on average  $p_{z,PP,\text{CM}} = 0$ . One defines a unique longitudinal boost by imposition of  
1551 this external constraint.

1552 The final two jigsaw rules used in this thesis was not used in the razor technique.  
1553 We describe them here.

The first kinematic ambiguity is the total mass of the invisible system  $M_I$ . We guess this to be:

$$M_I^2 = M_V^2 - 4M_{V_a}M_{V_b}. \quad (7.15)$$

1554 As we stated above, there is no need to “justify” the jigsaw rules, as they are in some  
1555 ways a mathematical trick to fully resolve the event kinematics. However in this case,  
1556 there is a nice property of this guess. The symmetry of the production mechanism,  
1557 where we have two decay products  $V_i$  and  $I_i$  produced from the decay of the same  
1558 heavy sparticle, is explicit with this jigsaw choice.

1559     The final jigsaw rule we employ in this thesis is used to resolve the “amount” of  
1560  $E_T^{\text{miss}}$  that “belongs” to each hemisphere, and therefore how to impose the transverse  
1561 boost onto each of i.e.  $P_a$  and  $P_b$  from  $PP$ . Equivalently, it can be seen as the  
1562 resolution of the kinematics of the  $I_a$  and  $I_b$  objects in the disquark and digluino  
1563 decay trees. Recall that at this point, we have already approximated the boost  
1564 of the  $PP$  frame. The choice we use is to minimize the masses  $P_a$  and  $P_b$ , while  
1565 simultaneously constraining  $P_a = P_b$ . As is the case in the last step, there is a  
1566 straightforward physical interpretation of this choice. In the signal models we are  
1567 considering,  $P_a$  and  $P_b$  are the estimated frames of the squark or gluino pair-produced  
1568 as a heavy resonance. We then of course expect  $M_{P_a} = M_{P_b}$ .

1569     The imposition of the decay trees, with ambiguities resolved through the jigsaw  
1570 rules, give a full set of boosts relating the frames of each decay tree. In each frame,  
1571 we have estimates for the frame mass and decay angles, which can be used in searches  
1572 for new physics. In the next section, we describe the variables that are used in this  
1573 thesis in more details.

## 1574     **7.3 Variables used in the search for zero lepton**

### 1575     **SUSY**

1576     We describe here the variables used in the search described in ???. These were  
1577 reconstructed using the RJR algorithm as just described, using the RestFrames  
1578 packages [124]. In these frames, the momenta of all objects placed into that branch  
1579 of the decay tree are available (after application of the approximated boost), and in  
1580 principle we can calculate any variable of interest such as invariant masses or the  
1581 angles between these objects. The truly useful set of variables are highly dependent  
1582 on the signal process, and we leave their discussion to the subsequent chapters. It is  
1583 useful to understand the philosophy employed in the construction of these variables.

1584 In general, we can split variables useful for searches for new physics into two  
1585 categories: *scaleful* and *scaleless* variables. In this search, we will use a set of scaleful  
1586 variables called the  $H$  variables. The scaleless variables will consists of ratios and  
1587 angles. In general, we want to limit the number of scaleful cuts we apply, for two  
1588 reasons. Different scaleful variables are often highly correlated, and this of course  
1589 limits the utility of additional cuts. Addtionally, selections based on many scaleful  
1590 variables often “over-optimize” for particular signal model of interest, especially as  
1591 related to the mass difference chosen between the sparticle and the LSP. To avoid  
1592 this, each decay tree will only use two scale variables, one of which quantifies the  
1593 overall mass scale of the event, and another which acts as a measure of the event  
1594 balance.

## 1595 **Squark and gluino variables**

1596 Taking our general philosophy to a particular case, we here describe the variables  
1597 used by the squark and gluino searches. We have a suite of scale variables which we  
1598 will call the  $H$  variables, and a suite of angles and ratios.

1599 As we have described above, the RJR algorithm gives us access to the masses of  
1600 each frame of interest. It maybe seem natural, then, that these variables would be the  
1601 most useful for discrimination of the signal from background processes. However, due  
1602 to the all hadronic state considered in this thesis, the that can be constructed such  
1603 as  $M_{PP}$  can be affected by extra QCD radiation, which can promote the background  
1604 processes to large scales. The  $H$  variables show a resilience to this effect. They  
1605 take their name from the commonly used variable  $H_T$ , which is the scalar sum of  
1606 the visible momentum. However, due to the RJR technique, we can evaluate these  
1607 variables in the non-lab frame, including longitudinal information. They are also  
1608 constructed with *aggregate* momenta using a similar mass minimization procedure  
1609 as we have already described.

We label these variables as  $H_{n,m}^F$ . The frame from where they are evaluated is denoted  $F$ ; practically, this means  $F \in \{\text{lab}, PP, P_a, P_b\}$ . When the discussion applies to both  $P_a$  and  $P_b$ , we will write  $P_i$ . The subscripts  $n$  and  $m$  denote the number of visible and invisible vectors considered, respectively. When there are more vectors available than  $n$  or  $m$ , we add up vectors using the hemisphere (megajet) jigsaw rule until there are  $n$  ( $m$ ) objects.<sup>2</sup> In the opposite case, where  $n$  or  $m$  is greater than the number of available objects, one simply considers the available objects. The  $H_{n,m}^F$  variables are then defined as

$$H_{n,m}^F = \sum_i^n |\vec{p}_{\text{vis},i}^F| + \sum_j^m |\vec{p}_{\text{inv},i}^F|. \quad (7.16)$$

It may not be clear that these variables encode independent information. Fundamentally, this is just an expression of the triangle inequality  $\sum |\vec{p}| \geq |\sum \vec{p}|$ . The different combinations can then include independent information. The final note on the  $H$  variables is that we can also consider purely transverse versions of these variables, which we will denote  $H_{T,n,m}^F$ . Including this view, it is easy to see how the  $H$  variables are extensions of the normal  $H_T$  variables, as

$$H_T = H_{T,\infty,0}^{\text{lab}}. \quad (7.17)$$

1610     Although the  $H$  variables are interesting in their own right, the true power of the  
 1611     RJR technique comes from the construction of scaleless variables with the technique.  
 1612     This is because the scaleless ratios and angles are in fact measured in the “right”  
 1613     frame, where right here means an approximation of the correct frame. This provides  
 1614     a less correlated set of variables than those measured in the lab frame, due to the  
 1615     corrections to the disparticle or sparticle system boosts from the RJR technique.  
 1616     For the search for noncompressed disquark production, we use will use the  
 1617     following set of RJR variables.

---

<sup>2</sup>Recall that these vectors are constructed by the imposition of the decay tree with the relevant jigsaw rules.

- 1618 •  $H_{1,1}^{PP}$  - scale variable useful for discrimination against QCD backgrounds and  
1619 used in a similar way to  $E_T^{\text{miss}}$

- 1620 •  $H_{T,2,1}^{PP}$  - scale variable providing information on the overall mass scale of the  
1621 event for disquark signal production. We will often call this the *full* scale  
1622 variable.

- 1623 •  $H_{T,1,1}^{PP}/H_{2,1}^{PP}$  - ratio used to prevent imbalanced events where the scale variable  
1624 is dominated by one high  $p_T$  jet or high  $E_T^{\text{miss}}$

- 1625 •  $p_{PP,z}^{\text{LAB}}/(p_{PP,z}^{\text{LAB}} + H_{T,2,1}^{PP})$  - ratio used to prevent significant boosts in the  
1626  $z$ -direction.  $p_{PP,z}^{\text{LAB}}$  is a measure of the total boost of the  $PP$  system from the lab  
1627 frame

- 1628 •  $p_{T,j2}^{PP}/H_{T,2,1}^{PP}$  - ratio to force the second leading jet in the  $PP$  frame to carry a  
1629 significant portion of the total scalar sum in that frame. This requirement is  
1630 another balance requirement, on the total  $p_T$  of that second jet in the  $PP$  frame.

1631 First, we note that there is an implicit requirement that each hemisphere has at least  
1632 one jet (to even reconstruct the  $P_a$  and  $P_b$  frames), these variables are implicitly using  
1633 two or more jets, as we expect in disquark production. The other important thing  
1634 to note is that all of the ratios use the full scale variable as the denominator. This  
1635 is sensible, as we expect all of these effects to be scaled with the full scale variable  
1636  $H_{T,2,1}^{PP}$ . We will see a similar behavior for the gluino regions, with a new full scale  
1637 variable.

1638 For the search for noncompressed digluino production, we use will use the following  
1639 set of RJR variables. Due to the increased complexity of the event topology with four  
1640 jets, there are additional handles we can exploit:

- 1641 •  $H_{1,1}^{PP}$  - same as disquark production

- 1642     •  $H_{T,4,1}^{PP}$  - scale variable providing information on the overall mass scale of the  
 1643       event for digluino signal production. As before, we often call this the *full* scale  
 1644       variable. Since this variable allows the jets to be separated in the *PP* frame, it  
 1645       is more appropriate for digluino production.
- 1646     •  $H_{T,1,1}^{PP}/H_{4,1}^{PP}$  - ratio used to prevent imbalanced events where the scale variable  
 1647       is dominated by one high  $p_T$  jet or high  $E_T^{\text{miss}}$
- 1648     •  $H_{T,4,1}^{PP}/H_{4,1}^{PP}$  - ratio used to measure the fraction of the total scalar sum of the  
 1649       momentum in the transverse plane. Digluino production is expected to be fairly  
 1650       central
- 1651     •  $p_{PP,z}^{\text{LAB}}/(p_{PP,z}^{\text{LAB}} + H_{T,4,1}^{PP})$  - ratio used to prevent significant boosts in the  
 1652        $z$ -direction
- 1653     •  $\min(p_{T,j2_i}^{PP}/H_{T,2,1_i}^{PP})$ - ratio to require the second leading jet in *both* squark-like  
 1654       hemispheres  $C_a$ and  $C_b$ to contain a significant portion of *that frame's* momenta.  
 1655       This is similar to the  $p_{T,j2}^{PP}/H_{T,2,1}^{PP}$  disquark discriminator, but applied to both  
 1656       hemispheres  $C_a$ and  $C_b$ .
- 1657     •  $\max(H_{1,0}^{P_i}/H_{2,0}^{P_i})$ - ratio requiring one jet in each of the  $P_i$  to not take too much  
 1658       of the total momentum of that frame. This ratio is generally a very loose cut.

## 1659 Compressed variables

1660 As we saw above, the decay tree imposed for compressed spectra is simpler. We do  
 1661 not attempt to fully reconstruct the details of the system recoiling of the ISR system,  
 1662 but use a straightforward set of variables in this case. One additional simplification  
 1663 is that all variables are force to be transverse in this case; we simply do not include  
 1664 the  $\eta/z$  information of the objects as inputs to the RJR reconstruction. We still use  
 1665 the philosophy of limiting our scaleful variables to just two. The compressed scenario  
 1666 uses the following set of RJR variables:

- 1667 •  $p_{T,S}^{\text{ISR}}$ - scale variable that is the magnitude of the total transverse momenta of all  
 1668 jets associated to the ISR system, as evaluated in the CM frame

- 1669 •  $R_{\text{ISR}} \equiv p_I^{\hat{\text{CM}}} \cdot p_{T,S}^{\hat{\text{CM}}} / p_{T,S}^{\text{CM}}$  - this ratio is our measurement for the ratio of the LSP  
 1670 mass to the compressed sparticle mass. These are the values in the CM frame  
 1671 In compressed cases, this should be large, as this estimates the amount of the  
 1672 total CM  $\rightarrow S$  boost is carried by the invisible system.

- 1673 •  $M_{T,S}$ - the transverse mass of the S system

- 1674 •  $N_{\text{jet}}^V$ - the number of jets associated to the visible system V

- 1675 •  $\Delta\phi_{\text{ISR},I}$ - the opening angle between the ISR system and the invisible system  
 1676 measured in the lab frame. As the invisible system is expected to carry much  
 1677 of the total  $S$  system momentum, this should be large, as we expect the ISR  
 1678 system to recoil directly opposite the  $I$  system in that case.

## 1679 Anti-QCD variables

1680 For the self-assembling tree, we construct two variables, which we combine to form a  
 1681 single variable which rejects QCD events. In this case, we use the mass minimization  
 1682 jigsaw, with a fully transverse version of the event (i.e. we set all jet  $z/\eta$  components  
 1683 to 0). This jigsaw defines the distance metric, and provides us with one or two jets  
 1684 known as the  $E_T^{\text{miss}}$  siblings. We define  $\vec{p}_{\text{sib}}$  as the sum of these jets, and define the  
 1685 following quantities.

We calculate a ratio observable which examines the relative magnitude of the sibling vector  $\vec{p}_{\text{sib}}$  and  $E_T^{\text{miss}}$ , and an angle relating  $\vec{p}_{\text{sib}}$  and  $E_T^{\text{miss}}$ :

$$R(\vec{p}_{\text{sib}}, E_T^{\text{miss}}) \equiv \frac{\vec{p}_{\text{sib}} \cdot \hat{E}_T^{\text{miss}}}{\vec{p}_{\text{sib}} \cdot \hat{E}_T^{\text{miss}} + |\vec{E}_T^{\text{miss}}|} \quad (7.18)$$

$$\cos \theta(\vec{p}_{\text{sib}}, E_T^{\text{miss}}) \equiv \frac{(\vec{p}_{\text{sib}} + \vec{E}_T^{\text{miss}}) \cdot \vec{p}_{\text{sib}} + \hat{E}_T^{\text{miss}}}{|\vec{p}_{\text{sib}}| + E_T^{\text{miss}}} \quad (7.19)$$

These observables are highly correlated, but taking the following fractional difference provides strong discrimination between SUSY signal and QCD background events:

$$\Delta_{\text{QCD}} \equiv \frac{1 + \cos \theta(\vec{p}_{\text{sib}}, E_{\text{T}}^{\text{miss}}) - 2R(\vec{p}_{\text{sib}}, E_{\text{T}}^{\text{miss}})}{1 + \cos \theta(\vec{p}_{\text{sib}}, E_{\text{T}}^{\text{miss}}) + 2R(\vec{p}_{\text{sib}}, E_{\text{T}}^{\text{miss}})}. \quad (7.20)$$

1686 We will use this variable in the next chapter.

1688 *A search for supersymmetric particles in zero lepton final  
 1689 states with the Recursive Jigsaw Technique*

1690 This section presents the details of the first search employing RJR variables as  
 1691 discriminating variables, as described in [120]. We will describe the simulation  
 1692 samples used, and then define the selections where we search for new SUSY  
 1693 phenomena, which we call the *signal regions* (SRs) Afterwards, we describe the  
 1694 background estimation techniques used in the analysis. Finally, we discuss the  
 1695 treatment of systematic uncertainties, and how we combine them using a likelihood  
 1696 method [125].

1697 **8.1 Simulation samples**

1698 We discussed the collision data sample provided by the LHC for the analysis in this  
 1699 thesis. We analyze a dataset of  $13.3 \text{ fb}^{-1}$  of collision data, at  $\sqrt{s} = 13 \text{ TeV}$ . To select  
 1700 events in data, we use the trigger system as previously discussed, and use the lowest  
 1701 unprescaled trigger which is available for a particular Standard Model background.  
 1702 We now discuss the simulation samples used for this search.

1703 Simulated data is fundamentally important to the ATLAS physics program.  
 1704 Calibrations, measurements, and searches use Monte Carlo (MC) simulations to  
 1705 compare with collision data. In this thesis, MC samples are used to optimize the  
 1706 signal region selections, assist in background estimation, and assess the sensitivity to  
 1707 specific SUSY signal models. The details of Monte Carlo production, accuracy, and

1708 utility are far beyond the scope of this thesis, but we provide a short description here.

1709 The first step is MC *generation*. A program is run which does a matrix-element  
1710 calculation which produces a set of outgoing particles from the parton interactions.  
1711 The output particles are *interfaced* [126] with the parton decays, showering, and  
1712 hadronization processes. This can be done by the same program or another tool  
1713 altogether. This produces a set of *truth* particles with their corresponding kinematics.

Physics process	Generator	Alternative generator	Cross-section normalization	PDF set	Parton shower	Tune
$W(\rightarrow \ell\nu) + \text{jets}$	SHERPA 2.2.0	MADGRAPH	NNLO	NNPDF3.0NNLO	SHERPA	SHERPA default
$Z/\gamma^*(\rightarrow \ell\bar{\ell}) + \text{jets}$	SHERPA 2.2.0	MADGRAPH	NNLO	NNPDF3.0NNLO	SHERPA	SHERPA default
$\gamma + \text{jets}$	SHERPA 2.1.1	-	LO	CT10	SHERPA	SHERPA default
$t\bar{t}$	Powheg-Box v2	Mc@NLO	NNLO+NNLL	CT10	PYTHIA 6.428	PERUGIA2012
Single top ( $Wt$ -channel)	Powheg-Box v2	Mc@NLO	NNLO+NNLL	CT10	PYTHIA 6.428	PERUGIA2012
Single top ( $s$ -channel)	Powheg-Box v2	Mc@NLO	NLO	CT10	PYTHIA 6.428	PERUGIA2012
Single top ( $t$ -channel)	Powheg-Box v1	Mc@NLO	NLO	CT10f4	PYTHIA 6.428	PERUGIA2012
$t\bar{t} + W/Z/WW$	MG5_aMC@NLO 2.2.3	-	NLO	NNPDF2.3LO	PYTHIA 8.186	A14
$WW, WZ, ZZ$	SHERPA 2.1.1	-	NLO	CT10	SHERPA	SHERPA default
Multijet	PYTHIA 8.186	-	LO	NNPDF2.3LO	PYTHIA 8.186	A14

Table 8.1: The Standard Model background Monte Carlo simulation samples used in this thesis. The generators, the order in  $\alpha_s$  of cross-section calculations used for yield normalization, PDF sets, parton showers and tunes used for the underlying event are shown. Alternative generators are only used for the major backgrounds.

1714 For each major background, we employ a baseline sample and alternative sample,  
1715 which we will use later to derive uncertainties on the theoretical cross-sections. The  
1716 choice of generators for each background is itself a quite broad topic, which we avoid  
1717 discussing here. A summary of the generators used is shown in tab. 8.1. In this thesis,  
1718 we will use SHERPA [127] to generate boson events:  $Z \rightarrow \ell\ell$ ,  $W \rightarrow \ell\nu$ , diboson, and  
1719 photon events. These are interfaced with the SHERPA’s parton showering model  
1720 [128]. The alternative samples for  $Z \rightarrow \ell\ell$  and  $W \rightarrow \ell\nu$  decays are generated  
1721 with MADGRAPH [129] interfaced with PYTHIA8 [130]. Single top and  $t\bar{t}$  events are  
1722 generated with POWHEGBox [131] interfaced with itself and the alternative samples  
1723 are generated with Mc@NLO [132] interfaced with HERWIG++ [133] QCD events  
1724 are generated with PYTHIA8 [130]. Events with  $t\bar{t}$  in association with a gauge boson  
1725 are generated in MG5\_aMC@NLO 2.2.3 [132] interfaced with PYTHIA8 [130].

1726 After generation of the truth level particles using the various generators interfaced

1727 with their parton showering models, we perform *simulation*. The detector response  
1728 to the truth particles is simulated, and simulated hits are produced. This procedure  
1729 ensures “as close as possible” treatment of simulation and collision data. In ATLAS,  
1730 this is done using the GEANT4 toolkit [134]. This toolkit outputs simulated detector  
1731 signals, on which we run the exact same reconstruction algorithms as described in  
1732 the previous chapters. This allows us to produce output simulation datasets for each  
1733 of the backgrounds in the analysis.

## 1734 8.2 Event selection

1735 This section describes the selection of the signal region events. We begin by describing  
1736 the *preselection*, which is used to remove problematic events and reduce the dataset  
1737 to a manageable size. We then describe the signal region strategy, and present the  
1738 signal regions used in the analysis.

### 1739 Preselection

1740 The preselection is used to reduce the dataset to that of interest in this thesis. The  
1741 preselection cuts are shown in Tab. 8.2. This selection is also used for the samples  
1742 used for background estimation, except for the lepton veto.

1743 The cuts [1] and [4] are a set of cleaning cuts to remove problematic events.  
1744 The *Good Runs List* is a centrally-maintained list of data runs which have been  
1745 determined to be “good for physics”. This determination is made by analysis of the  
1746 various subdetectors, and monitoring of their status. Event cleaning is used to veto  
1747 events which could be affected by noncollision background, noise bursts, or cosmic  
1748 rays.

1749 We require the lowest unprescaled  $E_T^{\text{miss}}$  trigger for the data run of interest, as  
1750 described previously, in cut [2]. The lepton veto is applied in cut [5]. These two cuts

1751 are only used for the signal region selection.

1752 The rest of the preselection is used for the signal region and control regions used  
1753 for background estimation. These cuts on scaleful variables used by previous searches  
1754 are mostly used for the reduction of the dataset to a manageable size. Signal models  
1755 with sensitivity to lower values of these scaleful variables have been ruled out by  
1756 previous searches [135]. The final cut is on  $m_{\text{eff}}$ , which is the scalar sum of all jets  
1757 and  $E_T^{\text{miss}}$ . This is the final discriminating variable used in the complementary search  
1758 to this thesis, which is also presented in [120].

Cut	Description	
1	Good Runs List	Veto events with intolerable detector errors
2	Trigger	HLT_xe70 (2015), HLT_xe80_tclcw_L1XE50, or HLT_xe100_mht_L1XE50 (2016)
3	Event cleaning	Veto for noncollision background, noise bursts, and cosmic rays
4	Lepton veto	No leptons with $p_T > 10$ GeV after overlap removal
5	$E_T^{\text{miss}}$ [GeV] >	250
6	$p_T(j_1)$ [GeV] >	200
7	$p_T(j_2)$ [GeV] >	50
8	$m_{\text{eff}}$ [GeV] >	800

Table 8.2: Preselection for the various event topologies used in the analysis.

## 1759 Signal regions

1760 We define a set of signal regions using the RJR variables previously described.  
1761 These signal regions are split into three general categories: squark pair production  
1762 SRs, gluino pair production SRs, and compressed production SRs. Within these  
1763 general SRs, we have a set of signal regions targeting different mass splittings of the  
1764 sparticle and LSP.

1765 A schematic of this strategy is shown in Fig. 8.1. This type of plane is how most  
1766 (*R*-parity conserving) SUSY searches are organized in both ATLAS and CMS. The

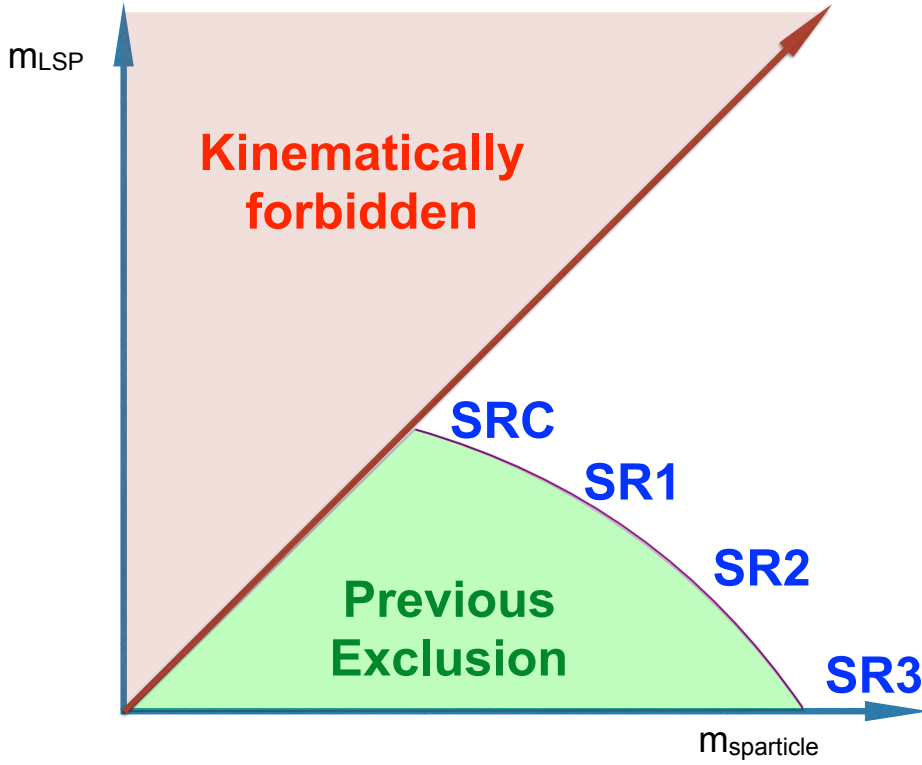


Figure 8.1: Schematic leading the development of the SUSY signal regions in this thesis. A variant of this schematic is used for most SUSY searches on ATLAS and CMS.

1767 horizontal axis is the mass of the sparticle considered. In the case of this thesis,  
 1768 this will be the squark or gluino mass. On the horizontal axis, we place the LSP mass.  
 1769 These are the two free parameters of the simplified models considered here. Our  
 1770 search occurs in this two-parameter space. Each signal region targets some portion  
 1771 of this plane. As shown in the figure, a new iteration of a search will use a set of  
 1772 signal regions which have sensitivity just beyond those of the previous exclusions.  
 1773 The choice of how many signal regions to use to fully cover this plane is in many  
 1774 ways a matter of judgment, as it is important to avoid over or under/over-fitting  
 1775 to the signal models of interest. To take the extreme example, one signal region  
 1776 will obscure the different phenomena in signal events with large versus small mass  
 1777 splittings, leading to underfitting. Binning as finely as possible<sup>1</sup> leads to overfitting  
 1778 due to the fluctuations present in the signal and background events passing the various

1779 selections selection. In this thesis, we use six squark signal regions, six gluino signal  
1780 regions, and five compressed regions.

1781 The full table defining all signal regions is shown in Tab. 8.3. In all cases, the  
1782 signal region selections contain a combination of scaleful and scaleless cuts. Emphasis  
1783 on cuts on scaleful variables provide stronger sensitivity to larger mass splittings,  
1784 while additional sensitivity to smaller mass splittings is found using stronger cuts  
1785 on scaleless variables. One envisions walking from SR1 (with tight scaleless cuts  
1786 and loose scaleful cuts) in Fig. 8.1 towards SR3 by loosening the scaleless cuts and  
1787 tightening the scaleful cuts. We will see this strategy at work in each set of signal  
1788 regions.

1789 We have already described the useful variables in the previous chapter. The  
1790 question is how to choose the optimal cuts for a given set of signal models, which are  
1791 grouped in the mass splitting space. This was done by a brute force scan over the  
1792 cut values, using a guess of integrated luminosity with a fixed systematic uncertainty  
1793 scenario; the value of the systematic uncertainty is motivated by that from previous  
1794 analyses. We choose the lowest cut value that maximizes the  $Z_{Bi}$ , as described in  
1795 [136]. This figure of merit gives conservative estimates, as compared to i.e.  $S/\sqrt{B}$ .  
1796 A figure showing an example of this selection tuning procedure is shown in Fig. 8.2.

1797 The compressed selections are split into five regions (SRC1-5), and due to the  
1798 simplified nature of the compressed decay tree, has sensitivity in both the gluino  
1799 and squark planes. The compressed regions target mass splittings with  $m_{\text{sparticle}} -$   
1800  $m_{\text{LSP}} \tilde{<} 200$  GeV. For the compressed region,  $M_{T,S}$  is the primary scaleful variable.  
1801 We can see the general strategy of lowering increasing scale cuts while decreasing the  
1802 scaleless cuts here. SRC1 targets the most compressed scenarios, with mass splittings  
1803 of less than 25 GeV, and has the loosest  $M_{T,S}$  cut coupled with the tightest  $R_{\text{ISR}}$  and

---

<sup>1</sup>This can be defined as having a signal region for each simulated signal sample, which for this analysis is  $\sim 100$ .

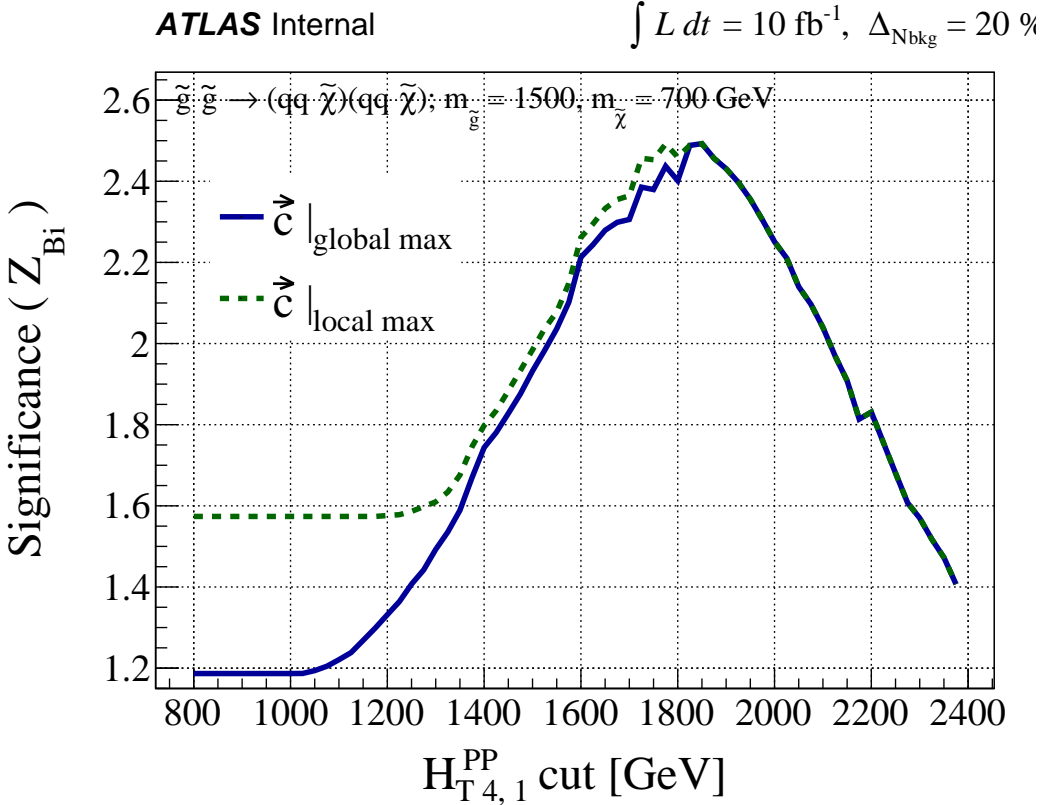


Figure 8.2: Optimization of the  $H_{T,4,1}^{PP}$  cut for a gluino signal model with  $(m_{\tilde{g}}, m_{\tilde{\chi}_1^0}) = (1500, 700)$  GeV assuming  $10 \text{ fb}^{-1}$  and an uncertainty of 20% on the background estimate.

1804      $\Delta\phi_{ISR,I}$  cuts. SRC4 and SRC5 target mass splittings of  $\sim 200$  GeV, and are coupled  
 1805     with the loosest scaleless cuts on  $R_{ISR}$  and  $\Delta\phi_{ISR,I}$ . We also note that SRC4 and  
 1806     SRC5 have differing cuts on  $N_{jet}^V$ , since these SRs are closest to the noncompressed  
 1807     regions, and can be seen as the “crossover” where the differences between squark and  
 1808     gluino production begins to become manifest.

1809     The squark regions (for noncompressed spectra) are organized into six signal  
 1810     regions. These are labeled by a numeral 1-3 and letter a/b. SRs sharing a common  
 1811     numeral i.e. SRS1a and SRS1b share a common set of scaleless cuts, while differing in  
 1812     the main scale variable  $H_{T,2,1}^{PP}$ . The two SRs for each set of scaleless cuts, only differing  
 1813     in the main scale variable, can be seen in a naïve way as providing sensitivity to a

1814 range of luminosity scenarios<sup>2</sup>. As before, we see that the scaleless cuts are loosened  
1815 as we tighten the scaleful cuts, as we move across the table from SRS1a to SRS3b.  
1816 This provides strong sensitivity to signal models with intermediate mass splittings with  
1817 SRS1a to large mass splittings with SR3b.

1818 The gluino signal regions are organized entirely analogously to the squark signal  
1819 regions. There are six gluino signal regions, again labeled via a numeral 1-3 and letter  
1820 a/b. Those SRs sharing a common numeral have a common set of scaleless cuts, but  
1821 differ in their main scale variable  $H_{T,4,1}^{PP}$ . The SRs follow scaleless vs scaleful strategy,  
1822 with SRG1 having the loosest scaleful cut cuts coupled with the strongest scaleless  
1823 cuts, and the converse being true in SRG3. As in the squark case, this strategy  
1824 provides strong expected sensitivity throughout the gluino-LSP plane.

---

<sup>2</sup>These SRs were defined before the entire collision dataset was produced, and thus needed to be robust in cases where the LHC provided significantly different than expected performance.

Targeted signal	$\tilde{s}\tilde{s}, \tilde{s} \rightarrow q\tilde{\chi}_1^0$									
Requirement	Signal Region									
	<b>RJR-S1</b>		<b>RJR-S2</b>		<b>RJR-S3</b>					
$H_{1,1}^{PP}/H_{2,1}^{PP} \geq$	0.6		0.55		0.5					
$H_{1,1}^{PP}/H_{2,1}^{PP} \leq$	0.95		0.96		0.98					
$p_{PP, z}/(p_{PP, z}^{lab} + H_{T, 2,1}^{PP}) \leq$	0.5		0.55		0.6					
$p_{j2, T}^{PP}/H_{T, 2,1}^{PP} \geq$	0.16		0.15		0.13					
$\Delta_{QCD} >$	0.001									
	<b>RJR-S1a</b>	<b>RJR-S1b</b>	<b>RJR-S2a</b>	<b>RJR-S2b</b>	<b>RJR-S3a</b>	<b>RJR-S3b</b>				
$H_{T, 2,1}^{PP}$ [GeV] >	1000	1200	1400	1600	1800	2000				
$H_{1,1}^{PP}$ [GeV] >	1000		1400		1600					
Targeted signal	$\tilde{g}\tilde{g}, \tilde{g} \rightarrow q\bar{q}\tilde{\chi}_1^0$									
Requirement	Signal Region									
	<b>RJR-G1</b>		<b>RJR-G2</b>		<b>RJR-G3</b>					
$H_{1,1}^{PP}/H_{4,1}^{PP} \geq$	0.35		0.25		0.2					
$H_{T, 4,1}^{PP}/H_{4,1}^{PP} \geq$	0.8		0.75		0.65					
$p_{PP, z}/(p_{PP, z}^{lab} + H_{T, 4,1}^{PP}) \leq$	0.5		0.55		0.6					
$\min(p_{j2, T, i}^{PP}/H_{T, 2,1}^{PP}) \geq$	0.12		0.1		0.08					
$\max(H_{1,0}^{Pi}/H_{2,0}^{Pi}) \leq$	0.95		0.97		0.98					
$  \frac{2}{3}\Delta\phi_{V,P}^{PP} - \frac{1}{3}\cos\theta_p   \leq$	0.5		—		—					
$\Delta_{QCD} >$	0									
	<b>RJR-G1a</b>	<b>RJR-G1b</b>	<b>RJR-G2a</b>	<b>RJR-G2b</b>	<b>RJR-G3a</b>	<b>RJR-G3b</b>				
$H_{T, 4,1}^{PP}$ [GeV] >	1000	1200	1500	1900	2300	2700				
$H_{1,1}^{PP}$ [GeV] >	600		800		900					
Targeted signal	compressed spectra in $\tilde{s}\tilde{s}$ ( $\tilde{s} \rightarrow q\tilde{\chi}_1^0$ ); $\tilde{g}\tilde{g}$ ( $\tilde{g} \rightarrow q\bar{q}\tilde{\chi}_1^0$ )									
Requirement	Signal Region									
	<b>RJR-C1</b>	<b>RJR-C2<sub>129</sub></b>	<b>RJR-C3</b>	<b>RJR-C4</b>	<b>RJR-C5</b>					
$R_{ISR} \geq$	0.9	0.85	0.8	0.75	0.70					
$\Delta\phi_{ISR, I} >$	3.1	3.07	2.95	2.95	2.95					

Targeted signal	compressed spectra in $\tilde{s}\tilde{s}$ ( $\tilde{s} \rightarrow q\tilde{\chi}_1^0$ ); $\tilde{g}\tilde{g}$ ( $\tilde{g} \rightarrow q\bar{q}\tilde{\chi}_1^0$ )				
Requirement	Signal Region				
	<b>RJR-C1</b>	<b>RJR-C2<sub>129</sub></b>	<b>RJR-C3</b>	<b>RJR-C4</b>	<b>RJR-C5</b>
$R_{ISR} \geq$	0.9	0.85	0.8	0.75	0.70
$\Delta\phi_{ISR, I} >$	3.1	3.07	2.95	2.95	2.95

## 8.3 Background estimation

We describe here the method of background estimation. In this thesis, we detail what is colloquially called a “cut-and-count” analysis. This is in contrast to a “shape fit” analysis, where one needs to consider the details of the variable distribution shapes. Instead, we must ensure the overall normalization of the Standard Model backgrounds are correct in the regions of phase space considered in the analysis. In order to do this, we define a set of *control regions* which are free of SUSY contamination based on the previously excluded analysis. We compare the number of events present in the control regions in simulation with that in data to define a *transfer factor* (TF). We extrapolate the number of expected events from each background using this transfer factor to translate from the , which provides our final estimate of the SM background in the corresponding signal region. To be explicit, each signal region SR has a corresponding set of control regions.

More precisely, for a given signal region, we are attempting to estimate the value  $N_{\text{SR}}^{\text{data}}$  for a given background. This value is estimated using the following equation:

$$N_{\text{SR}}^{\text{data,est}} = N_{\text{CR}}^{\text{data,obs}} \times \text{TF}_{\text{CR}} \equiv N_{\text{CR}}^{\text{data,obs}} \times \left( \frac{N_{\text{SR}}^{\text{MC}}}{N_{\text{CR}}^{\text{MC}}} \right) \quad (8.1)$$

where the transfer factor TF is taken directly from MC. The two ingredients to our estimation of  $N_{\text{SR}}^{\text{data,obs}}$  is thus  $N_{\text{CR}}^{\text{data,obs}}$  and the transfer factor taken from MC.

The transfer factor method is potentially more straightforward written in the following way:

$$N_{\text{SR}}^{\text{data,est}} = N_{\text{SR}}^{\text{MC}} \times \left( \frac{N_{\text{CR}}^{\text{data,obs}}}{N_{\text{CR}}^{\text{MC}}} \right) \equiv N_{\text{SR}}^{\text{MC}} \times \mu_{\text{CR}}. \quad (8.2)$$

In this form, the correction to the overall normalization is explicit. The ratio  $\frac{N_{\text{CR}}^{\text{data,obs}}}{N_{\text{CR}}^{\text{MC}}}$  which we call  $\mu$  informs us how to scale  $N_{\text{SR}}^{\text{MC}}$  in order to get the right overall normalization. The assumption made with this method is that the overall shape of the distribution should not change “that much” as one extrapolates to the signal region.

1845        The CR definitions are motivated and designed according to two (generally  
1846 competing) requirements:

- 1847        1. Statistical uncertainties due to low CR statistics  
1848        2. Systematic uncertainties related to the extrapolation from the CR to the SR.

1849        This motivates the desire to make the control regions as similar as possible  
1850        to the signal regions without risking signal contamination while ensuring high  
1851        purity in the targeted SM background.

1852        In principle, one can also apply data-driven corrections to the TF obtained for each  
1853        CR.

1854        In order to validate the transfer factors obtained from MC, we also develop a series  
1855        of *validation regions* (VRs). These regions are generally designed to be “in between”  
1856        the control region and signal region selections in phase space, and thus provide a  
1857        check on the extrapolation from the control regions into the signal regions. Despite  
1858        their closeness in phase space to the signal regions, they are also designed to have  
1859        low signal contamination.

1860        In practice, we perform this estimation procedure simultaneously across all  
1861        control regions; we describe this later. We only note this here since we can also  
1862        apply Eq.Eq. (8.1) to measure the contamination of a control region with another  
1863        background as well. This procedure accounts for the correlations between regions due  
1864        to correlated systematic uncertainties. We next describe the control region selection  
1865        for the major SM backgrounds for the analysis.

## 1866        **Control Regions**

1867        The primary backgrounds of note in this analysis are  $Z + \text{jets}$ ,  $W + \text{jets}$ ,  $t\bar{t}$ , and QCD  
1868        events. There is also a minor background from diboson events which is taken directly  
1869        from MC with an uncertainty of 50%. We describe the strategy to estimate these

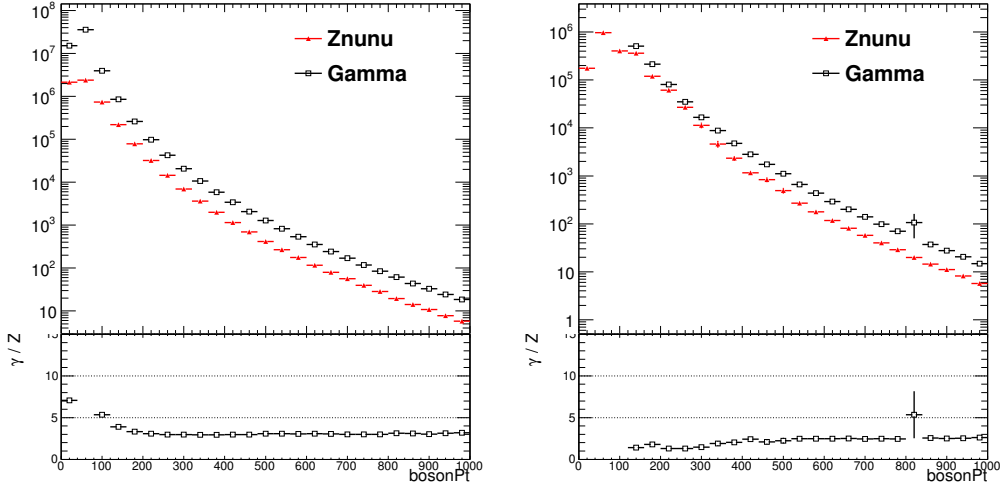
1870 various backgrounds here. A summary table is shown in Tab. 8.4. All distributions  
 1871 shown in this section use the scaling factors  $\mu$  from the background fits, which we  
 1872 describe later.

CR	SM background	CR process	CR event selection
Meff/RJR-CR $\gamma$	$Z(\rightarrow \nu\bar{\nu}) + \text{jets}$	$\gamma + \text{jets}$	Isolated photon
Meff/RJR-CRQ	Multi-jet	Multi-jet	$\Delta_{\text{QCD}} < 0$ reversed requirement on $H_{1,1}^{PP}$ (RJR-S/G) or $R_{\text{ISR}} < 0.5$ (RJR-C)
Meff/RJR-CRW	$W(\rightarrow \ell\nu) + \text{jets}$	$W(\rightarrow \ell\nu) + \text{jets}$	$30 \text{ GeV} < m_T(\ell, E_T^{\text{miss}}) < 100 \text{ GeV}$ , $b$ -veto
Meff/RJR-CRT	$t\bar{t}(\text{+EW})$ and single top	$t\bar{t} \rightarrow b\bar{b}qq'\ell\nu$	$30 \text{ GeV} < m_T(\ell, E_T^{\text{miss}}) < 100 \text{ GeV}$ , $b$ -tag

Table 8.4: Control regions used in this thesis.

1873 Events with a  $Z$  boson decaying to neutrinos in association with jets are the  
 1874 primary irreducible background in the analysis. These events have true  $E_T^{\text{miss}}$  from  
 1875 the decaying neutrinos, and can have significant values of the scaleful variables of  
 1876 interest. Naively, one might expect us to use  $Z \rightarrow \ell\ell$  as the control process of interest,  
 1877 as  $Z \rightarrow \ell\ell$  events are quite well-measured. Unfortunately, the  $Z \rightarrow \ell\ell$  branching ratio  
 1878 is about half of from  $Z \rightarrow \nu\nu$ , which necessitates loosening the control region selection  
 1879 significantly. This leads to unacceptably large systematic uncertainties in the transfer  
 1880 factor.

1881 Instead, photon events are used as the control region for the  $Z \rightarrow \nu\nu$  events. We  
 1882 label this photon control region as CRY. The photon is required to have  $p_T > 150 \text{ GeV}$   
 1883 to ensure the trigger is fully efficient. The kinematic properties of photon events  
 1884 strongly resemble those of  $Z$  events when the boson  $p_T$  is significantly above the  
 1885 mass of the  $Z$  boson. In this regime, the neutral bosons are both scaleless, and can  
 1886 be treated interchangeably, up to the differences in coupling strengths. Additionally,



(a) Boson  $p_T$  ratio as a function of true boson  $p_T$   
(b) Boson  $p_T$  ratio as a function of reconstructed boson  $p_T$

Figure 8.3

the cross-section for  $\gamma + \text{jets}$  events is significantly larger than  $Z + \text{jets}$  events above the  $Z$  mass. These features are shown in Fig. 8.3 in simulated  $Z \rightarrow \nu\nu$  truth and reconstructed events. The reconstructed  $Z \rightarrow \nu\nu$  events define the boson  $p_T$  as simply the  $E_T^{\text{miss}}$ . In truth events, one clearly sees the effect of the  $Z$  mass below  $\sim 100$  GeV, with a flattening of the ratio above  $\sim 300$  GeV. In reconstructed events, the effects are less clear at low boson  $p_T$ , primarily due to cut sculpting from i.e. the trigger requirement on photon events, which necessitates a higher  $p_T$  cut on photon events for the trigger to remain fully efficient. Still, it is clear that the ratio flattens out at high boson  $p_T$ , and we are justified in the use of CRY to model the  $Z + \text{jets}$  background.

The CRY kinematic selection is slightly looser in the scaleful variables for the noncompressed regions to provide sufficient control region statistics. This is chosen to be  $H_{1,1}^{PP} > 900$  GeV ( $H_{1,1}^{PP} > 550$  GeV) for the squark (gluino) regions to minimize the corresponding statistical and systematic uncertainties.

One additional correction scale factor is applied to  $\gamma + \text{jets}$  events before calculating the transfer factors. This is known as the  $\kappa$  method, which is used to determine the disagreement arising from the use of a LO generator for photon events vs. a NLO

1903 generator for  $Z$ +jets events, which can reduce the theoretical uncertainties from  
 1904 this disagreement. One can see this as a measurement of the k-factor for the LO  
 1905  $\gamma$ +jets sample. This is effectively done with an auxiliary CRZ region, defined using  
 1906 two leptons with an invariant mass close with 25 GeV of the Z mass. The correction  
 1907 factor derived for this purpose is  $\kappa = 1.39 \pm 0.05$ .

1908 Distributions of CRY in squark, gluino, and compressed regions are shown in  
 1909 Figs. 8.4 to 8.6. One can see the quite high purity of CRY in photon events from  
 1910 these plots.

Event with a  $W$  boson decaying leptonically via  $W \rightarrow \ell\nu$  can also enter the signal region. In this case, we use leptonically to include all leptons ( $e, \mu, \tau$ ). The  $W$ +jets events passing the event selection either have a hadronically-decaying  $\tau$ , with a neutrino supplying  $E_T^{\text{miss}}$ , or the case where a muon or electron is misidentified as a jet or missed completely due to the limited detector acceptance. To model this background, we use a sample of one-lepton events with a veto on b-jets, which we label CRW. The lepton is required to have  $p_T > 27$  GeV to guarantee a fully efficient trigger. We then treat this single lepton as a jet for purposes of the RJR variable calculations. We apply a kinematic selection on the transverse mass:

$$m_T = \sqrt{2p_{T,\ell}E_T^{\text{miss}}(1 - \cos\phi_e - E_\phi^{\text{miss}})}, \quad (8.3)$$

1911 around the  $W$  mass:  $30 \text{ GeV} < m_T < 100 \text{ GeV}$ . Checks in simulation shows that  
 1912 these requirements give a sample of high purity  $W \rightarrow \ell\nu$  background. Due to low  
 1913 statistics using the kinematic cuts imposed in the signal regions, the control region  
 1914 kinematic cuts are slightly loosened with respect to the signal region cuts. We use  
 1915 the loosest cut in any signal region as the control region selection for all signal  
 1916 regions. More clearly, the control region selection corresponding to each signal region  
 1917 is the *same*. As discussed above, this leads to a tolerable increase in the systematic  
 1918 uncertainty from the extrapolation from the CR to the SR when compared to the  
 1919 resulting statistical uncertainty.

1920      Distributions of CRW in squark, gluino, and compressed regions are shown in  
1921      Figs. 8.7 to 8.9. There is high purity in  $W$ +jets events in the control region  
1922      corresponding to all signal regions.

1923      Top events are also an important background, for the same reasons as the  
1924       $W$ +jets background, due to the dominant top decay channel of  $t \rightarrow Wb$ . For a  
1925      top event to be selected by the analysis criteria, as in the case of  $W$ +jets, we expect  
1926      a  $W$  to decay via a  $\tau$  lepton which decays hadronically or one a muon or electron to  
1927      be misidentified as a jet or be outside the detector acceptance. We are not so worried  
1928      about hadronic or all dileptonic tops: hadronic  $t\bar{t}$  events generally have low  $E_T^{\text{miss}}$   
1929      (and  $H_{1,1}^{PP}$ ) so they will not pass the kinematic cuts, while dileptonic  $t\bar{t}$  events have a  
1930      lower cross-section and good reconstruction efficiency from the two leptons. We are  
1931      thus primarily concerned with semileptonic  $t\bar{t}$  events with  $E_T^{\text{miss}}$  from the neutrino.  
1932      To model this background, we use the same selection as the  $W$  selection, but require  
1933      that one of the jets chosen by the analysis has at least one  $b$ -tag. This selection has  
1934      quite high purity, as we expect the  $t\bar{t}$  background to have two  $b$ -jets. Thus with  
1935      the 70%  $b$ -tagging efficiency working point used in this analysis, ignoring (small)  
1936      correlations between the two  $b$ -tags, we expect to tag one of the  $b$ -jets greater than  
1937      90% of the time. As with CRW, we need to loosen the cuts applied to CRT with  
1938      respect to the signal region in order to gain sufficient expected data statistics. We  
1939      use exactly the same scheme; the CRT corresponding to each SR is identical, due to  
1940      using the loosest set of cuts among the SRs. This comes at the cost of an increased  
1941      systematic uncertainty for this extrapolation, but it was determined that this tradeoff  
1942      resulted in the lowest overall uncertainty.

1943      Distributions of CRT in squark, gluino, and compressed regions are shown  
1944      in Figs. 8.10 to 8.12. There is high purity in top events in the control region  
1945      corresponding to all signal regions.

1946      The final important background is the QCD background. As briefly discussed in

1947 the previous chapter, QCD backgrounds are difficult, for a few reasons we describe  
1948 here. The large cross-section for QCD events means that even very rare extreme  
1949 mismeasurements can be seen in our signal regions. However, as these events are  
1950 very rare, one requires extreme confidence in the tails of the distributions to use  
1951 simulation as an input for background estimation. To avoid this, the strategy in  
1952 these cases is to apply a strong enough cut to expect *zero* QCD events in the signal  
1953 regions to avoid this issue. To produce a sample enriched in QCD, which we call CRQ,  
1954 we reverse the  $\Delta_{\text{QCD}}$  and  $H_{1,1}^{PP}$  cuts. This analysis uses the jet smearing method, as  
1955 described in [137]. This is a data-driven method which applies a resolution function  
1956 to well-measured QCD events, which also an estimate of the impact of the jet energy  
1957 mismeasurement on  $E_{\text{T}}^{\text{miss}}$  and subsequently the RJR variables.

1958 Distributions of CRQ in squark, gluino, and compressed regions are shown  
1959 in Figs. 8.13 to 8.15. There is high purity in top events in the control region  
1960 corresponding to all signal regions.

1961 The final background of note in this background is the diboson background. This  
1962 background is estimated directly from simulation. Due to the low cross-section of  
1963 electroweak processes, this background is not significant in the signal regions. We  
1964 assign a large ad-hoc 50% systematic on the cross-section, and do not attempt to  
1965 define a control region for this background.

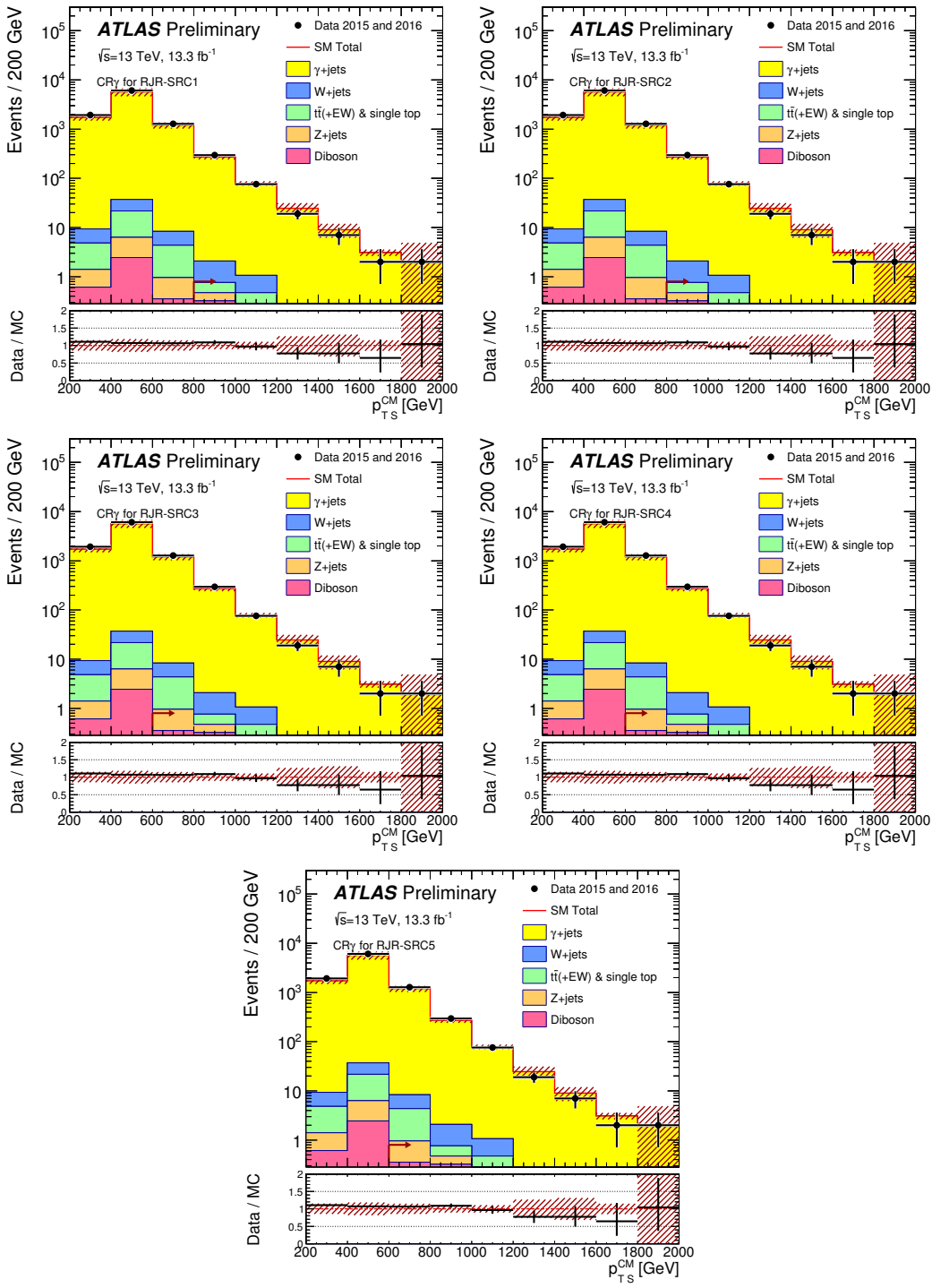


Figure 8.4: Scale variable distributions for the compressed CRY regions.

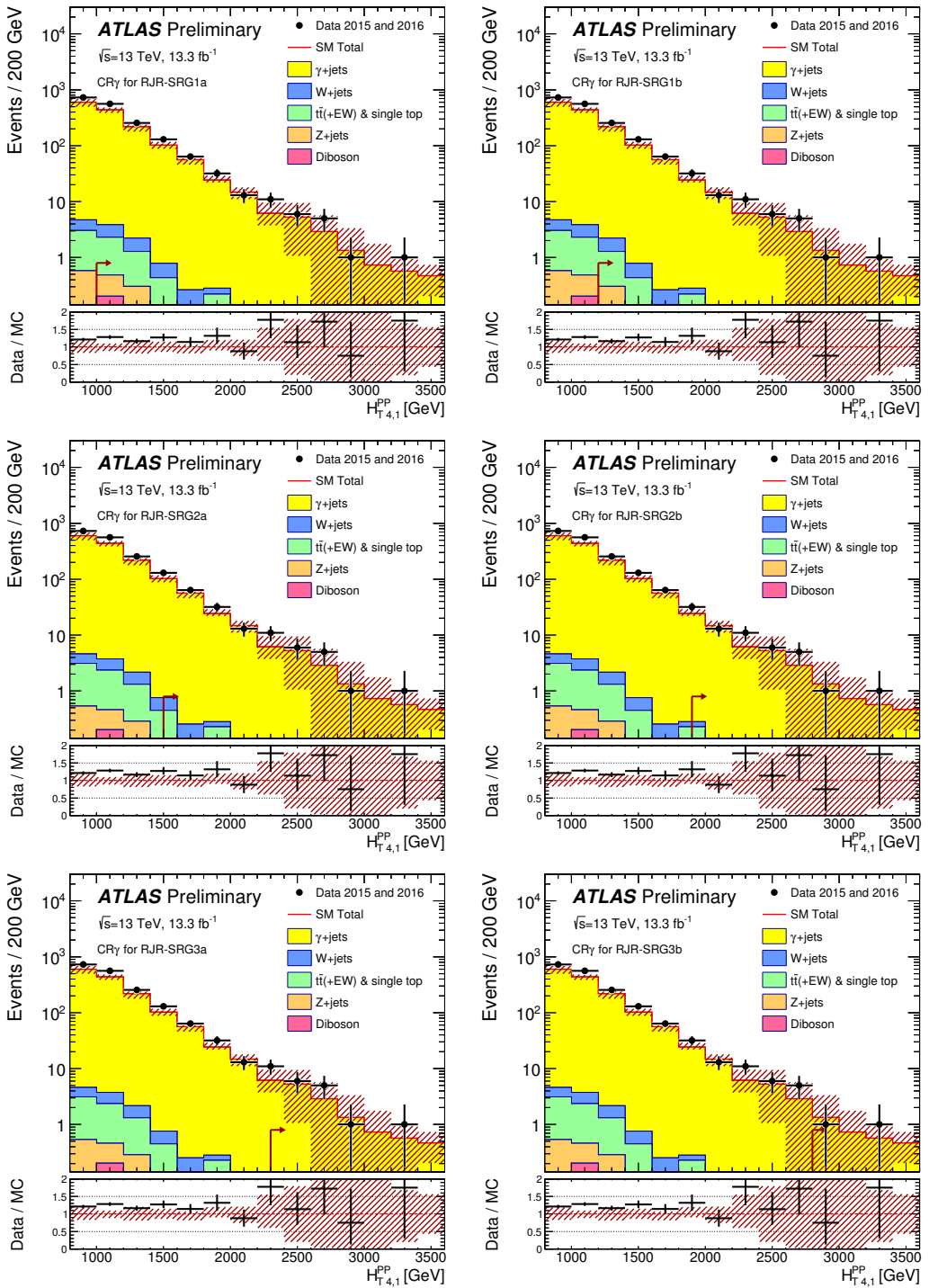


Figure 8.5: Scale variable distributions for the gluino CRY regions.

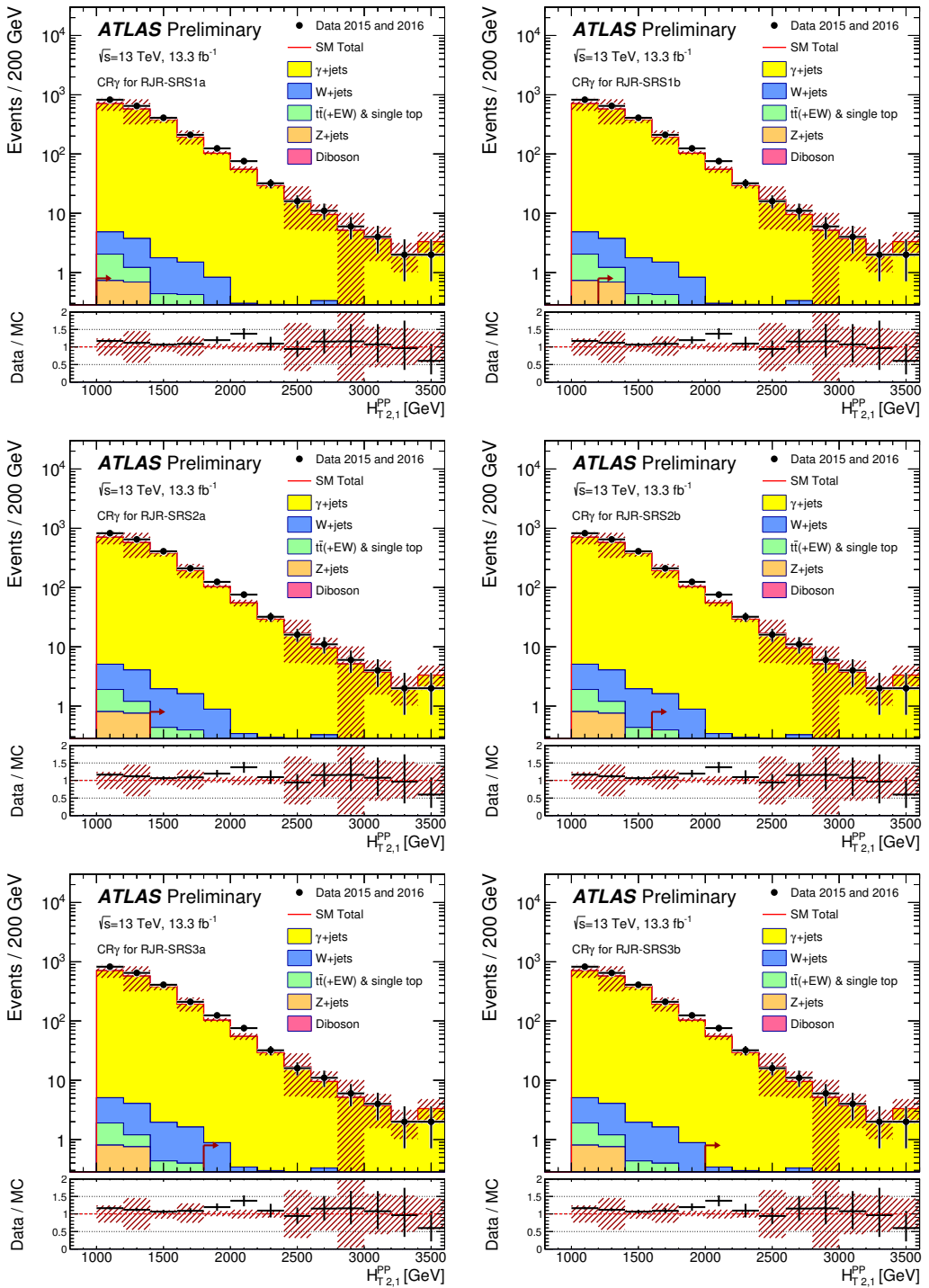


Figure 8.6: Scale variable distributions for the squark CRY regions.

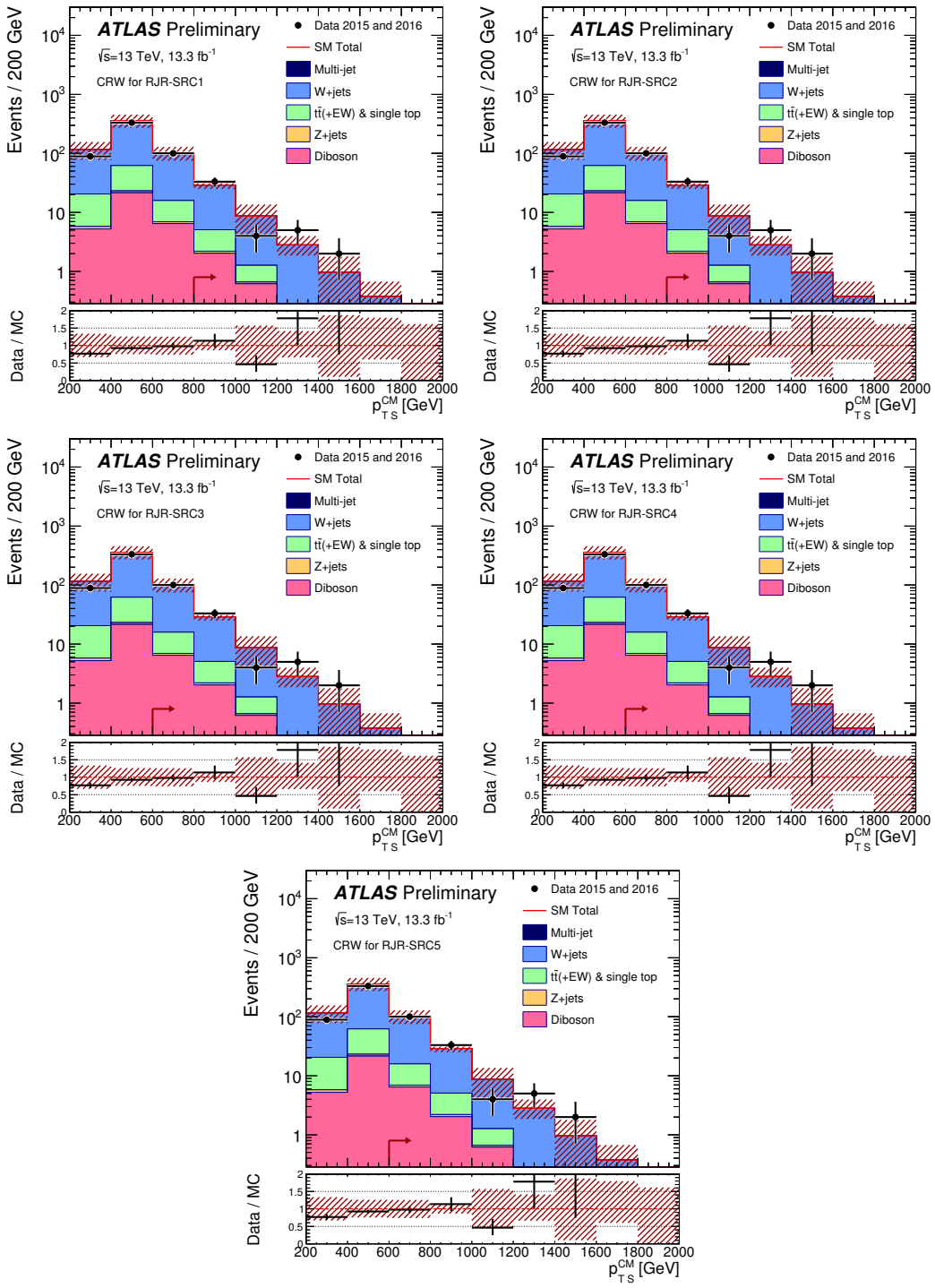


Figure 8.7: Scale variable distributions for the compressed CRW regions.

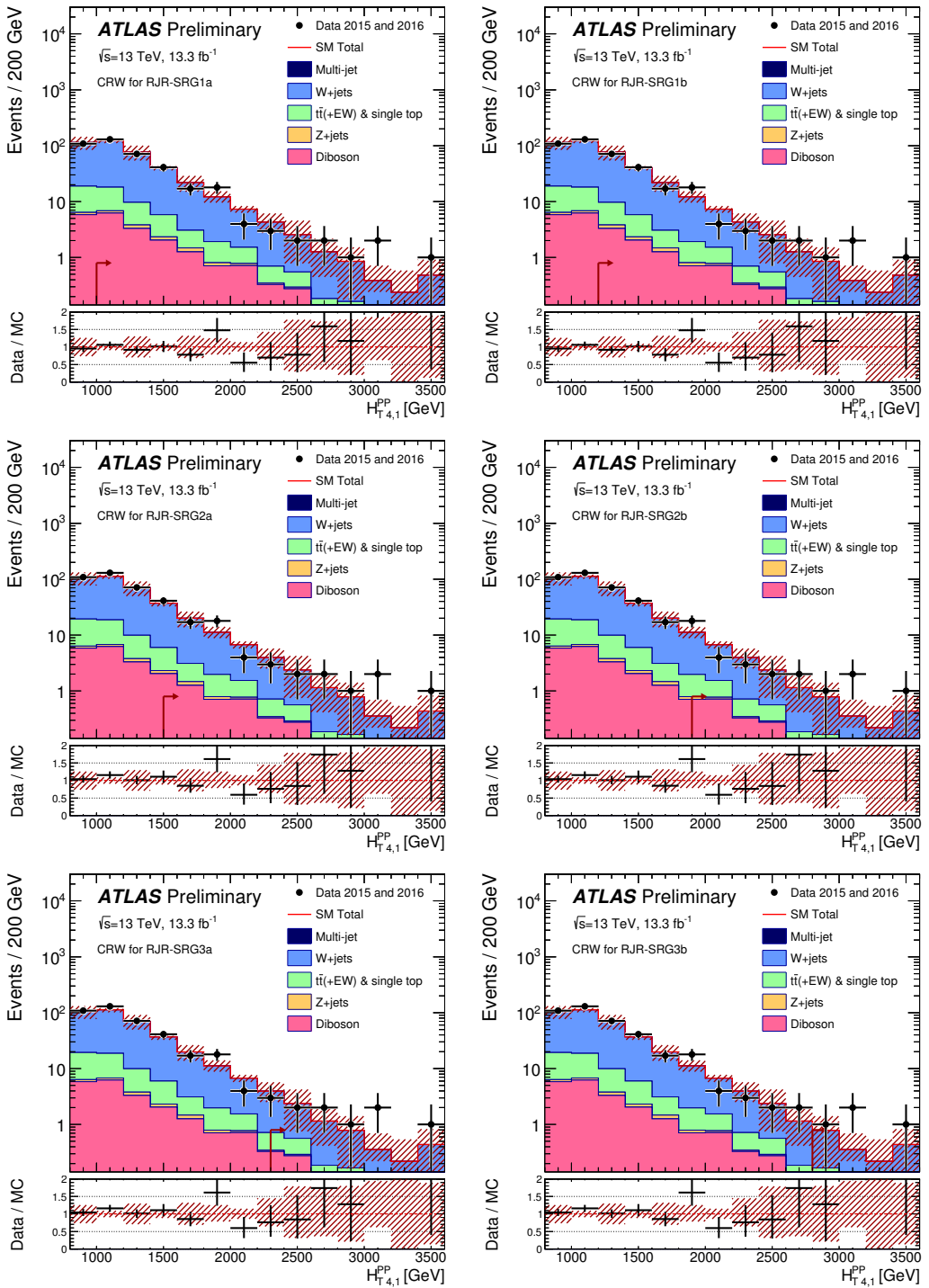


Figure 8.8: Scale variable distributions for the gluino CRW regions.

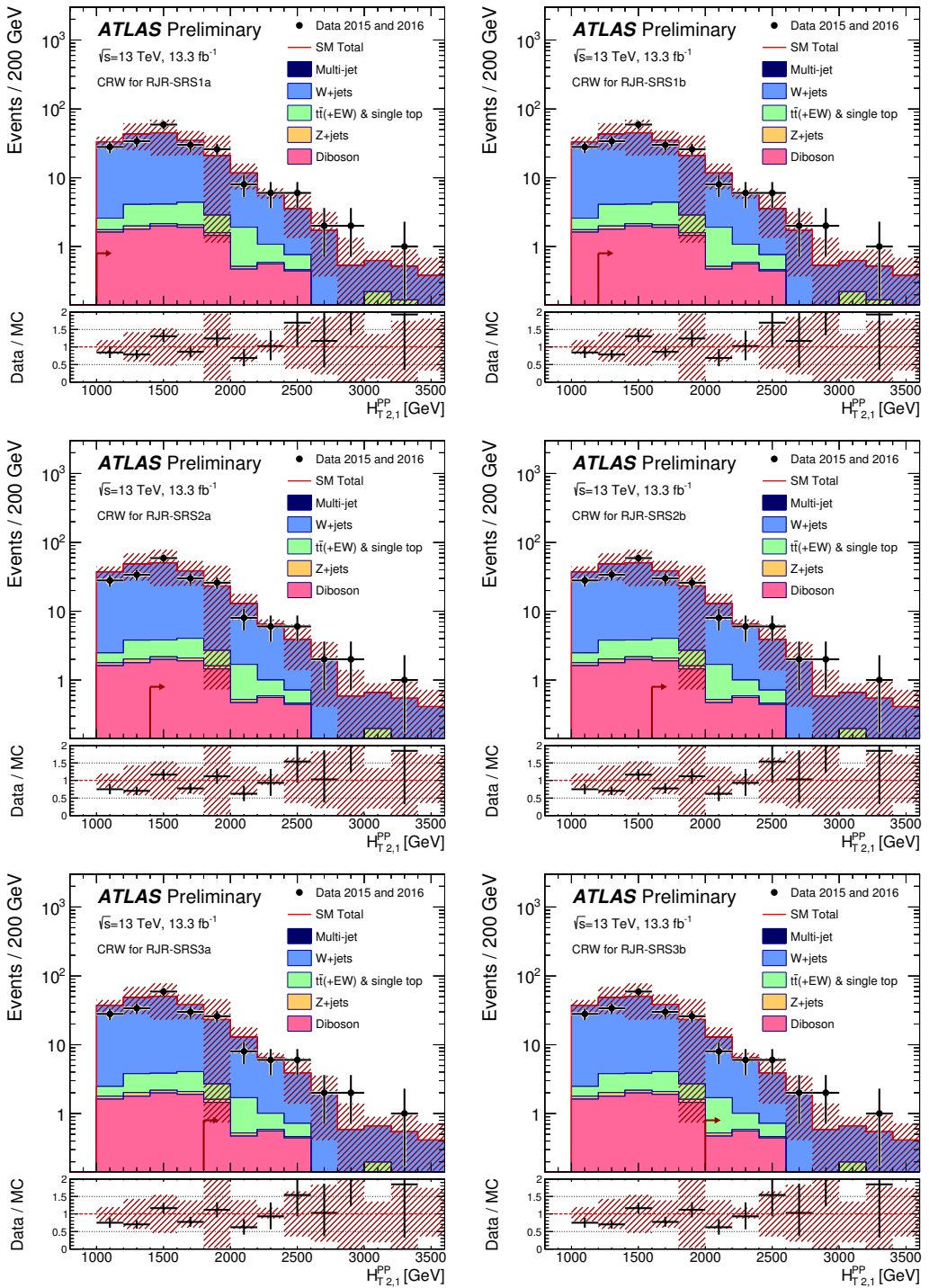


Figure 8.9: Scale variable distributions for the squark CRW regions.

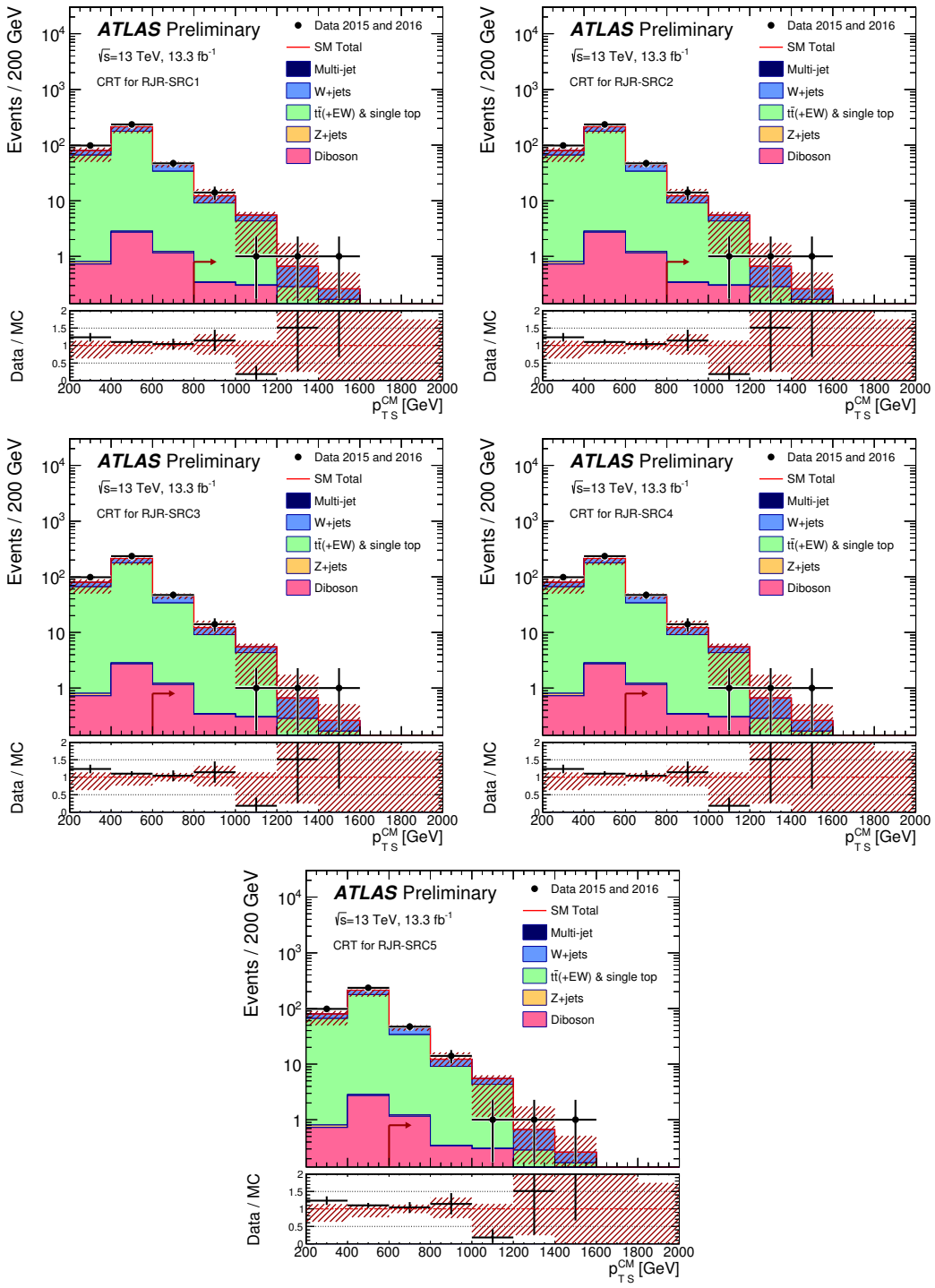


Figure 8.10: Scale variable distributions for the compressed CRT regions.

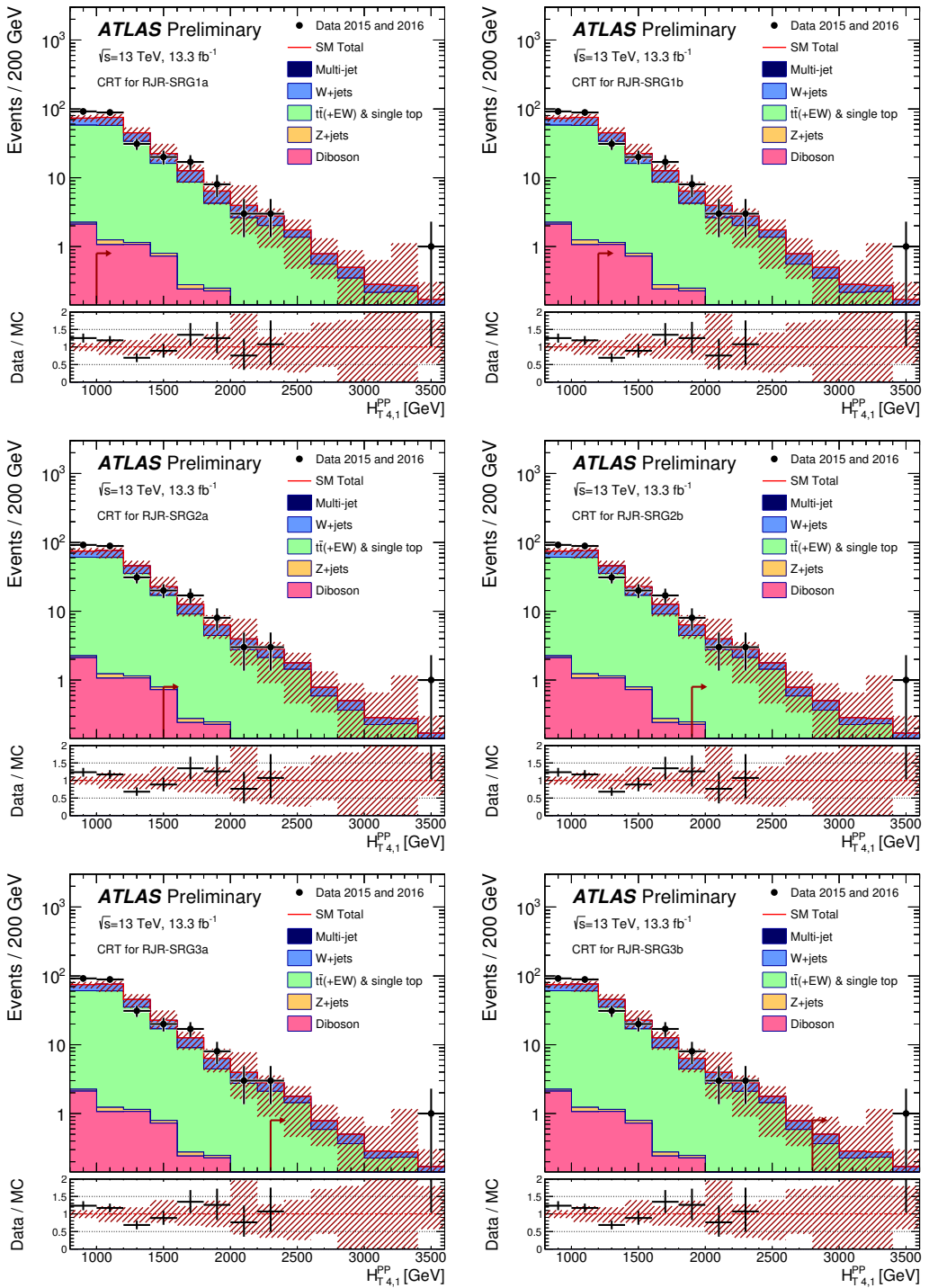


Figure 8.11: Scale variable distributions for the gluino CRT regions.

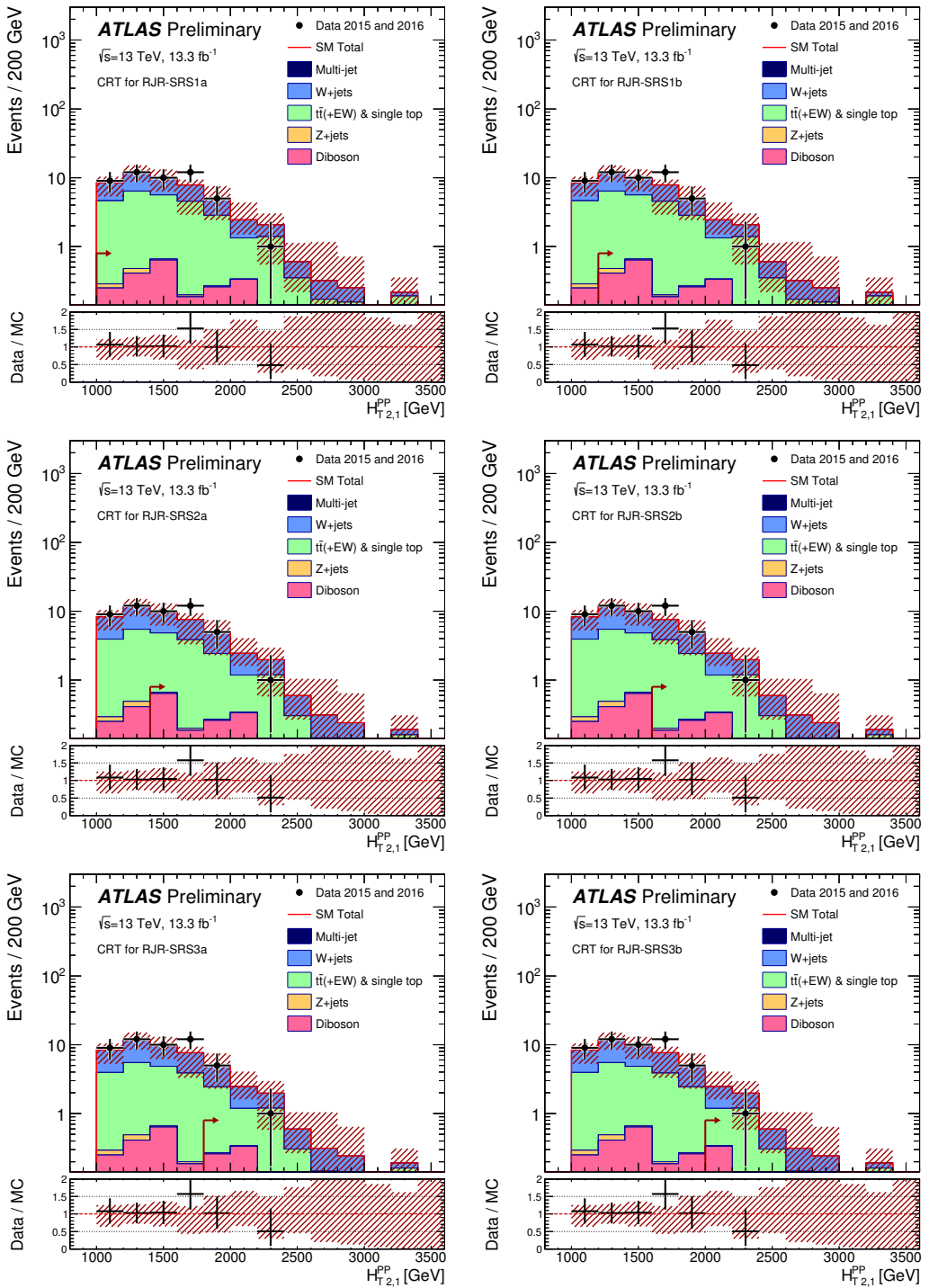


Figure 8.12: Scale variable distributions for the squark CRT regions.

1966 **Validation Regions**

1967 As discussed in general terms above, we define a set of validation regions to ensure  
1968 we can properly model the particular backgrounds as we move closer to the SRs in  
1969 phase space. We define at least one validation region for each major background.

1970 For the most important background  $Z \rightarrow \nu\nu$ , we use a series of validation regions.  
1971 The primary validation region, which we label as VRZ, is defined by selecting lepton  
1972 pairs of opposite sign and identical flavor which lie within  $\pm 25\text{ GeV}$  of the Z boson mass.  
1973 This selection has high purity for  $Z \rightarrow \ell\ell$  events as seen in simulation. We treat the  
1974 two leptons as contributions to the  $E_T^{\text{miss}}$  (as we did with the photon in CRY). This  
1975 selection uses the same kinematic cuts as the signal region. We also define two VRs  
1976 using the same event selection but looser kinematic cuts, which we label VRZa and  
1977 VRZb. VRZa has a loosened selection on  $H_{1,1}^{PP}$ , again to the loosest value among the  
1978 signal regions, as was done for CRW and CRt. VRZa has a loosened selection on  
1979 the primary scaleful variable ( $H_{T,2,1}^{PP}$  or  $H_{T,4,1}^{PP}$ ), again to the loosest value among the  
1980 signal regions, as was done for CRW and CRT. These two validation regions allow us  
1981 to test the modeling of each of these variables individually, as well as allowing more  
1982 validation region statistics in the signal regions with tighter cuts on these variables.

1983 For the compressed regions, these  $Z$  validation region were found lacking. The  
1984 leptons are highly boosted in the compressed case, and the lepton acceptance was  
1985 quite low due to lepton isolation requirements in  $\Delta R$ . Instead, two fully hadronic  
1986 validation region were developed for the compressed regions. The first, VRZc has  
1987 identical requirements to the signal regions with an inverted requirement on  $\Delta\phi_{ISR,I}$ .  
1988 From simulation, this region was found to be at least 50% pure in  $Z$  events, which  
1989 was considered enough to validate this background in this extreme portion of phase  
1990 space. For additional validation region statistics, we also developed VRZca, which  
1991 takes again uses the loosest set of cuts from each signal region. Note this means that  
1992 each compressed signal region has an identical VRZca.

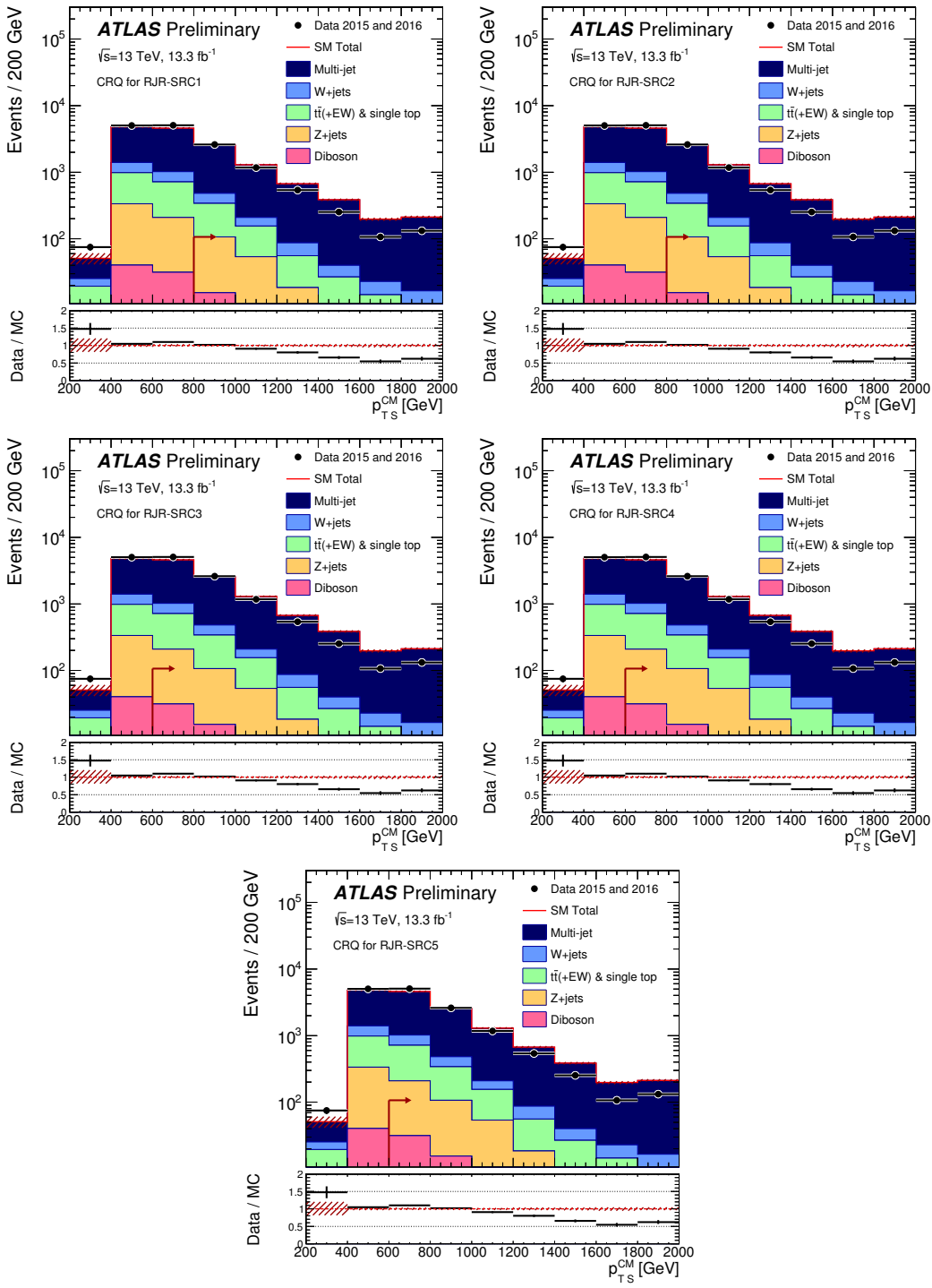


Figure 8.13: Scale variable distributions for the compressed CRQ regions.

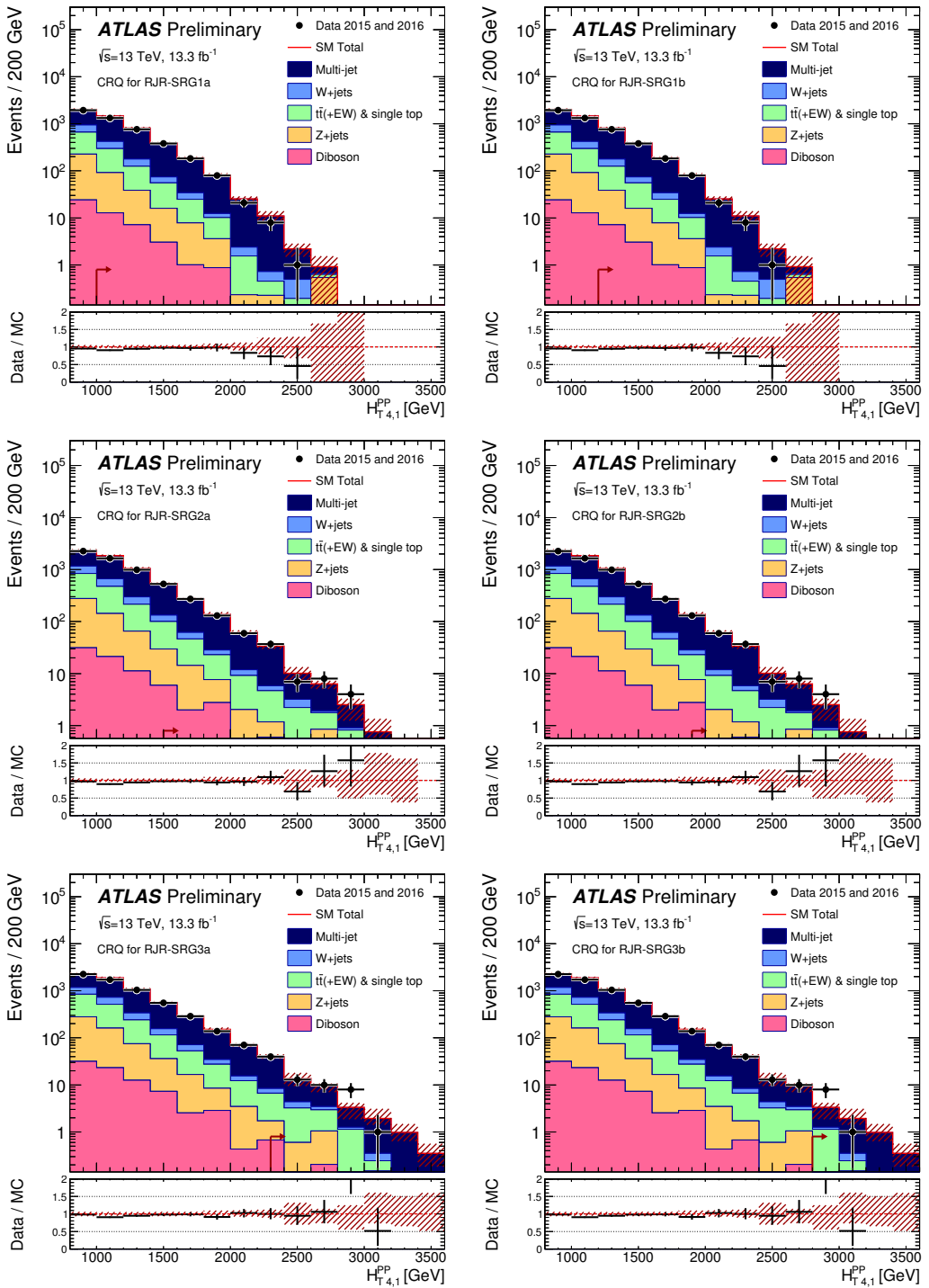


Figure 8.14: Scale variable distributions for the gluino CRQ regions.

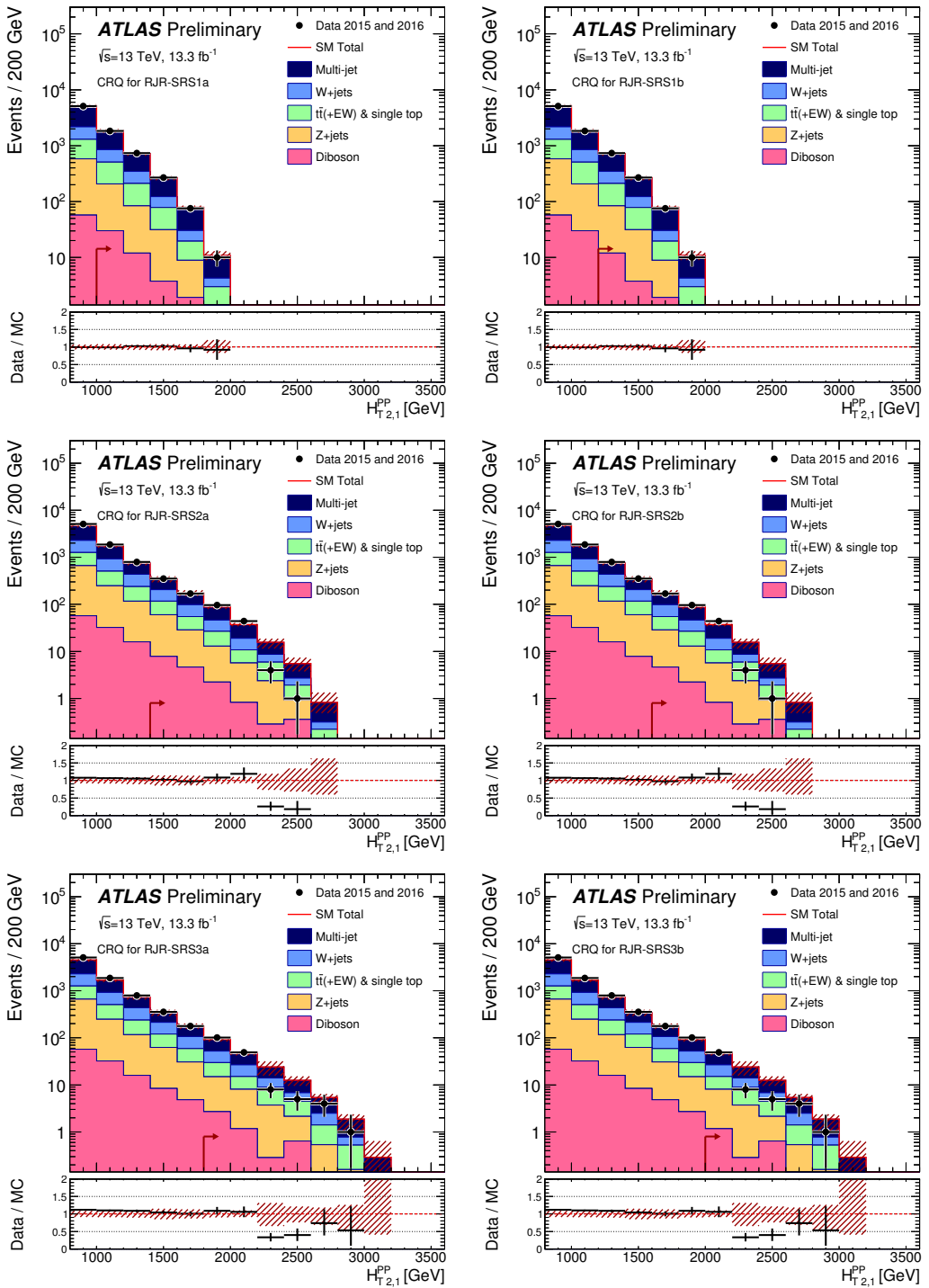


Figure 8.15: Scale variable distributions for the squark CRQ regions.

1993      The top and  $W$  validation regions use the same event selection as the correspond-  
 1994      ing control regions, as described above. However, unlike the control regions, these  
 1995      validation regions reimpose the SR scaleful variable selections, to be closer in phase  
 1996      space to the hadronic signal regions. In the same way as we did for VRZa and  
 1997      VRZb, we also define auxiliary VRs which loosen the cuts on the scale variables. We  
 1998      define VRTa (VRWa) as VRT (VRW) with the same loosened cut on  $H_{1,1}^{PP}$  and VRTb  
 1999      (VRWb) as VRT (VRW) with the same loosened cut on the primary scale variable.

2000      The final set of validation regions are those defined to check the estimation of  
 2001      the QCD background. VRQ is defined to be identical to the corresponding CRQ,  
 2002      but again we use the full SR region cuts for the scaleful variables. This selection is  
 2003      then closer to the corresponding signal region to validate the CRQ estimate. We also  
 2004      define the auxiliary validation regions VRQa and VRQb for the noncompressed signal  
 2005      regions. In this case, we reimpose one of the two inverted cuts in CRQ with respect  
 2006      to the signal regions, to make each one even closer to the SRs. In CRQa (CRQb), we  
 2007      reimpose the  $H_{1,1}^{PP}$  ( $\Delta_{\text{QCD}}$ ).

2008      For the compressed case, we again define a separate validation region, due to  
 2009      the special kinematics probed. We construct a validation region which is the same as  
 2010      CRQ, with  $.5 < R_{\text{ISR}} < R_{\text{ISR, SR}}$ , where  $R_{\text{ISR, SR}}$  is the cut on  $R_{\text{ISR}}$  in the corresponding  
 2011      SR. Again, this can be seen as probing “in between” the CR and SR in phase space.

The results of this validation can be seen in Fig. 8.16. Each bin is *pull* of the  
 validation region corresponding to a particular signal region. This is defined

$$\text{Pull} = \frac{N_{\text{obs}} - N_{\text{pred}}}{\sigma_{\text{tot}}} \quad (8.4)$$

2012      where  $\sigma_{\text{tot}}$  is the total uncertainty folding in all systematic uncertainties, which we  
 2013      will describe later. Assuming we have well-measured our backgrounds, we expect a  
 2014      Gaussian distribution of the pulls around 0, with a standard deviation of 1, as this  
 2015      is measuring the number of standard deviations around the mean. We can see there  
 2016      are few positive pulls (indicating an underestimation of the background), indicating

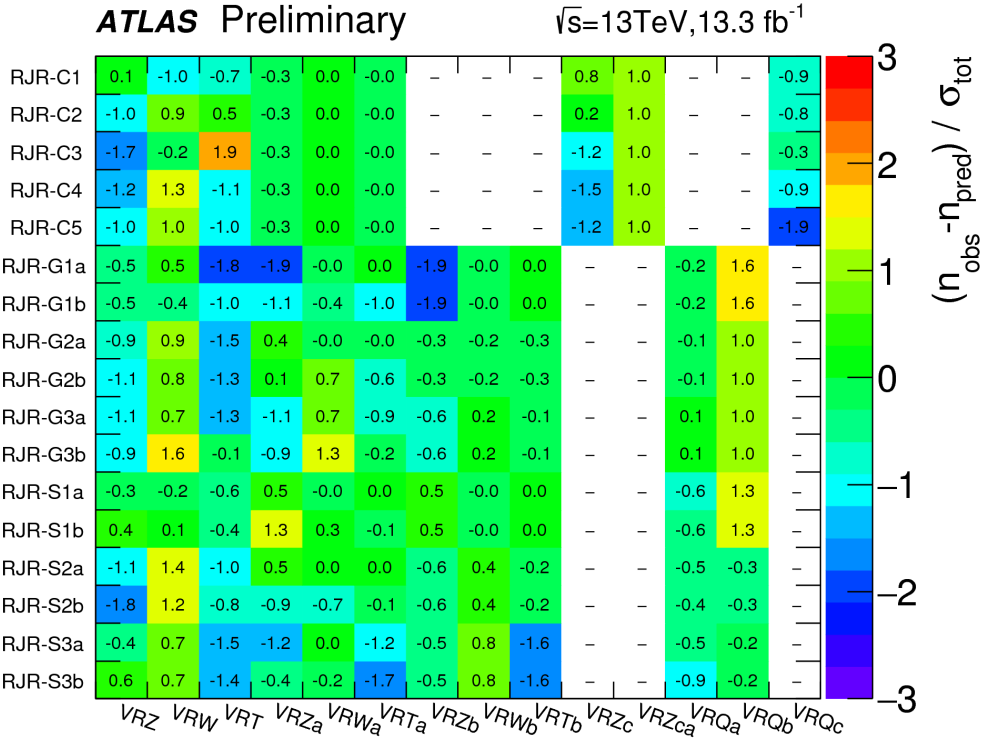


Figure 8.16: Summary of the validation region pulls

2017 we have conservatively measured the Standard Model backgrounds with our control  
2018 regions.

## 2019 Systematic Uncertainties

2020 In this section, we discuss the uncertainties considered. These generally fall into  
2021 four categories: theoretical generator uncertainties, uncertainties on the CR to SR  
2022 extrapolations, uncertainties on the data-driven transfer factor corrections, and object  
2023 reconstruction uncertainties. We discuss each of these categories here. A table  
2024 summarizing this section is in Tab. 8.5

Systematic	Uncertainty Description
alpha_GeneratorZ	Theoretical on $Z$ cross-section
alpha_generatorW	Theoretical on $W$ cross-section
alpha_generatorTop	Theoretical on $t$ cross-section
alpha_radiationTop	Theoretical on $t$ radiation tune
alpha_Pythia8Top	Theoretical on $t$ fragmentation tune
alpha_FlatDiboson	Flat on diboson cross-section
mu_Zjets	CRY extrapolation to SR
mu_Wjets	CRW extrapolation to SR
mu_Top	CRT extrapolation to SR
mu_Multijets	CRQ extrapolation to SR
alpha_Kappa	$\kappa$ factor
alpha_QCDError	Jet smearing
alpha_JET_GroupedNP_1	JES NP group 1
alpha_JET_GroupedNP_2	JES NP group 2
alpha_JET_GroupedNP_3	JES NP group 3
alpha_JER	JER
alpha_MET_SoftTrk_ResoPerp	Soft $E_T^{\text{miss}}$ resolution perpendicular to hard object system
alpha_MET_SoftTrk_ResoPara	Soft $E_T^{\text{miss}}$ resolution parallel to hard object system
alpha_MET_SoftTrk_Scale	Soft $E_T^{\text{miss}}$ scale

Table 8.5: Description of the systematic uncertainties in the analysis.

2025        The theoretical generator uncertainties are evaluated by using alternative sim-  
 2026        ulation samples or varying scale uncertainties. In the case of the  $Z+jets$  and  
 2027         $W+jets$  backgrounds, the related theoretical uncertainties are estimated by varying  
 2028        the renormalization, factorization, and resummation scales by two, and decreasing  
 2029        the nominal CKKW matching scale by 5 GeV and 10 GeV respectively. In  
 2030        the case of  $t\bar{t}$  production, we compare the nominal POWHEG-Box generator with  
 2031        MG5\_aMC@NLO, as well as comparing different radiation and generator tunes. As  
 2032        stated above, we account for the uncertainty on the small diboson background by  
 2033        imposition of a flat 50% uncertainty.

2034        The CR to SR extrapolation uncertainties, or what could be called the transfer

2035 factor uncertainties, are listed in Tab. 8.5 as  $\mu_{\text{--}}$ . There is one normalization factor  $\mu$   
2036 for each major background, and their uncertainties, especially  $\mu_Z$ , are often dominant  
2037 for the measurement in many signal regions. This uncertainty is generally dominated  
2038 by the statistical uncertainty in the CR.

2039 There are two uncertainties from the data-driven corrections to the transfer  
2040 factors. The first is the uncertainty on  $\kappa$ , which is measured using an auxiliary  $Z \rightarrow \ell\ell$   
2041 control region. This is labeled alpha\_Kappa. The other is the uncertainty is that  
2042 assigned to the jet smearing method, which is seen in the table as alpha\_QCDError.

2043 The final set of uncertainties are those related to object reconstruction. In the  
2044 case of the hadronic search presented, the important uncertainties are those assigned  
2045 to the jet energy and  $E_T^{\text{miss}}$ . The uncertainties on the lepton reconstruction and  
2046  $b$ -tagging uncertainties were found to be negligible in all SRs. The measurement  
2047 of the jet energy scale (JES) uncertainty is quite complicated, and described in  
2048 [138–140]. After a complicated procedure to decorrelate the various components  
2049 of the JES uncertainty, there are three components which remain, which are labeled  
2050 as alpha\_JET\_GroupedNP\_1,2,3. The jet energy resolution uncertainty is estimated  
2051 using the methods discussed in Refs. [140, 141], and is labeled alpha\_JER.

2052 The  $E_T^{\text{miss}}$  soft term uncertainties are described in [117, 118, 142]. The  
2053 uncertainty on the  $E_T^{\text{miss}}$  soft term resolution is parameterized into a component  
2054 parallel to direction of the rest of the event (the sum of the hard objects  $p_T$ )  
2055 and a component perpendicular to this direction. There is also an uncertainty  
2056 on the  $E_T^{\text{miss}}$  soft term scale. These are labeled as alpha\_MET\_SoftTrk\_ResoPara,  
2057 alpha\_MET\_SoftTrk\_ResoPerp, and alpha\_MET\_SoftTrk\_Scale.

## 2058 Fitting procedure

2059 This section describes the fitting procedure to properly account for the correlations  
2060 between the various uncertainties and the simultaneous fitting of the control and

2061 signal regions.

## 2062 Maximum likelihood fit

2063 To properly account for the systematic uncertainties and simultaneously fit the control  
2064 regions, we employ a maximum-likelihood fit as described in [125]. The likelihood  
2065 function  $\mathcal{L}$  is the product of the Poisson distributions governing the likelihood in each  
2066 of the signal regions and the corresponding control regions: We begin by considering  
2067 our event counts  $\mathbf{b}$  in a signal region with its corresponding signal regions. The  
2068 systematic uncertainties are included as a set of nuisance parameters  $\boldsymbol{\theta}$ .

The full likelihood function can be written [125]:

$$\mathcal{L}(n|\mu, \mathbf{b}) = P_{\text{SR}} \times P_{\text{CR}} \times C_{\text{syst}} \quad (8.5)$$

$$= P(n_S|\lambda_S(\mu_S, \mathbf{b}, \boldsymbol{\theta})) \times \prod_{i \in \text{CR}} P(n_i|\lambda_i(\mu_b, \mathbf{b}, \boldsymbol{\theta})) \times C_{\text{syst}}(\boldsymbol{\theta}^0, \boldsymbol{\theta}) \quad (8.6)$$

where  $P(n_i|\lambda_i(\mu, \mathbf{b}, \boldsymbol{\theta}))$  is a Poisson distribution conditioned on the event counts  $n_i$  in  
the  $i$ -th CR with mean parameter  $\lambda_i(\mu, \mathbf{b}, \boldsymbol{\theta})$ . The term  $C_{\text{syst}}(\boldsymbol{\theta}^0, \boldsymbol{\theta})$  is the probability  
density function with central values  $\boldsymbol{\theta}^0$  which are varied with the nuisance parameters  
 $\boldsymbol{\theta}$ . We model these as Gaussian distributions with unit width and mean zero:

$$C_{\text{syst}}(\boldsymbol{\theta}^0, \boldsymbol{\theta}) = \prod_{s \in S} G(\mu = \theta_s, \sigma = 1), \quad (8.7)$$

2069 where  $S$  is the set of systematic uncertainties considered in the analysis.

The terms  $\lambda_j$  for any region  $j$  can be expressed as

$$\lambda_j(\mu, \mathbf{b}, \boldsymbol{\theta}) = \sum_b \mu_b b_j \prod_{s \in S} (1 + \Delta_{j,b,s} \theta_s) \quad (8.8)$$

2070 The term  $\mu_b$  is the normalization factor associated to the background  $b$  with event  
2071 count  $b_j$  in the region  $j$ . The terms  $\Delta$  inside the product represent scale factors  
2072 freeing the model to account for the systematic uncertainties  $\theta_s$ .

2073 The process now is to maximize this likelihood function, given the free parameters  
2074  $\mu_b$  and the parameters  $\Delta$  associated to the systematics as nuisance parameters. This

2075 is done using the HISTFITTER package [125]. The normalization parameters  $\mu_b$  are  
2076 the primary output of this maximization, and are in fact the control regions' raison  
2077 d'être. This allows the magnitudes of each background process to be maximized *given*  
2078 *the actual control region event counts*. We can say the normalization parameters  
2079 are found such that the likelihood is maximized. The nuisance parameters are also  
2080 determined by this procedure, but do not have a straightforward

The final expected background prediction in each fit by region  $r_s$  is then given by

$$N_{\text{total background}} = \sum_b \mu_b N_{b,\text{MC}} \quad (8.9)$$

2081 **Background-only fit, model-independent fit, and**  
2082 **model-dependent fit**

2083 The maximum likelihood fit described above can be used with a variety of event count  
2084 inputs. We use three separate fit classes, which we call *background-only*, *model-*  
2085 *independent*, and *model-dependent* fits. In terms of the likelihood function inputs,  
2086 these can be seen as including a different list of event counts  $\mathbf{b}$

2087 In this section, we describe the fitting procedure employed, which properly  
2088 accounts for the correlations between the uncertainties through the use of a likelihood  
2089 fit as described in [125]. We use three classes of likelihood fits: *background-only*,  
2090 *model-independent*, and *model-dependent* fits. The background-only fits estimate the  
2091 background yields in each signal region. These fits use only the control region event  
2092 yields as inputs; they do not include the information from the signal regions besides  
2093 the simulation event yield. The cross-contamination between CRs is also fit by this  
2094 procedure. The systematic uncertainties described in the previous section are used as  
2095 nuisance parameters. This background only fit also estimates the background event  
2096 yields in the validation regions. When designing the analysis (before unblinding  
2097 the signal regions), checking the validation region agreement is the primary way to

2098 validate the consistency and accuracy of the background estimation procedure.

2099 In the case no excess is observed, we use a model-independent fit to set upper limits  
2100 on the possible number of possible beyond the Standard Model events in each SR.  
2101 These limits are derived using the same procedure as the background-only fit, with  
2102 two additional pieces of information included in the fitting procedure. We include  
2103 the SR event count, and a parameter known as the *signal strength*, defined as  $\mu =$   
2104  $\sigma/\sigma_{\text{BG}}$ . Using the  $CL_s$  procedure [143] and neglecting the possible (small) signal  
2105 contamination in control regions, we derive the the observed and expected limits on  
2106 the number of events from BSM phenomena in each signal region.

2107 Model-dependent fits are used to set exclusion limits on the specific SUSY  
2108 models considered in this thesis, particular the gluino or squark pair production  
2109 with various mass splittings. This can be seen as identical to the background-only  
2110 fit with an additional simulation input from the particular model of interest, with its  
2111 corresponding systematic uncertainties from detector effects accounted for as in the  
2112 background-only fit. As noted when we introduced Fig. 8.1, the exclusion contours  
2113 from previous model-dependent fits are the primary motivating factor in the design  
2114 of our signal regions. If no excess is found, we set limits on each of the simplified  
2115 signal models with various mass splittings.

2116

## Chapter 9

---

2117

### Results

2118 This chapter presents the results of the analysis presented in the previous chapter.  
2119 We present the full set of signal region distributions after applying the  $\mu$  factors  
2120 derived from the fitting procedure. We also present the systematic uncertainties in  
2121 each signal region properly accounting for the correlations of the uncertainties. As  
2122 no excess is observed, we show exclusion limits in the sparticle- $\tilde{\chi}_1^0$  plane based on  
2123 the results of the model-dependent fits and present the model-independent limits.

2124

## 9.1 Signal region distributions

2125 In Figs. 9.1 to 9.3, we can see the unblinded distributions of the last scale cut used  
2126 for each signal region. These distributions include the  $\mu$  normalization scale factors  
2127 derived from the fitting procedure. The systematic uncertainties are also shown.  
2128 Each plot shows the distribution from a signal model which is targetted by the given  
2129 signal region.

2130 These distributions have all cuts applied except for the cut on this scale variable,  
2131 which allows us to see the additional discrimination provided by the given variable.  
2132 Since signal regions with the same numeral have identical cuts except for that on the  
2133 main scale variable, we show (a) and (b) on the same figure. The left-most (right-  
2134 most) arrow shown is the location of the a (b) cut applied in the analysis. We call  
2135 these plot  $N - 1$  plots, where  $N$  refers to the number of cuts applied in the analysis.  
2136 The full set of  $N - 1$  plots in the signal regions for the other variables used in the

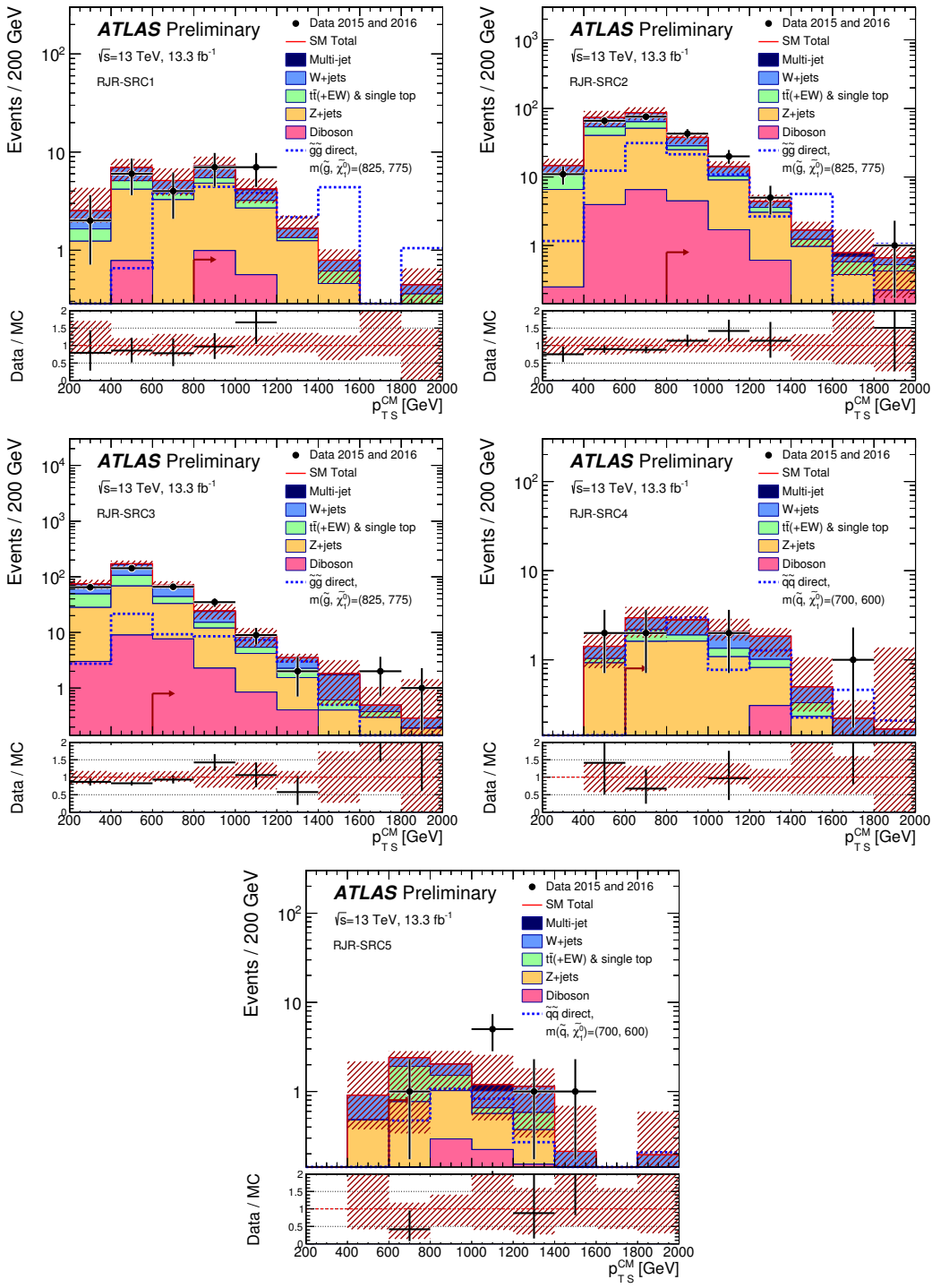


Figure 9.1: Scale variable distributions for the compressed signal regions.

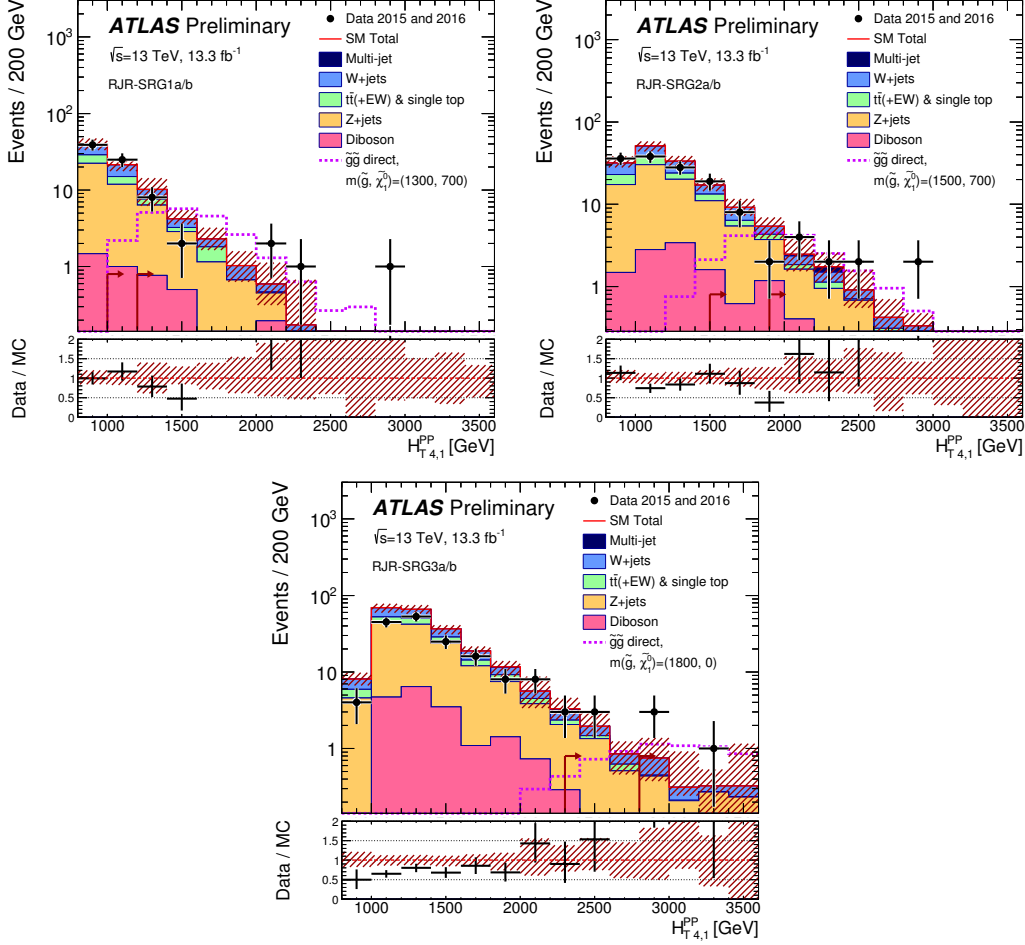


Figure 9.2: Scale variable distributions for the gluino signal regions.

analysis are shown in Sec. 9.4.

A figure showing a summary of the pulls in all of the SRs is shown in Fig. 9.4. This figure shows the integrated data and simulation values above the cut values in the N-1 plots, with the corresponding statistical and systematic uncertainties, for all signal regions simultaneously. The systematic uncertainties will be discussed in the next section. From this plot, we can see there is no significant excess of events over the Standard Model background.

This information is also presented in Tab. 9.2. The table includes the expectations from simulation before applying the  $\mu$  normalization factor, as well as the model-independent limits we will discuss later.

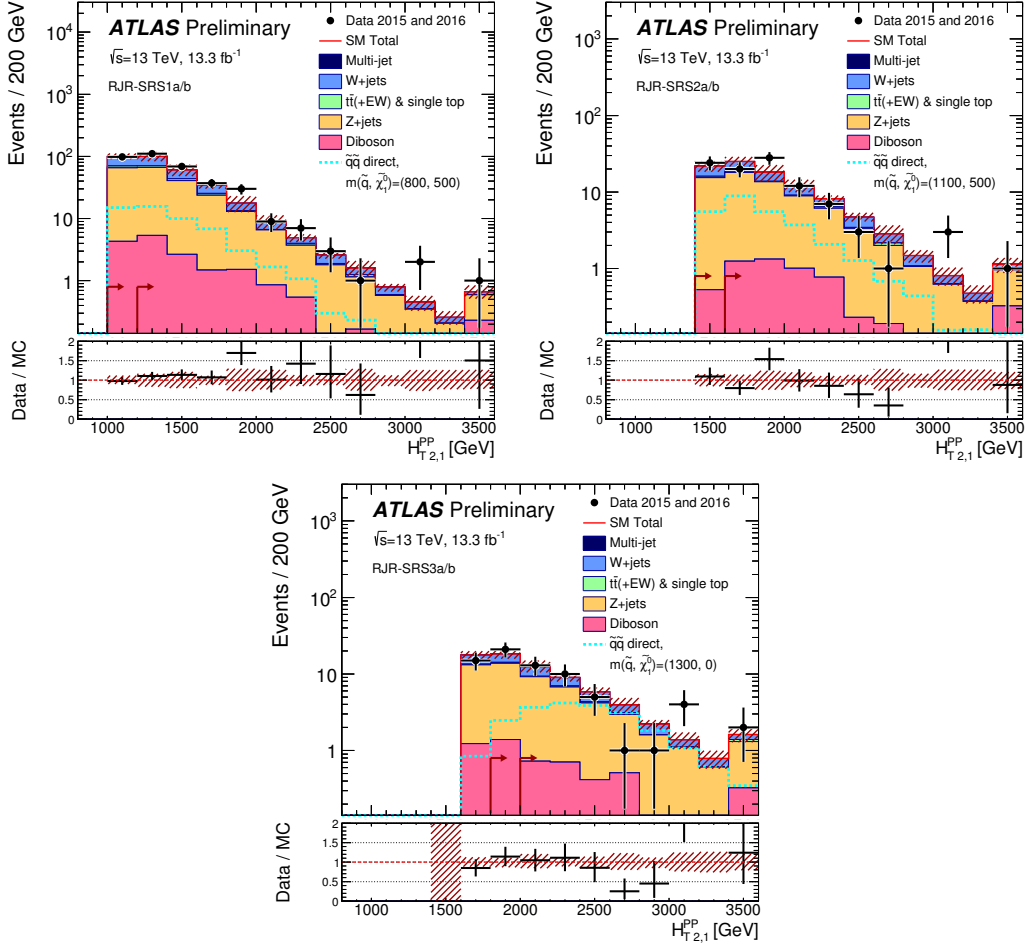


Figure 9.3: Scale variable distributions for the squark signal regions.

2147

We now consider the final values of the systematic uncertainties.

2148

## 9.2 Systematic Uncertainties

2149 This section considers the results of Tab. 9.1. This table is a summary of the resulting  
 2150 systematic uncertainties on the background estimation in each signal region, properly  
 2151 accounting for systematic uncertainties. These uncertainties are expressed both as a  
 2152 relative uncertainty and absolute uncertainty. As correlations are properly treated,  
 2153 the absolute uncertainties do not add in quadrature, although most uncertainties are  
 2154 relatively uncorrelated. We discuss the general trends in the systematic uncertainties

2155 for each type of signal region.

2156 In the squark regions, the total uncertainties range from 10% to 11%. We note  
2157 that the uncertainties on the  $Z$ , both theoretical and  $\Delta_{\mu, Z+\text{jets}}$  account for the largest  
2158 on the background estimate in each signal region. The  $\kappa$  factor uncertainty, which is  
2159 also an uncertainty on the  $Z$  estimate, is also significant at 4% in each region. The  
2160  $Z \rightarrow \nu\nu$  contribution to the squark regions is the primary irreducible background, so  
2161 even when relatively well-measured, the uncertainty on its event yield dominates the  
2162 overall uncertainty. There are also significant uncertainties from the  $W$ , top, and flat  
2163 diboson uncertainties, although these are subdominant. We note that the uncertainty  
2164 due to statistics of the MC simulation samples are very small for the squark case; this  
2165 is a reflection of the “looseness” of these regions, as the MC statistics are sufficient  
2166 for all of the major backgrounds.

2167 The gluino regions have overall larger uncertainties than the squark regions,  
2168 between 10% and 25%, due to a multitude of factors. The  $Z$  related uncertainties  
2169 all contribute significantly to the final background yield uncertainties. These  
2170 are relatively similar to the squark  $Z$  uncertainties. The  $W$ , top, and diboson  
2171 uncertainties are all significantly more important than in the squark case however. In  
2172 the gluino case, we also see that the limited simulation statistics begin to significantly  
2173 affect the measurement of the Standard Model background. These are all reflections  
2174 of the overall “tighter” quality of the gluino regions, as indicated by the event yields.  
2175 The  $\Delta_\mu$  uncertainties are affected by this due to the need to use overall looser  
2176 control regions, while the theory uncertainties are more affected by small statistical  
2177 fluctuations between different generators. The low statistics is particularly clear in  
2178 SRG3b, where the simulation statistics account for a very large 14% uncertainty.

2179 The compressed regions have systematic uncertainties ranging from 10% to 19%.  
2180 For the tighter regions, SRC1, SRC4, and SRC5, we see a large contribution from  
2181 the lack of MC statistics. SRC1 and SRC4 should a large value for the  $W$  theory

2182 uncertainty, while all compressed regions show a large uncertainty on the  $Z$  estimate.  
2183 These large uncertainties result from the fact that we are probing extreme phase  
2184 space in boson  $p_T$  with the compressed regions. SRC5 shows large top and jet/ $E_T^{\text{miss}}$   
2185 uncertainties; these uncertainties are more pronounced in this region than the other  
2186 compressed region due to the  $N_{\text{jet}}^V > 3$  cut, and thus the uncertainty in this region is  
2187 quite affected by fluctuations in the top, jet, or  $E_T^{\text{miss}}$  uncertainties.

### 2188 9.3 Limits and Model-dependent Exclusions

2189 In Tab. 9.1, we show the statistical significance  $Z$  for each signal region. We calculate  
2190 this using the fitted simulation mean compared with the observed event counts in  
2191 each region. There is no significant excess in each region; the highest excess is in  
2192 SRG3b, which is only  $Z_{\text{SRG3b}} = 1.55$ . This information is summarized in Fig. 9.4.  
2193 We thus set model-independent and model-dependent limits.

2194 As no significant excess is observed in any of the signal regions of this analysis  
2195 after estimating the background using the background-only fit, we set limits on the  
2196 model-independent and model-dependent cross sections.

2197 The model-independent limits are shown in Tab. 9.1. We present the limits on  
2198 the new physics cross section in each SR. The observed and expected limits  $S_{\text{obs}}^{95}$  and  
2199  $S_{\text{exp}}^{95}$  are reported for the potential contribution from new physics in each region.  
2200 Including the acceptance  $\epsilon$ , the model-independent limits in most signal regions are  
2201 of  $\sim 1 - 2$  fb. One should note that the (b) version of each signal region is strictly  
2202 tighter in the primary scale cut, and thus provides a stronger limit when we observe  
2203 no excess, as seen here.

2204 Additionally, we derive exclusion limits for the simplified models considered in this  
2205 thesis. These are the models with pair-production of squark pairs with inaccessible  
2206 gluinos, and gluino pairs with inaccessible squarks. They correspond directly to the

Channel	RJR-S1a	RJR-S1b	RJR-S2a	RJR-S2b	RJR-S3a	RJR-S3b
Total bkg	334	233	96	75	56	37
Total bkg unc.	$\pm 35$ [10%]	$\pm 25$ [11%]	$\pm 10$ [10%]	$\pm 8$ [11%]	$\pm 6$ [11%]	$\pm 4$ [11%]
MC statistics	—	$\pm 2.6$ [1%]	$\pm 1.5$ [2%]	$\pm 1.3$ [2%]	$\pm 1.0$ [2%]	$\pm 0.7$ [2%]
$\Delta\mu_{Z,+jets}$	$\pm 20$ [6%]	$\pm 14$ [6%]	$\pm 4$ [4%]	$\pm 2.9$ [4%]	$\pm 2.2$ [4%]	$\pm 1.5$ [4%]
$\Delta\mu_{W,+jets}$	$\pm 10$ [3%]	$\pm 7$ [3%]	$\pm 3.1$ [3%]	$\pm 2.3$ [3%]	$\pm 1.6$ [3%]	$\pm 1.1$ [3%]
$\Delta\mu_{Top}$	$\pm 6$ [2%]	$\pm 4$ [2%]	$\pm 1.5$ [2%]	$\pm 1.1$ [1%]	$\pm 0.9$ [2%]	$\pm 0.6$ [2%]
$\Delta\mu_{Multijet}$	$\pm 0.09$ [0%]	$\pm 0.05$ [0%]	$\pm 0.02$ [0%]	—	—	—
CR $\gamma$ corr. factor	$\pm 12$ [4%]	$\pm 8$ [3%]	$\pm 4$ [4%]	$\pm 2.9$ [4%]	$\pm 2.2$ [4%]	$\pm 1.4$ [4%]
Theory Z	$\pm 23$ [7%]	$\pm 16$ [7%]	$\pm 7$ [7%]	$\pm 6$ [8%]	$\pm 4$ [7%]	$\pm 2.8$ [8%]
Theory W	$\pm 4$ [1%]	$\pm 5$ [2%]	$\pm 0.4$ [0%]	$\pm 0.11$ [0%]	$\pm 1.5$ [3%]	$\pm 1.2$ [3%]
Theory Top	$\pm 4$ [1%]	$\pm 2.7$ [1%]	$\pm 0.8$ [1%]	$\pm 0.7$ [1%]	$\pm 0.6$ [1%]	$\pm 0.4$ [1%]
Theory Diboson	$\pm 9$ [3%]	$\pm 6$ [3%]	$\pm 2.8$ [3%]	$\pm 2.6$ [3%]	$\pm 2.1$ [4%]	$\pm 1.4$ [4%]
Jet/MET	$\pm 3.3$ [1%]	$\pm 1.5$ [1%]	$\pm 0.6$ [1%]	$\pm 0.6$ [1%]	$\pm 1.2$ [2%]	$\pm 1.0$ [3%]
Multijet method	$\pm 0.7$ [0%]	$\pm 0.4$ [0%]	$\pm 0.08$ [0%]	—	—	—
Channel	RJR-G1a	RJR-G1b	RJR-G2a	RJR-G2b	RJR-G3a	RJR-G3b
Total bkg	40	18.8	27.8	8.5	5.8	1.7
Total bkg unc.	$\pm 4$ [10%]	$\pm 2.5$ [13%]	$\pm 3.4$ [12%]	$\pm 1.4$ [16%]	$\pm 1.1$ [19%]	$\pm 0.4$ [24%]
MC statistics	$\pm 1.6$ [4%]	$\pm 1.0$ [5%]	$\pm 1.2$ [4%]	$\pm 0.6$ [7%]	$\pm 0.4$ [7%]	$\pm 0.23$ [14%]
$\Delta\mu_{Z,+jets}$	$\pm 1.5$ [4%]	$\pm 0.7$ [4%]	$\pm 1.6$ [6%]	$\pm 0.5$ [6%]	$\pm 0.4$ [7%]	$\pm 0.1$ [6%]
$\Delta\mu_{W,+jets}$	$\pm 0.9$ [2%]	$\pm 0.4$ [2%]	$\pm 1.2$ [4%]	$\pm 0.31$ [4%]	$\pm 0.28$ [5%]	$\pm 0.1$ [6%]
$\Delta\mu_{Top}$	$\pm 0.8$ [2%]	$\pm 0.33$ [2%]	$\pm 0.9$ [3%]	$\pm 0.23$ [3%]	$\pm 0.07$ [1%]	$\pm 0.1$ [6%]
$\Delta\mu_{Multijet}$	$\pm 0.1$ [0%]	—	$\pm 0.03$ [0%]	$\pm 0.02$ [0%]	—	—
CR $\gamma$ corr. factor	$\pm 1.2$ [3%]	$\pm 0.6$ [3%]	$\pm 0.8$ [3%]	$\pm 0.26$ [3%]	$\pm 0.19$ [3%]	$\pm 0.05$ [3%]
Theory Z	$\pm 2.3$ [6%]	$\pm 1.1$ [6%]	$\pm 1.6$ [6%]	$\pm 0.5$ [6%]	$\pm 0.4$ [7%]	$\pm 0.1$ [6%]
Theory W	$\pm 1.1$ [3%]	$\pm 1.3$ [7%]	$\pm 0.3$ [1%]	$\pm 0.7$ [8%]	$\pm 0.6$ [10%]	$\pm 0.16$ [9%]
Theory Top	$\pm 1.2$ [3%]	$\pm 0.7$ [4%]	$\pm 1.0$ [4%]	$\pm 0.4$ [5%]	$\pm 0.4$ [7%]	$\pm 0.26$ [15%]
Theory Diboson	$\pm 1.3$ [3%]	$\pm 0.8$ [4%]	$\pm 1.5$ [5%]	$\pm 0.6$ [7%]	$\pm 0.31$ [5%]	$\pm 0.13$ [8%]
Jet/MET	$\pm 1.0$ [3%]	$\pm 0.6$ [3%]	$\pm 0.4$ [1%]	$\pm 0.17$ [2%]	$\pm 0.22$ [4%]	$\pm 0.05$ [3%]
Multijet method	$\pm 0.24$ [1%]	$\pm 0.12$ [1%]	$\pm 0.5$ [2%]	$\pm 0.4$ [5%]	—	—
Channel	RJR-C1	RJR-C2	RJR-C3	RJR-C4	RJR-C5	
Total bkg	14.5	59	110	10.5	7.3	
Total bkg unc.	$\pm 2.2$ [15%]	$\pm 6$ [10%]	$\pm 11$ [10%]	$\pm 1.5$ [14%]	$\pm 1.4$ [19%]	
MC statistics	$\pm 0.7$ [5%]	$\pm 1.7$ [3%]	$\pm 2.4$ [2%]	$\pm 0.6$ [6%]	$\pm 0.6$ [8%]	
$\Delta\mu_{Z,+jets}$	$\pm 0.5$ [3%]	$\pm 1.9$ [3%]	$\pm 2.5$ [2%]	$\pm 0.31$ [3%]	$\pm 0.13$ [2%]	
$\Delta\mu_{W,+jets}$	$\pm 0.4$ [3%]	$\pm 1.7$ [3%]	$\pm 5$ [5%]	$\pm 0.4$ [4%]	$\pm 0.25$ [3%]	
$\Delta\mu_{Top}$	$\pm 0.33$ [2%]	$\pm 1.3$ [2%]	$\pm 4$ [4%]	$\pm 0.31$ [3%]	$\pm 0.4$ [5%]	
$\Delta\mu_{Multijet m}$	—	$\pm 0.1$ [0%]	$\pm 0.06$ [0%]	—	$\pm 0.1$ [1%]	
CR $\gamma$ corr. factor	$\pm 0.5$ [3%]	$\pm 1.8$ [3%]	$\pm 2.3$ [2%]	$\pm 0.29$ [3%]	$\pm 0.13$ [2%]	
Theory Z	$\pm 0.8$ [6%]	$\pm 3.5$ [6%]	$\pm 4$ [4%]	$\pm 0.6$ [6%]	$\pm 0.24$ [3%]	
Theory W	$\pm 1.3$ [9%]	$\pm 0.03$ [0%]	$\pm 2.0$ [2%]	$\pm 1.0$ [10%]	$\pm 0.13$ [2%]	
Theory Top	$\pm 0.5$ [3%]	$\pm 1.3$ [2%]	$\pm 3.2$ [3%]	$\pm 0.6$ [6%]	$\pm 0.9$ [12%]	
Theory Diboson	$\pm 1.0$ [7%]	$\pm 4$ [7%]	$\pm 6$ [5%]	$\pm 0.27$ [3%]	$\pm 0.4$ [5%]	
Jet/MET	$\pm 0.5$ [3%]	$\pm 1.5$ [3%]	$\pm 3.1$ [3%]	$\pm 0.24$ [2%]	$\pm 0.5$ [7%]	
Multijet method	$\pm 0.09$ [1%]	$\pm 0.4$ [1%]	$\pm 2.1$ [2%]	—	$\pm 0.18$ [2%]	

Table 9.1: Breakdown of the dominant systematic uncertainties in the background estimates for the RJR-based search. The individual uncertainties can be correlated, and do not necessarily add in quadrature to the total background uncertainty.  $\Delta_\mu$  uncertainties are the result of the control region statistical uncertainties and the systematic uncertainties entering a specific control region. In brackets, uncertainties are given relative to the expected total background yield, also presented in the Table. Empty cells (indicated by a ‘-’) correspond to uncertainties  $< 0.1\%$ .

Signal Region	RJR-S1a	RJR-S1b	RJR-S2a	RJR-S2b	RJR-S3a	RJR-S3b
MC expected events						
Diboson	17	13	5.6	5.1	4.2	2.8
Z/ $\gamma^*$ +jets	231	163	63	48	36	24
W+jets	97	66	22	16	11	7.8
$t\bar{t}$ (+EW) + single top	15	10	2.9	2.1	1.7	1.1
Fitted background events						
Diboson	$17 \pm 9$	$13 \pm 7$	$5.6 \pm 2.8$	$5.1 \pm 2.6$	$4.2 \pm 2.1$	$2.8 \pm 1.4$
Z/ $\gamma^*$ +jets	$207 \pm 33$	$146 \pm 23$	$65 \pm 9$	$50 \pm 7$	$37 \pm 5$	$25.0 \pm 3.5$
W+jets	$95 \pm 9$	$65 \pm 7$	$24.1 \pm 2.9$	$18.3 \pm 2.3$	$12.8 \pm 2.8$	$8.7 \pm 2.0$
$t\bar{t}$ (+EW) + single top	$14 \pm 7$	$9 \pm 5$	$2.1 \pm 1.7$	$1.6 \pm 1.3$	$1.3 \pm 1.0$	$0.8 \pm 0.7$
Multi-jet	$0.71^{+0.71}_{-0.71}$	$0.41^{+0.41}_{-0.41}$	$0.08^{+0.09}_{-0.08}$	—	—	—
Total Expected MC	362	253	93	72	53	36
Total Fitted bkg	$334 \pm 35$	$233 \pm 25$	$96 \pm 10$	$75 \pm 8$	$56 \pm 6$	$37 \pm 4$
Observed	368	270	99	75	57	36
$\langle\epsilon\sigma\rangle_{\text{obs}}^{95}$ [fb]	7.6	6.5	2.2	1.7	1.6	1.1
$S_{\text{obs}}^{95}$	101	86	29	23	22	15
$S_{\text{exp}}^{95}$	$78^{+27}_{-21}$	$61^{+22}_{-16}$	$28^{+11}_{-8}$	$23^{+9}_{-7}$	$20^{+8}_{-6}$	$16^{+7}_{-5}$
$p_0$ (Z)	0.20 (0.84)	0.12 (1.17)	0.44 (0.15)	0.50 (0.00)	0.44 (0.14)	0.50 (0.00)
Signal Region	RJR-G1a	RJR-G1b	RJR-G2a	RJR-G2b	RJR-G3a	RJR-G3b
MC expected events						
Diboson	2.6	1.6	2.9	1.1	0.62	0.26
Z/ $\gamma^*$ +jets	18	8.8	13	4.2	3.1	0.83
W+jets	11	4.7	7.7	2.0	1.9	0.63
$t\bar{t}$ (+EW) + single top	7.4	3.1	4.4	1.1	0.34	0.03
Fitted background events						
Diboson	$2.6 \pm 1.3$	$1.6 \pm 0.8$	$2.9 \pm 1.5$	$1.1 \pm 0.6$	$0.6 \pm 0.4$	$0.26 \pm 0.14$
Z/ $\gamma^*$ +jets	$21.1 \pm 3.1$	$10.2 \pm 1.6$	$14.3 \pm 2.5$	$4.5 \pm 0.8$	$3.3 \pm 0.6$	$0.88 \pm 0.19$
W+jets	$10.8 \pm 1.7$	$4.6 \pm 1.4$	$6.7 \pm 1.3$	$1.7 \pm 0.7$	$1.6 \pm 0.7$	$0.55 \pm 0.2$
$t\bar{t}$ (+EW) + single top	$5.4 \pm 1.6$	$2.3 \pm 0.9$	$3.4 \pm 1.4$	$0.8 \pm 0.5$	$0.26^{+0.45}_{-0.26}$	$0.02^{+0.26}_{-0.02}$
Multi-jet	$0.24 \pm 0.24$	$0.12 \pm 0.12$	$0.5 \pm 0.5$	$0.4 \pm 0.4$	—	—
Total Expected MC	39	18	29	8.7	5.9	1.7
Total Fitted bkg	$40 \pm 4$	$18.8 \pm 2.5$	$27.8 \pm 3.4$	$8.5 \pm 1.4$	$5.8 \pm 1.1$	$1.7 \pm 0.4$
Observed	39	14	30	10	8	4
$\langle\epsilon\sigma\rangle_{\text{obs}}^{95}$ [fb]	1.1	0.56	1.1	0.71	0.64	0.55
$S_{\text{obs}}^{95}$	15	7.5	15	9.4	8.5	7.3
$S_{\text{exp}}^{95}$	$16^{+7}_{-4}$	$10^{+5}_{-3}$	$14^{+6}_{-4}$	$7.6^{+3.5}_{-2.0}$	$7.0^{+2.5}_{-2.1}$	$4.2^{+1.9}_{-0.5}$
$p_0$ (Z)	0.50 (0.00)	0.50 (0.00)	0.36 (0.35)	0.31 (0.50)	0.21 (0.81)	0.06 (1.55)
Signal Region	RJR-C1	RJR-C2	RJR-C3	RJR-C4	RJR-C5	
MC expected events						
Diboson	1.9	7.1	11	0.54	0.75	
Z/ $\gamma^*$ +jets	8.8	36	46	5.8	2.5	
W+jets	3.5	16	43	3.8	2.3	
$t\bar{t}$ (+EW) + single top	1.9	7.2	20	1.7	2.5	
Fitted background events						
Diboson	$1.9 \pm 1.0$	$7 \pm 4$	$11 \pm 6$	$0.54 \pm 0.29$	$0.8 \pm 0.5$	
Z/ $\gamma^*$ +jets	$7.7 \pm 1.1$	$32 \pm 5$	$40 \pm 6$	$5.0 \pm 0.8$	$2.2 \pm 0.4$	
W+jets	$3.3 \pm 1.4$	$14.5 \pm 1.7$	$40 \pm 5$	$3.56 \pm 1.0$	$2.14 \pm 0.35$	
$t\bar{t}$ (+EW) + single top	$1.5 \pm 0.6$	$5.8 \pm 1.8$	$16 \pm 5$	$1.4 \pm 0.7$	$2.0 \pm 1.1$	
Multi-jet	$0.09 \pm 0.09$	$0.4 \pm 0.4$	$2.1 \pm 2.1$	—	$0.18 \pm 0.18$	
Total Expected MC	16	67	124	12	8.3	
Total Fitted bkg	$14.5 \pm 2.2$	$59 \pm 6$	$110 \pm 11$	$10.5 \pm 1.5$	$7.3 \pm 1.4$	
Observed	14	69	115	5	8	
$\langle\epsilon\sigma\rangle_{\text{obs}}^{95}$ [fb]	0.76	2.2	2.5	0.35	0.61	
$S_{\text{obs}}^{95}$	10	29	34	4.7	8.1	
$S_{\text{exp}}^{95}$	$11^{+5}_{-3}$	$21^{+9}_{-6}$	$30^{+12}_{-8}$	$8.1^{+3.0}_{-2.3}$	$7.4^{+2.9}_{-1.8}$	
$p_0$ (Z)	0.50 (0.00)	0.18 (0.92)	0.37 (0.32)	0.50 (0.00)	0.39 (0.30)	

Table 9.2: Numbers of events observed in the signal regions used in the RJR-based analysis compared with background expectations obtained from the fits described in the text. Empty cells (indicated by a ‘-’) correspond to estimates lower than 0.01. The p-values ( $p_0$ ) give the probabilities of the observations being consistent with the estimated backgrounds. For an observed number of events lower than expected, the p-value is truncated at 0.5. Between parentheses,  $p$ -values are also given as the number of equivalent Gaussian standard deviations (Z). Also shown are 95% CL upper limits on the visible cross-section ( $\langle\epsilon\sigma\rangle_{\text{obs}}^{95}$ ), the visible number of signal events ( $S_{\text{obs}}^{95}$ ) and the number of signal events ( $S_{\text{exp}}^{95}$ ) given the expected number of background events (and  $\pm 1\sigma$  excursions of the expectation).

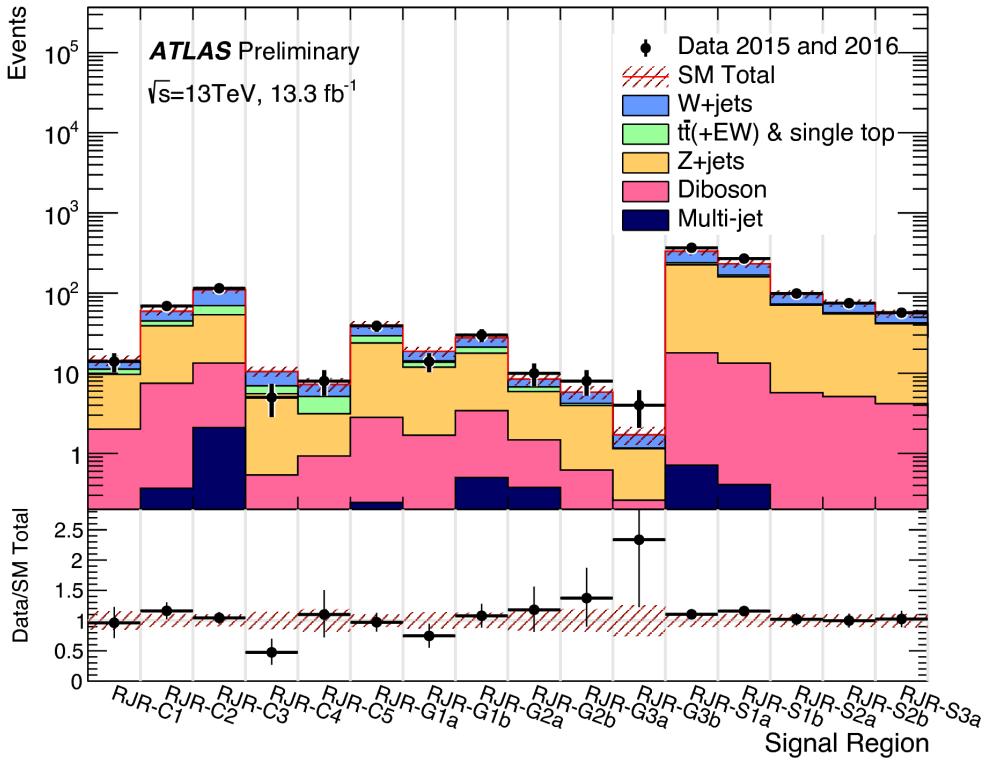


Figure 9.4: Summary of the signal region pulls

2207 Feynman diagrams shown previously. The free parameters of these simplified models  
 2208 are the relevant sparticle mass and the mass of the LSP  $\tilde{\chi}_1^0$ . We set limits in a plane  
 2209 of these free parameters.

2210 The exclusion limits are shown in Fig. 9.5. Gray text is imposed on the plane at the  
 2211 point of each simplified model with masses  $(m_{\text{sparticle}}, m_{\tilde{\chi}_1^0})$ . This gray text indicates  
 2212 the signal region which provided the best sensitivity at that point, as measured by the  
 2213 background-only fit. For each simplified signal model, we run the model-dependent fit  
 2214 described in the last chapter, where the signal model signal strength  $\mu_{\text{sig}}$  is included  
 2215 as an additional free parameter. The signal sample is also allowed to freely contribute  
 2216 to the control regions due to signal contamination. This produces a  $\text{CL}_s$   $p$ -value for  
 2217 each signal model in the plane, and we can find those with  $p = 0.05$  to set a 95%  
 2218 exclusion limit.

2219 In the squark- $\tilde{\chi}_1^0$  plane, we observe that the limits from the 2015 dataset are far  
2220 extended in all directions. The expected and observed exclusions are similar, which  
2221 is a reflection of the compatibility of the expected Standard Model event counts and  
2222 observed event counts in the squark regions. A squark with mass of 1350 GeV or less  
2223 is excluded by the analysis in direct decays to a quark and LSP. In the compressed  
2224 spectra, we have extended limits significantly over the 2015 result in the region of 600-  
2225 700 GeV in squark mass with an LSP of 450 GeV to 600 GeV. We note that directly  
2226 along the kinematically-forbidden diagonal, the shape of the exclusions is affected  
2227 by the interpolation between the signal models considered. This could be rectified  
2228 by inclusion of additional compressed signal models. The limits in the intermediate  
2229 with an LSP of  $\sim$ 450-500 GeV are not far extended beyond the previous dataset. We  
2230 also note that every signal region designed to provide sensitivity to this simplified  
2231 model (all SRS regions and SRC1-4) is chosen as the best region at least once in  
2232 the plane, indicating that each signal region provided additional sensitivity to squark  
2233 phenomena.

2234 Another curiosity is the fact that a gluino region, SRG2a is chosen as the optimal  
2235 region in the squark- $\tilde{\chi}_1^0$  plane, when the squark mass is  $\sim$ 700 GeV. Generally, the  
2236 squark regions are looser than the gluino regions, as seen in their overall event counts.  
2237 One could see this as an indication that the next iteration of the analysis should have  
2238 an additional tight squark region here. Another possibility is that this region also  
2239 benefits from the compressed region strategy of using an ISR jet. As the gluino  
2240 regions require four jets from the imposition of the gluino decay tree, these could be  
2241 capturing events where a two jet ISR system recoils off the disquark system.

2242 In the gluino- $\tilde{\chi}_1^0$  plane, the limits on gluino masses in the simplified model where  
2243 gluinos decay to two jets and an  $\tilde{\chi}_1^0$  are again far extended beyond the 2015 dataset.  
2244 We note in most of the plane, the expected limit is significantly stronger than the  
2245 observed limit; for example, the gluino mass limit is more than 50 GeV stronger in

2246 the case of a massless  $\tilde{\chi}_1^0$ . As much of the phase space is covered by SRG3a and  
2247 SRG3b, this results from the small statistical fluctuation upward in these regions.  
2248 Again, we note that every gluino signal region is the best choice at some point in this  
2249 plane. This is an indication of the utility of the signal region strategy employed in  
2250 this thesis, as each point provides additional sensitivity to new SUSY models.

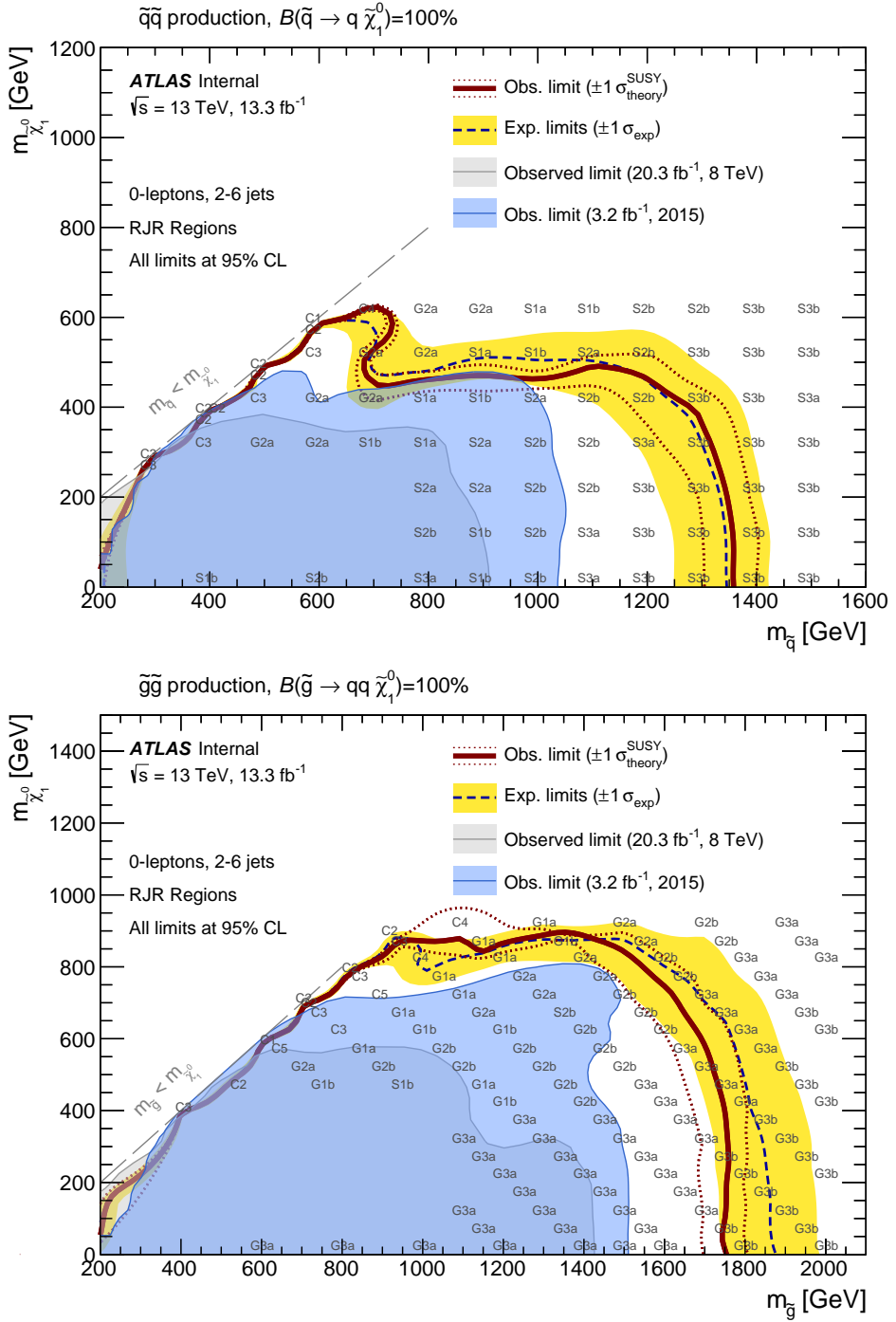


Figure 9.5: Exclusion limits for direct production of (a) light-flavour squark pairs with decoupled gluinos and (b) gluino pairs with decoupled squarks. Exclusion limits are obtained by using the signal region with the best expected sensitivity at each point. The blue dashed lines show the expected limits at 95% CL, with the yellow bands indicating the  $1\sigma$  excursions due to experimental and background-only theoretical uncertainties. Observed limits are indicated by maroon curves where the solid contour represents the nominal limit, and the dotted lines are obtained by varying the signal cross-section by the renormalization and factorization scale and PDF uncertainties. Results are compared with the observed limits obtained by the previous ATLAS searches with no leptons, jets and missing transverse momentum [135, 144].

---

2251

## *Conclusion*

2252 Here you can write some introductory remarks about your chapter. I like to give each  
2253 sentence its own line.

2254 When you need a new paragraph, just skip an extra line.

## **2255 9.4 New Section**

2256 By using the asterisk to start a new section, I keep the section from appearing in the  
2257 table of contents. If you want your sections to be numbered and to appear in the  
2258 table of contents, remove the asterisk.



---

*Bibliography*

- 2260 [1] O. Perdereau, *Planck 2015 cosmological results*,  
2261 AIP Conf. Proc. **1743** (2016) p. 050014.
- 2262 [2] N. Aghanim et al.,  
2263 *Planck 2016 intermediate results. LI. Features in the cosmic microwave*  
2264 *background temperature power spectrum and shifts in cosmological parameters*  
2265 (2016), arXiv: [1608.02487 \[astro-ph.CO\]](https://arxiv.org/abs/1608.02487).
- 2266 [3] J. S. Schwinger,  
2267 *On Quantum electrodynamics and the magnetic moment of the electron*,  
2268 Phys. Rev. **73** (1948) p. 416.
- 2269 [4] S. Laporta and E. Remiddi,  
2270 *The Analytical value of the electron (g-2) at order alpha\*\*3 in QED*,  
2271 Phys. Lett. **B379** (1996) p. 283, arXiv: [hep-ph/9602417 \[hep-ph\]](https://arxiv.org/abs/hep-ph/9602417).
- 2272 [5] S. Schael et al., *Precision electroweak measurements on the Z resonance*,  
2273 Phys. Rept. **427** (2006) p. 257, arXiv: [hep-ex/0509008 \[hep-ex\]](https://arxiv.org/abs/hep-ex/0509008).
- 2274 [6] S. L. Glashow, *Partial Symmetries of Weak Interactions*,  
2275 Nucl. Phys. **22** (1961) p. 579.
- 2276 [7] S. Weinberg, *A Model of Leptons*, Phys. Rev. Lett. **19** (1967) p. 1264.
- 2277 [8] A. Salam, *Weak and Electromagnetic Interactions*,  
2278 Conf. Proc. **C680519** (1968) p. 367.
- 2279 [9] M. Gell-Mann, *A Schematic Model of Baryons and Mesons*,  
2280 Phys. Lett. **8** (1964) p. 214.
- 2281 [10] G. Zweig, “An SU(3) model for strong interaction symmetry and its  
2282 breaking. Version 2,” *DEVELOPMENTS IN THE QUARK THEORY OF*  
2283 *HADRONS. VOL. 1. 1964 - 1978*, ed. by D. Lichtenberg and S. P. Rosen,  
2284 1964 p. 22,  
2285 URL: <http://inspirehep.net/record/4674/files/cern-th-412.pdf>.

- 2286 [11] S. Weinberg, *Implications of Dynamical Symmetry Breaking*,  
2287 Phys. Rev. **D13** (1976) p. 974.
- 2288 [12] S. Weinberg, *Implications of Dynamical Symmetry Breaking: An Addendum*,  
2289 Phys. Rev. **D19** (1979) p. 1277.
- 2290 [13] E. Gildener, *Gauge Symmetry Hierarchies*, Phys. Rev. **D14** (1976) p. 1667.
- 2291 [14] L. Susskind, *Dynamics of Spontaneous Symmetry Breaking in the*  
2292 *Weinberg-Salam Theory*, Phys. Rev. **D20** (1979) p. 2619.
- 2293 [15] S. P. Martin, “A Supersymmetry Primer,” 1997,  
2294 eprint: [arXiv:hep-ph/9709356](https://arxiv.org/abs/hep-ph/9709356).
- 2295 [16] V. C. Rubin and W. K. Ford Jr., *Rotation of the Andromeda Nebula from a*  
2296 *Spectroscopic Survey of Emission Regions*, Astrophys. J. **159** (1970) p. 379.
- 2297 [17] M. S. Roberts and R. N. Whitehurst,  
2298 “*The rotation curve and geometry of M31 at large galactocentric distances*,  
2299 Astrophys. J. **201** (1970) p. 327.
- 2300 [18] V. C. Rubin, N. Thonnard, and W. K. Ford Jr.,  
2301 *Rotational properties of 21 SC galaxies with a large range of luminosities and*  
2302 *radii, from NGC 4605 /R = 4kpc/ to UGC 2885 /R = 122 kpc/*,  
2303 Astrophys. J. **238** (1980) p. 471.
- 2304 [19] V. C. Rubin et al., *Rotation velocities of 16 SA galaxies and a comparison of*  
2305 *Sa, Sb, and SC rotation properties*, Astrophys. J. **289** (1985) p. 81.
- 2306 [20] A. Bosma,  
2307 *21-cm line studies of spiral galaxies. 2. The distribution and kinematics of*  
2308 *neutral hydrogen in spiral galaxies of various morphological types.*,  
2309 Astron. J. **86** (1981) p. 1825.
- 2310 [21] M. Persic, P. Salucci, and F. Stel, *The Universal rotation curve of spiral*  
2311 *galaxies: 1. The Dark matter connection*,  
2312 Mon. Not. Roy. Astron. Soc. **281** (1996) p. 27,  
2313 arXiv: [astro-ph/9506004](https://arxiv.org/abs/astro-ph/9506004) [astro-ph].
- 2314 [22] M. Lisanti, “Lectures on Dark Matter Physics,” 2016,  
2315 eprint: [arXiv:1603.03797](https://arxiv.org/abs/1603.03797).
- 2316 [23] H. Miyazawa, *Baryon Number Changing Currents*,  
2317 Prog. Theor. Phys. **36** (1966) p. 1266.

- 2318 [24] J.-L. Gervais and B. Sakita, *Generalizations of dual models*,  
 2319 *Nucl. Phys.* **B34** (1971) p. 477.
- 2320 [25] J. Gervais and B. Sakita,  
 2321 *Field theory interpretation of supergauges in dual models*,  
 2322 *Nucl. Phys. B* **34** (1971) p. 632.
- 2323 [26] Y. A. Golfand and E. P. Likhtman, *Extension of the Algebra of Poincare  
 2324 Group Generators and Violation of p Invariance*,  
 2325 *JETP Lett.* **13** (1971) p. 323, [*Pisma Zh.Eksp.Teor.Fiz.* 13:452-455, 1971].
- 2326 [27] A. Neveu and J. H. Schwarz, *Factorizable dual model of pions*,  
 2327 *Nucl. Phys. B* **31** (1971) p. 86.
- 2328 [28] A. Neveu and J. H. Schwarz, *Quark Model of Dual Pions*,  
 2329 *Phys. Rev. D* **4** (1971) p. 1109.
- 2330 [29] D. V. Volkov and V. P. Akulov, *Is the Neutrino a Goldstone Particle?*  
 2331 *Phys. Lett. B* **46** (1973) p. 109.
- 2332 [30] J. Wess and B. Zumino,  
 2333 *A Lagrangian Model Invariant Under Supergauge Transformations*,  
 2334 *Phys. Lett. B* **49** (1974) p. 52.
- 2335 [31] A. Salam and J. A. Strathdee, *Supersymmetry and Nonabelian Gauges*,  
 2336 *Phys. Lett. B* **51** (1974) p. 353.
- 2337 [32] S. Ferrara, J. Wess, and B. Zumino, *Supergauge Multiplets and Superfields*,  
 2338 *Phys. Lett. B* **51** (1974) p. 239.
- 2339 [33] J. Wess and B. Zumino, *Supergauge Transformations in Four-Dimensions*,  
 2340 *Nucl. Phys. B* **70** (1974) p. 39.
- 2341 [34] J. D. Lykken, “Introduction to supersymmetry,” *Fields, strings and duality. Proceedings, Summer School, Theoretical Advanced Study Institute in Elementary Particle Physics, TASI’96, Boulder, USA, June 2-28, 1996*, 1996  
 2342 p. 85, arXiv: [hep-th/9612114](https://arxiv.org/abs/hep-th/9612114) [hep-th],  
 2343 URL: [http://lss.fnal.gov/cgi-bin/find\\_paper.pl?pub=96-445-T](http://lss.fnal.gov/cgi-bin/find_paper.pl?pub=96-445-T).
- 2346 [35] A. Kobakhidze, “Intro to SUSY,” 2016, URL: <https://indico.cern.ch/event/443176/page/5225-pre-susy-programme>.
- 2348 [36] G. R. Farrar and P. Fayet, *Phenomenology of the Production, Decay, and  
 2349 Detection of New Hadronic States Associated with Supersymmetry*,  
 2350 *Phys. Lett. B* **76** (1978) p. 575.

- 2351 [37] ATLAS Collaboration,  
 2352 *Search for the electroweak production of supersymmetric particles in*  
 2353  $\sqrt{s} = 8 \text{ TeV}$  *pp collisions with the ATLAS detector,*  
 2354 *Phys. Rev. D* **93** (2016) p. 052002, arXiv: [1509.07152 \[hep-ex\]](#).
- 2355 [38] ATLAS Collaboration, *Summary of the searches for squarks and gluinos*  
 2356 *using  $\sqrt{s} = 8 \text{ TeV}$  pp collisions with the ATLAS experiment at the LHC,*  
 2357 *JHEP* **10** (2015) p. 054, arXiv: [1507.05525 \[hep-ex\]](#).
- 2358 [39] ATLAS Collaboration, *ATLAS Run 1 searches for direct pair production of*  
 2359 *third-generation squarks at the Large Hadron Collider,*  
 2360 *Eur. Phys. J. C* **75** (2015) p. 510, arXiv: [1506.08616 \[hep-ex\]](#).
- 2361 [40] CMS Collaboration, *Search for supersymmetry with razor variables in pp*  
 2362 *collisions at  $\sqrt{s} = 7 \text{ TeV}$ , Phys. Rev. D* **90** (2014) p. 112001,  
 2363 arXiv: [1405.3961 \[hep-ex\]](#).
- 2364 [41] CMS Collaboration, *Inclusive search for supersymmetry using razor variables*  
 2365 *in pp collisions at  $\sqrt{s} = 7 \text{ TeV}$ , Phys. Rev. Lett.* **111** (2013) p. 081802,  
 2366 arXiv: [1212.6961 \[hep-ex\]](#).
- 2367 [42] CMS Collaboration, *Search for Supersymmetry in pp Collisions at 7 TeV in*  
 2368 *Events with Jets and Missing Transverse Energy,*  
 2369 *Phys. Lett. B* **698** (2011) p. 196, arXiv: [1101.1628 \[hep-ex\]](#).
- 2370 [43] CMS Collaboration, *Search for Supersymmetry at the LHC in Events with*  
 2371 *Jets and Missing Transverse Energy, Phys. Rev. Lett.* **107** (2011) p. 221804,  
 2372 arXiv: [1109.2352 \[hep-ex\]](#).
- 2373 [44] CMS Collaboration, *Search for supersymmetry in hadronic final states using*  
 2374  *$M_{T2}$  in pp collisions at  $\sqrt{s} = 7 \text{ TeV}$ , JHEP* **10** (2012) p. 018,  
 2375 arXiv: [1207.1798 \[hep-ex\]](#).
- 2376 [45] CMS Collaboration, *Searches for supersymmetry using the  $M_{T2}$  variable in*  
 2377 *hadronic events produced in pp collisions at 8 TeV, JHEP* **05** (2015) p. 078,  
 2378 arXiv: [1502.04358 \[hep-ex\]](#).
- 2379 [46] CMS Collaboration, *Search for new physics with the  $M_{T2}$  variable in all-jets*  
 2380 *final states produced in pp collisions at  $\sqrt{s} = 13 \text{ TeV}$ , JHEP* (2016),  
 2381 arXiv: [1603.04053 \[hep-ex\]](#).
- 2382 [47] ATLAS Collaboration, *Multi-channel search for squarks and gluinos in*  
 2383  $\sqrt{s} = 7 \text{ TeV}$  *pp collisions with the ATLAS detector at the LHC,*  
 2384 *Eur. Phys. J. C* **73** (2013) p. 2362, arXiv: [1212.6149 \[hep-ex\]](#).

- 2385 [48] Y. Grossman, “Introduction to the SM,” 2016, URL: <https://indico.fnal.gov/sessionDisplay.py?sessionId=3&confId=11505#20160811>.
- 2386
- 2387 [49] W Buchmuller and C Ludeling, *Field Theory and Standard Model* (Sept. 2006) p. 70, URL: <https://cds.cern.ch/record/984122>.
- 2388
- 2389 [50] P. W. Higgs, *Broken Symmetries and the Masses of Gauge Bosons*,  
2390 Phys. Rev. Lett. **13** (1964) p. 508.
- 2391 [51] ATLAS Collaboration, *Observation of a new particle in the search for the*  
2392 *Standard Model Higgs boson with the ATLAS detector at the LHC*,  
2393 Phys. Lett. B **716** (2012) p. 1, arXiv: [1207.7214 \[hep-ex\]](https://arxiv.org/abs/1207.7214).
- 2394 [52] CMS Collaboration, *Observation of a new boson at a mass of 125 GeV with*  
2395 *the CMS experiment at the LHC*, Phys. Lett. B **716** (2012) p. 30,  
2396 arXiv: [1207.7235 \[hep-ex\]](https://arxiv.org/abs/1207.7235).
- 2397 [53] A. Chodos et al., *A New Extended Model of Hadrons*,  
2398 Phys. Rev. **D9** (1974) p. 3471.
- 2399 [54] A. Chodos et al., *Baryon Structure in the Bag Theory*,  
2400 Phys. Rev. **D10** (1974) p. 2599.
- 2401 [55] J. C. Collins, D. E. Soper, and G. F. Sterman,  
2402 *Factorization of Hard Processes in QCD*,  
2403 *Adv. Ser. Direct. High Energy Phys.* **5** (1989) p. 1,  
2404 arXiv: [hep-ph/0409313 \[hep-ph\]](https://arxiv.org/abs/hep-ph/0409313).
- 2405 [56] K. A. Olive et al., *Review of Particle Physics*,  
2406 Chin. Phys. **C38** (2014) p. 090001.
- 2407 [57] N. Cabibbo, *Unitary Symmetry and Leptonic Decays*,  
2408 Phys. Rev. Lett. **10** (1963) p. 531, [[648\(1963\)](#)].
- 2409 [58] M. Kobayashi and T. Maskawa,  
2410 *CP Violation in the Renormalizable Theory of Weak Interaction*,  
2411 Prog. Theor. Phys. **49** (1973) p. 652.
- 2412 [59] W. F. L. Hollik, *Radiative Corrections in the Standard Model and their Role*  
2413 *for Precision Tests of the Electroweak Theory*,  
2414 Fortsch. Phys. **38** (1990) p. 165.
- 2415 [60] D. Yu. Bardin et al.,  
2416 *ELECTROWEAK RADIATIVE CORRECTIONS TO DEEP INELASTIC*

- 2417            *SCATTERING AT HERA! CHARGED CURRENT SCATTERING,*  
 2418            *Z. Phys. C***44** (1989) p. 149.
- 2419 [61] D. C. Kennedy et al.,  
 2420            *Electroweak Cross-Sections and Asymmetries at the Z0,*  
 2421            *Nucl. Phys. B***321** (1989) p. 83.
- 2422 [62] A. Sirlin, *Radiative Corrections in the SU(2)-L x U(1) Theory: A Simple*  
 2423            *Renormalization Framework*, *Phys. Rev. D***22** (1980) p. 971.
- 2424 [63] S. Fanchiotti, B. A. Kniehl, and A. Sirlin,  
 2425            *Incorporation of QCD effects in basic corrections of the electroweak theory*,  
 2426            *Phys. Rev. D***48** (1993) p. 307, arXiv: [hep-ph/9212285 \[hep-ph\]](#).
- 2427 [64] C. Quigg, “Cosmic Neutrinos,” *Proceedings, 35th SLAC Summer Institute on*  
 2428            *Particle Physics: Dark matter: From the cosmos to the Laboratory (SSI*  
 2429            *2007): Menlo Park, California, July 30- August 10, 2007*, 2008,  
 2430            arXiv: [0802.0013 \[hep-ph\]](#),  
 2431            URL: [http://lss.fnal.gov/cgi-bin/find\\_paper.pl?conf-07-417](http://lss.fnal.gov/cgi-bin/find_paper.pl?conf-07-417).
- 2432 [65] S. R. Coleman and J. Mandula, *All Possible Symmetries of the S Matrix*,  
 2433            *Phys. Rev. 159* (1967) p. 1251.
- 2434 [66] R. Haag, J. T. Lopuszanski, and M. Sohnius,  
 2435            *All Possible Generators of Supersymmetries of the s Matrix*,  
 2436            *Nucl. Phys. B***88** (1975) p. 257.
- 2437 [67] A. Salam and J. A. Strathdee, *On Superfields and Fermi-Bose Symmetry*,  
 2438            *Phys. Rev. D***11** (1975) p. 1521.
- 2439 [68] S. Dimopoulos and H. Georgi, *Softly Broken Supersymmetry and SU(5)*,  
 2440            *Nucl. Phys. B***193** (1981) p. 150.
- 2441 [69] S. Dimopoulos, S. Raby, and F. Wilczek,  
 2442            *Supersymmetry and the Scale of Unification*, *Phys. Rev. D***24** (1981) p. 1681.
- 2443 [70] L. E. Ibanez and G. G. Ross,  
 2444            *Low-Energy Predictions in Supersymmetric Grand Unified Theories*,  
 2445            *Phys. Lett. B***105** (1981) p. 439.
- 2446 [71] W. J. Marciano and G. Senjanovic,  
 2447            *Predictions of Supersymmetric Grand Unified Theories*,  
 2448            *Phys. Rev. D***25** (1982) p. 3092.

- 2449 [72] L. Girardello and M. T. Grisaru, *Soft Breaking of Supersymmetry*,  
 2450 *Nucl. Phys.* **B194** (1982) p. 65.
- 2451 [73] D. J. H. Chung et al.,  
 2452 *The Soft supersymmetry breaking Lagrangian: Theory and applications*,  
 2453 *Phys. Rept.* **407** (2005) p. 1, arXiv: [hep-ph/0312378 \[hep-ph\]](#).
- 2454 [74] J. Hisano et al., *Lepton flavor violation in the supersymmetric standard*  
 2455 *model with seesaw induced neutrino masses*, *Phys. Lett.* **B357** (1995) p. 579,  
 2456 arXiv: [hep-ph/9501407 \[hep-ph\]](#).
- 2457 [75] F. Gabbiani et al., *A Complete analysis of FCNC and CP constraints in*  
 2458 *general SUSY extensions of the standard model*,  
 2459 *Nucl. Phys.* **B477** (1996) p. 321, arXiv: [hep-ph/9604387 \[hep-ph\]](#).
- 2460 [76] F. Gabbiani and A. Masiero,  
 2461 *FCNC in Generalized Supersymmetric Theories*,  
 2462 *Nucl. Phys.* **B322** (1989) p. 235.
- 2463 [77] J. S. Hagelin, S. Kelley, and T. Tanaka, *Supersymmetric flavor changing*  
 2464 *neutral currents: Exact amplitudes and phenomenological analysis*,  
 2465 *Nucl. Phys.* **B415** (1994) p. 293.
- 2466 [78] J. S. Hagelin, S. Kelley, and V. Ziegler, *Using gauge coupling unification and*  
 2467 *proton decay to test minimal supersymmetric SU(5)*,  
 2468 *Phys. Lett.* **B342** (1995) p. 145, arXiv: [hep-ph/9406366 \[hep-ph\]](#).
- 2469 [79] D. Choudhury et al.,  
 2470 *Constraints on nonuniversal soft terms from flavor changing neutral currents*,  
 2471 *Phys. Lett.* **B342** (1995) p. 180, arXiv: [hep-ph/9408275 \[hep-ph\]](#).
- 2472 [80] R. Barbieri and L. J. Hall, *Signals for supersymmetric unification*,  
 2473 *Phys. Lett.* **B338** (1994) p. 212, arXiv: [hep-ph/9408406 \[hep-ph\]](#).
- 2474 [81] B. de Carlos, J. A. Casas, and J. M. Moreno,  
 2475 *Constraints on supersymmetric theories from mu —> e gamma*,  
 2476 *Phys. Rev.* **D53** (1996) p. 6398, arXiv: [hep-ph/9507377 \[hep-ph\]](#).
- 2477 [82] J. A. Casas and S. Dimopoulos,  
 2478 *Stability bounds on flavor violating trilinear soft terms in the MSSM*,  
 2479 *Phys. Lett.* **B387** (1996) p. 107, arXiv: [hep-ph/9606237 \[hep-ph\]](#).
- 2480 [83] C. Borschensky et al., *Squark and gluino production cross sections in pp*  
 2481 *collisions at  $\sqrt{s} = 13, 14, 33$  and 100 TeV*,  
 2482 *Eur. Phys. J.* **C74** (2014) p. 3174, arXiv: [1407.5066 \[hep-ph\]](#).

- 2483 [84] M. Klasen, M. Pohl, and G. Sigl, *Indirect and direct search for dark matter*,  
 2484 Prog. Part. Nucl. Phys. **85** (2015) p. 1, arXiv: [1507.03800](https://arxiv.org/abs/1507.03800) [hep-ph].
- 2485 [85] L. Evans and P. Bryant, *LHC Machine*, JINST **3** (2008) S08001.
- 2486 [86] Vladimir Shiltsev, “Accelerator Physics and Technology,” Aug. 2016,  
 2487 URL: [https://indico.fnal.gov/sessionDisplay.py?sessionId=3&](https://indico.fnal.gov/sessionDisplay.py?sessionId=3&confId=11505#20160811)  
 2488 [confId=11505#20160811](https://indico.fnal.gov/sessionDisplay.py?sessionId=3&confId=11505#20160811).
- 2489 [87] *LEP design report*, Copies shelved as reports in LEP, PS and SPS libraries,  
 2490 Geneva: CERN, 1984, URL: <https://cds.cern.ch/record/102083>.
- 2491 [88] ATLAS Collaboration,  
 2492 *The ATLAS Experiment at the CERN Large Hadron Collider*,  
 2493 JINST **3** (2008) S08003.
- 2494 [89] G. Aad et al., *ATLAS pixel detector electronics and sensors*,  
 2495 JINST **3** (2008) P07007.
- 2496 [90] ATLAS Collaboration, *ATLAS Insertable B-Layer Technical Design Report*,  
 2497 ATLAS-TDR-19 (2010), URL: <http://cdsweb.cern.ch/record/1291633>.
- 2498 [91] ATLAS Collaboration,  
 2499 *Operation and performance of the ATLAS semiconductor tracker*,  
 2500 JINST **9** (2014) P08009, arXiv: [1404.7473](https://arxiv.org/abs/1404.7473) [hep-ex].
- 2501 [92] ATLAS Collaboration, *2015 start-up trigger menu and initial performance*  
 2502 *assessment of the ATLAS trigger using Run-2 data*,  
 2503 ATL-DAQ-PUB-2016-001 (2016),  
 2504 URL: <https://cds.cern.ch/record/2104298>.
- 2505 [93] ATLAS Collaboration, *Performance of the ATLAS Inner Detector Track and*  
 2506 *Vertex Reconstruction in High Pile-Up LHC Environment*,  
 2507 ATLAS-CONF-2012-042, 2012,  
 2508 URL: <https://cds.cern.ch/record/1435196>.
- 2509 [94] ATLAS Collaboration, *Early Inner Detector Tracking Performance in the*  
 2510 *2015 Data at  $\sqrt{s} = 13$  TeV*, ATL-PHYS-PUB-2015-051, 2015,  
 2511 URL: <https://cds.cern.ch/record/2110140>.
- 2512 [95] K Hamano, A Morley, and A Salzburger,  
 2513 “Track Reconstruction Performance and Efficiency Estimation using different  
 2514 ID geometry samples,” tech. rep. ATL-COM-PHYS-2012-1541,  
 2515 plots for a poster at HCP: CERN, Oct. 2012,  
 2516 URL: <https://cds.cern.ch/record/1489674>.

- 2517 [96] ATLAS Collaboration,  
 2518 *Electron reconstruction and identification efficiency measurements with the*  
 2519 *ATLAS detector using the 2011 LHC proton–proton collision data,*  
 2520 *Eur. Phys. J. C* **74** (2014) p. 2941, arXiv: [1404.2240 \[hep-ex\]](#).
- 2521 [97] ATLAS Collaboration, *Topological cell clustering in the ATLAS calorimeters*  
 2522 *and its performance in LHC Run 1* (2016), arXiv: [1603.02934 \[hep-ex\]](#).
- 2523 [98] ATLAS Collaboration, *Jet energy resolution in proton–proton collisions at*  
 2524  $\sqrt{s} = 7 \text{ TeV}$  *recorded in 2010 with the ATLAS detector,*  
 2525 *Eur. Phys. J. C* **73** (2013) p. 2306, arXiv: [1210.6210 \[hep-ex\]](#).
- 2526 [99] ATLAS Collaboration, *Electron performance measurements with the ATLAS*  
 2527 *detector using the 2010 LHC proton–proton collision data,*  
 2528 *Eur. Phys. J. C* **72** (2012) p. 1909, arXiv: [1110.3174 \[hep-ex\]](#).
- 2529 [100] M. Aaboud et al., *Measurement of the photon identification efficiencies with*  
 2530 *the ATLAS detector using LHC Run-1 data* (2016),  
 2531 arXiv: [1606.01813 \[hep-ex\]](#).
- 2532 [101] ATLAS Collaboration, *Electron and photon energy calibration with the*  
 2533 *ATLAS detector using LHC Run 1 data*, *Eur. Phys. J. C* **74** (2014) p. 3071,  
 2534 arXiv: [1407.5063 \[hep-ex\]](#).
- 2535 [102] “Electron and photon energy calibration with the ATLAS detector using  
 2536 data collected in 2015 at  $\sqrt{s} = 13 \text{ TeV}$ ,”  
 2537 tech. rep. ATL-PHYS-PUB-2016-015, CERN, Aug. 2016,  
 2538 URL: <https://cds.cern.ch/record/2203514>.
- 2539 [103] ATLAS Collaboration, *Muon reconstruction performance of the ATLAS*  
 2540 *detector in proton–proton collision data at  $\sqrt{s} = 13 \text{ TeV}$ ,*  
 2541 *Eur. Phys. J. C* **76** (2016) p. 292, arXiv: [1603.05598 \[hep-ex\]](#).
- 2542 [104] ATLAS Collaboration, *Jet energy measurement with the ATLAS detector in*  
 2543 *proton–proton collisions at  $\sqrt{s} = 7 \text{ TeV}$* , *Eur. Phys. J. C* **73** (2013) p. 2304,  
 2544 arXiv: [1112.6426 \[hep-ex\]](#).
- 2545 [105] ATLAS Collaboration,  
 2546 *Jet energy measurement and its systematic uncertainty in proton–proton*  
 2547 *collisions at  $\sqrt{s} = 7 \text{ TeV}$  with the ATLAS detector,*  
 2548 *Eur. Phys. J. C* **75** (2015) p. 17, arXiv: [1406.0076 \[hep-ex\]](#).
- 2549 [106] S. D. Ellis and D. E. Soper,  
 2550 *Successive combination jet algorithm for hadron collisions,*  
 2551 *Phys. Rev. D* **48** (1993) p. 3160, arXiv: [hep-ph/9305266 \[hep-ph\]](#).

- 2552 [107] M. Cacciari and G. P. Salam, *Dispelling the  $N^3$  myth for the  $k_t$  jet-finder*,  
2553 Phys. Lett. B **641** (2006) p. 57, arXiv: [hep-ph/0512210](#).
- 2554 [108] M. Cacciari, G. P. Salam, and G. Soyez, *The anti- $k_t$  jet clustering algorithm*,  
2555 JHEP **04** (2008) p. 063, arXiv: [0802.1189 \[hep-ph\]](#).
- 2556 [109] *Particle-Flow Event Reconstruction in CMS and Performance for Jets, Taus,  
2557 and MET* (2009).
- 2558 [110] ATLAS Collaboration,  
2559 *Tagging and suppression of pileup jets with the ATLAS detector*,  
2560 ATLAS-CONF-2014-018, 2014,  
2561 URL: <https://cds.cern.ch/record/1700870>.
- 2562 [111] M. Cacciari, G. P. Salam, and G. Soyez, *The Catchment Area of Jets*,  
2563 JHEP **04** (2008) p. 005, arXiv: [0802.1188 \[hep-ph\]](#).
- 2564 [112] G. Aad et al., *Performance of b-Jet Identification in the ATLAS Experiment*,  
2565 JINST **11** (2016) P04008, arXiv: [1512.01094 \[hep-ex\]](#).
- 2566 [113] ATLAS Collaboration,  
2567 *Optimisation of the ATLAS b-tagging performance for the 2016 LHC Run*,  
2568 ATL-PHYS-PUB-2016-012 (2016),  
2569 URL: <https://cds.cern.ch/record/2160731>.
- 2570 [114] G. Aad et al., *Performance of algorithms that reconstruct missing transverse  
2571 momentum in  $\sqrt{s} = 8$  TeV proton-proton collisions in the ATLAS detector*  
2572 (2016), arXiv: [1609.09324 \[hep-ex\]](#).
- 2573 [115] ATLAS Collaboration,  
2574 *Prospects for Supersymmetry discovery based on inclusive searches at a*  
2575 *7 TeV centre-of-mass energy with the ATLAS detector*,  
2576 ATL-PHYS-PUB-2010-010, 2010,  
2577 URL: <https://cds.cern.ch/record/1278474>.
- 2578 [116] ATLAS Collaboration,  
2579 *Expected sensitivity studies for gluino and squark searches using the early*  
2580 *LHC 13 TeV Run-2 dataset with the ATLAS experiment*,  
2581 ATL-PHYS-PUB-2015-005, 2015, URL:  
2582 <https://atlas.web.cern.ch/Atlas/GROUPS/PHYSICS/PUBNOTES/ATL-PHYS-PUB-2015-005>.
- 2584 [117] ATLAS Collaboration, *Expected performance of missing transverse  
2585 momentum reconstruction for the ATLAS detector at  $\sqrt{s} = 13$  TeV*,

- 2586           ATL-PHYS-PUB-2015-023, 2015,  
 2587           URL: <https://cds.cern.ch/record/2037700>.
- 2588 [118] ATLAS Collaboration,  
 2589           *Performance of missing transverse momentum reconstruction with the*  
 2590           *ATLAS detector in the first proton–proton collisions at  $\sqrt{s} = 13$  TeV,*  
 2591           ATL-PHYS-PUB-2015-027, 2015,  
 2592           URL: <https://cds.cern.ch/record/2037904>.
- 2593 [119] P. Jackson, C. Rogan and M. Santoni, *Sparticles in Motion - getting to the*  
 2594           *line in compressed scenarios with the Recursive Jigsaw Reconstruction*  
 2595           (2016), arXiv: [1607.08307 \[hep-ph\]](https://arxiv.org/abs/1607.08307).
- 2596 [120] ATLAS Collaboration,  
 2597           *Further searches for squarks and gluinos in final states with jets and missing*  
 2598           *transverse momentum at  $\sqrt{s} = 13$  TeV with the ATLAS detector,*  
 2599           ATLAS-CONF-2016-078, 2016,  
 2600           URL: <https://cds.cern.ch/record/2206252>.
- 2601 [121] C. Rogan, *Kinematical variables towards new dynamics at the LHC* (2010),  
 2602           arXiv: [1006.2727 \[hep-ph\]](https://arxiv.org/abs/1006.2727).
- 2603 [122] M. R. Buckley et al.,  
 2604           *Super-Razor and Searches for Sleptons and Charginos at the LHC*,  
 2605           Phys. Rev. **D89** (2014) p. 055020, arXiv: [1310.4827 \[hep-ph\]](https://arxiv.org/abs/1310.4827).
- 2606 [123] CMS Collaboration, *Search for supersymmetry using razor variables in*  
 2607           *events with b-tagged jets in pp collisions at  $\sqrt{s} = 8$  TeV,*  
 2608           Phys. Rev. D **91** (2015) p. 052018, arXiv: [1502.00300 \[hep-ex\]](https://arxiv.org/abs/1502.00300).
- 2609 [124] Chris Rogan, “RestFrames,” URL: <http://restframes.com>.
- 2610 [125] M. Baak et al., *HistFitter software framework for statistical data analysis*,  
 2611           Eur. Phys. J. **C75** (2015) p. 153, arXiv: [1410.1280 \[hep-ex\]](https://arxiv.org/abs/1410.1280).
- 2612 [126] M. L. Mangano et al., *Matching matrix elements and shower evolution for*  
 2613           *top-quark production in hadronic collisions*, JHEP **01** (2007) p. 013,  
 2614           arXiv: [hep-ph/0611129 \[hep-ph\]](https://arxiv.org/abs/hep-ph/0611129).
- 2615 [127] T. Gleisberg et al., *Event generation with SHERPA 1.1*,  
 2616           JHEP **02** (2009) p. 007, arXiv: [0811.4622 \[hep-ph\]](https://arxiv.org/abs/0811.4622).
- 2617 [128] S. Schumann and F. Krauss,  
 2618           *A Parton shower algorithm based on Catani-Seymour dipole factorisation*,  
 2619           JHEP **03** (2008) p. 038, arXiv: [0709.1027 \[hep-ph\]](https://arxiv.org/abs/0709.1027).

- 2620 [129] F. Maltoni and T. Stelzer,  
 2621 *MadEvent: Automatic event generation with MadGraph*,  
 2622 *JHEP* **02** (2003) p. 027, arXiv: [hep-ph/0208156 \[hep-ph\]](#).
- 2623 [130] T. Sjöstrand et al., *An Introduction to PYTHIA 8.2*,  
 2624 *Comput. Phys. Commun.* **191** (2015) p. 159, arXiv: [1410.3012 \[hep-ph\]](#).
- 2625 [131] S. Alioli et al., *A general framework for implementing NLO calculations in shower Monte Carlo programs: the POWHEG BOX*, *JHEP* **06** (2010) p. 043,  
 2626 arXiv: [1002.2581 \[hep-ph\]](#).
- 2628 [132] J. Alwall, R. Frederix, S. Frixione, V. Hirschi, F. Maltoni, O. Mattelaer, H.  
 2629 -S. Shao, T. Stelzer, P. Torrielli, M. Zaro,  
 2630 *The automated computation of tree-level and next-to-leading order differential*  
 2631 *cross sections, and their matching to parton shower simulations*,  
 2632 *JHEP* **07** (2014) p. 079, arXiv: [1405.0301 \[hep-ph\]](#).
- 2633 [133] S. Frixione et al., *NLO QCD corrections in Herwig++ with MC@NLO*,  
 2634 *JHEP* **01** (2011) p. 053, arXiv: [1010.0568 \[hep-ph\]](#).
- 2635 [134] S. Agostinelli et al., *GEANT4: A simulation toolkit*,  
 2636 *Nucl. Instrum. Meth. A* **506** (2003) p. 250.
- 2637 [135] ATLAS Collaboration,  
 2638 *Search for squarks and gluinos in final states with jets and missing transverse*  
 2639 *momentum at  $\sqrt{s} = 13$  TeV with the ATLAS detector*,  
 2640 *Eur. Phys. J. C* **76** (2016) p. 392, arXiv: [1605.03814 \[hep-ex\]](#).
- 2641 [136] R. D. Cousins, J. T. Linnemann, and J. Tucker,  
 2642 *Evaluation of three methods for calculating statistical significance when*  
 2643 *incorporating a systematic uncertainty into a test of the background-only*  
 2644 *hypothesis for a Poisson process*, *Nucl. Instrum. Meth. A* **595** (2008) p. 480.
- 2645 [137] ATLAS Collaboration, *Search for squarks and gluinos with the ATLAS*  
 2646 *detector in final states with jets and missing transverse momentum using*  
 2647  *$4.7 \text{ fb}^{-1}$  of  $\sqrt{s} = 7$  TeV proton-proton collision data*,  
 2648 *Phys. Rev. D* **87** (2013) p. 012008, arXiv: [1208.0949 \[hep-ex\]](#).
- 2649 [138] ATLAS Collaboration, *Jet energy measurement with the ATLAS detector in*  
 2650 *proton-proton collisions at  $\sqrt{s} = 7$  TeV*, *Eur. Phys. J. C* **73** (2013) p. 2304,  
 2651 arXiv: [1112.6426 \[hep-ex\]](#).
- 2652 [139] ATLAS Collaboration, *Single hadron response measurement and calorimeter*  
 2653 *jet energy scale uncertainty with the ATLAS detector at the LHC*,  
 2654 *Eur. Phys. J. C* **73** (2013) p. 2305, arXiv: [1203.1302 \[hep-ex\]](#).

- 2655 [140] ATLAS Collaboration, *Jet Calibration and Systematic Uncertainties for Jets*  
2656 *Reconstructed in the ATLAS Detector at  $\sqrt{s} = 13 \text{ TeV}$ ,*  
2657 ATL-PHYS-PUB-2015-015, 2015,  
2658 URL: <https://cds.cern.ch/record/2037613>.
- 2659 [141] ATLAS Collaboration, *Jet energy resolution in proton-proton collisions at*  
2660  *$\sqrt{s} = 7 \text{ TeV}$  recorded in 2010 with the ATLAS detector,*  
2661 *Eur. Phys. J. C* **73** (2013) p. 2306, arXiv: [1210.6210 \[hep-ex\]](https://arxiv.org/abs/1210.6210).
- 2662 [142] ATLAS Collaboration,  
2663 *Performance of algorithms that reconstruct missing transverse momentum in*  
2664  *$\sqrt{s} = 8 \text{ TeV}$  proton–proton collisions in the ATLAS detector* (2016),  
2665 arXiv: [1609.09324 \[hep-ex\]](https://arxiv.org/abs/1609.09324).
- 2666 [143] G. J. Feldman and R. D. Cousins,  
2667 *A Unified approach to the classical statistical analysis of small signals*,  
2668 *Phys. Rev. D* **57** (1998) p. 3873,  
2669 arXiv: [physics/9711021 \[physics.data-an\]](https://arxiv.org/abs/physics/9711021).
- 2670 [144] ATLAS Collaboration, *Search for squarks and gluinos with the ATLAS*  
2671 *detector in final states with jets and missing transverse momentum using*  
2672  *$\sqrt{s} = 8 \text{ TeV}$  proton–proton collision data*, *JHEP* **09** (2014) p. 176,  
2673 arXiv: [1405.7875 \[hep-ex\]](https://arxiv.org/abs/1405.7875).



---

2674

## *The Standard Model*

2675

2676 **Compressed region N-1 plots**

add some  
text or cut  
this

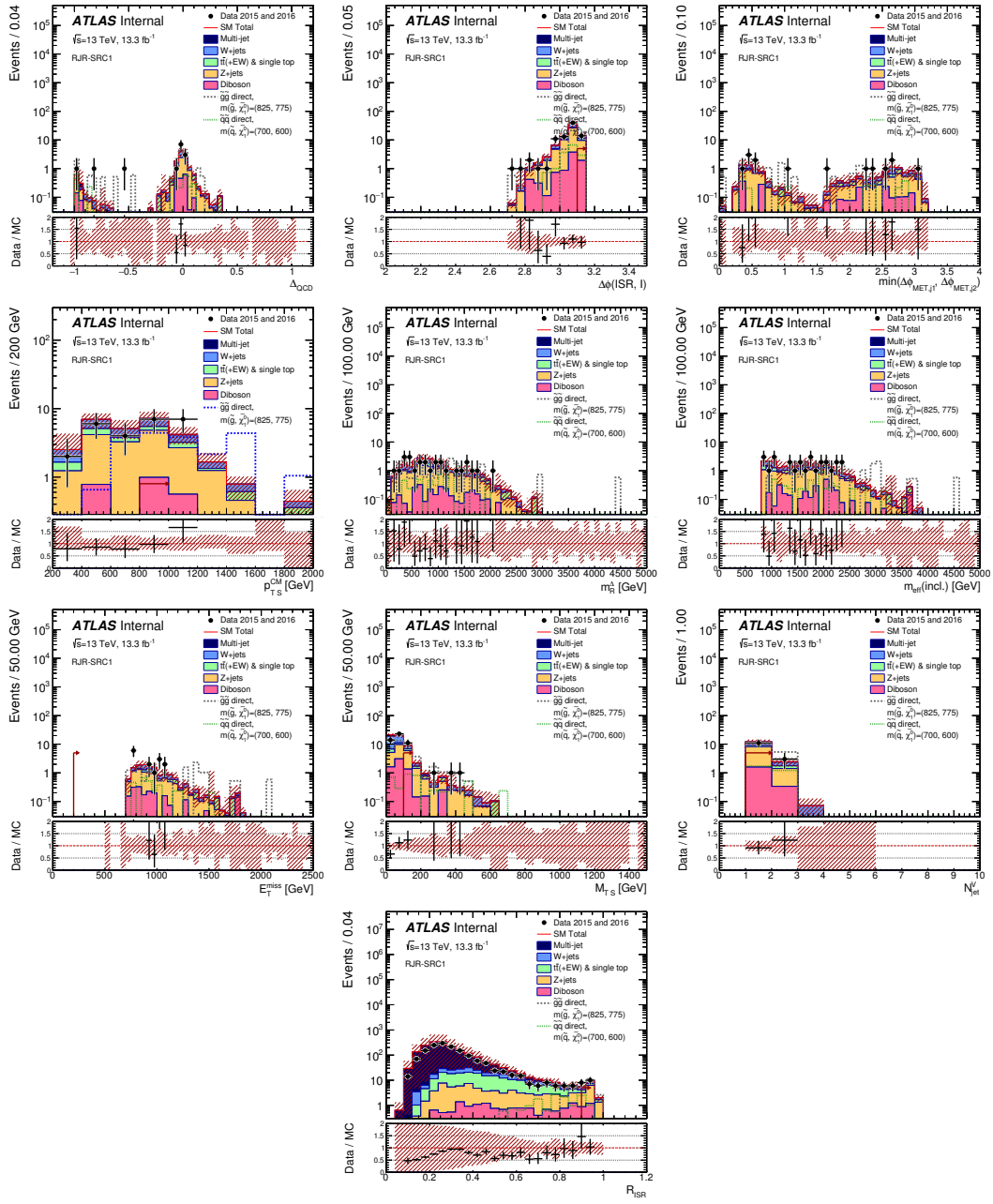


Figure 1

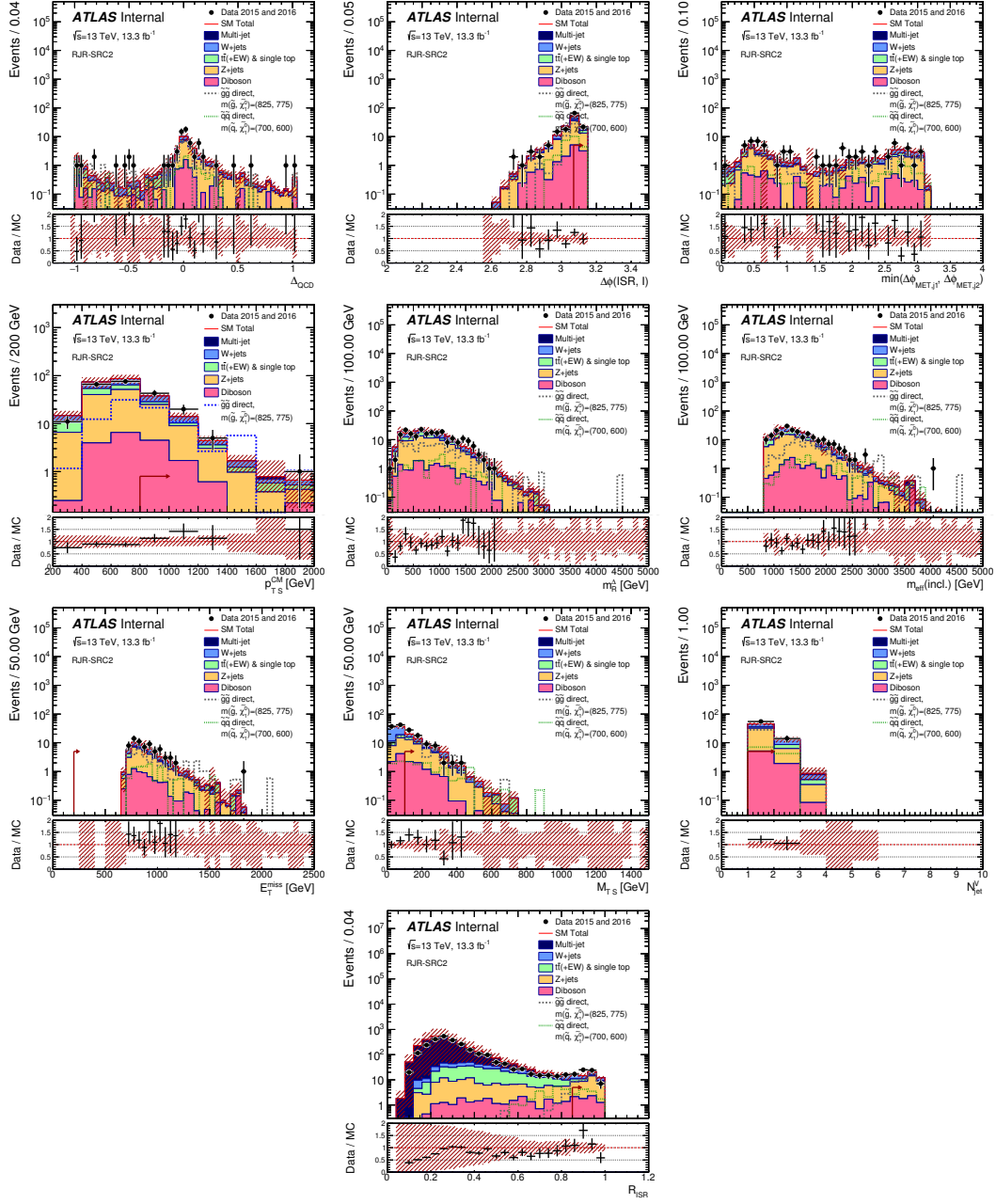


Figure 2

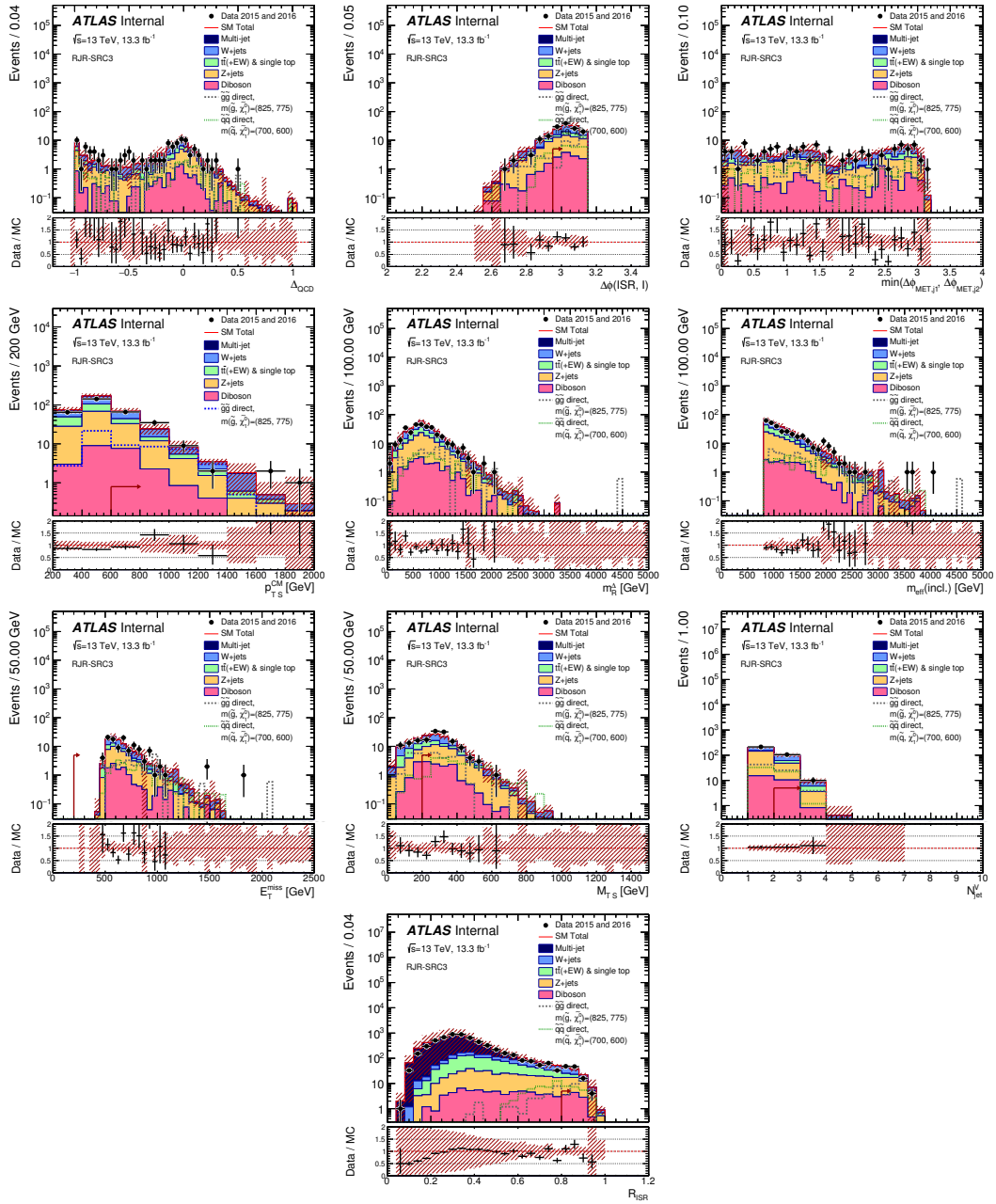


Figure 3

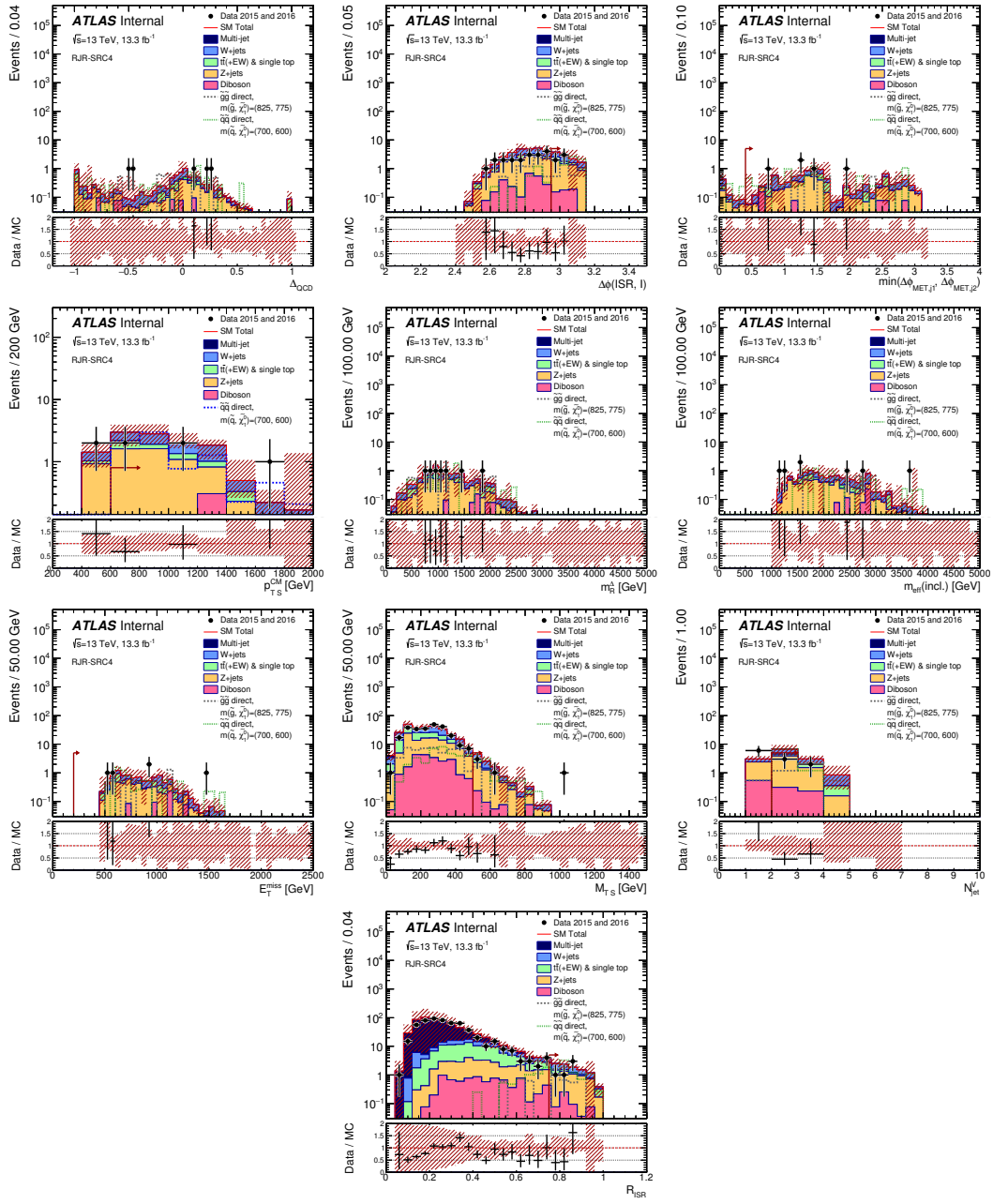


Figure 4

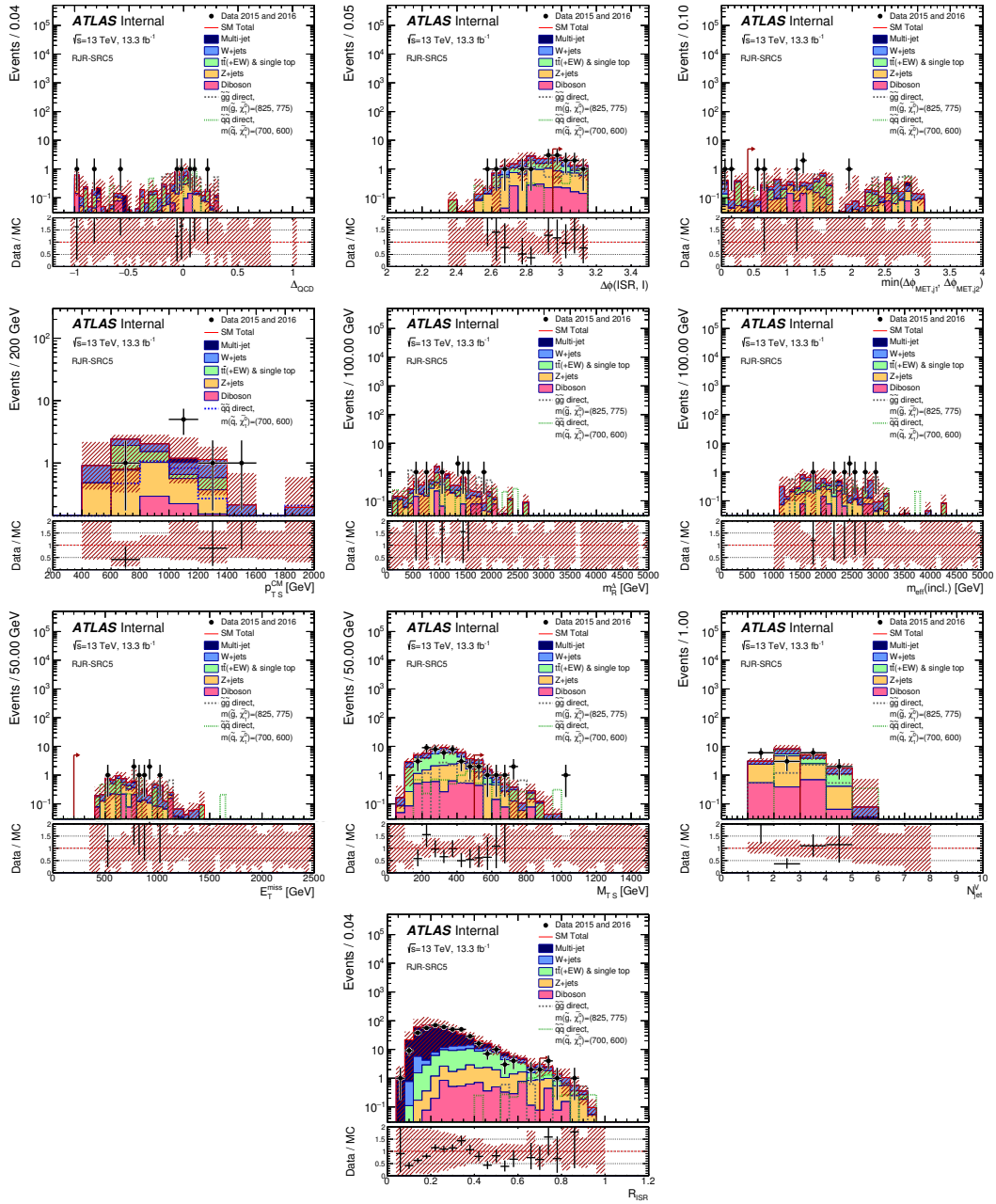


Figure 5

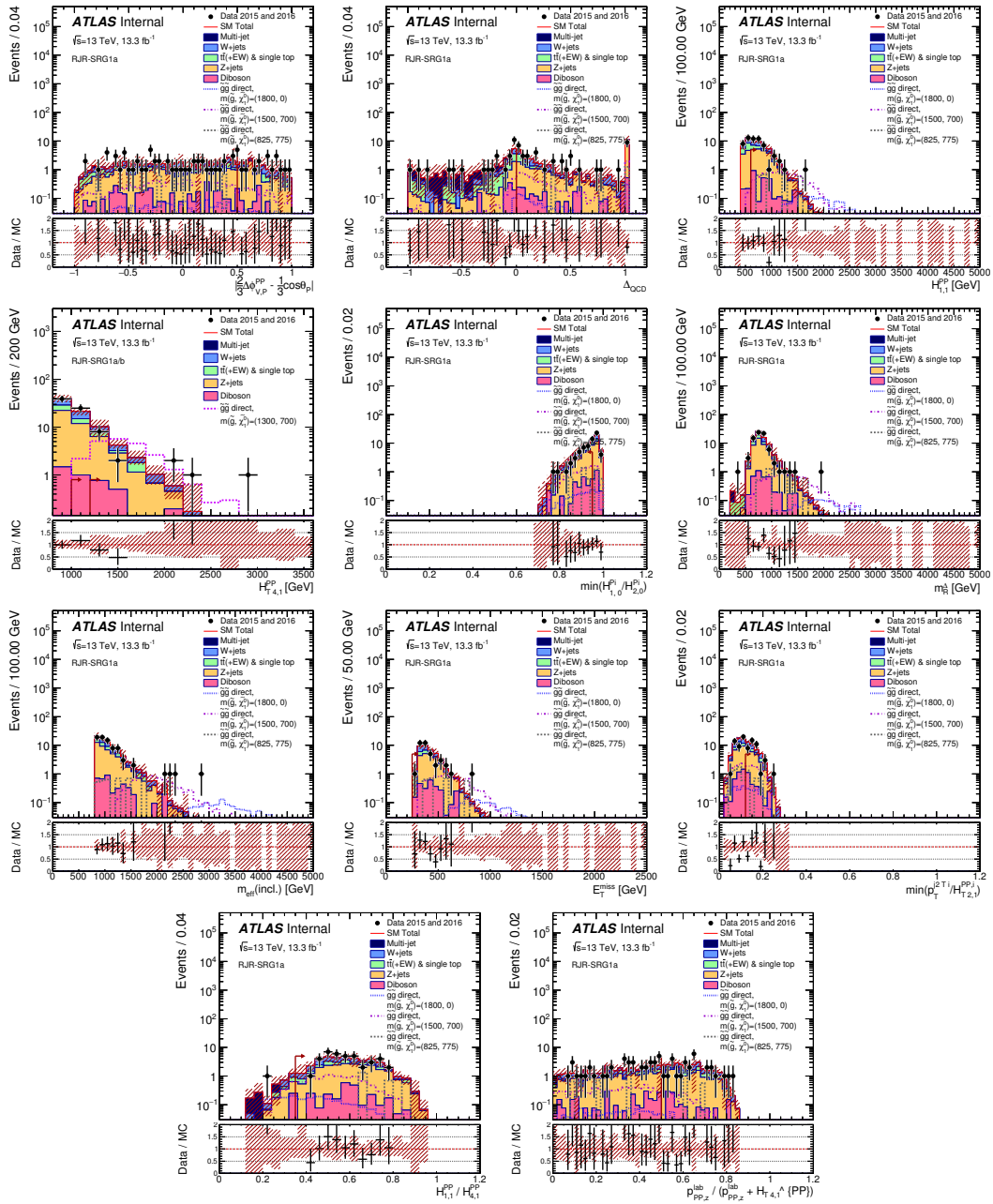


Figure 6

Figure 7

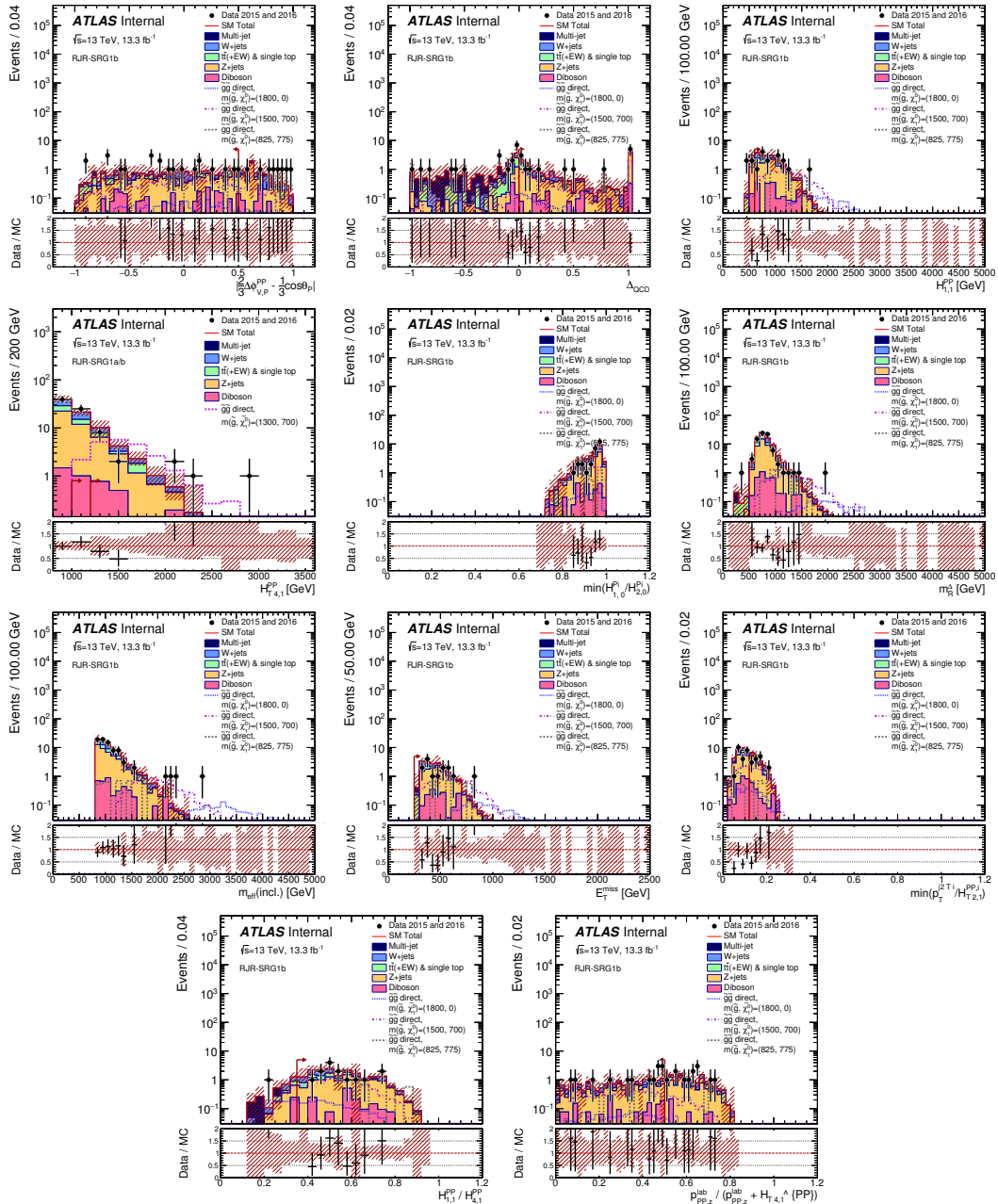


Figure 8

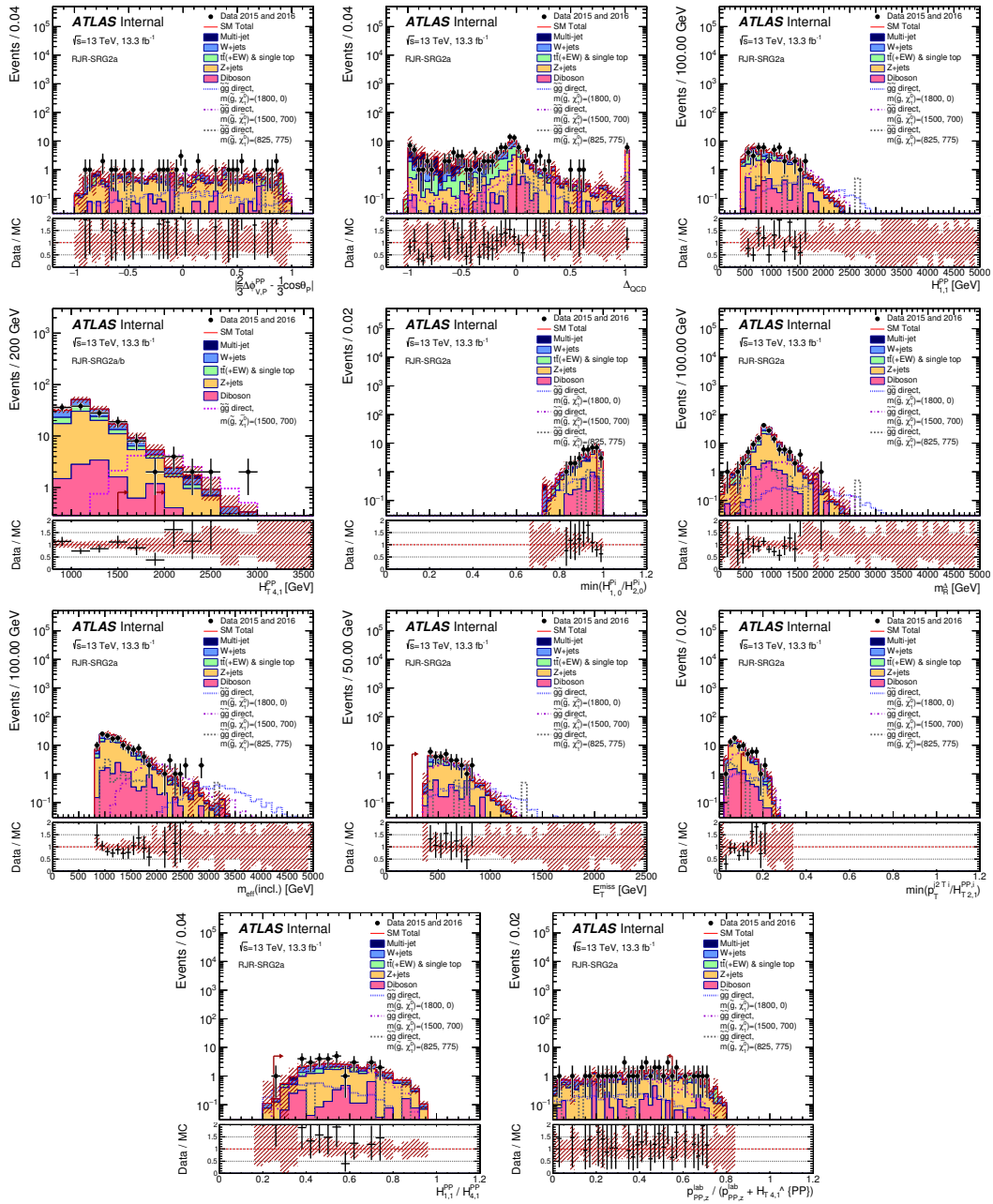


Figure 9

Figure 10

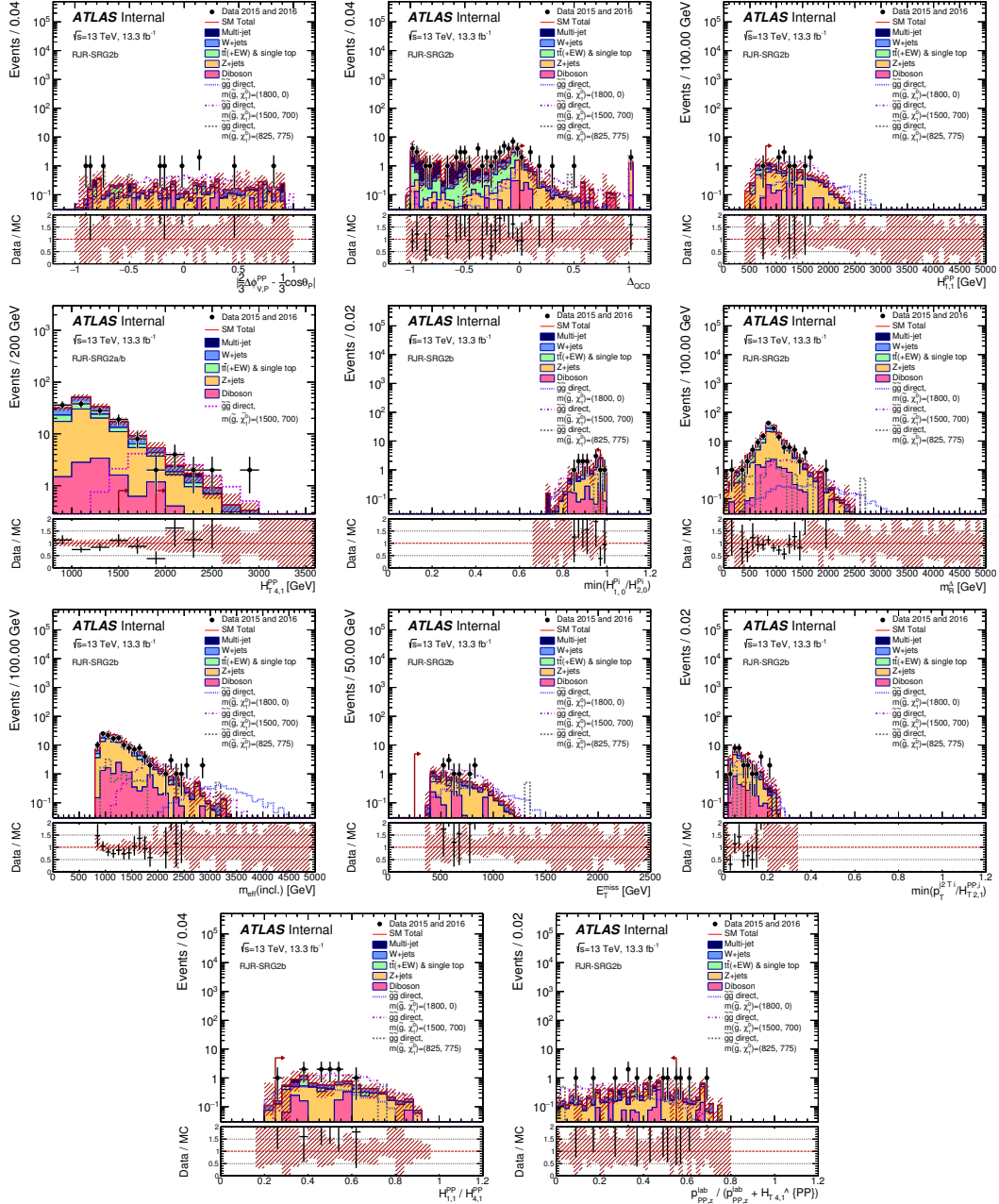


Figure 11

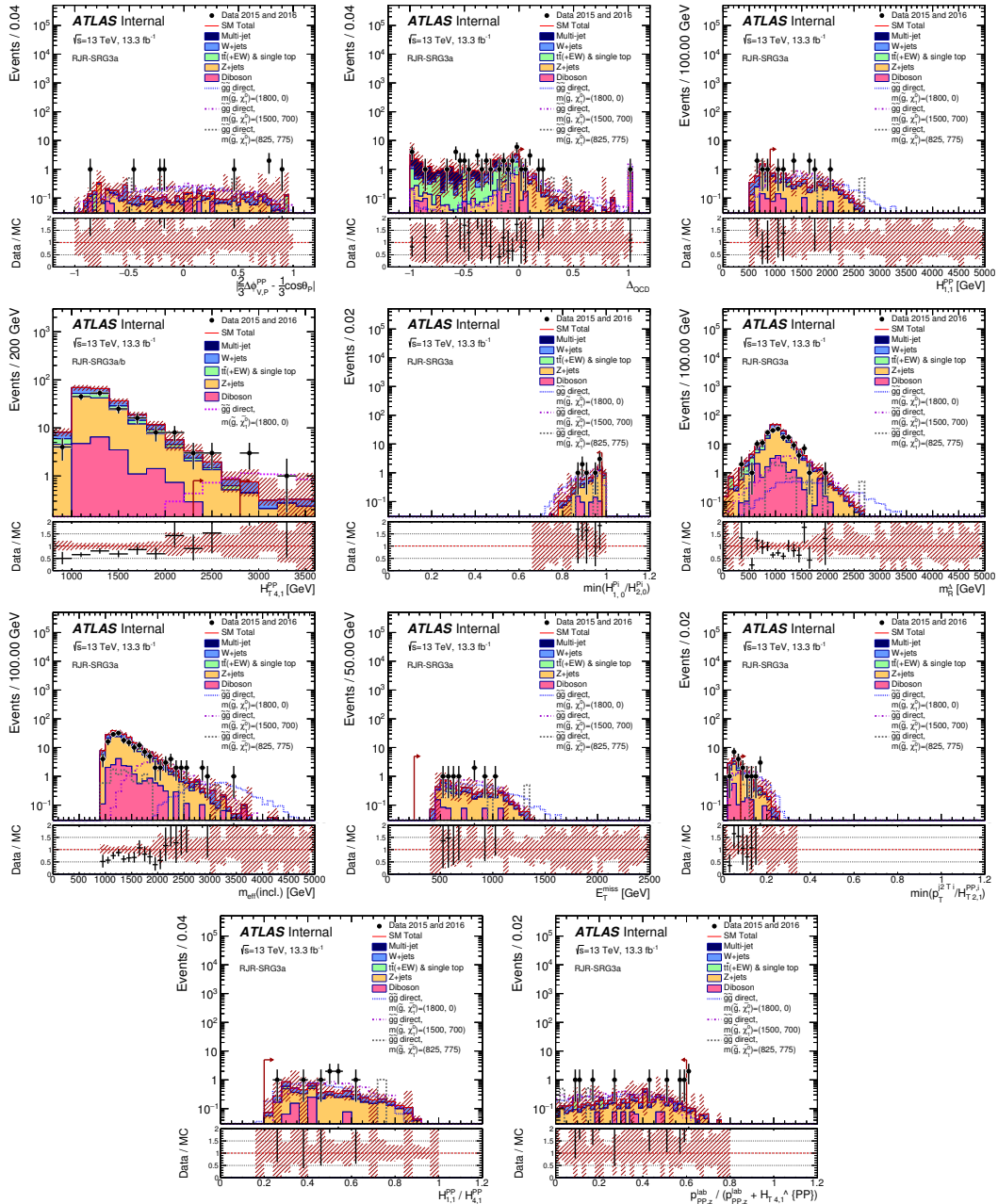


Figure 12

Figure 13

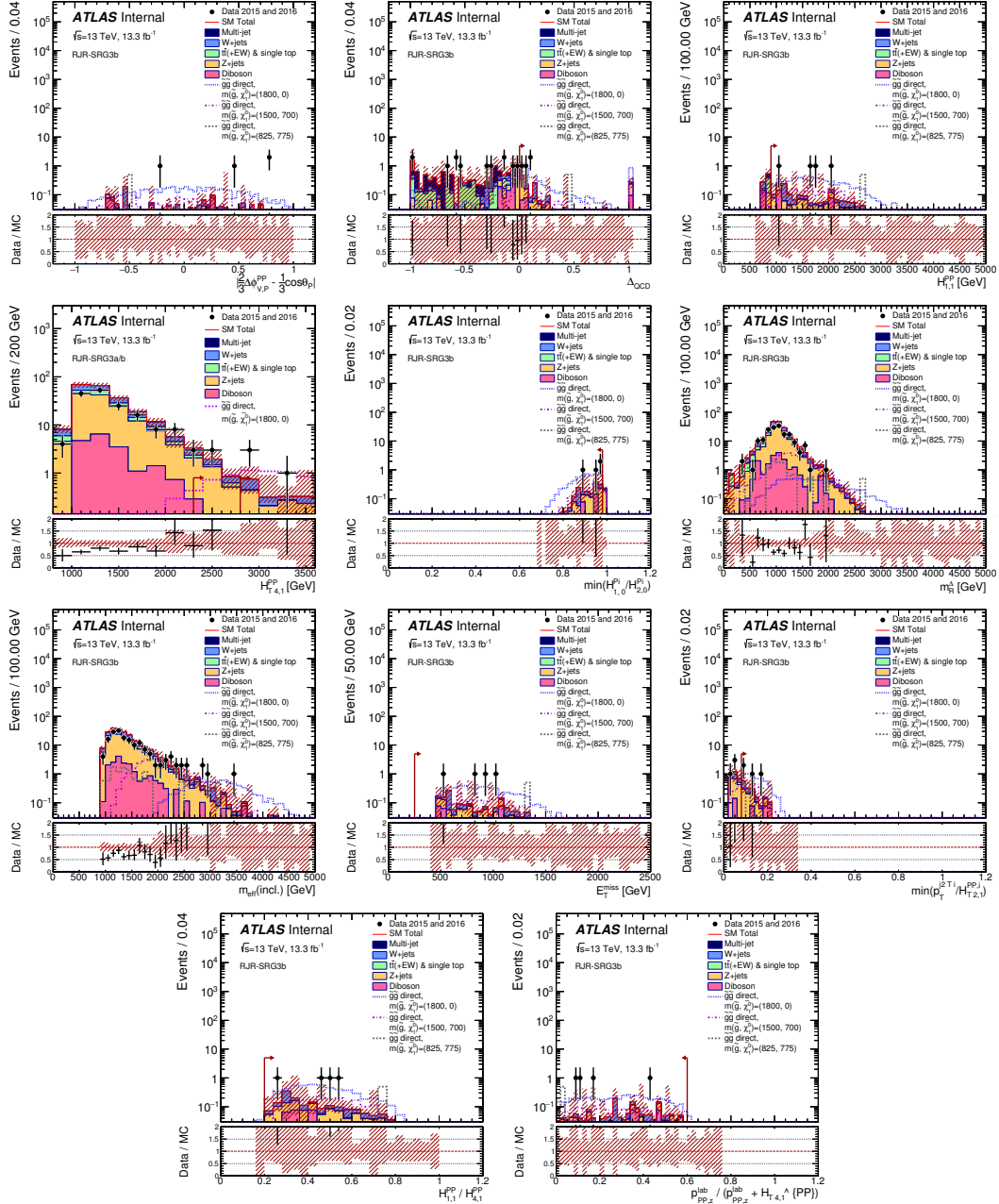


Figure 14

Figure 15

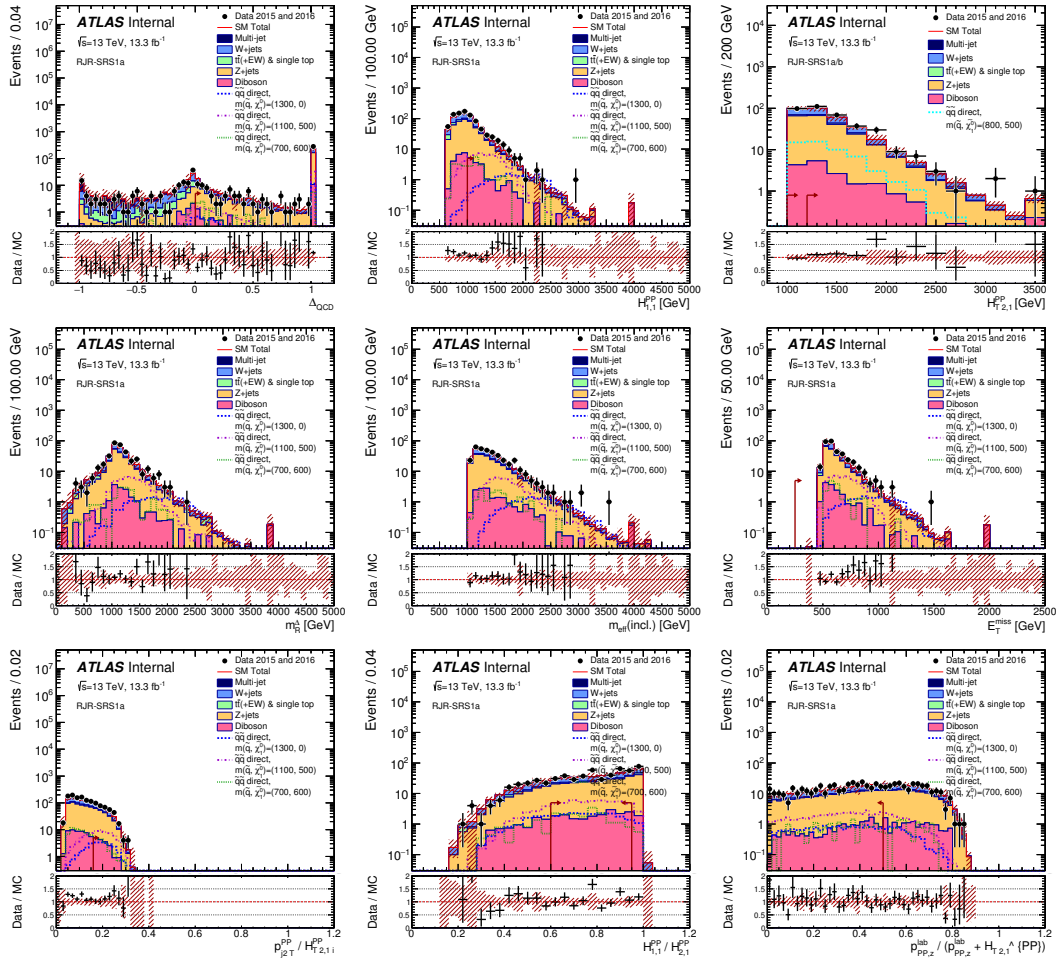


Figure 16

Figure 17

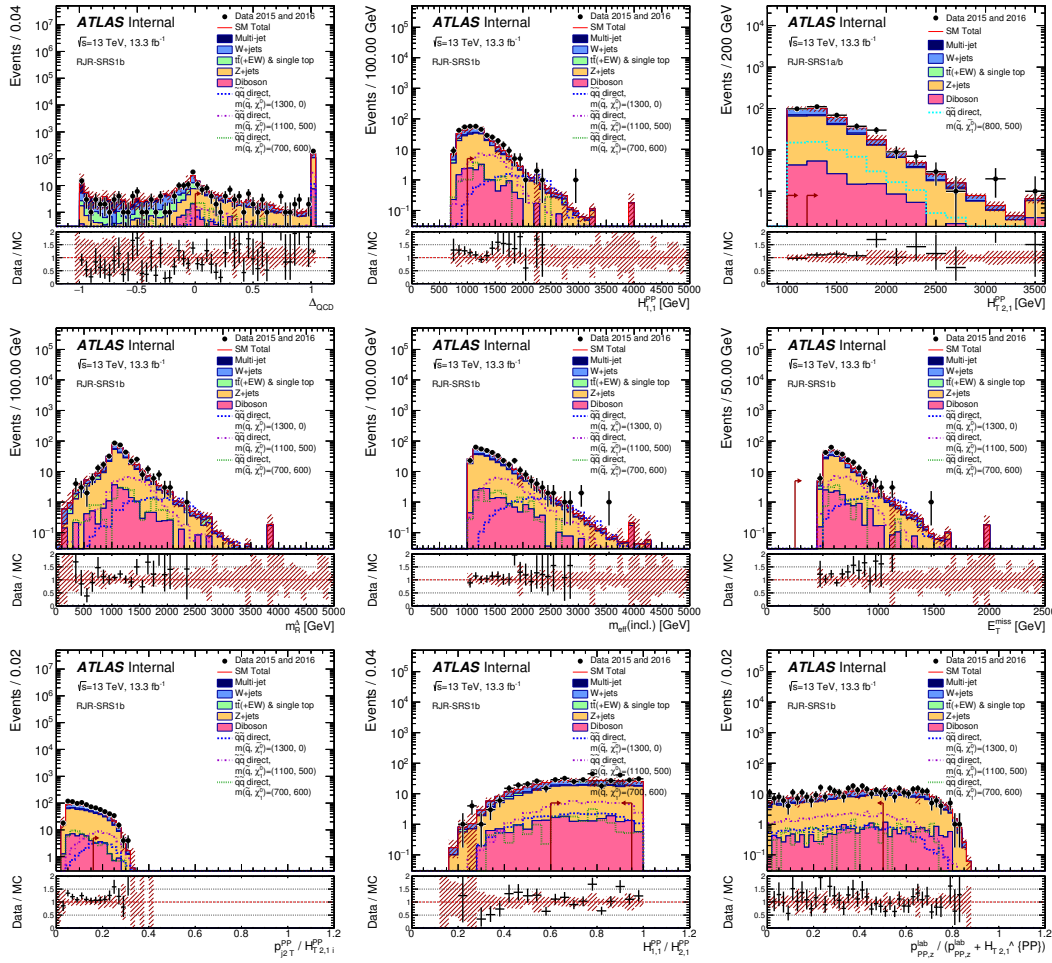


Figure 18

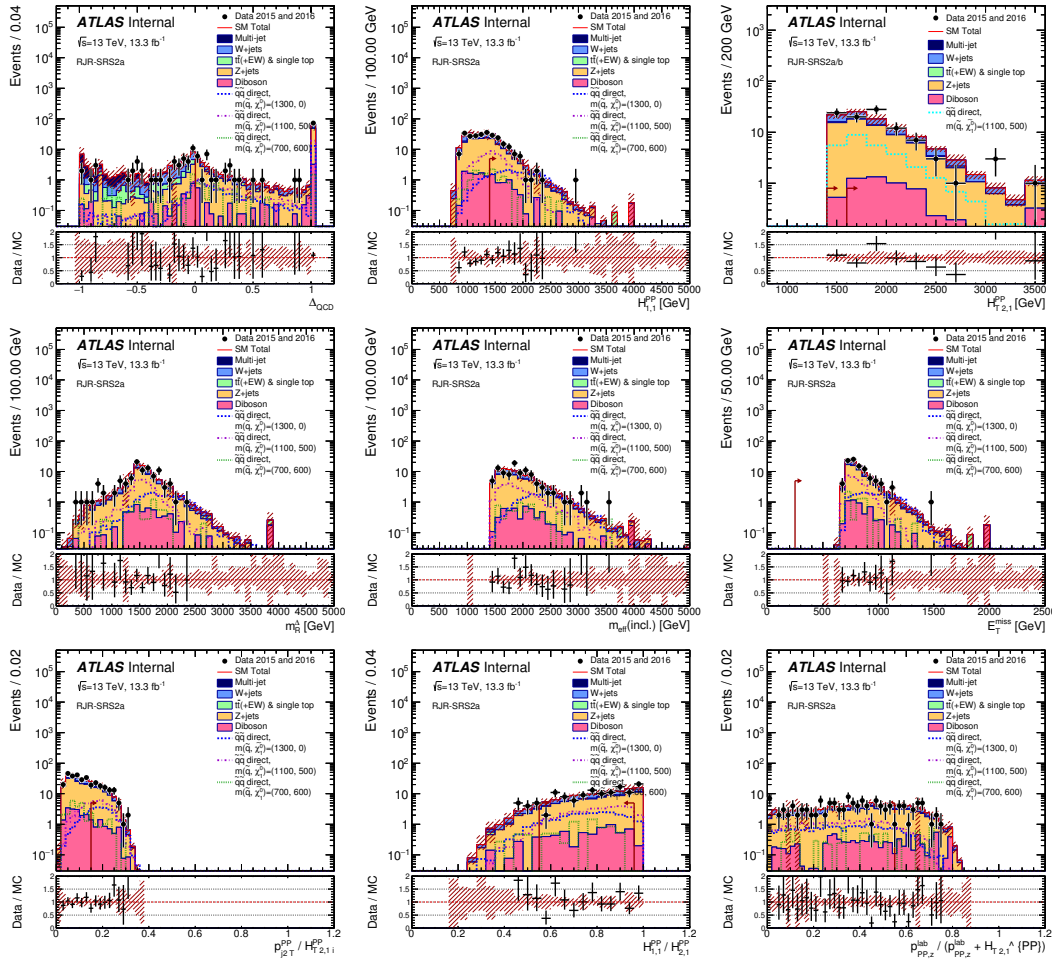


Figure 19

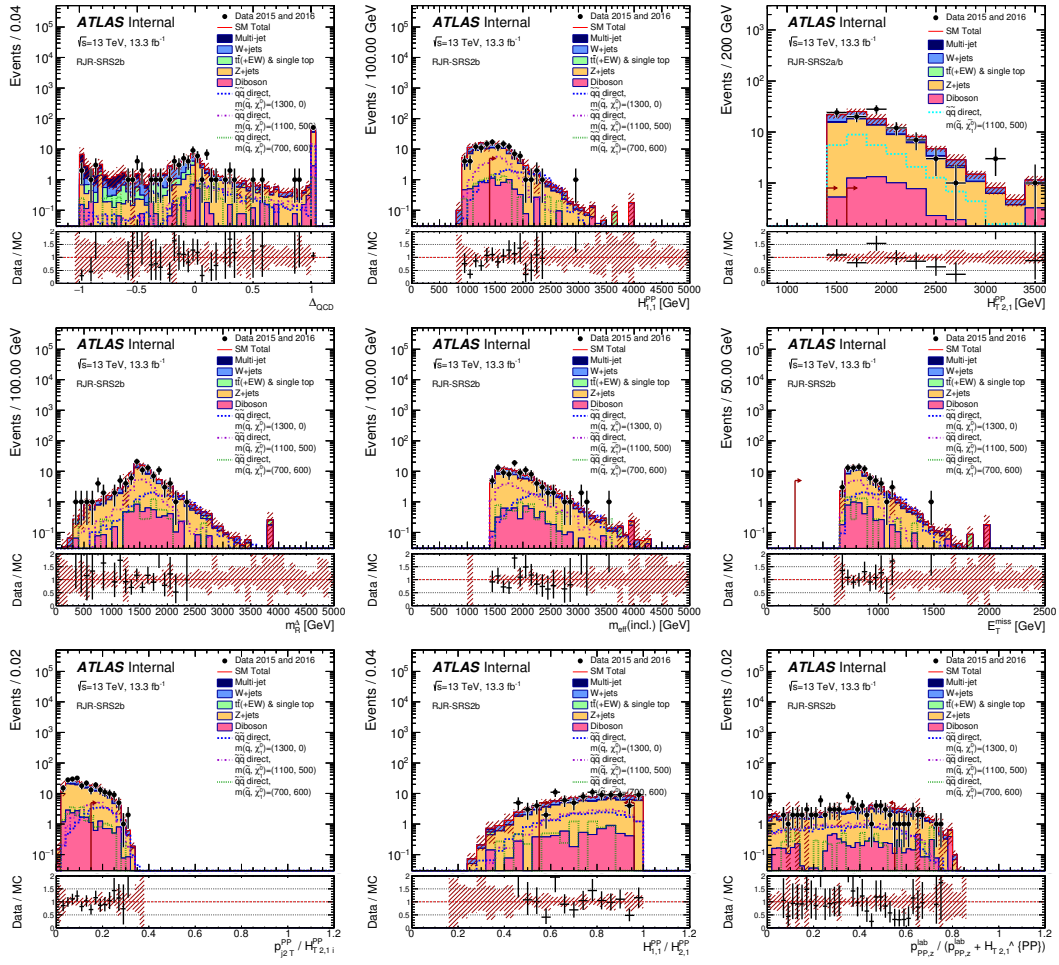


Figure 20

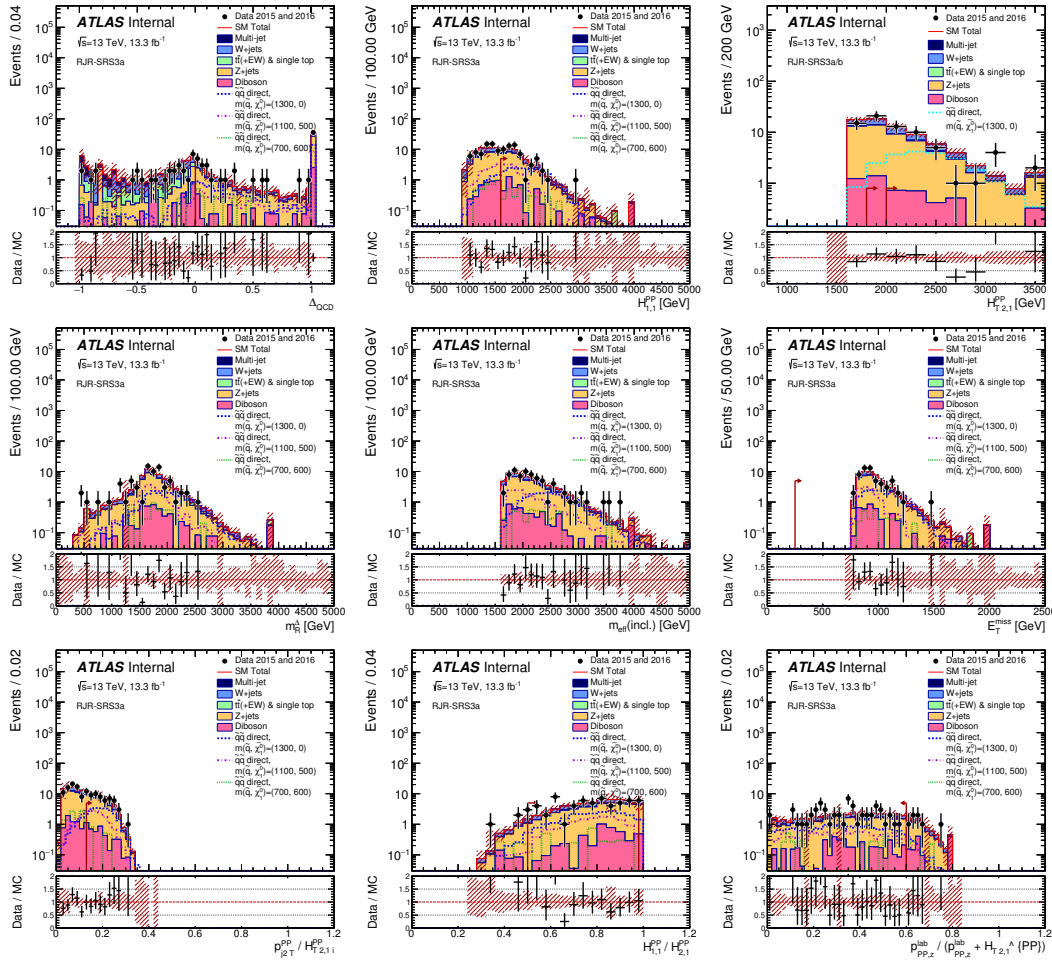


Figure 21

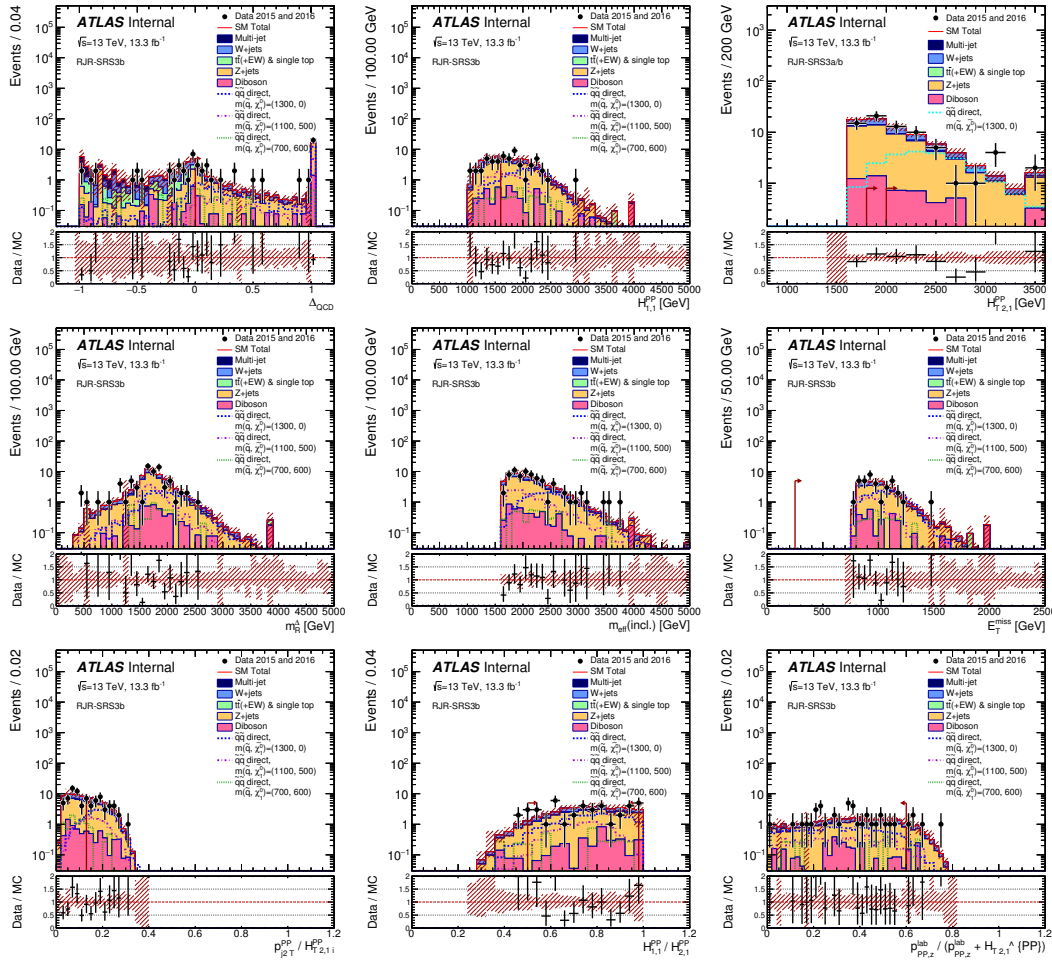


Figure 22